SURFACE AND INTERNAL STRUCTURES OF CONTINUOUSLY-CAST STAINLESS STEELS

by

Rolf Sandor Laki M.Sc. (Stockholm)

Thesis submitted in fulfilment of the requirements for the degree of Doctor of Philosophy at the Department of Metallurgy, University of Sheffield.

August 1984

To my parents

ACKNOWLEDGEMENTS

I would like to thank Professors G.J. Davies, B.B. Argent and G.W. Greenwood for the provision of research facilities and the University of Sheffield for financial support.

I am extremely grateful to my supervisors Dr. J. Beech and Professor G.J. Davies for their invaluable guidance and continued encouragement throughout this research work.

My gratitude is due to the technical staff of the Department of Metallurgy, in particular Mr. E. Needham, Mr. A. Harvey and Mr. S. Bater for their assistance with the casting operations.

I would like to thank my colleagues in the Department, in particular R. Pratt, A. Ogilvy, C. Desideri, I. Estrada, M. Mendez and L. Elias for many useful discussions and their friendship throughout my stay.

SUMMARY

Surface ripple formation in ferritic (17% and 20%Cr) and austenitic (18%Cr-8%Ni to 25%Cr-20%Ni) stainless steels has been studied using an up-hill teeming technique. The extent of ripple formation decreases with increasing superheat, increasing teeming rate and increasing surface roughness of the mould walls. Austenitic stainless steels exhibit more severe rippling than ferritic grades. Within the austenitic range of alloys, the highly alloyed grades show enhanced surface rippling as compared with low alloyed austenitic alloys.

Both experimental results and data from modelling studies presented in the literature have shown that ripples are formed by periodic freezing of the meniscus.

In conjunction with a non-steady state heat transfer model, a new method for the treatment of curved boundaries in finite difference analysis has been established in order to give a more accurate representation of heat flow in the meniscus region.

Good agreement between predictions and experimental observations of the influence of the nature of gas atmospheres on surface ripple formation in ingots has been shown. In relationship to continuous casting the healing time was found to have a stronger influence on the degree of meniscus solidification than the mould/metal heat transfer coefficient. For the continuous casting of steel slabs it has been shown that there is a significant influence of the thermal conductivity of the casting flux and the thickness of the flux layer between the mould and the strand. In addition, solidification characteristics were shown to influence the extent of meniscus solidification. The variation of ripple formation between different austenitic alloys is attributed to

differences in physical strength of the solidifying shell.

Measurements of the δ-ferrite content show a variation across continuously-cast slabs. A numerical model based on finite difference analysis of heat transfer and the diffusion-controlled transformation of δ-ferrite to austenite, allowing for a moving boundary, has been developed for continuous casting of slabs. The predictions showed good agreement between measured and predicted secondary dendrite arm spacings for columnar structures and that the cross-sectional variation of δ-ferrite is determined by the casting speed and the spray intensities in the secondary cooling zone.

CONTENTS

Page

CHAPTER 1

Introduction

Continuous casting is, together with the oxygen processes, considered to be the largest and most important development in the metallurgical industry in modern times. The process can be said to have had its breakthrough in the second half of the 1950's, when continuous casting of steel became feasible, and its development has since been very rapid.

Through the years, numerous researches have been carried out on the process. To date, the major effort has been towards improving the engineering-side of the process and thus, there is still a lack of general knowledge of the metallurgical events taking place in the solidifying material as it passes through a continuous casting machine.

As with any other metallurgical process, continuous casting has its own characteristic defects. In the literature, a whole variety of defects have been reported, such as cracks of various types, oscillation marks and centre-line defects.

Oscillation marks are a defect which mainly has been studied in carbon steels. For example, it is well known that steels containing 0.1%C have the poorest surface quality in terms of oscillation marks. In the literature, it has recently been established that the main mechanism for the formation of this defect is the heat transfer in the meniscus region, which causes the meniscus to solidify. The same mechanism also operates in the formation of surface ripples on static, chill-cast ingots. The emphasis of the research concerning ripples and oscillation marks on ferrous alloys has, to date, been put on carbon steels. However, in the present work, ripple and oscillation mark formation on stainless steels is investigated. The influence of solidification mode, i.e. ferritic, ferritic/austenitic and austenitic solidification, on ripple formation is studied together with the effect of principal casting parameters such as teeming rate, rate of heat extraction and superheat, using an up-hill teeming technique. In order to assess further the solidification kinetics in the meniscus region during casting and to simulate the conditions prevailing in this area during continuous casting, a 2-dimensional heat transfer model is presented, in which special attention is given to the curved boundary of the system.

Furthermore, the variation of δ-ferrite across continuously-cast stainless steel slabs is examined. Also, in order to study the influence of casting parameters on the δ-ferrite distribution during continuous casting, a 1-dimensional heat transfer model is presented, which predicts microstructural features such as secondary dendrite arm spacings and fraction δ-ferrite.

Thus, after a review of the literature (Chapter 2), the development of the numerical models is presented in Chapter 3. The experimental techniques adopted are given in Chapter 4, which is followed by a presentation and discussion of the experimental results (Chapter 5). Correlation of the observations with the predictions of the numerical analyses is given in Chapter 6. Conclusions drawn in the present work are given in Chapter 7, together with suggestions for further work.

CHAPTER 2

Literature Review

2.1 Solidification of Stainless Steels.

2.1.1 The phase diagrams.

The basic information on the solidification paths of austenitic stainless steels is given by the ternary equilibrium diagram for the Fe-Cr-Ni system (Figure 2.1). In Figure 2.2, the projection of the boundary lines of the three phase field ($L+\delta+\gamma$) in the system is given. It can be seen that close to the Fe-corner, there is a transition from peritectic to eutectic equilibria when moving from the Fe-Ni to the Cr-Ni edge of the system. In all, four solid phases are identified[1]; three solid solutions (austenite, δ-ferrite and martensite) and one intermetallic phase (σ). The latter phase has been shown to have no influence on the melting equilibria[2,3]. A very comprehensive survey of the Fe-Cr-Ni system has been presented by Rivlin and Raynor[4]. Vertical sections through constant Cr and Ni compositions, respectively, provide a general guide for commercial austenitic stainless steels (Figures 2.3 and 2.4).

As the above-mentioned ternary system gives fundamental information on austenitic stainless steels, the binary system Fe-Cr provides a basis for the understanding of ferritic stainless steels. Figure 2.5 shows that Fe and Cr exhibit complete solid solubility at all compositions at high temperatures, the stable phase being ferrite. As a consequence, the range of existence of austenite is restricted, thus forming the γ-loop.

2.1.2 Solidification of ferritic stainless steels.

From the constitution of the binary phase diagram Fe-Cr, it can be seen that the solidification path is simple in ferritic stainless steels. Ferritic grades usually contain 12 to 28%Cr[5], thus avoiding the γ-loop. However, if the carbon and nitrogen contents are too high, the γ-loop expands, since these elements are both austenite stabilisers. For example, if the sum of C and N is 0.13% (given equal weight), a chromium content of 24% in the alloy will be required to avoid completely the austenite loop[6,7]. Austenite formed on cooling can be transformed to martensite at room temperature, thus causing embrittlement. The austenite usually precipitates as a grain boundary network and as laths within the grains[5].

The high degree of compositional uniformity found in the dendritic structure of ferritic stainless steels can be attributed to the significant atomic mobility in ferrite, the diffusion rate being approximately 100 times greater in ferrite than in austenite[8]. This means that in ferritic grades, it can be assumed that there is complete mixing in both the solid and the liquid during freezing and, thus, equilibrium solidification (the lever rule) is applicable to this type of alloy[8]. In fully austenitic alloys, the assumption of complete mixing in the solid is not valid due to slower diffusion rates. Thus, a Scheil-type of segregation model[9] has to be used in these alloys since this model is based on the assumption that there is complete mixing in the liquid and no mixing in the solid during solidification.

2.1.3 Solidification of austenitic stainless steels.

Depending on the alloy content, austenitic stainless steels can solidify in four different modes[10-12]. These are commonly expressed in terms of their dependence on the amount of the austenite stabiliser, nickel, present, i.e.

Type A (19/6-8) $L \rightarrow L + \delta \rightarrow \delta \xrightarrow{\text{solid-state}} \delta + \gamma$

Type B (19/10) $L \rightarrow L + \delta \rightarrow L + \delta + \gamma \rightarrow \delta + \gamma$

Type C (19/12) $L \rightarrow L + \gamma \rightarrow L + \gamma + \delta \rightarrow \gamma + \delta$

Type D (19/14) $L \rightarrow L + \gamma \rightarrow \gamma$

Another way of describing this has been put forward by Hammar[13], who introduced the factor Φ, which is a function of the Cr and Ni equivalents as,

$$\Phi = Ni_{eq} - 0.75Cr_{eq} + 0.257$$

where

$$Ni_{eq} = \%Ni + 0.31x\%Mn + 22x\%C + 14.2x\%N$$
$$Cr_{eq} = \%Cr + 1.37x\%Mo$$

If $\Phi<0$, ferritic solidification will occur and if $\Phi>0$, the alloy freezes to austenite. When $\Phi=0$, precipitation of both ferrite and austenite is to be expected. In welding, other definitions of the solidification modes in austenitic stainless steels have been used.

Experimental work on Type A alloys[12] showed that although the solid-state transformation was evident, some ferrite transformed during quenching after solidification. The temperature interval during which the reaction $\delta \rightarrow \delta + \gamma$ takes place was 4 to 14°C, the ferrite and austenite produced having significantly different compositions from those of the solid and liquid during solidification. The above-mentioned solid-state reaction occurs at a temperature (approximately 1350°C in 18/8-alloys) which is dependent on the growth rate and which decreases with increasing growth rate[14].

Type B alloys solidify primarily to δ-ferrite but this process is interrupted by the precipitation of austenite when the three phase region (L+δ+γ) of the system is reached. The austenite can grow by either a peritectic or an eutectic reaction. It has been suggested, with the aid of the phase diagram, that a so-called "halo" eutectic reaction is most likely to occur[12,14]. However, the cross-over point between the peritectic and the eutectic reactions is not well established and the similarity between the formation of Type B structures and structures in other peritectic alloy systems suggests that the peritectic reaction could be taking place in the three phase region[14]. Recently, it has been suggested that the transition from the peritectic to the eutectic reaction occurs when the Ni and Cr contents are roughly 12 and 19%, respectively[15]. Furthermore, it has been found that the phase which precipitates first is dependent on the nitrogen content and the cooling rate. Austenite precipitates when the nitrogen content is high and the cooling rate is low[16]. Additionally, depending on the segregation pattern obtained, it has been observed that the last interdendritic liquid can solidify to δ-ferrite[17].

The mechanisms involved in the solidification of Type C alloys are more uncertain. Fredriksson[18] found, using a uni-directional solidification technique, that δ-ferrite and austenite dendrites can grow simultaneously side by side. The explanation for this was that the difference in composition between the two phases is too small to produce an ordinary coupled eutectic structure[19]. A similar explanation has been put forward by McTighe[16]. Another mechanism presented in the literature is the eutectic "halo" reaction, δ-ferrite being the phase precipitating on the circumference of the primary austenite[12].

The solidification of Type D alloys is by far the simplest and most straight forward of all austenitic stainless steels. As can be seen from Figure 2.2, the liquid never reaches the three phase region ($L+\delta+\gamma$), thus only austenite is expected to precipitate throughout the whole temperature range and this is in agreement with reports in the literature[12,13,20].

Microsegregation in austenitic stainless steels is such that when austenitic solidification occurs, the ferrite stabilising elements, e.g. Cr, Mo, Si, Al, Nb and Ti are rejected by the solid[13,20-23]. Some nickel can, during austenitic freezing, segregate to the liquid. This is due to the partitioning of the element and to the slow diffusion rate in austenite. The elements accumulating in the liquid during ferritic freezing are mainly Ni, C and N.

2.1.4 δ-ferrite in austenitic stainless steels.

From the previous section, it can be appreciated that austenitic stainless steels often exhibit a structure consisting of both austenite and δ-ferrite. It has been found that the δ-phase has the following effects on the steel,

(i) it contributes to the prevention of hot cracking during solidification in casting and welding[24-30];

(ii) it causes an increase in proof stress and tensile strength by dispersion hardening of the steel[31-33];

(iii)it causes a deterioration of the hot workability of the steel[34-41]. This is associated with the δ-ferrite/austenite interface and the most detrimental effect is experienced when the interfacial area is at a maximium[42].

In addition to the obvious influence of chemical composition, the δ-ferrite is also influenced by both deformation and changes in cooling rate.

When deforming the steel plastically, an increase in internal energy will take place. This, together with a reduction of diffusion distances, causes an acceleration of the transformation of δ-ferrite to austenite[43,44]. It has also been found that an increase in the degree of strain reduces the ferrite content[45].

The influence of cooling rate on the δ-ferrite content is of great importance during solidification and subsequent cooling to room temperature. In an austenitic weld metal (18.2Cr-10Ni), it was found that at low solidification rates, a fairly high initial ferrite content was present, but the subsequent slow cooling below the solidus temperature caused a reduction of the final ferrite content[25]. Heat treatment of as-cast 19/10-alloys followed by cooling at different rates at sub-solidus temperatures also showed that a decrease in the cooling rate between 1300^{o}-1000^{o}C causes a decrease in the δ-ferrite content[44].

Nassar[46] investigated unidirectionally-solidified ingots of both Type A and B alloys and found that higher cooling rates resulted in higher ferrite contents.

In steady-state experiments of Type A, B and C alloys, it was observed that an increase in the temperature gradient and/or the growth rate had no influence on the final δ-ferrite content[12]. The same conclusions were deduced from results obtained from Type B alloys[47].

Pereira[14] found that with decreasing growth rate, less δ-ferrite is formed from the liquid, but the difference is eliminated by the time the solidus is reached. It was also observed that the δ-ferrite content increases with increasing cooling rate and that it is the residence time between the solidus and approximately 1000°C that determines the final ferrite content. Furthermore, Type C alloys were observed to be very sensitive to changes in growth rate, simultaneous growth of both austenite and δ-ferrite taking place at low rates and austenitic growth followed by ferrite precipitation occurring at higher growth rates.

Although contradictory results have been presented in the literature as regards the amount of δ-ferrite in castings and its dependence on cooling rate[46,48-51], it is well established that the δ-ferrite varies considerably across an ingot section[14,44,49,52-53]. The lowest ferrite content is observed at the edges in chill-castings with a gradual increase to a maximum further in from the surface, followed by a decrease at the centre. The cooling rate in ingots varies such that it decreases from the surface towards the core and then increases at the centre[54,55]. This variation in the δ-ferrite content has been attributed to the time spent in the temperature region immediately after solidification[14,49]. The low δ-ferrite content at the surface of chill-castings has been explained by the faster cooling rate, which produces fine dendrite arms and hence, facilitates a more rapid homogenisation on cooling in the sub-solidus region[5,13,14].

Takeuchi[52] investigated the influence of electromagnetic stirring on the δ-ferrite distribution in continuously-cast stainless steel blooms. Above a certain critical stirring intensity, a uniform ferrite distribution could be obtained. The critical stirring intensity depended on the steel grade. Furthermore, in the so-called white bands formed due to the stirring, a high δ-ferrite content was found in a 304-steel. This was attributed to the depletion of austenite stabilising elements (C, Mn, Ni) at the solidification front by the washing effect produced by stirring.

Kinoshita et al.[56] examined the dissolution of δ-ferrite in continuously-cast 18/8 stainless steel slabs and found that at a 1/4 of the thickness (no slab-dimensions given), the ferrite content was at a minimum. This was believed to be caused by reheating during the casting process.

The morphology of the δ-ferrite in as-cast structures depends on solidification mode and cooling rate. In Type A alloys, the austenite is formed by a Widmanstatten transformation[12,14,17,57-59]. The morphology of the thus formed residual δ-ferrite has been termed "lathy", although it is the austenite that forms the laths[60-62]. This type of δ-phase has been observed to have a Kurdjumov-Sachs type orientation relationship[63] with the austenite[61].

In the microstructure found in Type B alloys, in which the austenite is formed around the ferrite during solidification, the residual δ-ferrite in the dendrite cores is commonly referred to as "skeletal"[64] or "vermicular"[58,62,65]. In addition, a structure described as a cell-like network has been found in this type of alloy[16,58,59,62,66]. It is not clear whether this latter morphology is associated with the skeletal or lathy morphologies or is a transition between the two. In the ordinary skeletal structure it has been observed that the ferrite has no crystallographical relationship with the austenite[62], whereas a Kurdjumov-Sachs relationship has been suggested to be prevailing in the cell-like network[66]. In an analysis utilising STEM (Scanning Transmission Electron Microscopy) it was found that the same concentration profiles of the solute elements are present across the δ-ferrite/austenite interfaces in both the skeletal and the cell-like network morphologies[64,67]. This indicates that the formation of the latter type of ferrite is diffusion controlled.

The morphology of the δ-ferrite in Type C steels is the least well-established. Pereira[14] found that as the ferrite precipitates on the circumference of the austenite, it continues to grow directly from the liquid. However, as the temperature decreases, the stability of the δ-phase decreases, resulting in a transformation to austenite. As a consequence of the slow diffusion rates at lower temperatures, some un-transformed ferrite can be found in the as-cast structures. In the case of dendritic growth of both phases from the liquid, other morphologies are observed[14,16,18,19].

The thus-formed δ-ferrite in "austenitic" stainless steels can, on subsequent cooling to room temperature, transform further to σ-phase[68-70]. Furthermore, on reheating to 1200°C a reversion of this phase transformation, i.e. the formation of δ-ferrite from σ-phase, has been observed[70].

2.2 Ripple Formation during Casting.

Ripples are transverse surface depressions on castings. The nomenclature for this defect found in the literature is often related to the casting process, procedure or appearance, e.g.:

Surface ridge	-Electro slag remelting (ESR) when meniscus freezing has occurred.
Surface corrugations	-ESR when the defect is due to changes in power supply.
Meniscus mark	-Used for experimental ingots.
Wrinkle	-Continuous casting of billets.
Ripple mark	-Direct chill casting and continuous casting of billets.
Oscillation mark	-Continuous casting.
Reciprocation mark	-Continuous casting.
Teeming lap	
Cold shut	
Double teem	-Overflow of the solidified meniscus.
Lapped interface	
Misrun	

In the following the term ripples or ripple formation will be used as a general name for the surface depressions formed during solidification.

2.2.1 Occurrence of surface ripples.

One of the first reports of ripples in castings was made in 1919 by Andrew et al.[71]. It was recognised that the ripples, considered as peculiarities rather than defects, were formed under strong chill conditions during slow teeming and at low superheats. The influence of teeming rate and superheat on the number of reject castings was investigated by Thomas[72], who found that when the casting temperature and speed were increased, the number of rejects due to cracks increased, while the number of rejects due to ripples decreased.

In a study concerning the surface appearance of continuously-cast non-ferrous metals, Waters[73,74] studied ripple formation in statically-cast lead ingots, using a high-speed cine camera[74]. It was found that the casting speed had a significant influence on ripple formation. Using a similar photographical technique, Thornton[75] observed, in a study of the effect of mould dressings on ingot structures, that ripple formation is dependent on factors such as mould temperature, superheat, teeming rate, oxidation of the steel surface and the volatility of the mould dressing. The appearance of the ripples was dependent on the mould coating. In general, mould coatings improve the surface quality in terms of ripple formation[75-81].

The adoption of moulds with various degrees of surface roughness, which in essence has the same effect as using mould coatings in so far as the rate of heat extraction is concerned, has shown that the rougher the mould wall, the smaller the extent of ripple formation[80-82].

The gas atmosphere in the meniscus region has also been reported to have a significant influence on the appearance of ripples[81-83]. An atmosphere of helium gives more severe rippling than atmospheres of oxygen or nitrogen[83]. The effect of different mould material/atmosphere combinations on ripple formation have been studied by Tomono et al[84,85]. The behaviour and shape of the meniscus as the melt rose in the mould was observed by filming through a quartz window built into the mould system. An attempt was made to express theoretically the shape of the meniscus in terms of the surface tension of the liquid. This failed close to the mould wall (2-5mm), presumably due to the the influence of other parameters such as gas, lubricant, melt chemistry, temperature, gravity and other forces acting in the region. Ackermann et al.[81] investigated the surface appearance of pure Sn and Al as a function of different atmospheres. The severest surface rippling occurred in helium atmospheres, whereas the smoothest surfaces were produced when casting in vacuum. Similar observations have been made by other workers[84-86].

As mentioned previously, the casting speed influences the occurrence of ripples[72,74,75]. It has, in general, been observed that with increasing teeming rate, the surface rippling diminishes and the inter-ripple distance becomes smaller[80-82]. Stemple et al.[87] found the opposite effect as regards the inter-ripple distance. However, the validity of these results is questionable since, in the experimental procedure used, there seems to have been poor independent control of the superheat and teeming rate. In fact, the superheat varied between 18°C and 131°C in the results which were presented as a function of casting speed. This makes it quite possible for the influence of one of these two parameters to influence the results which are due to the other.

In a similar way to the teeming rate, the superheat affects ripple formation in that the severity is reduced by an increase in the casting temperature[71,72,75,80-82]. Again, Stemple et al.[87] presented contradictory findings but the same criticism as above can explain the discrepancy.

In most experimental studies of surface rippling in casting reported in the literature, low melting point materials have been used. As mentioned previously, pure Sn and Al was used by Ackermann et al.[81] and it was found that Al exhibited the deepest ripples, whereas the largest number of ripples was produced on the Sn ingot. This was attributed to differences in surface tension, thermal properties and melting points. Other model systems used are pure Pb[73,74,82], Sn-Pb alloys[87] and organic analogues[80,85].

One of the most well-known systems in which the alloy content has been found to have a significant influence on surface rippling is carbon steel. In a study of the heat flux during the continuous casting of steels, Singh and Blazek[88] found that the poorest surface appearance occurred in alloys with 0.1%C, the heat flux being at a minimum around this composition. The same observations have been made in both continuous casting[89] and static casting[80,90-92].

2.2.2 Mechanisms of ripple formation.

Several mechanisms have been proposed to explain surface rippling during casting. One of the first was dependent on the surface tension of the liquid against the solid formed at the mould wall[73,74]. Based on experience from direct-chill casting of Al-alloys, Siebel et al.[93] suggested that contraction of the shell caused remelting and bleeding, thus giving rise to rippling. Similar proposals have been put forward by other research workers[94,95]. The major observation which Thornton[75] made from cine films was that solidification occurred over the meniscus. The solid tip then regained contact with the mould wall by bending back due to the ferrostatic pressure building up during teeming. This is in agreement with observations made on Al-alloys[96] and steels[84,97]. Jacobi[98] obtained results similar to those presented by Singh and Blazek[88] for continuous casting. This led to the theory that the shrinkage due to the δ-ferrite to austenite transformation induces ripple formation below the meniscus. The same conclusions were drawn by Grill et al.[89].

The concept of meniscus freezing as the phenomenon causing ripples was firmly established by Saucedo[80], who in a thorough investigation studied ripples on the products of a whole range of casting processes, consistently finding evidence for meniscus solidification. The severe rippling occurring in carbon steels around 0.1%C was confirmed. However, the conclusions made elsewhere[88,89,98] about the ferrite to austenite transformation causing the defect due to shrinkage were shown to be incorrect, as evidenced by ripple formation on chill-cast bismuth, which expands on solidification.

An attempt to distinguish between three different surface features on chill castings has been presented by Wray[82]. These were:

Type I -Closely spaced grooves that reflect the thermally-induced corrugation of the solidifying shell near its leading edge. The spacing of the grooves decreases with increasing casting speed.

Type II -Larger wrinkles that are associated with the uneven thickening of the shell, such thickening being presumably due to uneven temperature distribution on the mould surface. The spacing increases with increasing casting speed.

Type III -Surface laps formed by periodic freezing of the meniscus.

It was observed that the type III feature occurred only at low casting speeds and type II at higher speeds. Therefore, it is questionable whether or not both type II and III features actually are caused by meniscus freezing, the only difference being that at higher speeds the solid meniscus is thinner since there is less time available for the solidification of the meniscus. Thus, the ferrostatic pressure building up inside the solid meniscus causes it to bend back. The uneven thickening of the shell is due to the difference in heat transfer between rippled and non-rippled areas.

The observations made by Tomono[84,85], and lately by Ackermann[81], merely serve as confirmation of the conclusions put forward by Saucedo[80]. Stemple et al.[87] suggested that wave motion of the liquid surface during teeming can be a major cause of ripple formation. However, based on metallographical evidence presented in the literature[80,85,99], this is unlikely. Instead, surface wave motion can explain the presence of so-called intermediate ripples[80,87] and the above-mentioned type I features. Support for this is provided by the observation of the rather insensitive behaviour of the latter as regards the influence of casting parameters[80,82,87].

2.3 Continuous Casting of Steels.

2.3.1 The continuous casting process.

The development of the continuous casting process, which, together with the oxygen steelmaking processes, is one of the most important metallurgical advances, has been very rapid during the last two decades. In 1958 there were 17 plants in operation outside the USSR and in 1964 the number was 104. By 1976, the number had risen to over 2000 continuous casting machines with an annual capacity exceeding 100 million tons[100]. It is expected that by 1985, 56% of the output of crude steel in the world will be continuously-cast[101]. The financial and technical advantages over the ingot route are[101],

(i) fewer processing steps in steel production;

(ii) reduced investment costs;

(iii) reduced manning and labour costs;

(iv) reduced energy consumption and costs;

(v) improved yield;

(vi) improved quality in certain products.

In terms of operating costs, it has been found that for billets a continuously-cast product costs between 88 and 96% of the cost via the ingot route, depending on steel plant, caster and throughput. For slabs, the value can be as low as 81%. The yield from liquid steel to semi-finished product for rolling is 80-85% by the ingot route and 95-98% by the continuous casting process.

A general lay-out of a continuous casting machine is shown in Figure 2.6. There, it can be seen that the main constituents are the ladle, tundish, mould, secondary cooling zone, withdrawal unit, radiation cooling zone and cutting unit.

2.3.2 Cooling in the mould.

The mould is probably one of the most important parts of the continuous casting machine. Many of the defects found in continuously-cast products have been related to the fundamental processes taking place in the mould, ranging from breakouts to surface cracks and shape defects[102].

In the first continuous casting machines, the mould was straight with the strand moving vertically downwards. When higher casting speeds and thicker sections were required, this design was changed to machines with a straight mould with bending/straightening rolls or a curved mould with straightening rolls in order to keep the height of the plant reasonably low.

The materials used in the mould are usually copper or copper alloys, plated with chromium to improve wear resistance. The two most common type of moulds are the block- and the plate-moulds[103-105]. The block-mould has its mould cavity machined from a cast or forged copper block and vertical cooling-water channels drilled around the perimeter. The plate-mould consists of four copper plates which are attached to steel backing plates, with water channels either in the steel or copper plates, thus forming an adjustable mould. The block moulds are usually used for casting beam blanks, blooms and billets, whilst the plate moulds are commonly used for slab casting. For smaller sections, tubular section moulds are used.

An oscillating movement of the mould was introduced in order to prevent sticking of the steel to the mould wall, thus reducing the risk of breakouts due to rupture of the skin. This was first done by Junghans[106,107]. The next step in the development of the oscillating mould was the employment of "negative strip"[103], which means that the mould, during the downstroke, travels slightly faster than the strand, thus further avoiding sticking of the metal to the mould wall. Currently, a stroke of 5-8mm and an oscillation frequency of 50-200 cycles,min^{-1} is common in practice. The trends for the future are in the direction of a shorter stroke and a higher frequency.

During casting, lubricant is fed into the mould. There are two main types of lubricant, oils such as rapeseed oil or other vegetable oils, mainly used in billet casting[105] and, secondly, casting powders for slab casting. These powders typically having a base composition of 30%CaO, 30%SiO_2 and up to 10%Al_2O_3[108]. The main functions of a casting powder are[108]:

(i) avoiding the formation of solid crusts on the top surface of the liquid by reducing heat losses;

(ii) avoiding atmospheric oxidation of the liquid;

(iii) the formation of a lubricating film between the strand and the mould wall, thus decreasing wear of the mould and the frictional forces on the strand;

(iv) to provide a liquid slag cover;

(v) to allow for more regular solidification of the shell by modifying the heat transfer to the mould.

As soon as the process has reached steady-state, the heat flux (for the case of slab casting) becomes uni-directional. The heat from the liquid is removed in three basic steps[102,109-111]:

(i) conduction and radiation across the gap separating the mould and the strand;

(ii) conduction through the mould wall;

(iii) convection at the mould/cooling-water interface.

In the upper part of the mould, the gap in (i) above mainly consists of lubricant, whereas towards the lower end, due to the solidification shrinkage, the gap contains lubricant and gas. When a casting powder is used the thickness of the melted powder between the mould and the strand has been found to be between 0.1 and 2.0mm in the meniscus region, depending on the powder and the casting conditions[112-115], but values as low as 0.01mm have been reported[116]. Three different layers can be distinguished in the casting flux above the metal, these being (from the metal and upwards) liquid, sintered and solid powder, respectively. The thickness of the liquid layer depends on the melting characteristics of the powder and can be of the order of 0-5mm[117].

On the other hand, when oil is used as a lubricant, it has a minor effect on the shell thickness developed in the mould[118]. However, in the upper half of the mould a more significant difference in the heat flux was found, the oil causing the strongest heat extraction (Figure 2.7).

2.3.3 Secondary cooling zone.

In the mould approximately 15-20% of the heat content of the liquid metal is removed[119,120]. Thus, the secondary cooling zone constitutes an important part of the continuous casting process as regards the solidification and shell growth of the strand.

As the strand moves through the secondary cooling zone, it is cooled by water sprays which are situated between the supporting rolls. This design makes it easier to control the rate of heat extraction than is the case for the mould[121]. Also, the zone is commonly divided into several segments which in turn can be controlled independently of each other, thus facilitating overall process control. A schematic representation of the conditions prevailing in the spray zone is shown in Figure 2.8. From this it can be appreciated that the strand surface can experience temperature variations of the order of 200°C or more[122]. Furthermore, in order to achieve effective cooling, the water pressure has to be above a certain critical level so as to make it possible for the water to penetrate the layer of steam present on the hot strand surface[118,119]. To improve the flexibility and efficiency of the spray zone, developments involving mixed cooling systems of water and compressed air[122] and atomised water systems[123] have been made. In addition, the adoption of computer aided process control of the secondary cooling zone is becoming increasingly more common in industry[124,125].

Since the high temperature properties vary considerably between different alloys, the set-up of the cooling conditions in the secondary zone is determined by the alloy being cast. Consequently, factors such as cast section, permissible extent of bulging between the rolls, solidification characteristics, solid-state precipitation, allowed reheating and optimal temperature at the unbending point are also important in this aspect[105,118,121,122,126-131].

2.3.4 Solidification in continuous casting.

Due to the way in which the heat is extracted during continuous casting, a very steep temperature gradient is attained in the solidifying strand. Thus, the cooling rates achieved in continuous casting are much higher than those in conventional ingot casting. This, together with the dynamic nature of the process, constitute major factors which make continuous casting very complex and difficult to understand thoroughly in terms of the growth of the shell and its properties.

In the mould, the solidification front is affected by the fluid flow produced by the momentum of the input stream during casting. This effect tends to terminate a short distance below the mould and thus, the solid formed is to some extent exposed to a washing effect from the liquid[132,133].

As the strand leaves the mould, it has to have a sufficient shell thickness and be free from cracks in order to withstand the ferrostatic pressure of the liquid. Thus, entering the secondary cooling zone, the water sprays in the upper part of the zone have to be set so that no remelting, which causes breakouts, can occur. Also, in this region it is important that sufficient thickness of the shell is achieved so that bulging between the rolls is minimised as the effects of the ferrostatic head increase during the descent. As the thickness of the solid increases, the influence of the water sprays decreases and the rate controlling step in the heat transfer process becomes the ability of solid to extract heat[105,118,119,134]. Thus, the spray intensities are commonly decreased further down in the secondary cooling zone.

In the literature several investigations have been presented concerning the depth of the liquid pool and the development of the solid skin during casting. A common feature of most of these is that they apply to very specific conditions, such as the type of casting machine, mould design, strand shape/size, casting speed and alloy cast. The methods used involve:

(i) the study of drained shells obtained by either accidental or deliberate breakouts[88,119,134,135];

(ii) the investigation of the shell profile by the addition of chemical tracers (FeS) or radioactive isotopes (Au^{198}) to the liquid[136-141]. This applies to regions with strong convection so as to delineate the position of the inner surface of the shell. The strand is sectioned afterwards and either sulphur printing or autoradiography is performed. The determination of the liquid pool depth is done by the addition of heavy radioactive pellets, which are then located with the aid of a Geiger counter[137,139,140];

(iii) the location of the mushy zone by shooting a steel nail into the shell[105,141,142]. The nail dissolves completely in the liquid and partially in the mushy zone.

The results from these studies have been used to derive empirical relationships for shell growth[140,143-147]. These are commonly of polynomial form, i.e. $d=at^b$ or $d=at^b+c$ where d is the thickness, a, b, and c are constants, and t is time. The accuracy of the equations is highly dependent on the experimental method used and its reliability.

In the meniscus region, cooling rates of the order of 100^oCs^{-1} are obtained during casting[80,89]. Thus, secondary dendrite arm spacings of less than 10 microns can be found near the surface of the strand[80,148]. The arm spacings increase with distance from the surface[148] and the spacings in the central regions are determined by the size of the strand.

As in ingots, continuously-cast strands have an as-cast structure consisting of a chill, a columnar and an equiaxed zone[141,149]. Since a steep thermal gradient normally exists during continuous casting, a tendency towards an extensive columnar zone is usually found. The extent of this depends on the strand size and the superheat in the liquid[141,149]. With large columnar zones, defects such as centre-line porosity and segregation are common[149,150]. In order to overcome this and to increase the size of the equiaxed zone, electromagnetic stirring (EMS) is now commonly applied to solidifying continuously-cast sections[149,151]. The stirrers are usually placed in the mould, the secondary cooling zone or at a position where the final solidification occurs. A combination of these stirrers can be applied to one caster. In-mould stirring has been found to increase the proportion of equiaxed structure, presumably by improving the dissipation of the superheat and encouraging fragmentation of dendrite arms in the mould which then grow and form equiaxed crystals[151]. Also, the incidence of pinholes, blowholes and inclusion entrapment in the surface regions is decreased. Stirrers below the mould have a greater influence on centre-line defects than in-mould stirrers. A common denominator for electromagnetic stirring is the presence of a so-called white band in the strands, especially from stirrers below the mould. They consist of a solute depleted zone formed by a washing effect from the stirred liquid in the mushy zone.

2.4 Oscillation Mark Formation in Continuous Casting.

Oscillation marks are one of the most common features in continuously-cast strands. As for ripples on chill-cast ingots, several mechanisms have been presented in the literature to explain the formation of oscillation marks.

As mentioned in Section 2.2.2, the results obtained by Waters in a study of the continuous casting of non-ferrous alloys[73,74] led to the conclusion that the surface tension holds back the liquid from the solid, thus forming surface depressions (Figure 2.9).

The shrinkage-based mechanism put forward by Singh and Blazek[88] and later by Grill et al.[89] (Figure 2.10) for steels was preceded by a similar mechanism for non-ferrous alloys suggested by Collins[95]. The major difference between these proposals is that Collins believed that the entire upper part of the shell pulls away from the mould wall, the shell being self-supporting. When the liquid has risen sufficiently, i.e. when the metallostatic pressure is adequate, the meniscus breaks and the metal regains contact with the mould wall. However, this mechanism was only considered applicable to light alloys.

One of the first measures taken in order to reduce cracking and rippling in steels was the introduction of the oscillating mould[106,107] and the spring-mounted mould based on the compression-release techinque[103]. It was suggested that the surface defect which was still observed, was formed by the tearing of the shell during the up-stroke due to adhesion to the mould wall. This mechanism was adopted by Savage et al.[107,152] and was widely accepted. Later on the same author gave a more detailed explanation of the cyclic formation of what were then termed "lap-marks"[153] (Figure 2.11). It was suggested that the top part of the solid skin is torn off during the mould up-stroke. This element is carried upwards a fraction of the up-stroke length, assuming that some slipping occurs. On the following down-stroke, the top edge of the element penetrates the liquid meniscus and a lap is thus formed. From this, the widely used term "healing time" was introduced (c.f. Section 2.3.2). This was defined as the time during which the mould on a down-stroke is travelling at a speed greater or equal to the strand velocity.

It was not until investigations showed that the oscillation mode does not affect the frictional forces in the mould[154] and that these forces are an order of magnitude too small to cause a fracture of the shell[155], that doubts arose about the validity of the above-mentioned theories. Also, the introduction of casting fluxes further deepened the doubts. In fact, the use of casting powders in bloom and slab casting resulted in the so-called "piston effect" theory. In Figure 2.12 a schematic representation of the mechanism as suggested by Emi et al.[156]

is shown. The overhanging solid slag rim pumps molten slag into the gap between the mould and the strand during the down-stroke, i.e. during the healing time. The pressure pushes the top edge of the shell into the steel melt and during the subsequent up-stroke, the ferrostatic pressure causes the deformed edge to bend back.

The possibility of meniscus freezing having a role in the formation of oscillation marks was suggested by Riboud et al.[112] and Tomono[85]. The former proposed three different mechanisms (Figure 2.13). The first was that of overflow of the solid part of the meniscus. The second was the same as the first with the only difference that the solid meniscus is remelted when overflow occurs. The third mechanism is basically the same as the one suggested by Emi[156]. The mechanism proposed by Tomono[85] is shown in Figure 2.14. He considered two possible events, the first being the overflowing and the second the bending back of the solid meniscus.

Attention was again focussed on the behaviour of 0.1%C-steels by Wolf et al.[157]. It was suggested that microsegregation of tramp elements such as P and S determines the effective shell thickness and, hence, its apparent mechanical properties. Since there is a minimum in segregation around 0.1%C, it was proposed that at this composition the shell is strong enough to allow shrinkage to occur and, thus, to produce uneven growth and rough surfaces.

The concept of partial solidification of the meniscus as the main cause of oscillation mark formation was also put forward by Saucedo[80]. This was pointed out as a result of extensive metallographical studies of commercially-produced strands.

Using a continuous casting mould simulator, Takeuchi et al.[158,159] found that the depth of the oscillation marks increased with increasing healing time. Similarly, when the oscillation frequency is increased, the depth of the marks is observed to diminish[160].

With reference to stainless steels, austenitic grades with a Ni/Cr-ratio of 0.55[161] and highly-alloyed steels[162] (25Cr-20Ni) have a tendency to exhibit poor surface qualities. The latter grade is referred to in the literature as a "difficult-to-cast" alloy in continuous casting[162].

The actual presence of a solidified meniscus has been observed to give rise to sub-surface defects[114,163]. When casting Ti-stabilised stainless steel (SUS 321), TiN-clusters were found entrapped under the solid meniscus and on its upper surface was slag, which had been entrapped by the overflowing liquid[114].

One of several types of cracks found in continuously-cast strands are the so-called transverse cracks. These are normally located near or at the bottom of oscillation marks[85,160,164]. The cracks may be nucleated in the sub-surface region where the thermal stresses are theoretically predicted to be the highest[85]. There is some uncertainty as to whether they form in the mould[85] or further down in the machine[160,165]. In grain-refined low carbon steel cracks have been shown to follow ferrite-decorated austenite grain boundaries[127]. Reports on the surface quality of continuously-cast stainless steels reveal that austenitic grades such as SUS 310S, 316L and 321 exhibit a propensity to transverse crack formation[162,166]. The causes are considered to be the segregation of S and P to the grain boundaries as well as thermal shrinkage[162].

2.5 Modelling of Continuous Casting.

The complexity of the continuous casting process and hence, the variety of parameters that can be changed during the process implies that the modelling of continuous casting has a significant potential in process control.

In the literature, numerous studies involving mathematical simulation of heat flow in continuous casting have been presented, aiming for an understanding of the temperature distribution, shell growth and the depth of the liquid pool. Among the most used analytical techniques is the integral profile method developed by Hills[144,167]. This was applied to continuous casting by allowing the heat extraction to change with distance below the meniscus[140,167]. The same approach was adopted for the virtual adjunct method[91,168-171] (VAM). This analysis, which is mathematically exact, has the advantage over the Hills approach of requiring considerably less computation time, incorporating a complete description of the thermal characteristics and being more flexible in terms of the variation of heat extraction with distance.

However, in the modelling of industrial casting processes, the analytical models have limited applicability. The main restrictions[172] involve the treatment of the latent heat of fusion during solidification, the extent of the mould/metal system and the allowance for temperature dependent properties (e.g. thermal conductivity). Thus, the versatility of numerical methods provides a useful means for the analysis of continuous casting. One of the first models presented was that developed by Mizikar[145]. The model, which is based on one-dimensional unsteady-state heat flow using explicit finite-difference analysis, was applied to the continuous casting of slabs. One of the special features involved was the allowance for convective heat transfer in the liquid by boosting the thermal conductivity by a factor of seven, i.e. $k_{eff}=7xk_l$. This is a common method of representing the improved heat transfer due to convection. An alternative method has been described by Clyne[172]. The technique involves the definition of a thermal boundary layer in front of the growing dendrite tips. In this layer heat transfer is by conduction only, whereas on the outside no thermal gradients exist due to convection. The values of the thickness of the layer available are limited[173].

Fluid flow in the mushy zone was accounted for by Shin[174] who allowed for an effective thermal conductivity as a function of fraction liquid. The relationship obtained was,

$$k_{eff} = k_s(1 + 6f_l^2)$$

for the case of using a factor of seven for the effective conductivity in the bulk liquid (k_s is the conductivity of the solid). The analogy for this is that flow through interdendritic channels is governed by the same laws that describe the flow of liquids through porous media[175-177] such that the effective permeability of the dendritic array varies as f_l^2.

The evolution of the latent heat of fusion provides another obstacle in the numerical analysis of solidification processes. Using a modification of the model by Mizikar, Lait et al.[140] assumed that the latent heat was released in a linear fashion between the liquidus and equilibrium solidus temperature using enthalpy as the dependent variable. Depending on steel grade, it was assumed that 75-95% of the latent heat was released in a linear manner and the remainder at the solidus temperature. It was found that this arbitrary choice did not have any significant influence on the calculated rate of solidification. Considering the latent heat as a heat source (for solidification), Clyne[172,178] expressed it as being dependent on the rate of change of fraction solid, which was then substituted into a relationship where the latent heat removal is dependent on the change of f_s with temperature. Other methods involve the use of an effective specific heat[145] and the allowance for all the latent heat to be evolved at the liquidus temperature[179]. Additional methods are given elsewhere[172,180-183].

One of the major difficulties in the numerical analysis of the continuous casting process is the accuracy of the surface boundary conditions. In the mould, it is common to apply an empirical relationship for the change of heat flux with time spent in the mould, i.e. with distance[140,145]. The most widely used relationship is based on the results by Savage and Pritchard[107], which were obtained from experiments on water-cooled static moulds. This was found to give reasonable agreement with industrial data[145]. However, the general lack of industrial data makes it difficult to compare results obtained from modelling with measurements and the accuracy of the predictions using this relationship have been questioned[171].

The characteristics of heat transfer in the secondary cooling zone are very complex since they are influenced by parameters such as spray intensity, nozzle type, spray angle, nozzle position and cooling from support rolls. Thus, it is common to assign the efficiency of cooling to a heat transfer coefficient, which is obtained from empirical equations. These are usually a function of water spray intensity and cooling water temperature[126,184]. However, spray cooling data are still very incomplete, thus limiting an appropriate assessment of the models developed.

In the radiation cooling zone the heat is extracted mainly by radiation and it is common to apply the Stefan-Boltzmann equation for this part of the process[121,140,174].

Studies involving the numerical analysis of the heat transfer and solidification characteristics in the meniscus region are still very scarce in the literature, despite the increasing need for a complete understanding of the mechanisms responsible for the formation of surface defects in continuous casting.

Saucedo et al.[80,185] developed a two-dimensional model for unsteady-state heat transfer in the meniscus region during casting. From this, consistent results were obtained as regards the influence of casting parameters on surface rippling. They indicated that the normal healing time used in continuous casting is sufficient for meniscus freezing to occur. However, in the model the meniscus was approximated by a stair-like geometry and the validity of this approach is questionable since, close to the mould wall, the slope of the meniscus is very steep. Thus, the treatment will be incomplete in the vicinity of the mould wall, unless an extremely small grid size is adopted.

Recently, a one-dimensional heat transfer model applied to the meniscus region has been described[81]. The meniscus was treated as a function of surface tension, density of metal and gravity. The validity of this treatment is doubtful since Tomono[85] has shown that this type of approach fails close to the mould wall, i.e. at an essential part of the system. In the analysis, comparisons were made between experimental results (c.f. Section 2.2) and predictions. The time, over which solidification was allowed to occur, was determined by the relationship $t=b/V_c$, where t is the "residence time", b and V_c are the meniscus height and casting speed, respectively. The overall heat transfer coefficient was taken as a function of distance between the mould and the metal being determined by conduction in the medium above the meniscus, reaching a maximum of 11.0 $kWm^{-2}K^{-1}$ where the mould and the metal make contact. This is a rather high value, despite the use of He-gas in the system. In predictions of meniscus freezing in pure Al a casting speed of 5 mms^{-1} was used, leading to a residence time of 1.76s. This resulted in solidification of the meniscus to a distance of approximately 2 mm from the mould wall (considering no superheat in the liquid). Furthermore, an attempt was made to model the overflow of liquid over the solid meniscus. This was done by considering free fall of the overflowing liquid and a dependence of the wetting angle between the solid and the liquid, which determines the forces acting on the metal. Such an approach can be considered as rather crude since no account is taken of the possible bending back of the meniscus. Consequently, correlation between the experimental and predicted ripple spacings and depths as a function of casting speed was rather poor. In Section 6.1.5, the results from this model and a two-dimensional model developed in the present work are further explored.

The finite element method has also been applied to heat flow analysis in continuous casting[186,187]. However, the technique has been more commonly applied to stress analysis and hence, bulging and related crack formation has been modelled[188-194], this often being achieved in conjunction with a finite-difference model to obtain the thermal field. In addition, studies concerning the stress distribution in the strand while it is in the mould[195,196] and in the mould itself[197,198] have proved to be useful applications of the method.

Another application of numerical techniques to continuous casting lies in the optimisation of the process, considering metallurgical criteria and technological constraints[199]. However, this type of application is only useful if the various parts which comprise the model are sufficiently accurate.

CHAPTER 3

The Development of Continuous Casting Models

The use of numerical analysis is becoming increasingly more common in industry and in research carried out at universities and other institutions. This is due to two main reasons, the first one being the complexity of the process under investigation. Here, the main purpose of modelling is to be able to isolate variables so that their individual influence on the process can be assessed. The second and equally important purpose for numerical treatment of processes lies in the cost of special equipment, which is often necessary for a thorough experimental investigation of various phenomena. The continuous casting of metals provides an excellent example of this, since the development of laboratory scale casters and pilot plant casters can prove to be expensive. In addition, the development of computer hardware is nowadays such that powerful and versatile computers, which are not too expensive, are commonly available.

Thus, in the present work, two numerical models were developed. The first involves two dimensional heat flow in the meniscus region during ingot casting and continuous casting and is applied to both an austenitic stainless steel and carbon steels. The second model, which considers the whole continuous casting process, is based on one dimensional heat transfer analysis. The predicted thermal history of the strand constitutes the basis for predictions of microstructural features such as secondary dendrite arm spacings and δ-ferrite content in continuously-cast 18/10-type stainless steels.

3.1 Heat Transfer in the Meniscus Region.

In order to analyse further the extent of meniscus freezing under various conditions, a numerical heat flow model was developed, utilizing the explicit finite difference method in two dimensions considering non-steady-state conditions. Since one of the boundaries of the system is curved due to the physical shape of the meniscus, special attention was given to the numerical treatment of a curved boundary.

In the treatment of curved boundaries in two dimensional finite difference analysis, there are two common approaches in use. One involves a change in the size of the imposed grid, making the nodes coincide with the boundary. The second method utilizes a stair-like approximation in which a geometry which resembles a staircase is used to give the best fit to the boundary.

As mentioned in Section 2.5, Saucedo[80,185] adopted the staircase method in an analysis of heat transfer and solidification kinetics in the meniscus region. However, in commercial processes such as continuous casting and electroslag remelting, there is a layer and a film of casting flux/slag on the melt and between the mould and the solidified metal, respectively. This situation is difficult to model with accuracy when using the staircase approximation. A further major disadvantage of this approximation and the variable-grid approximation is the requirement of a very small grid size in order to describe accurately the system close to the mould wall where the slope of the meniscus is very steep. This makes it necessary to adopt a small time increment in order to maintain mathematical stability during the computations when an explicit analysis is used. Hence, a significant increase in computing times results.

3.1.1 Governing equation.

The equation describing two dimensional, non-steady-state heat flow in an isotropic melt is[181],

$$\frac{\partial H}{\partial t} = \frac{1}{\rho}\left[\frac{\partial}{\partial x}(K\frac{\partial T}{\partial x}) + \frac{\partial}{\partial y}(K\frac{\partial T}{\partial y})\right] \qquad .....(3.1)$$

here being expressed in terms of enthalpy. If a temperature dependent thermal conductivity is considered, equation (3.1) becomes a non-linear partial differential equation,

$$\frac{\partial H}{\partial t} = \frac{1}{\rho}\left[K(\frac{\partial^2 T}{\partial x^2} + \frac{\partial^2 T}{\partial y^2}) + \frac{\partial K}{\partial T}\{(\frac{\partial T}{\partial x})^2 + (\frac{\partial T}{\partial y})^2\}\right] \qquad .....(3.2)$$

This makes finite difference methods such as the Peaceman-Rachford[200] method or the Crank-Nicholson[201] implicit method, which both have the advantage of always being stable for any time increment used in the solution, less attractive. The former technique, which is an alternating explicit/implicit analysis, was developed for the solution of linear partial differential equations.

Thus, a fully explicit finite difference techinque can be effectively used to solve equation (3.2) taking into account a temperature dependent thermal conductivity in the form $K_{m,n} = A + BT_{m,n}$. The finite difference expression for an internal node, adopting a forward difference approximation for the enthalpy and a central difference approximation for the temperature[202], and using the direct substitution method[181], then becomes,

$$H^{t+1}_{m,n} = H^{t}_{m,n} + \frac{\Delta t}{\rho}\left[\frac{K_{m,n}}{\Delta x^2}(T_{m+1,n} + T_{m-1,n} + T_{m,n+1} + T_{m,n-1} - 4T_{m,n}) + \frac{B_{m,n}}{4\Delta x^2}\{(T_{m+1,n} - T_{m-1,n})^2 + (T_{m,n+1} - T_{m,n-1})^2\}\right] \qquad .....(3.3)$$

3.1.2 Curved boundary.

From the above it can be appreciated that finite difference analysis in two dimensions involves the use of five nodes in the calculation of, for example, the temperature of any internal node, i.e. the previous temperature of the central node together with the four surrounding nodes[202]. Considering a system containing a curved boundary, an imposed orthogonal grid can intersect this in four different ways with reference to the node next to the boundary as shown in Figure 3.1. (In the following, the point of intersection will be referred to as a "fictitious" node.) A type 1 intersecion occurs when two of the surrounding nodes have been cut off. Types 2 and 3 occur when one node has been cut off in either the horizontal or the vertical direction, respectively. A special case arises when the boundary passes through the central node. This forms a type 4 intersection. Knowing the shape of the boundary (c.f. Section 3.1.4), a step-wise tracing of the system can be carried out by dividing each grid square into increments to locate the intersections. This is then followed by an identification process to determine the type of each intersection and its exact location. Derivations of the finite difference equations for nodes next to the curved boundary together with the fictitious nodes at the intersections with the grid are given in Appendix I.

3.1.3 Physical systems.

The model presented was applied to the meniscus region during casting. The system consists of the midface of the upper part of an ingot or strand at the instant when the liquid makes contact with the mould, as shown in Figure 3.2. (The casting flux present in the meniscus region during continuous casting is not shown in Figure 3.2.) This situation is arrived at by considering that, for a short period, the meniscus formed against the mould wall can be kept static or at least be restricted to a very small displacement. The reason for this is that during casting, the relative displacement of the melt surface and the mould wall is not steady due to turbulence and/or rocking movements of the pool, thus creating an intermittent movement[185].

In systems where the mould is oscillating or the strand is intermittently withdrawn, the meniscus remains in stationary contact with the mould for a short period. In continuous casting, this period of time is the healing time and a typical value for this is 0.3 s[80,118,160,161,203].

Although solidification theory suggests that no solid is formed before the superheat has been dissipated, some solidification can take place at an early stage if the chilling power of the heat sink is strong enough, as a result of the steep temperature gradient produced.

It should be emphasised that any predictions made from calculations during, for example, the healing time can only be interpreted as the as-formed depth of the oscillation mark. The reason for this is that the final as-cast depth depends on how much remelting, bleeding or bending back of the partially-solid meniscus occurs as the liquid level increases, together with the nature of the fluid flow in the liquid flux during slab casting.

3.1.4 Meniscus shape.

Since the shape of the meniscus is a complex function of several parameters[80,85,185], an empirical equation was adopted to describe its geometry[80,185],

$$y = U[1 - \exp(-Px)]^{Z} \qquad \text{.....(3.4)}$$

where the constants P and Z are approximately 0.4 and 0.5, respectively, for carbon steels in contact with gaseous atmospheres. The parameter U describes the height of the meniscus from the point where it meets the mould wall to the horizontal surface. This is commonly of the order of 10mm for steels[85].

3.1.5 Initial and boundary conditions.

The initial conditions imposed on the system were,

$$\text{(i)} \quad T_{m,n} = T_p \qquad x \geq 0\ ,\ y \leq y(x)\ ,\ t = 0$$

$$\text{(ii)} \quad T_{m,n} = T_A \qquad x \geq 0\ ,\ y > y(x)\ ,\ t \geq 0$$

where T_p is the pouring temperature and y(x) is the boundary determined by equation (3.4). Condition (ii) is applied when a gas atmosphere over the meniscus is being considered.

For the right hand boundary and the boundary at the bottom of the system, which are both interfaces at which no heat flow is taking place, the following conditions are applicable,

$$\text{(iii)} \quad -K\frac{\partial T}{\partial x} = 0 \qquad x = x_{max}, \; y \geq 0, \; t \geq 0$$

$$\text{(iv)} \quad -K\frac{\partial T}{\partial y} = 0 \qquad x \geq 0, \; y = 0, \; t \geq 0$$

In the present analysis, the boundaries x_{max} and $y = 0$ were chosen to be at a distance of 10 mm from the mould wall and 10 mm below the point where the mould and the metal meet, respectively. This is based on the assumption that during the short time interval of the analysis, the heat flow in or out of the system is negligible. When a gas atmosphere was considered, the boundary conditions at the mould/metal interface and on the meniscus were,

$$\text{(v)} \quad q = h(T_{m,n} - T_M) \qquad x = 0, \; 0 \leq y \leq y(0), \; t \geq 0$$

$$\text{(vi)} \quad q = h_{con}(T_w - T_A) + \sigma\varepsilon(T_w^4 - T_A^4) \qquad x \geq 0, \; y = y(x), \; t \geq 0$$

where T_w denotes the temperature of an intersection. For the situation where a casting flux/slag is present in the form of a film between the mould and the metal and a layer on the meniscus (Figure 3.3), conditions (v) and (vi) become,

$$\text{(vii)} \quad q = \frac{k_f}{s}(T_{m,n} - T_{sx}) \qquad x = 0, \; 0 \leq y \leq y(0), \; t \geq 0$$

$$\text{(viii)} \quad q = \frac{k_f}{X}(T_w - T_{sx}) + \frac{k_f}{Y}(T_w - T_{sy}) \qquad x \geq 0, \; y = y(x), \; t \geq 0$$

assuming that the heat flux through the casting flux due to radiation is negligible. The parameters k_f and s are the thermal conductivity of the flux and the film thickness, respectively. T_{sx}, T_{sy}, X and Y are the temperature of the flux at the mould wall, the temperature at the interface between sintered and liquid flux, the distance from the mould wall to an intersection and the distance from the interface between liquid and sintered flux to an intersection, respectively. The parameter Y is obtained by adopting a thickness l of the layer of liquid flux on the metal defined at the horizontal part of the meniscus, i.e. $Y = 10.0 + U + l - y(x)$. In Appendix I the finite-difference equation for the mould/metal boundary condition is given.

3.1.6 Calculation of fraction solid.

In the analysis of the behaviour of carbon steels in the meniscus region, equilibrium solidification was assumed, i.e. the lever rule was applied. The invariant temperatures T_L and T_S were determined by the equations[204],

Liquidus

$L \rightarrow \delta$-ferrite $\quad 0.0 < \%C < 0.52$

$$T_L = 1537.0 - 104.2(\%C)^{3/2} \qquad .....(3.5)$$

$L \rightarrow \gamma$ $\quad 0.52 \leq \%C \leq 4.27$

$$T_L = 1514.0 - 41.05(\%C)^{3/2} \qquad .....(3.6)$$

Solidus

$L \rightarrow \delta$-ferrite $\quad 0.0 \leq \%C \leq 0.11$

$$T_S = 1537.0 - 345.45(\%C) \qquad .....(3.7)$$

Peritectic $\quad 0.11 < \%C < 0.16$

$$T_S = 1499.0 \qquad \text{.....(3.8)}$$

$L \rightarrow \delta \rightarrow \gamma \qquad 0.16 \leq \%C \leq 2.0$

$$T_S = 1529.0 - 187.5(\%C) \qquad \text{.....(3.9)}$$

The lever rule expressed in terms of temperature is,

$$f_s = \frac{T_L - T_{m,n}}{T_L - T_S} \qquad \text{.....(3.10)}$$

Using the definition of the enthalpies at the liquidus and the solidus temperature, it can be shown that the fraction solid can be calculated from the enthalpies as[80],

$$f_s = \frac{H_L - H_{m,n}}{H_L - H_S} \qquad \text{.....(3.11)}$$

When applying the model to other alloys such as stainless steels, non-equilibrium solidification behaviour according to Scheil was used. This approach is based on the assumption that during the short time period of the analysis no, or very little, back-diffusion takes place during solidification. The validity of this assumption was verified by using a numerical model for back-diffusion during solidification described elsewhere[205]. Thus, the fraction solid as a function of temperature is given by,

$$f_s = 1 - \left[\frac{T_f - T_{m,n}}{T_f - T_L}\right]^{\frac{1}{(k-1)}} \qquad \text{.....(3.12)}$$

where T_f is the melting temperature for the solvent and k is the partition coefficient. Assuming that the latent heat of fusion is released in a linear manner with fraction liquid, the calculation of f_s was carried out by solving equation (3.12) and the following equations, using the Newton-Raphson iteration method,

$$H_{m,n} = c_p(T_{m,n} - T_A) + (1 - f_s)L_f \qquad .....(3.13)$$

$$H_f = c_p(T_f - T_A) + L_f \qquad .....(3.14)$$

$$H_L = c_p(T_L - T_A) + L_f \qquad .....(3.15)$$

From a knowledge of f_s, the temperature can subsequently be calculated, using equations (3.12) or (3.13). Thus, a conversion from enthalpy to temperature for a node in the mushy region has been achieved, taking into account the latent heat of solidification. A further example of the versatility of the enthalpy method in the modelling of solidification processes is given in Appendix II, where a numerical treatment of the solidification kinetics during Vacuum Arc Remelting (VAR) is presented.

Since, when using the Scheil equation to describe the solidification process, no indication is given of when the material is fully solid[206], it was assumed that this was so when f_s=0.95. This is only valid for systems in which, for example, no eutectic reaction takes place during solidification.

The thermal conductivity in the liquid was assumed to be seven times greater than in the solid to allow for convection[145]. In the mushy zone, the convection was accounted for by using the approach developed by Shin[174], i.e. the conductivity varies as a function of f_l^2,

$$K = (1 + 6f_l^2)(A + BT) \qquad .....(3.16)$$

3.1.7 Stability and rigidity criteria.

In two dimensional heat transfer analysis using the explicit finite difference method, space and time increments have to be chosen so as to obtain a mathematically convergent and stable solution. This is, in the case of an internal node in a quadratic orthogonal grid, determined by the expression[207],

$$\frac{(\Delta x)^2}{\alpha \Delta t} \geq 4$$

where α is the thermal diffusivity. From this it can be appreciated that once a value of Δx has been selected, the choice of Δt is limited. In addition, the smaller the grid size the more accurate the solution becomes, but due to the square-relationship with Δt , the slower the solution will proceed. At the interface between the mould and the metal, the above relationship becomes[181],

$$\frac{(\Delta x)^2}{\alpha \Delta t} \geq 2\left(\frac{h \Delta x}{K} + 2\right)$$

where h and K are the heat transfer coefficient and the thermal conductivity of the metal, respectively. In the present analysis, a Δt of 10^{-4} seconds was found to give a stable and convergent solution for $\Delta x = 0.5$ mm.

In traditional casting processes, it has been suggested that during solidification, a dendritic array starts to behave in a rigid manner when the fraction solid is greater than 0.2[208-210]. Thus, the meniscus freezing is described for f_s=0.2 in the form of iso-fs curves.

In Appendix III a line-by-line description of the computer program, which was written in Fortran IV for an ICL 1906S computer, is given. A schematic flow diagram of the program is shown in Figure 3.4.

3.2 Modelling of Continuous Casting of Slabs.

In this section, a heat transfer model based on the approach by Mizikar[145] is presented. The predicted thermal history is then used for microstructural predictions based on experimental data presented elsewhere[14].

3.2.1 Heat transfer model.

In the continuous casting of slabs, heat transfer is essentially one dimensional. This is arrived at by considering a position at the middle of a wide face where the heat transfer along the width of the slab is negligible. Also, the heat conduction in the withdrawal direction (z-direction) is normally small. Thus, a thin horizontal slice of a length equal to half the thickness of the slab and initially located at the meniscus can be considered (Figure 3.5). As the rate at which the slice moves downwards is determined by the casting speed, the relative velocity will be zero, thus cancelling any influence of bulk heat flow. The thus-achieved one-dimensional unsteady-state heat transfer can be expressed by the following equation, which is in terms of enthalpy and takes into account a temperature dependent thermal conductivity,

$$\frac{\partial H}{\partial t} = \frac{1}{\rho}\left[K\frac{\partial^2 T}{\partial x^2} + \frac{\partial K}{\partial T}\left(\frac{\partial T}{\partial x}\right)^2\right] \qquad .....(3.17)$$

The initial and boundary conditions applicable for the solution of this equation are,

$$\text{(i)} \quad T_m = T_p \qquad 0 \le x \le \frac{D}{2}, \quad t = 0$$

$$\text{(ii)} \quad -K\frac{\partial T}{\partial x} = 0 \qquad x = 0, \quad t \ge 0$$

$$\text{(iii)} \quad -K\frac{\partial T}{\partial x} = q \qquad x = \frac{D}{2}, \quad t \ge 0$$

At the beginning, the temperature of the slice is uniform and equal to that of the incoming liquid (T_p). At the centre ($x = 0$), no heat transfer occurs due to identical temperature profiles on both sides of the centreline. There the temperature is determined by[145],

$$T_1^{t+1} = \frac{4}{3}T_2^{t+1} - \frac{1}{3}T_3^{t+1} \qquad .....(3.18)$$

which is obtained by substituting a second order forward difference approximation for the distance derivative and solving for T_1^{t+1}. At the surface, the heat transfer is determined by the heat flux q.

The explicit finite difference equation to be solved for an internal node, using a linear temperature dependence of the thermal conductivity (c.f. Section 3.1.1) is,

$$H_m^{t+1} = H_m^t + \frac{\Delta t}{\rho}\left[\frac{K_m}{\Delta x^2}(T_{m+1} + T_{m-1} - 2T_m) + \frac{B_m}{4\Delta x^2}(T_{m+1} - T_{m-1})^2\right] \qquad ...(3.19)$$

The thermal conductivity in the mushy zone is assumed to vary with fraction liquid according to equation (3.16). However, since the convection caused by the pouring stream is likely to disappear in the regions immediately below the mould, the convection factor in the liquid was assumed to decrease in a linear manner from 7 to 1 in the first spray cooling zone. This assumption is only valid for the modelling of a continuous casting machine in which the nowadays common submerged casting tube with side-ways pointing holes is used.

At the surface of the slab (node n), equation (3.19) becomes, using boundary condition (iii),

$$H_n^{t+1} = H_n^t + \frac{\Delta t}{\rho}\left[\frac{K_n}{\Delta x^2}(T_{n-1} - T_n) - q\Delta x + \frac{B_n}{\Delta x^2}\left(\frac{q}{K_n}\right)^2\right] \qquad \text{.....(3.20)}$$

In the mould, the heat flux q is commonly expressed as a function of time[140,145,174] (c.f. Section 2.5), i.e.,

$$q = 2680 - 335t^{\frac{1}{2}} \qquad (\mathrm{kWm^{-2}}) \qquad \text{.....(3.21)}$$

As the slice moves down in the mould, this expression simulates the reduction of heat extraction as a result of, for example, air-gap formation.

Entering the secondary cooling zone, q is determined by,

$$q = h(T_n - T_W) \qquad \text{.....(3.22)}$$

where h and T_W are the heat transfer coefficient for a spray zone and the temperature of the cooling water, respectively. The adoption of a heat transfer coefficient is a simplification of the very complex conditions prevailing in this cooling zone (c.f. Section 2.3.3). The heat transfer coefficient is commonly expressed empirically as a function of water flow rate. For example, Nozaki[126] expressed this as,

$$h = 0.333W^{0.55} \qquad .....(3.23)$$

where W is the water flow rate ($l sec^{-1}$). However, the availability of data for this is limited and when obtainable, the application is usually restricted to specific machines, cooling systems and casting conditions.

In the radiation cooling zone, the rate of heat extraction is assumed to be controlled by radiation. Thus, the Stefan-Boltzmann equation is applicable,

$$q = \sigma\varepsilon(T_n^4 - T_A^4) \qquad .....(3.24)$$

The value for the emissivity ε is normally 0.8 for an oxidized surface[181]. σ and T_A are the Stefan-Boltzmann constant and an ambient temperature, respectively.

The heat transfer model presented was applied to 18/10-type stainless steel. Since non-equilibrium solidification occurs during the major part of the freezing range of this type of alloy, solidification according to the Scheil equation was assumed. This is based on the fact that the development of austenite around the δ-ferrite results in a departure from what otherwise is close to equilibrium solidification (c.f. Section 2.1). Thus, the fraction liquid at any temperature in the mushy zone was calculated using equation (3.12) ($f_l = 1 - f_s$). The solidus temperature was assumed to be reached when $f_s = 0.95$.

In this model, a conversion from enthalpy to temperature was achieved by solving the following equations (c.f. Section 3.1.6),

$$f_l = \left[\frac{T_f - T_m}{T_f - T_l}\right]^{\frac{1}{(k-1)}} \qquad .....(3.25)$$

$$f_l = \frac{H_m - c_p(T_m - T_A)}{H_f} \qquad .....(3.26)$$

using the Newton-Raphson iteration method,

$$T_1 = T_0 + \frac{f(T)}{df(T)} \qquad .....(3.27)$$

In the calculations, a mesh size of 10 mm was used in a slab with a half-thickness of 110 mm. A stable and convergent solution for this was obtained using a time increment of 0.9 s.

3.2.2 Calculation of dendrite arm spacings.

In the work by Pereira[14], the secondary dendrite arm spacings as a function of cooling rate were investigated for the four different solidification modes occurring in austenitic stainless steels. It was found that the spacings are independent of solidification mode and hence, the results all fell on the same line (Figure 3.6). The cooling rates were obtained by measuring the slopes on temperature profiles achieved from thermal analysis of static castings using different moulds. The temperature range over which the slopes were measured was from immediately below the liquidus plateau down to 1280°C. From these results (Figure 3.6), it can be derived that the dendrite arm spacings in austenitic grades vary with cooling rate as,

$$\lambda_2 = 63.91(GR)^{-0.347} \qquad .....(3.28)$$

where λ_2 is the secondary dendrite arm spacings in μm and GR is the cooling rate in Ks^{-1}.

In order to predict the variation of secondary dendrite arm spacings across a continuously-cast slab, equation (3.28) was included in the heat transfer model presented in the previous section. The cooling rate at each node was calculated by obtaining the time spent between (T_l - 5.0°C) and 1280°C. However, it was realised that a mesh size of 10 mm (c.f. Section 3.2.1) was too coarse to describe accurately the solidification taking place in the mould, since this is where high cooling rates and steep temperature gradients are prevailing in the first skin to solidify. Thus, a refined mesh was adopted in the mould. The influence of Δx = 2.5mm and Δx = 1.25mm was investigated and it was found that for identical casting conditions, there were no significant differences in the results from these mesh sizes. Hence, in the mould, a spacial increment of 2.5 mm was used and below the mould, a mesh size of 10 mm was used.

3.2.3 Calculation of fraction δ-ferrite.

Previously[14], a simple model for the dissolution of non-equilibrium phases developed by Singh et al.[211] was adopted for the study of the influence of temperature and time on δ-ferrite content in 18/10-steels during homogenisation. However, one of the major draw-backs of this model concerns the assumption that only small amounts of the unstable phase (δ-ferrite) are present, which meant that any motion of the phase boundary could be neglected. During solidification and cooling of a type B alloy (18/10), the δ-ferrite content decreases from a maximum of approximately 57% at 1435°C (Figure 3.7) down to 22% around the solidus temperature (1404°C). This is followed by a further reduction in the volume fraction of δ on subsequent cooling to about 900-1000^{o}C, which is where the diffusion rates in δ and γ become too slow to allow for further significant transformation. From this, it can be appreciated that factors such as moving phase boundaries, geometry and temperature dependence of the diffusion coefficients in austenite and ferrite are of significance. This situation is not possible to model analytically and thus, a numerical approach has to be adopted.

In the present analysis, a model developed by Tanzilli and Heckel[212,213] was used. It takes into account that the two phases involved are finite in extent and also that the transformation is diffusion controlled, allowing for a moving interface. Initially, this model was presented for three different geometries, these being planar, cylindrical and spherical, respectively. Since a secondary dendrite arm of δ-ferrite with an envelope of austenite around it resembles a cylinder, this geometry was utilized in the analysis. The system adopted is shown in Figure 3.8.

The distance from the centre of the cylinder to the outer boundary is determined by half the secondary dendrite arm spacing and the distance from the centre to the boundary between δ and γ is given by $\frac{f^{\delta}\lambda_2}{2}$ where f^{δ} is the fraction δ-ferrite.

The partial differential equations determining the concentration profiles in the two phases are,

$$\frac{\partial C^{\delta}}{\partial t} = \frac{1}{R}\frac{\partial}{\partial R}(RD^{\delta}\frac{\partial C^{\delta}}{\partial R}) \qquad .....(3.29)$$

and

$$\frac{\partial C^{\gamma}}{\partial t} = \frac{1}{R}\frac{\partial}{\partial R}(RD^{\gamma}\frac{\partial C^{\gamma}}{\partial R}) \qquad .....(3.30)$$

where R is the distance from the centre, C^{δ} and C^{γ} are the concentrations of chromium in δ and γ, respectively, and D^{δ} and D^{γ} are the interdiffusion coefficients in the respective phase. At the boundary between δ and γ the following interface mass balance is applicable,

$$(C_{\delta\gamma} - C_{\gamma\delta})\frac{d(\xi/2)}{dt} = D^{\gamma}\left[\frac{\partial C^{\gamma}}{\partial R}\right]_{R=\frac{\xi^{+}}{2}} - D^{\delta}\left[\frac{\partial C^{\delta}}{\partial R}\right]_{R=\frac{\xi^{-}}{2}} \qquad \text{.....(3.31)}$$

where $C_{\delta\gamma}$ and $C_{\gamma\delta}$ are the interface concentrations in ferrite and austenite, respectively and $\frac{\xi}{2}$ is the radius of the ferrite.

Considering a concentration profile across half a dendrite arm as shown in Figure 3.9, the following boundary conditions were applied,

(i) $\frac{\partial C}{\partial R} = 0\ ,\quad R = \frac{\lambda_2}{2}$ in the austenite

(ii) $\frac{\partial C}{\partial R} = 0\ ,\quad R = 0$ in the ferrite

(iii) $C = C_{\gamma\delta}\ ,\quad R = \frac{\xi^{+}}{2}$

(iv) $C = C_{\delta\gamma}\ ,\quad R = \frac{\xi^{-}}{2}$

The initial conditions applicable are,

(v) $C = C_{0\gamma}\ ,\quad t = 0$ in the austenite

(vi) $C = C_{0\delta}\ ,\quad t = 0$ in the ferrite

In the case of complete homogenisation, i.e. when both depletion of the unstable phase and normalisation of the concentration gradients are considered, the average composition has to be taken into account[212]. However, for the purpose of this analysis, only the variation of fraction δ-ferrite was considered since the thermal history in the continuous casting of stainless steels does not allow for complete homogenisation.

Due to the fact that the phases are changing their thickness continuously during cooling, equations (3.29), (3.30) and (3.31) are not sufficient for the solution of the problem. However, a solution can be obtained by using the Murray-Landis[214] variable-grid space transformation, which, at an internal point (whose location is always a constant percentage of the instantaneous phase thickness), describes the time rate of change of concentration for node i as,

$$\frac{dC_i}{dt} = \frac{\partial C_i}{\partial R_i}\left(\frac{dR_i}{dt}\right) + \frac{\partial C_i}{\partial t} \qquad .....(3.32)$$

where $\frac{\partial C_i}{\partial t}$ is the contribution from equations (3.29) and (3.30). The rate of travel of the node is related to the interface velocity by,

$$\frac{dR_i}{dt} = \frac{R_i}{(\xi/2)}\frac{d(\xi/2)}{dt} \qquad .....(3.33)$$

By combining equations (3.32) and (3.33), the time rate of change of the concentration at an internal node in δ-ferrite is,

$$\frac{dC_i^\delta}{dt} = \frac{R_i}{(\xi/2)}\frac{\partial C_i}{\partial R_i}\frac{d(\xi/2)}{dt} + \frac{\partial C_i^\delta}{\partial t} \qquad .....(3.34)$$

At an internal point in the austenite, equation (3.34) becomes,

$$\frac{dC_i^{\gamma}}{dt} = \left[\frac{\frac{\lambda_2}{2} - R_i}{\frac{\lambda_2}{2} - \frac{\xi}{2}}\right] \frac{\partial C_i}{\partial R_i} \frac{d(\xi/2)}{dt} + \frac{\partial C_i^{\gamma}}{\partial t} \qquad \text{.....(3.35)}$$

At the boundary between the ferrite and the austenite, equations (3.34) and (3.35) are coupled through the interface mass balance (equation (3.31)), whose solution yields the velocity of the interface. The complete explicit finite difference equations for the internal nodes in δ and γ, the equation for the interface mass balance and the boundary condition at the centre of the δ-ferrite are given in Appendix IV.

In the analysis, three major assumptions are made,

(a) the interdiffusion coefficients are independent of concentration,

(b) the interface concentrations are time-independent,

(c) the molar volumes of the phases are equal.

The assumption in (c) is involved when the average concentration is considered. An example of this is when the model is applied to a system with particles dispersed in a matrix. Knowing the size of the particles (l) and the average composition ($\overline{C}$), the extent of the diffusion field around the particles can be determined by $L^m = \frac{l^m}{\overline{C}}$, where m=1, 2 and 3 for planar, cylindrical and spherical geometry, respectively and $\overline{C}$ is given as an atomic fraction.

The above model was built into the heat transfer model presented in Section 3.2.1, using the dendrite arm spacings as obtained from the approach given in Section 3.2.2. The procedure for the calculations can be divided into two main steps. The first involves the heat flow part, during which the dendrite arm spacings are predicted. In the second step, the heat flow part is re-initiated to provide the thermal history for the calculations of fraction δ-ferrite using the previously calculated arm spacings. Prior to these calculations, the diffusion coefficients were obtained by taking an average temperature defined by the "old" and the "new" temperature of the nodes. Each node in the coarse mesh used in the heat flow part was then sub-divided into a finer mesh, which was used for the ferrite determination. The duration of the calculation of fraction δ-ferrite at each position in the strand was determined by the time increment used in the heat flow part. When all the nodes from centre to surface of the slab had been covered, a new set of temperatures was calculated and the process was repeated, using the previously determined ferrite-mesh.

In the present analysis, the initial mesh imposed across half a secondary dendrite arm spacing at a given node consisted of 20 sub-nodes with equal spacing. For the dendrite arm spacings predicted, a time increment of 0.007 s was found to give a stable solution for the ferrite part.

The calculations of fraction δ-ferrite were initiated by the provision of a starting temperature and a corresponding percentage of δ-ferrite, which, for example, can be obtained from Figure 3.7. In Appendix V a line-by-line description of the computer program, which was written in Fortran IV for an ICL 1906S computer, is given. A schematic flow diagram of the program is shown in Figure 3.10.

CHAPTER 4

Experimental Procedure

4.1 Ingot Casting.

From the literature review, it can be appreciated that the mechanism proposed for oscillation mark formation also operates in ordinary chill casting. Hence, experiments were carried out on a casting system, which is a laboratory scale bottom-pouring arrangement initially designed by Saucedo[80]. This set-up has the advantage over direct-pouring systems in that splashing and formation of double skin is avoided. Also, measurement of casting parameters and a steady rise of the liquid in the mould is facilitated by up-hill teeming.

4.1.1 Mould system.

The experimental casting system consisted of tundish, downsprue (with choke), runner, ingate and mould cavity (Figure 4.1).

In order to ensure a steady rate of teeming, a tundish of the wall and weir type was developed (Figure 4.2). This design makes the velocity of the rising metal in the mould less sensitive to fluctuations in the pouring rate. The gap between the wall and the bottom of the tundish was set at 20 mm and the weir was 60 mm high. The entire cavity in the tundish had the dimensions 225x80x95 mm.

The downsprue, which was 300 mm long, was tapered so as to form the choke in the casting system. In the experiments performed at a "normal" teeming rate, the choke was 8-9 mm in diameter. This caused the metal to rise at a rate ranging from approximately 2 m,min^{-1} close to the inlet to 0.8 m,min^{-1} at the end of teeming.

A 250 mm long runner with a cross section of 25x25 mm was utilized between the downsprue and the mould cavity. At the end situated below the choke, a cylindrical well base 32 mm in diameter and 30 mm deep (measured from the bottom of the runner) was positioned in order to reduce the inertia of the liquid and to control the flow. In order to ensure an even flow through the mould inlet and to allow for the collection of dross carried with the "first" liquid as the system is purged, the mould ingate was placed approximately 50 mm from the other end of the runner.

The tapered ingate was 25x25 mm at the lower end and 40x40 mm at the bottom of the mould cavity, the depth of the ingate being 65 mm. This large taper was adopted in order to avoid jet effects and to reduce the turbulence of the incoming liquid.

The mould cavity, with dimensions 300x90x75 mm, was formed by four detachable mould walls with different surface roughness; one water-cooled copper plate (Figure 4.3) and three steel plates (25 mm thick). The surface roughness of one of the steel plates and the copper plate was obtained by grinding with 600 grade Emery paper. The remaining two steel plates had their roughness produced by machined vertical grooves (pitch 1mm-depth 0.4mm and pitch 0.6mm-depth 0.1mm, respectively). In Figure 4.4, the mould walls used are shown.

The separate parts of the casting system were made by using purpose-built steel boxes, containers and wooden patterns. The material used for the moulding of the sections was Chelford medium size grain silica sand mixed with Harmark Gas Bond. The moulded parts were dried in a gas stove at 400°C for 4 hours.

4.1.2 Preparation of alloys.

The desired compositions were obtained by careful weighing of the charge materials. Armco Iron was used as base material together with small amounts of bolt punchings so as to achieve the correct weight. The major alloying elements, chromium and nickel, were added in the form of Carbonyl Nickel Pellets and Chromium Briquettes together with small amounts of Japanese Electrolytic Flake Chrome. Silicon metal and Electrolytic Manganese Flake were used to make up the minor constituents. The chemical compositions of these materials are given in Table 4.1.

4.1.3 Casting procedure.

Prior to the assembling of the mould system, loose sand was removed from each part. In order to obtain the best fit of the parts, minor dimensional adjustments were undertaken by careful filing. This was undertaken in order to avoid any escape of liquid during pouring. After assembling the system, further precautions against leaks were taken by sealing any gaps with CC60-cement. The surfaces of the mould plates were cleaned using 600 grade Emery paper and a wire brush for the ground and the rough plates, respectively, after which the mould walls were assembled using a special clamping device. In Figure 4.5, the assembled mould system is shown.

The melting of the alloys was carried out using a 56 lb capacity induction furnace with a Sillimanite crucible.

When the melt had reached the required pouring temperature, one of two teeming techniques was employed, depending on the superheat required. For high superheats, the liquid was teemed straight into the tundish using a trolley with a platform, which was controlled by a lift-mechanism and onto which the mould system was placed. This facilitated controlled teeming conditions. Experiments at low superheats were performed by first pouring the metal from the furnace into a pre-heated 25 kg steel ladle lined with Mansfield Red Sand and then into the tundish.

The casting time was recorded for each experiment, the timing commencing at the moment the liquid entered the mould cavity and stopped at the end of the teem.

4.1.4 Thermal analysis.

During melting, the temperature in the furnace was measured using a Pt/Pt-13%Rh dip thermocouple which was protected by a disposable silica sheath. This thermocouple was connected to a direct-reading wall indicator with the range 1350-1750^{o}C, reading to the nearest 5^{o}C.

Prior to making each casting, the liquidus temperature of the alloy was measured by teeming a small portion of liquid into a standard, cup-shaped shell mould (50 mm diameter and 62 mm deep). A 0.08 mm Pt/Pt-13%Rh thermocouple protected with a silica sheath was fitted in the bottom of the cup. The cup was attached to a special support unit from which leads were connected to a Servoscribe potentiometric recorder (SE laboratories). A stable reference temperature was obtained using a cold junction in a ice/water mixture. The recorder was set at 100% back-off, 10 mV full scale deflection and a chart speed of 120 mm,min^{-1}. Thus, cooling curves were obtained and the pouring temperature could be selected, depending on the required superheat.

In order to monitor the inlet temperature in the mould and its variation during teeming, a 0.5 mm Pt/Pt-13%Rh thermocouple was used. The wires were threaded through twin bore recrystallised alumina tubing and inserted in a silica sheath. The thermocouple was inserted through a hole in one of the mould walls 25 mm above the inlet and centred in the mould cavity. It was connected to a second channel of the Servoscribe recorder, the setting being the same as described above, using the same cold junction.

4.2 Casting in Controlled Atmospheres.

The experiments in controlled atmospheres were carried out in an Efco Edwards vacuum induction furnace. Melting of the alloys was performed in a 10 kg capacity alumina crucible. Due to the spacial constraints of the unit and the lower melting capacity, a smaller mould system was used.

The wall and weir type tundish was replaced by a slightly smaller tundish with only a weir (20 mm high) and with the cavity dimensions 180x80x90 mm. The downsprue used was 200 mm long. A runner with the dimensions 17x17x190 mm was employed. Its well base was 22 mm in diameter and provided a 20 mm deep cavity. The distance between the end of the runner and the inlet was 30 mm. The tapered inlet was 22 mm deep, the size changing from 17x17 mm at the lower end to 26x26 mm at the bottom of the mould cavity. In addition, the water-cooled copper plate was replaced by a ground steel plate, which was identical to the one used previously. The dimension of the mould cavity was 300x75x75 mm with this set of mould plates. In Figure 4.6, the arrangement used in the experiments is shown.

In this melting unit, the temperature could only be measured in the crucible with an externally controlled Pt/Pt-13%Rh dip thermocouple. However, knowing the liquidus temperatures for the alloys cast in air, pouring temperatures based on the liquidus temperatures could be selected in order to ensure consistency. Together with control of the melting procedure, timing of the experiments was carried out by observation through a window in the lid of the furnace.

The required 'atmosphere' was obtained by first evacuating the chamber to 10µm Hg pressure followed by the admission of either 10cm of argon or between 58 and 60cm of helium. For the purpose of calculations in the present work, the reduced pressure of 10cm argon was considered as a vacuum.

4.3 Examination of Surfaces and Structures.

When the castings had cooled to room temperature, the mould assembly was removed and the runner sliced from the ingot using a slitting wheel. This was followed by measurements of the dimensions of the ingot. Photographic records of each of the ingot surfaces were obtained using a De Vere bellows camera. In order to achieve good reproduction of the surfaces, oblique illumination was adopted.

Samples for examination of the structures in the vicinity of ripples were obtained by transverse sectioning of the ingots using a band saw. The slices, which were 20 mm thick, were then cut into specimens of appropriate size, these being taken from midface regions. The remnants of the slices were used to take drillings for conductimetric analysis and for analysis in a Quantometer. The specimens were mounted in bakelite so as to produce surfaces which were flat (i.e. at the ingot surface). Using a standard metallographical procedure, the polished specimens were etched in solutions, which were selected depending on alloy content (see Appendix VI). Micrographs from the structures were obtained using a 35 mm Zeiss Photomicroscope (for high magnifications) and a Wild Photomacroscope M400 (for low magnifications).

4.4 Investigation of Continuously-Cast Strands.

The surfaces of the as-received sections of continuously-cast stainless steel slabs were cleaned and photographed, using a Contax RTS 35 mm camera.

Specimens for the examination of microstructures in the vicinity of oscillation marks were produced using a procedure similar to that described in Section 4.3. The etchants used are given in Appendix VI.

The samples used for the determination of the δ-ferrite content were obtained by cutting sections perpendicular to the direction of heat flow at intervals of 10 mm across the thickness of the slabs. The surface area of the specimens was approximately 20x20 mm. Samples for the determination of the secondary dendrite arm spacings were obtained by cutting slices parallel to the direction of heat flow.

The secondary dendrite arm spacings were measured on photographs taken at different distances from the surface of the slabs, thus giving a cross-sectional variation.

The variation of the δ-ferrite content across the slabs was obtained using a Swift Point Counter. Due to the fine structure of as-cast δ-ferrite, a x100 oil immersion lens was used, bringing the total magnification to x1250. This greatly facilitated visual judgement during the measurements. In each sample, between 1800 and 2000 points were counted. As a cross check on the results from the point counting, magnetic measurements were performed using a battery-powered Ferritector (by Elcometer). This is in essence a small magnetic probe which is applied to the surface of the specimen, the probe being connected to a scale via a flexible lead. The instrument is based on the measurement of magnetic flux density. When using this type of magnetic method for measurements, the results do not only depend on the amount of δ-ferrite, but also on its permeability, which, in turn, depends on the shape, size, texture and chemical composition of the ferrite. Thus, the results obtained from measurements using the Ferritector were only used for the purpose of verifying or discarding trends observed in the results from the point counting.

CHAPTER 5

Observations of Surfaces and Structures

5.1 Surface Appearance of Experimental Ingots.

The influence of mould roughness, teeming rate, superheat, alloy content and atmosphere on surface ripple formation has been studied using laboratory scale stainless steel castings. The chemical compositions of the alloys cast are given in Table 5.1. The same mould arrangement was used for all the castings produced in air. In the castings produced in the controlled-atmosphere furnace, the water-cooled copper plate was replaced by a ground steel plate. The casting parameters measured during teeming in air and in the controlled-atmosphere furnace are given in Tables 5.2 and 5.3, respectively.

5.1.1 Mould roughness.

In Figure 5.1(a)-(c) the surfaces of a fully ferritic stainless steel alloy (cast 3299) solidified against rough, semi-rough and water-cooled copper plates, respectively, can be seen. In the case of the rough mould wall, the ingot surface has reproduced the mould surface except close to the corners, where the chilling power of the mould is stronger.

The surfaces developed on a fully austenitic casting (cast 5333) are shown in Figure 5.2(a)-(d), where it can be seen that this alloy has a similar surface appearance to that shown in Figure 5.1 with respect to the rough mould wall. This was a general observation applicable to all castings made in air.

For the semi-rough mould wall, the variation of the severity of surface rippling between different castings was more pronounced. A comparison of Figures 5.1(b) and 5.2(b) reveals that for this mould wall, other variables such as superheat and alloy content begin to have an influence on the surface appearance of the ingots.

The surfaces formed against the ground steel plate and the water-cooled copper plate exhibited surface ripples in all cases studied in the present work, albeit with varying severity. When comparing Figures 5.2(c) and 5.2(d) no appreciable difference between the ingot surfaces solidified against the ground steel plate and the water-cooled copper plate is apparent. This observation was made on all castings and thus, for the casting conditions selected, the chilling power of these two mould walls was very similar during the initial stages of solidification. This was verified by the measurement of primary dendrite arm spacings, which was carried out parallel and close to the ingot surface (within 1mm).

5.1.2 Teeming rate.

The influence of teeming rate on surface rippling can be seen in Figure 5.3, where the surfaces produced on two fully austenitic alloys (casts 5522 and 5551) of the same alloy composition and solidified against a ground steel plate in a helium atmosphere are shown. The teeming time for the two castings was approximately 8 and 25 seconds, respectively. It can be seen clearly that the number of ripples formed on the surface at the lower teeming rate is significantly less than for the higher teeming rate. A semi-quantitative way of showing this is to count the number of ripples per 20mm (NR) on the surfaces and plot this parameter against distance along the ingot[80]. This type of measurement was only carried out on the castings teemed in the controlled-atmosphere furnace since, in air, oxide formation can make the results meaningless (cf. Figure 5.2(b)). In Figure 5.4 the results from measurements of NR on the surfaces shown in Figure 5.3 are presented and it can be appreciated from this that the number of ripples differ by a factor of up to 4 between the two surfaces. Another difference is the depth and shape of the ripples, these being deeper and rounder at the lower teeming rate, especially half-way between the bottom and the top of the ingot. Furthermore, a tendency towards ripples of rounder shape and increased depth can be seen near the top surface of the casting with the higher teeming rate (t=8s), i.e. where the teeming rate decreases, which is consistent with the above-mentioned observations.

5.1.3 Superheat.

The superheat of the incoming liquid is, together with the teeming rate, a casting parameter which, when increased, has the effect of reducing the severity of surface rippling. This can be seen in Figure 5.5 where the surfaces of two fully austenitic castings (casts 5203 and 5298) of the same composition are shown. The difference in superheat between the experiments was approximately 20K, the other parameters being maintained constant. Although the casting with the lower superheat was teemed with a superheat of 10K, which in itself can be enough to reduce surface rippling, an appreciable difference in rippling and in particular in ripple depth occurs, the ripples being shallower at the higher superheat.

5.1.4 Alloy content.

The influence of alloy content on surface rippling was studied on fully ferritic stainless steels, austenitic stainless steels with different solidification modes and fully austenitic grades with high and low contents of Cr and Ni.

In two fully ferritic alloys studied, the difference in Cr-content was ~3% (casts 5299 and 5275). These alloys solidify completely to ferrite but have a subsequent solid-state ferrite-austenite-martensite transformation, the latter being dependent on the amount of Cr and carbon (see Section 2.1.2). The casting conditions were the same in both cases with the exception of a marginal difference in teeming time (Table 5.2). Figures 5.1(c) and 5.6 show that there is no appreciable difference in the surface appearance of the two castings.

In Section 2.1.3 the different solidification modes occurring in austenitic stainless steels as a function of Ni-content were described. The influence of three of these modes on the surface ripple formation was investigated, these being Types A, B and D, i.e. alloys with the compositions 18/8, 18/10 and 18/14, respectively. Figures 5.7 and 5.5(a) show that the 18/8-alloy (cast 5202) has very shallow ripples, whereas the surface of the 18/10-alloy (cast 5282) has comparatively deeper ripples. The severest rippling was produced in the 18/14-alloy (cast 5203).

The effect of alloy content on ripple formation within one mode of solidification (Type D) may be seen when Figures 5.5(b) and 5.2(c) are compared. These alloys have the compositions 18/14 and 25/20, respectively. The castings were made under similar conditions, the superheat being high in both cases. The casting with the higher alloy content produced a surface with a significantly higher degree of meniscus freezing, the surface quality being very poor indeed. In order to ensure that this difference in surface rippling was not due to the formation of a thicker and stronger layer of oxide on the melt during the teeming of the high-alloyed steel, experiments were also carried out in a controlled atmosphere. In Figure 5.8 examples of the surfaces produced on casts 5522 (18/14) and 5525 (25/20) are shown, these ingots having been solidified in a helium atmosphere. Again, it is clear that the casting with the higher alloy content has the severest surface rippling. The difference in surface appearance between these two alloys is shown further in Figure 5.9 where the steel with the higher alloy content has a lower NR than has the 18/14-alloy, this being in the upper two-thirds of the ingot.

5.1.5 Atmosphere.

In order to study the influence of the atmosphere on the extent of rippling, castings were produced in vacuum and in a helium atmosphere. In terms of heat transfer, the main differences between these atmospheres are that in vacuum only radiative heat transfer takes place where the metal is not in contact with the mould, whereas in helium a combination of radiative and convective or conductive heat transfer occurs, depending on position. Also, helium has a relatively high thermal conductivity[215].

Figures 5.10(a) and (b) show results from these experiments (casts 5550 and 5522), the surfaces having solidified against the semi-rough mould wall. There is a considerable difference in the surface appearance between the two castings in terms of surface rippling. Figures 5.8(a) and 5.10(c) show a more pronounced difference on surfaces which have been formed against a ground steel mould wall. It was also found that surfaces formed in vacuum had a lower NR than those formed on the ingots cast in the helium atmosphere (Figure 5.11). Whilst noticeable, the ripples counted on the surfaces produced in vacuum were in most cases lines rather than actual surface depressions (Figure 5.10(c)). All castings made in helium atmospheres showed rippling on surfaces which had solidified against rough mould walls. As mentioned in Section 5.1.1, this was not the case for any of the castings produced in air, indicating the significance of the type of atmosphere on surface ripple formation.

5.2 Structures in the Vicinity of Ripples and Oscillation Marks.

The preceding section showed how various parameters influenced the surface appearance of the experimental ingots in terms of surface ripples. This section deals with the results of the microstructural investigation of the ingots. The results are presented so as to facilitate comparisons between surface observations and the sub-surface microstructures. Thus, results are formulated in terms of the influence of casting parameters and alloy composition. In addition, the microstructures found in the vicinity of oscillation marks are presented. Samples from three continuously-cast stainless steel slabs (known commercially as 18/8-, 302- and 316-type steels) were also examined and the compositions of these are given in Table 5.4. The etchants used for the different alloys are given in Appendix VI.

5.2.1 Influence of casting parameters.

In Section 5.1.1 the strong influence of the surface roughness of the mould walls on surface rippling was shown. The main parameter affected by varying the roughness of the mould wall is the heat flux. Thus, by changing the surface topography of the mould a corresponding change in the microstructure in the regions close to the ingot surface in terms of coarseness is to be expected. That this is so is shown in Figure 5.12 where the structures obtained from cast 5550 (vacuum, 18/14-alloy) can be seen. The structures are from the faces solidified against the rough, semi-rough and ground steel plates, respectively. A distinct difference in the coarseness of the microstructures is observed. The structure is very fine in the areas solidified against the ground steel plates and also, a distinguishable difference between the structures formed against the semi-rough and rough mould walls exists.

Significant changes on surface rippling are produced by varying the teeming rate. Knowing that the primary mechanism for ripple formation is the partial solidification of the meniscus beyond the point where mould and metal is in immediate contact, it is to be expected that a reduction of the teeming rate will allow more meniscus freezing to take place. In Figure 5.13 structures found in the surface region for the higher teeming rate studied are shown (cast 5522, helium, t=8s). Here the prominent features are the fineness of the structure and the shape of the surface depressions. However, no overflows and lapped interfaces are present, indicating that considerable bending-back of the partially-solidified meniscus has occurred. An example of the structures found in the sub-surface regions at the low teeming rate (t=25s) is shown in Figure 5.14 (cast 5551, helium). Here, several aspects different from those mentioned above are apparent. The major one is the rather unusual presence of a coarser structure (than that in the ingot interior) close to the surface. Furthermore, in the upper part an overflow has occurred and further down two smaller depressions exist, one in the region of coarse surface structure with a second depression located where a transition between fine and coarse structure occurs. A further example of the structures found in the upper part of the areas with a coarse structure is shown in Figure 5.15(a). There, the remnants of the tip of the solid meniscus which has been overflowed can be seen, creating a dendrite-looking feature almost parallel to the ingot surface. This tip has been formed by primary growth from the solid surface into the liquid and after/during the overflow, growth has occurred into the overflowing liquid. Further down, evidence for acceleration of the solidification rate by growth from existing coarse dendrites is seen. Another example of the latter is shown in Figure 5.15(b), taken from the vicinity of a small depression located below the area shown in Figure 5.15(a).

It would be expected that an increase in the superheat would result in the formation of a thinner solid skin and a smaller amount of meniscus freezing. This leads to smaller overflows and an increased incidence of the bending-back of the meniscii. In Figure 5.16(a) the structure developed in a rippled region at "low" superheat (cast 5203) is shown. A fairly thick skin with fine dendritic structure is evident together with a substantial overflow. Also, signs of the early stages of the formation of a tear as the solid meniscus has been bent back are observeable. In addition, the shape of the overflow indicates that wetting of the solid meniscus has occurred during overflow. When the superheat of the liquid is increased, a more pronounced bending-back of the solid meniscus takes place (Figure 5.16(b)), thus creating a smoother ingot surface. Bleeding become more frequent at higher superheats (Figure 5.16(c)), and this results from the remelting of thin parts of the solid skin, e.g. in the vicinity of existing ripples. Additional examples of structures developed at high and low superheats in different alloys are given in Figure 5.17.*

In Section 5.1.5 it was shown that the atmosphere has a significant influence on the incidence of surface rippling. This was demonstrated by the castings made in vacuum or in a helium atmosphere. The difference in the structures developed in these castings can be seen in Figures 5.12 and 5.13. An appreciable difference in the fineness of the microstructures close to the ingot surface is seen, indicating a lower cooling rate in the casting made in vacuum. In addition, the dissimilarity in the ripple depth of the surfaces is clearly evident.

5.2.2 Effect of alloy content.

The microstructures developed in the regions of the shallow ripples on the surface of the 18/8-alloy (Type A, cast 5202) are shown in Figure 5.18. The existence of both total bending-back and a combination of bending-back and overflow is evident. In the case of total bending-back, signs of lateral flow of liquid originating from a bleed elsewhere in the ripple can be seen, thus artificially producing a smoother surface of the ingot.

In the 18/10-alloy (cast 5282) both comparatively larger overflows (Figure 5.19(a)) and complete bending-back (Figure 5.19(b)) are present. In the latter figure a difference in the δ-ferrite content (intra-

*Here it can be seen that both bending back (Figure 5.17(b)) and overflow (Figure 5.17(d)) can occur in the same ingot.

dendritic) between rippled and non-rippled areas is clear, showing the influence of thermal history on the microstructure in these regions.

The fully austenitic alloys (18/14 and 25/20) also exhibited overflow and bending-back of the partially-solidified meniscus. Structures found in the 18/14-alloys are shown in Figures 5.13, 5.16(a) and 5.20 and in the 25/20-alloys in Figures 5.17(a) and 5.21. A comparison of Figures 5.13 and 5.21 (identical casting conditions) reveals a rounder shape and larger depth of the ripples in the more highly alloyed steel (cf. Section 5.1.4). It can also be seen that the 18/14-steel does not show any evidence of overflow (Figure 5.13), which is not the case for the 25/20-steel (Figure 5.21) in which a lapped interface is present.

5.2.3 Oscillation marks.

As mentioned previously, the microstructures in the vicinity of oscillation marks (OSM) in three commercially produced stainless steel slabs (18/8-, 302- and 316-type) were examined in the present study. In Figure 5.22, the external surfaces of these strands are shown and it is clear that the 18/8-alloy has the deepest OSM's and the 316-steel the shallowest marks.

The structures present in the deep OSM's of the 18/8-type steel are shown in Figure 5.23. Apart from evidence of meniscus solidification, signs of lateral flow of liquid from bleeding elsewhere in the OSM's are also present. Some bending-back of the partially-solidified meniscii is observeable and in one case (Figure 5.23(b)), this has caused the meniscus to break in two places during the bending. In the case of the 302- and 316-steels, which have the comparatively smoother external surfaces, lapped interfaces were found in both alloys

(Figure 5.24). When comparing the structures of these two alloys, the 316-alloy shows overflows extending over a longer distance and a more pronounced bending-back than the 302-steel. Furthermore, in the latter alloy several equiaxed dendrites are present close to the strand surface, indicating a low superheat in the liquid during casting.

5.3 δ-Ferrite Distribution in Continuously-Cast Slabs.

In the following the experimental results from the measurements of the δ-ferrite content across sections of continuously-cast slabs are presented. The alloys investigated were the same as those examined in the previous section and the thicknesses of the slabs were 150mm (302- and 316-alloys) and 155mm (18/8-alloy), respectively.

In Figure 5.25 examples of the microstructural features of the δ-ferrite across the 18/8-slab are shown. The significant difference in the coarseness of the ferrite can be clearly seen. It can also be noticed that towards the centre of the slab, some inter-dendritic δ-ferrite is present.

As mentioned in Section 4.4, measurements were carried out using both point counting and a Ferritector. This was done in order to make it possible to interpret the trends in the results obtained despite a large statistical error in the point counting. This error is due to the low volume fractions of δ-ferrite present in the types of alloys studied.

The cross-sectional variation of δ-ferrite in the 18/8-slab is shown in Figure 5.26. At the surfaces of the slab the lowest ferrite contents can be observed. In addition, an increase in the volume fraction further in from the surfaces followed by a decrease at approximately 50 and 110 mm is seen. After these depressions, the content increases again and at the centre another depression occurs. The trend is similar in the 302- and 316-slabs (Figures 5.27 and 5.28), although in the latter the ferrite content is lower and the trend not so pronounced. The 302-slab shows the greater variation between the surfaces and the interior and has in general a similar ferrite content to that of the 18/8-steel. Furthermore, in all three cases the variation of the δ-ferrite content is not symmetrical around the centre line of the slabs. In the 18/8- and 302-slabs the results from the Ferritector were consistently higher than those from the point counting, whereas in the 316-alloy the opposite was the case for most of the points.

5.4 Discussion.

5.4.1 Ripples and oscillation marks.

The experimental results from the investigation of the influence of mould roughness on the surface rippling showed clearly that this parameter is of great importance when a smooth casting surface is to be produced. Since a variation of the mould roughness in essence implies a change in the contact area between the metal and the mould, a corresponding change in the rate of heat extraction will occur. Evidence for this was shown by the microstructure in Figure 5.12. Thus, the main parameter causing surface ripple formation is the heat flux from the metal to the mould. This is in good agreement with results previously reported in the literature[80-82,87].

A measure, which has been shown to reduce the severity of surface rippling, is an increase in the casting speed[80-82,87]. This is due to a reduction in the time available for solidification along the meniscus. Hence, an increased casting speed causes the ripples to become more superficial but at the same time the interripple distance will decrease, i.e. the number of ripples/unit length increases (Figure 5.4). Evidence for the longer time available for meniscus freezing at low casting speed was shown in the microstructures in Figures 5.14 and 5.15 where it could be seen that a fairly thick layer of solid was formed along the meniscus (coarse structure) which subsequently was bent back towards the mould wall, producing a finer internal structure. The latter was due to an increase in the rate of heat extraction as the gap between the mould and the meniscus became narrower during the bending back. The two smaller depressions observed in Figure 5.14 are a result of the solid meniscus being bent back.

As a higher casting speed reduces rippling so in a similar way, an increase in superheat causes a reduction in the extent of meniscus solidification (Figures 5.5 and 5.16(b)). This is simply due to the higher heat content of the liquid, which has to be removed during a given time interval in order to promote extensive solidification. The observations made in the present work are in good agreement with those made elsewhere[80-82]. However, Stemple et al.[87] did not observe any influence of superheat in the Sn-Pb alloys investigated (varied between 18^{o}C and 131^{o}C). This is probably due to the small size of the casting system used (ingot size 36x20x90mm). In addition, in the latter work both the casting speed and the superheat were altered between experiments which meant that these parameters can have an influence upon each other.

The results of the measurements of the variation of surface rippling in stainless steels as a function of alloy content showed that going from lower alloyed grades (i.e. ferritic steels), through the "austenitic" grades with different solidification modes, to the fully austenitic alloy with high Cr and Ni content increased the severity of rippling (Figures 5.1(c), 5.6, 5.7 and 5.8). The reason for this general difference between ferritic and austenitic grades is the well established fact that ferritic stainless steels have a significantly lower physical strength than the austenitic alloys[216]. This means that bending-back of the solid meniscus is more difficult in austenitic alloys. The observed difference between the fully ferritic and the 18/8-alloy can be attributed to the solute content, since they have similar solidification characteristics and both are ferritic in the temperature range of concern (close to the liquidus). Thus, the higher solute content in the 18/8-alloy provides a stronger solid phase by solid-solution hardening and again, the solid meniscus is less prone to being bent back. The same interpretation is applicable to account for the observed differences in rippling between the 18/14- and 25/20-alloys, since the solidification characteristics are similar[20] and the 25/20-grade has a higher strength than the 18/14-alloy[36,217]. The microstructures found in these steels give further indication of the inability of the partially-solid meniscus in the high alloyed steel to bend back during teeming (Figures 5.13 and 5.21). In relation to continuous casting, it has been reported in the literature that in more highly alloyed stainless steels it is more difficult to produce good surface quality than in less alloyed steels[162]. The similarity of the surface rippling observed in the 17Cr- and 20Cr-steels indicates that in this case the difference in solute content is too small to have a significant influence on the strength of the solid formed in the meniscus region.

The difference in ripple formation between the castings carried out in vacuum and in a helium atmosphere (Figures 5.8(a), 5.9(c), 5.10 and 5.11) is in good agreement with reports in the literature[81,83]. The results from the studies of both the influence of teeming rate, and the use of different atmospheres, which vary the heat flux in the meniscus region, provide good evidence for the concept of the partial solidification of the meniscus being the main cause for ripple formation. The difference in heat flux between the two atmospheres was mirrored in the microstructures (Figures 5.12 and 5.13). In addition, the lower NR in the casting made in vacuum as compared with that cast in a helium atmosphere (Figure 5.11) is due merely to the almost complete absence of surface rippling on the vacuum-cast ingot (Figure 5.10(a) and (c)).

When studying the external surfaces of continuously-cast strands, it has to be recognised that such strands can have different depths of oscillation marks due principally to two factors. The first is a consequence of differences in parameters such as alloy content, superheat and casting speed and the second is attributable to the setting of the rolls in the secondary cooling zone (supporting and withdrawal rolls), which can induce plastic deformation of the strand during casting[128]. Thus, it is not strictly correct to compare different strands in terms of oscillation mark formation unless they have been cast under identical conditions and in the same continuous casting machine.

In the present study, the 316-slab showed signs of deformation (Figure 5.22). In all slabs studied, evidence for overflowed and sometimes bent-back meniscii was available in the microstructures (Figures 5.23 and 5.24).

A possible explanation for the observed breakages of the overflown meniscus during bending-back, which has not been considered previously, is the so-called Vogel-Cantor-Doherty mechanism for fragmentation of solid in liquid metals during solidification[218]. The mechanism is based on the formation of high-angle boundaries by recrystallization of the solid during induced deformation, which is followed by melting of the boundaries due to wetting.

The observation of equiaxed dendrites close to the strand surface indicates that, although the superheat in the tundish has been sufficient to prevent clogging in the casting tube during the process, a major part of the superheat has been dissipated over the relatively short distance between the tube and the wide face of the mould. The same observation has also been reported in the literature[163,219].

5.4.2 δ-ferrite .

The variation of the δ-ferrite content across the commercial slabs studied, which solidify primarily to ferrite followed by the formation of austenite by the peritectic reaction and transformation, is due to two main factors. Firstly, the cooling conditions between the liquidus and solidus temperatures determine the dendrite arm spacings in the solid. The second factor is the cooling pattern in the solid below the solidus temperature. The dendrite arm spacing determines the diffusion distances for the subsequent peritectic reaction and transformation and, to some extent, the original ferrite content at the solidus, whereas the cooling pattern controls the extent of the diffusion-controlled transformation to austenite. Thus, the observations made represent the influence of the combination of variations in diffusion distances and temperatures.

The low ferrite content at the strand surfaces (Figures 5.25, 5.26 5.27 and 5.28) is a result of small dendrite arm spacings and a sufficiently long time above approximately 1000°C, where the diffusion rates have been found to be adequate for the peritectic transformation to take place[14]. The increase in ferrite content up to approximately 20 mm from the surfaces indicates that the thermal gradient in the solid skin has been too steep in relation to the dendrite arm spacings to allow a uniform ferrite content. Since the thickness of the shell solidified in the mould commonly is of the order of 20 mm[91,118,121,140], the above mentioned features are due to the conditions prevailing in the mould. The subsequent decrease of ferrite further in from the surface indicates that, while the thermal gradients are becoming less steep in the solid in the spray-zone, the diffusion distances are small enough to allow for the transformation of δ-ferrite. The increase in ferrite content towards the centre of the slabs shows that as the dendrite arm spacings increase, the rate of transformation becomes slower. The sudden decrease in ferrite content near the centre-line is due to both segregation and an increase in cooling rate towards the end of solidification.

In Section 5.3, it was observed that, in the 18/8- and 302-slabs, the Ferritector indicated higher ferrite contents than was obtained from the point counting. This is due to the influence of texture and morphology on the magnetic measurements[14]. The opposite effect found in the 316-slab can be attributed to a further transformation of the remanent ferrite to σ-phase[68-70], i.e. the formation of a non-magnetic phase.

The non-symmetrical distribution of δ-ferrite on either side of the centre-line indicates that the cooling of the strand is uneven for the different surfaces. This can be due to several factors. For example, the type of mould (curved, straight) and the alignment of the rolls and the spraying conditions in the secondary cooling zone, can all influence the thermal history of the strand.

CHAPTER 6

Correlation of Models with Observations

In this chapter comparisons are made between the experimental results presented in the previous chapter and the predictions from the numerical analyses. This allows for further assessments of the influence of different parameters on solidification and cooling. In addition, the possible effects of parameters, which are difficult to study experimentally, are investigated.

6.1 Meniscus Solidification.

In the following, results from the two-dimensional analysis of the heat flow in the meniscus region during casting are presented and discussed in relation to the experimental observations. The parameters and conditions adopted in the analysis are essentially those prevailing during the continuous casting of steels.

In the analysis, it was assumed that austenitic stainless steel has the same meniscus shape and height as carbon steels. In Tables 6.1 and 6.2, the parameters used in the modelling are given.

6.1.1 Effect of casting parameters.

In the results from the experiments in which the influence of surface roughness of the mould wall was examined, it was clearly shown that the rougher the mould the less the extent of ripple formation (Figures 5.1 and 5.2). Since this is due to differences in the area of contact between the mould and the metal and, hence, differences in the heat transfer coefficients, this situation can effectively be simulated by varying the mould/metal interface resistance. In Figure 6.1, the results from such an analysis are shown for heat transfer coefficients ranging from 1.4 to 6.0 $kWm^{-2}K^{-1}$ and for the time period for solidification of 0.3 s. Although there was no superheat present in the system, only a small part of the meniscus solidified, thus predicting shallow ripples for the larger h-values and no ripple formation for the lower ones. This is in good agreement with the experimental observations. However, it has to be emphasised that the predictions made using a constant convective heat transfer coefficient are rather conservative since, close to the mould wall, conduction heat transfer through the air will take place. In fluid flow analysis, this is determined by the product of the Grashof number (Gr) and Prandtl number (Pr) together with the Nusselt number (Nu)[220]. Thus, in the real situation stronger heat transfer is to be expected where the gap between the mould and the meniscus is small. This will cause the iso-f_s curves for the different h-values to move further up the meniscus.

The influence of teeming rate on ripple formation (Figure 5.3) can, in terms of the numerical analysis, be modelled by altering the time for solidification. To simulate a helium atmosphere (Table 6.2), solidification times ranging from 0.15 to 0.9 s were used. The results from this investigation are shown in Figure 6.2. Since, in the experiments, the average casting speed varied by a factor of approximately 3, comparisons of the curves representing for example 0.15 and 0.45s can be made. From this it can be appreciated that there is excellent agreement between experimental and predicted results in terms of casting speed. Furthermore, as with the influence of mould roughness, the predictions made are conservative.

The effect of superheat on the extent of meniscus solidification can readily be simulated by altering the initial temperature field in the model. In Figure 6.3, the results from this analysis are shown. It is clear that with increasing superheat, the meniscus freezing is retarded. Again, this is compatible with the experimental observations (Figure 5.5).

These correlations confirm that the main mechanism for ripple formation is the partial solidification of the meniscus during casting. The extent of ripple formation is reduced by decreasing the mould/metal heat transfer coefficient, increasing the casting speed and/or increasing the teeming temperature. Furthermore, these observations are in good agreement with results from numerical analyses of solidification in the meniscus region presented in the literature[81,185].

6.1.2 Effect of atmosphere.

The conditions prevailing in the controlled-atmosphere furnace were simulated by using different values for the convective heat transfer coefficient, h_{con}, and the emissivity of the metal surface (Table 6.2). In Figure 6.4 the results from such a procedure are given. The effect of convective heat transfer can be seen, despite the fact that these predictions can only be interpreted in terms of the relative influence of the atmosphere, since the absolute values of h_{con} are not known. The validity of the model is verified by the good agreement with experimental results (Figure 5.10) and observations reported in the literature[81,83]. However, two points must be made. Firstly, the use of a constant h_{con} value underestimates the real situation (c.f. Section 6.1.1), the difference between the atmospheres being considerable since, in vacuum, no convection or conduction takes place between the mould and the metal in the meniscus region. Secondly, in a real casting, the heat transfer coefficient between the mould and the metal where they are in contact is dependent on the atmosphere since the cavities in the surface of the mould, which are present due to its roughness, are filled with the atmosphere. This influence of the atmosphere on the mould/metal heat transfer coefficient has been observed experimentally[83].

6.1.3 Effect of casting flux.

The effect of casting flux and its properties on the solidification kinetics in the meniscus region during continuous casting is extremely difficult to study experimentally. Thus, a numerical model for such an assessment would be extremely useful. Previously, an appropriate model has not been available and, moreover, the thermo-physical properties of casting fluxes were unknown until very recently. In the following, a systematic analysis of the possible influence of casting powder and its different properties on meniscus solidification during continuous casting of slabs is given.

When a casting flux or slag is present as a layer on the meniscus and as a film between the mould and the metal, the shape of the meniscus is different from the shape found in association with the gaseous atmosphere. In the present study, equation 3.4 (c.f. Section 3.1.4) gave the best fit to observed meniscus shapes in investigations made elsewhere[85] when the constants P and Z were taken as 0.2 and 0.6, respectively.

In the continuous casting of steels, the superheat in the tundish is commonly of the order of 30°C. However, as mentioned in Section 5.4.1, results from measurements of the temperature distribution in the liquid in the mould have shown that a significant part of the superheat has been dissipated before the metal reaches the mould wall[163,219]. Thus, in the following analysis a superheat of $5^{o}C$ was used. Furthermore, the thermal resistance between the metal and the flux is assumed to be negligible. This is based on the fact that complete wetting of the strand by the liquid flux minimises any interface resistances. The values adopted for T_{sx} and T_{sy} (c.f. Section 3.1.5 and Figure 3.3) were $200^{o}C$[198,221] and $1100^{o}C$, respectively, the latter being a common melting temperature for casting fluxes and slags[112,222]. It may be argued that the value adopted for T_{sx} is too low, since values higher than this have been reported in the literature[112]. However, based on results from more careful investigations carried out by Ohmiya et al.[221], the value selected in this investigation is justified. Also, in the real situation, this temperature depends on the casting flux used. This is due to differences in the extent of sticking between the oscillating mould and the solid part of the flux film. In addition, it was assumed that the temperature profile across the flux is linear, i.e. any influence of differences in the conductivity between the glassy, crystalline and liquid layers present in the flux[115,221,222] was neglected.

The thermal conductivity of the casting flux, k_f, has been found to be of the order of 1.2 $Wm^{-1}K^{-1}$ at about $300^{o}C$ and 1.5 $Wm^{-1}K^{-1}$ at $1000^{o}C$[222]. Thus, a value of 1.5 $Wm^{-1}K^{-1}$ was adopted. In the solutions, a healing time of 0.3s was used.

In Figure 6.5, the influence of the film thickness s on the extent of meniscus freezing is shown. It is clear that the film thickness plays an important part in the formation of oscillation marks. Based on the knowledge of the consumption of casting powder during continuous casting, it has been suggested that lubricating films of the order of 0.1 mm can exist in the mould[112,195]. However, it is believed that this only constitutes the thickness of the liquid part of the film due to the presence of a solid layer, which is attached to the mould wall during the process[221,223]. Another property of the liquid casting flux, which can be of importance in terms of heat flow is the viscosity. In fluid flow analysis it is known that for a given thickness and velocity of a fluid, the nature of the flow is determined by the viscosity, which determines whether the flow is going to be laminar or turbulent. This is commonly expressed in terms of the Reynolds number[224] (Re). Thus, if the casting flux has a low viscosity, turbulent flow may occur, which changes the heat flow from being controlled by conduction solely to convective heat transfer. However, there is still a lack of knowledge about the phenomena taking place in the flux during casting.

The thickness of the layer l of casting flux on the liquid steel is mainly determined by the rate of sintering and the melting rate of the powder[225]. In the analysis it was found that for the value of T_{sy} used, the thickness of the layer had no appreciable influence on the extent of meniscus freezing. This is due to the rather flat temperature gradient, which is present in the liquid part of the flux on the metal.

From the above, it is clear that depending on the casting powder used, different behaviour in terms of meniscus solidification is to be expected. For example, if a flux with low viscosity and high melting rate is used, l and s will be small. (A high viscosity and low melting rate would have the opposite effect.) The results from the different values of s can also be interpreted as describing the situation which can occur if the conditions prevailing in a given mould are such that the film (and layer thickness) of flux varies with position around the mould. Although these results indicate that a casting powder with a high viscosity and a low melting rate would be beneficial for the reduction of formation of oscillation marks, such a powder could have detrimental effects on the lubrication of the strand due to insufficient hydrodynamic lubrication.

In a similar manner to the influence of s, the thermal conductivity of the casting flux can be expected to have a considerable influence on the solidification of the meniscus. That this is the case is shown in Figure 6.6. This can also be seen as a way of obtaining the effect of an increased rate of heat extraction due to the occurrence of convective heat transfer in the liquid flux. Furthermore, it has recently been observed that the effective thermal conductivity of casting fluxes exhibits a significant increase when the flux melts[226]. Thus, the overall rate of heat extraction will be greater and more pronounced meniscus freezing will result.

As mentioned previously, the meniscus shape has been observed to change when a casting flux is applied. In order to investigate the influence of the shape of the meniscus, the values 0.4 and 0.5 for P and Z, respectively, were adopted for the case of a casting flux (i.e. the shape for gaseous atmospheres). The shape used for gaseous atmospheres shows a steeper slope close to the mould wall and thus, more meniscus freezing takes place. This gives a general indication of the effect of a change of the meniscus shape, which, in a real situation, can occur when in-mould electromagnetic stirring is applied (Figure 6.7).

From the results presented above it is clear that although the main functions of a casting powder are to protect the melt from oxidation, absorb inclusions and provide a lubricating film, its properties also play an important part in meniscus solidification and, hence, oscillation mark formation. Thus, properties of the flux such as thermal conductivity, sintering rate and melting rate have to be considered from the point of view of oscillation marks if a strand surface with as shallow marks as possible is to be produced. In addition, it has recently been suggested that if the healing time is increased, the lubrication of the strand is improved[115]. This would lead to an increase in the amount of meniscus solidification (c.f. Section 6.1.1 and Figure 6.2). Thus, optimum conditions have to be found, taking these aspects into account. Furthermore, as shown in earlier work[80,185] and in the present study, an increase in the superheat significantly reduces meniscus freezing. However, in continuous casting a consistent increase in the superheat may be difficult to achieve in practice. Thus, a reduction in the heat transfer rate in the meniscus region becomes more important. This may be accomplished either by reducing the heat transfer in the mould itself[80,185] or by the selection or development of a casting flux with a low thermal conductivity. It has to be emphasised that this mainly applies to the continuous casting of slabs, since the basic understanding of phenomena in the meniscus region during the continuous casting of billets, where oil is common as a lubricant, is still very limited. However, based on Figure 2.7 it may be suggested that the rate of heat extraction has to be reduced by, for example, modifying the heat transfer in the mould itself in the meniscus region if a smooth strand-surface is to be produced in billet casting.

6.1.4 Effect of alloy content.

In order to assess the influence of alloy content on meniscus freezing, carbon steels with different carbon contents and an austenitic stainless steel were investigated. The difficulty of producing good surface quality on strands of continuously-cast carbon steels with around 0.1%C is well known[88,89]. Figure 6.8 shows the predictions made and it can be seen that the stainless steel and the 0.1%C steel behave similarly in terms of meniscus freezing, whereas for the higher carbon contents, less rippling is predicted. It should be appreciated that this is due not only to a variation in the mechanical properties (c.f. Section 5.4.1) but also due to a difference in the solidification characteristics of the alloys. Hence, both the mechanical strength of the solid and the solidification characteristics have to be taken into account when assessing oscillation mark formation on a strand of a continuously-cast alloy.

6.1.5 Comparison with a one-dimensional model.

As mentioned in Section 2.5, Ackermann et al.[81] developed a one-dimensional heat transfer model for the analysis of meniscus freezing. In this section, the results from the two-dimensional model developed in the present work are compared and discussed in relation to those of the uni-dimensional analysis[81].

In Table 6.1 the data are given, which were used in the 1-D model to simulate the behaviour of pure aluminium during chill-casting in a helium atmosphere. In the 1-D analysis, the time period during which heat is extracted from the meniscus was defined as a function of casting speed, i.e. $t=b/V_c$ where t is the so-called residence time and b and V_c are the meniscus height and the casting speed, respectively. Since a casting speed of 5 mms^{-1} and a meniscus height of 8.8 mm were considered, the value of t was 1.76 s. A shape of the meniscus identical to that used in the 1-D analysis was obtained by taking the values 0.12 and 0.5 for P and Z, respectively (c.f. Section 3.1.4, Equation 3.4). The 2-D model was modified so that,

(i) the rate of heat extraction between the mould and the metal below the meniscus was determined by the equivalent to a heat transfer coefficient of 11 $kWm^{-2}K^{-1}$, which was the value used in the 1-D model,

(ii) on the meniscus, the heat transfer was controlled by conduction through the helium to the mould wall and by radiation heat transfer,

(iii) a temperature-independent thermal conductivity for the aluminium was assumed.

It should be emphasised that due to the philosophy behind the 1-D analysis, any element in the metal, which is located <u>above</u> the level of contact between the mould and the metal (i.e. above the triple-point mould-metal-atmosphere), spends a time period there which is <u>less</u> than the residence time. For any element located <u>below</u> the point of contact, heat transfer for a time period, which is <u>longer</u> than the residence time takes place. This is to be compared with the situation in the two-dimensional analysis where each element of the system is considered in the calculations throughout a given time-interval.

The predictions made by the 2-D model together with those of the 1-D analysis are shown in Figure 6.9. Here, it can be seen that for the boundary conditions used, the nature of the heat transfer in the meniscus region is clearly two-dimensional. For example, it can be appreciated that, when using 1-D analysis, any element located beyond the triple-point does not "feel" the very high rate of heat extraction which occurs where the mould and the metal are in contact. The results from the 2-D analysis clearly show that above the contact-point, heat is extracted both by conduction through the atmosphere and by conduction in the metal itself downwards to the mould/metal interface. The fact that the duration of heat transfer below the contact-point is, in reality, longer than the residence time casts further doubts upon the validity of a 1-D treatment. Furthermore, the definition of the residence time as put forward by Ackermann et al.[81] represents a non-realistic situation since, in a real situation, the meniscus will not keep its shape for about two seconds during casting. Thus, it is considered that the situation as defined in Section 3.1.3 describes the real situation more accurately. It is also of some concern that such a high heat transfer coefficient is used in the 1-D model. Values commonly used are in the order of 1.0 to 2.0 $kWm^{-2}K^{-1}$ for chill casting[80].

6.2 Structures of Continuously-Cast Slabs.

In the following, the results from the microstructural predictions of the one-dimensional heat transfer model applied to the continuous casting of 18/10-type austenitic stainless steel slabs are presented and discussed.

During the initial analysis, it was found that when applying Equation 3.21 (c.f. Section 3.2.1) in the mould, the cooling conditions so determined were not sufficient for realistic dendrite arm spacings at the surface of the slab to be predicted. Thus, in the upper part of the mould, heat was assumed to be conducted through a layer of casting flux in a similar manner to that described in Sections 3.1.5 and 6.1.3. In the results presented here, it was considered that, from the point at which the meniscus joins the mould to a point some 150 mm down the strand, a 0.5 mm thick film of casting flux was present. Below this point, Equation 3.21 was applied. In order to make sure that the cooling conditions in the mould in terms of heat flux were realistic, the total amount of heat extracted in the mould was monitored and compared with data compiled by Lait et al.[140]. These data were obtained by measuring the total heat flux in several different continuous casting moulds. A further check on the cooling conditions in the mould was achieved by recording the thickness of the solid skin at the exit of the mould and comparing it with results from the literature[118,121]. Furthermore, it has to be emphasised that, in the model, no account was taken of the possible influence of solid-state back-diffusion (i.e. coarsening) in the calculations of the secondary dendrite arm spacings, since this is embodied in the equation and constants used (c.f. Equation 3.28). Also, the formation of equiaxed crystals in the central regions of the slab was neglected. This point implies that the predicted arm spacings (λ_2) will be underestimates in the central regions of the slab.

The superheat of the liquid in the mould was assumed to be $10^{o}C$, this being taken as an average between the lower superheat at the surface of the slab and the higher temperatures prevalent in the vicinity of the central and upper portions of the mould.

Adopting the above-mentioned conditions, the secondary dendrite arm spacings were calculated. Having these values, the model was re-initiated (c.f. Section 3.2.3) in order to predict fraction δ-ferrite across the slab. During the first trial runs of the model it was observed that the value of the chromium content on the γ-side of the δ/γ-interface ($C^{\gamma\delta}$) (c.f. Section 3.2.3) was a very sensitive parameter in terms of the predicted content of δ-ferrite. This is a parameter which is very difficult to determine experimentally and thus, a value of $C_{Cr}^{\gamma\delta}$ was assumed so that realistic amounts of δ-ferrite could be predicted.

The data used in the model were the same as those given in Table 6.1 for stainless steel. In Table 6.3, the values of the different parameters used in the diffusion-part of the model are given.

Due to the lack of data for heat transfer coefficients for the secondary cooling zone available in the literature and, in particular, data for the continuous casting of stainless steels, the model was used with values as presented by Nozaki et al.[126] and by Larrecq et al.[199] for casting of carbon steels, assuming that there is no difference between the practices for carbon and stainless steels. In Table 6.4, the machine-data utilised are given.

The two sets of heat transfer data for the secondary cooling zone presented by Nozaki et al.[126] were part of a study of surface-crack formation on 220 mm thick slabs cast at 1 $mmin^{-1}$. The second set of data was a result of the analysis, which produced a decrease in the occurrence of cracks. Thus, by adopting these two sets of data, the influence of cooling intensity in the different spray zones on δ-ferrite variation can be obtained, all the other casting parameters being the same. In Table 6.4 it can be seen that the heat transfer data used in the modified spray pattern are in general higher than those used in the first pattern, except for the first two spray-zones. In Figures 6.10(a)-(c) and 6.11(a)-(c), the results from this analysis are shown in terms of predicted thermal history at different distances from the surface of the slab, predicted λ_2-variation across the slab and predicted δ-variation across the slab, respectively. From the variation in λ_2 for the two cooling systems (Figures 6.10(b) and 6.11(b)) it can be appreciated that the less severe cooling in the first few spray zones in the modified system results in a slightly coarser structure close to the surface, whereas the opposite is the case from approximately half-way between the surface and the centre. The corresponding variation in δ-ferrite content (Figures 6.10(c) and 6.11(c)), which is here represented as a series of profiles at the un-bending point (15.8m below the meniscus) and at room temperature (i.e. assuming that there is no change in ferrite content below 900°C), shows that, in the case of the more intense cooling system, more δ-ferrite is present at room temperature, except close to the surface. Furthermore, it is interesting to notice that with the weaker cooling system, the temperature in the interior of the slab is still high enough at the un-bending point to allow for further transformation of δ-ferrite. This is emphasised by the reheating of the surface regions, which also causes a continuation of the transformation. In the modified cooling system, a smaller extent of transformation from the un-bending point and onwards occurs. From the thermal profiles (Figures 6.10(a) and 6.11(a)) it can be seen that the temperatures of the central regions are still fairly high at the un-bending point for this cooling system. However, since the surface temperatures are very low, a steep gradient exists in the slab and this produces a high cooling rate and thus inhibits any significant transformation. The predicted pool depths for the two spray systems showed a difference of 0.6m (13.6 and 13.0m, respectively), which is in good agreement with the results by Nozaki et al.[126]

In the work by Larrecq et al.[199], two sets of heat transfer data (Table 6.4) were presented for the casting of 210mm thick carbon steel slabs. The first set of data was for a conventional spray pattern used together with a casting speed of 0.9 $mmin^{-1}$, whereas the second set was a result of an investigation concerning the achievement of optimum conditions for high yield considering metallurgical and technological constraints. This led to the introduction of an optimum casting speed (1.075 $mmin^{-1}$) and a corresponding spray-cooling pattern. In Table 6.4 it can be seen that the increase in casting speed was essentially compensated for by increasing the heat extraction in spray-zones 3 to 6. The results from the application of these data to stainless steel are shown in Figures 6.12(a)-(c) and 6.13(a)-(c). From the predicted thermal histories (Figures 6.12(a) and 6.13(a)), the enhanced cooling in the modified system does not result in lower temperatures across the slabs at the un-bending point. This is accounted for by the change in casting speed. Furthermore, the cooling conditions in the slabs obtained using the conventional spray pattern resulted in the coarsest dendrite arm spacings (Figures 6.12(b) and 6.13(b)). The predictions of the δ-ferrite content show that for both cooling systems (and casting speeds), a significant reduction of the δ-ferrite content occurs on cooling from the unbending point and onwards (Figures 6.12(c) and 6.13(c)). This is particularly the case for the optimised system where, at the un-bending point, the ferrite content is still fairly high in the interior of the slabs due to the higher casting speed used. The influence of the modification of the cooling system and of the casting speed on the solidification process was further shown by the difference in pool depth, which was 1.7m deeper with the optimised system than with the conventional cooling pattern (13.7 and 12m, respectively).

In the above analyses, the predicted cross-sectional variation of the secondary dendrite arm spacings all showed the same trend. At the surface, realistic values were obtained (approximately 10μm). Further in from the surface, the spacings increased to a peak-value, followed by a decrease towards the centre of the slab. This decrease is due to the increase in cooling rates, which results from the heat flow characteristics. In Figure 6.14, the values of λ_2 in the 155 mm thick 18/8-slab, which was investigated previously, can be seen. It can be noticed that the arm spacings do not decrease with distance into the slab as predicted by the model. This is due to the formation of an equiaxed structure in the central regions (Figure 6.15). The equiaxed crystals have grown at a slow rate, and have had considerable time to coarsen. The conditions under which equiaxed crystals grow are not well established from the stand-point of heat flow and thus, the modelling of their formation and growth is difficult.

One of the major discrepancies between the general cross-sectional variation of δ-ferrite, which was observed in the commercial samples (c.f. Section 5.3) and the variation predicted by the numerical analysis is in the δ-content in the regions close to the slab-surface. In the experimental measurements, very low ferrite contents were found in these regions, whereas in the numerical analysis, high contents were predicted consistently. The reason for this is not known, but a possible explanation is that in a real situation, less δ-ferrite is present around the solidus temperature than was assumed in the model. This may be due to the high cooling rates prevalent in this region. These cooling rates are significantly higher than those previously studied by, for example, uni-directional solidification. Thus, the use of an initial fraction δ-ferrite of 22% at the solidus temperature (which is taken from uni-directional solidification experiments[14]) independent of position (i.e. cooling rate) may be the source of the discrepancies. It may be, therefore, that the 'start δ-ferrite content' will vary across the section.

In the central regions of the slabs, there was a consistent decrease in the predicted δ-ferrite contents, which is in agreement with the trends observed in the commercial samples. This is despite the fact that there was a discrepancy in measured and predicted dendrite arm spacings in these regions. A possible reason for this is that in the case of the model-predictions, relatively fine spacings were obtained, which provides short diffusion distances in combination with a relatively long time spent between T_S and 900°C. This will allow a considerable amount of transformation to occur. In the case of real slabs, the diffusion distances are long due to the sizes of the equiaxed crystals, but these crystals also spend a considerable time at higher temperatures, especially around the solidus temperature. This compensates for the long diffusion distances and thus, the end-results from the predictions and the measurements are similar as far as the general trend is concerned. Also, in point counting it is possible that inter-dendritic δ-ferrite in the central portions (Figure 5.25(d)) was measured in addition to the skeletal form. This means that in terms of the diffusion-controlled transformation, even less ferrite is present in the centre of the slabs. Furthermore, as can be seen in Figure 6.15, the skeletal structure of the δ-ferrite is replaced by the so-called cell-like morphology towards the centre of the slab (c.f. Section 2.1.4). (N.b. In Figure 6.15(a), the microstructure at the edge of a white band can be seen.) The reason for this breakdown of the skeletal structure is possibly a combination of time of transformation and solute concentration[227]. Although this implies that the morphology assumed in the numerical model is not present in the central regions throughout the transformation, the results from the modelling and the measurements indicate that the system follows the kinetics of a diffusion-controlled process with a skeletal morphology. In addition, it is interesting to note that although the commercial slabs, in which the δ-ferrite was measured, were of different thicknesses and cast in continuous casting machines different from those considered in the model, there are similarities in the trends of the cross-sectional variation of δ-ferrite which compare well with the predictions made for the thicker slabs. This is particularly the case with the 18/8-slab (Figure 5.26) and the results from the conventional cooling system as given by Nozaki et al.[126] (Figure 6.10(c)).

In the numerical diffusion-model adopted, it was assumed that the interface concentrations $C^{\delta\gamma}$ and $C^{\gamma\delta}$ are constant throughout the transformation. In the real situation, this might not be the case and it is possible to include a variation of these concentrations in the analysis adopted. However, such a procedure would lead to a significant increase in the complexity of the model and this was considered to be beyond the scope of the present work. Also, if the interface concentrations vary during the transformation, the extent of the variation and the actual values of these variations are unknown.

The predictions made from the different continuous casting machines and casting conditions indicate that it is very important to obtain reliable heat transfer data if any alterations in the casting practice are to be assessed with reasonable accuracy. Having obtained these data, the above-presented model can prove to be a useful tool in terms of the understanding of thermal and structural behaviour during continuous casting. For example, if in the case of a stainless steel grade, the characteristics of σ-phase formation are known, the results from the model can be used to assess the position and the extent of the σ-formation, since, as mentioned in Section 2.1.4, δ-ferrite can transform to the brittle σ-phase on cooling.

CHAPTER 7

Conclusions and Suggestions for Further Work

7.1 Conclusions.

In the present analysis, ripple formation on stainless steels showed a similar dependence on casting parameters as that reported in the literature for other alloys. From the experimental observations, the following conclusions can be drawn.

(i) In fully ferritic, austenitic with primary precipitation of δ-ferrite and fully austenitic stainless steels, the severity of ripple formation is reduced with increasing mould roughness.

(ii) An increase in casting speed decreases the depth and decreases the spacing of the ripples.

(iii) The severity of rippling decreases when the superheat is increased.

(iv) When going from fully ferritic grades through the ferritic/austenitic to the fully austenitic stainless steels with high Cr and Ni contents, the severity of rippling increases due to an increase in the physical strength of the solidifying shell.

(v) Casting in a highly conductive atmosphere (He) results in more severe rippling than in the case of an atmosphere with low thermal conductivity (vacuum), which verifies that the main mechanism for ripple formation is heat transfer controlled. In order to achieve a more complete understanding of solidification in the meniscus region during casting, a 2-dimensional, non-steady state heat transfer model with a complete treatment of the curved boundary has to be employed. From the results of such an analysis, the following conclusions can be drawn.

(vi) Good agreement exists between predicted and experimental results on the influence of different gas atmospheres on the incidence of surface rippling.

(vii) The results from the effect of superheat are in good agreement with experimental observations (c.f. (iii) above).

(viii) The healing time in continuous casting has a stronger influence on meniscus solidification than the mould/metal heat transfer coefficient.

(ix) The thermal conductivity of casting flux has a significant influence on solidification in the meniscus region.

(x) The film thickness of the casting flux between the mould and the metal is an important parameter in terms of meniscus freezing.

(xi) Variation in the film thickness between the strand and mould wall can produce differences in the depths of the oscillation marks.

(xii) The melting rate and sintering characteristics of casting powder have a significant influence on oscillation mark formation (c.f. (x) and (xi) above).

(xiii) The shape of the meniscus influences oscillation mark and ripple formation.

(xiv) The solidification characteristics of an alloy influence the severity of oscillation marks and ripples.

(xv) The formation of ripples and oscillation marks is controlled by 2-dimensional rather than 1-dimensional heat transfer.

From the measurements and numerical analysis of δ-ferrite content across continuously-cast stainless steel slabs, it may be concluded that,

(xvi) the variation of δ-ferrite across continuously-cast slabs is mainly determined by the cooling pattern used in the secondary cooling zone,

(xvii) the δ-ferrite content is determined by a combination of diffusion distances and thermal history,

(xviii) the variation of secondary dendrite arm spacing with distance from the mould wall can be predicted with reasonable accuracy for a columnar zone using numerical heat transfer analysis,

(xix) it is possible that the δ-ferrite content is dependent on cooling rate during unsteady-state growth, and

(xx) it is feasible to use numerical analyses for microstructural predictions in commercial processes.

7.2 Suggestions for Further Work.

From the results and conclusions presented regarding ripple and oscillation mark formation, it can be appreciated that further work is necessary for the determination of the physical properties of alloys at high temperatures. This is necessary in order to assess further the strength of the solid formed in the meniscus region during casting and, in turn, the extent of ripple and oscillation mark formation. Furthermore, there is scope for research to be carried out on casting powders and their influence on the formation of surface depressions.

Also, the effect of oil as a lubricant on the formation of oscillation marks needs to be determined. This can be effectively studied on a laboratory-scale using the same experimental technique as used in the present work by feeding the oil into the mould under controlled conditions during teeming.

In terms of δ-ferrite in austenitic stainless steels, there is a need for information on the $\delta \rightarrow \gamma$ transformation during unsteady-state solidification and cooling. In addition, the concentration gradients on either side of the δ/γ-interface should be determined (using STEM-analysis).

REFERENCES

1. E.C. Bain and W.E. Griffiths, Trans.AIME,75(1927)166
2. P. Schaftmeister and R. Ergang, Arch. Eisenh.,12(1939)459
3. A.J. Bradley and H.J. Goldschmidt, J.I.S.I.,144(1941)273
4. V.G. Rivlin and G.V. Raynor, Int.Met.Rev.,25(1980)21
5. "A Guide to Solidification of Steels",(Jernkontoret, Stockholm)1977:p.81
6. R.H. Kaltenhauser, Met.Eng.Quart.,11(1971)41
7. W. Schmidt and O. Jarleborg, "Ferritic Stainless Steels with 17%Cr", Climax Molybdenum Co Publ.(1979)
8. H. Fredriksson, Scand.J.Met.,5(1976)27
9. E. Scheil, Z. Metallkunde,34(1942)70
10. S. Kato, H. Yoshida and N. Chino, Tetsu-to-Hagane,63(1977)61
11. G. Blanc and R. Tricot, Mem.Sci.Rev.Met.,68(1971)735
12. M.N. Eruslu, Ph.D. Thesis,University of Sheffield,1976
13. O. Hammar and U. Svensson, "Solidification and Casting of Metals", (The Metals Society, London)1979:p.88
14. O.J. Pereira, Ph.D. Thesis,University of Sheffield,1979
15. H. Fredriksson and J. Stjerndahl, Met.Sci.,16(1982)575
16. J.M. McTighe, Ph.D. Thesis,University of Sheffield,1975
17. H. Fredriksson, Met.Trans.,3(1972)2989
18. H. Fredriksson, "Solidification and Casting of Metals", (The Metals Society, London)1979:p.131
19. H. Fredriksson, ibid.,155
20. As 5,p.147
21. F.B. Pickering, "Physical Metallurgy and Design of Steels", (Appl.Sci.Publ.,Barkins)1978:p.201
22. U. Siegel and M. Gunzel, Neue Hutte,18(1973)422

23. U. Siegel and M. Gunzel, ibid.,519

24. Y. Arata, F.Matsuda and S. Katayama, Trans.J.W.R.I.,5(1976)35

25. G.L. Petrov et al., Weld.Prod.,(1967)No2,1

26. S.A. Iodkovskii et al., Russ.Cast.Prod.,(1971)No10,418

27. A.E. Runov, Weld.Prod.,(1971)No6,24

28. A. Astrom, B. Loberg, B. Bengtsson and K.E. Easterling, Met.Sci.,10(1976)225

29. H. Nakamura, Tetsu-to-Hagane,63(1977)872

30. G. Jolley and J.E. Geraghty, "Solidification and Casting of Metals", (The Metals Society, London)1979:p.411

31. K.J. Irvine et al., J.I.S.I.,207(1969)1017

32. F.B. Pickering, "Towards improved Ductility and Toghness", Climax Molybdenum Co. Symp.,9,Kyoto,1972

33. J. Tanabe et al., Japan Steelworks Tech. News,10(1972)1

34. J.H. Decroix, A.M. Neveu and R.J. Castro, "Deformation under Hot Working Conditions",(The Iron and Steel Institute)1968:p.135

35. P.A. Portevin, Rev.Met.,67(1970)761

36. K.A. Bywater and T. Gladman, Met.Tech.,8(1976)358

37. T.F.L. Muller, Ph.D. Thesis,University of Sheffield,1967

38. H.F. Merrick et al., Met.Trans.,4(1973)828

39. M. Hildebrand, Neue Hutte,12(1972)724

40. K. Skuin. et al., Neue Hutte,13(1973)663

41. K. Mayland, R.W. Welburn and A. Nicholson, Met.Tech.,8(1976)350

42. F.B. Pickering, Int.Met.Rev.,21(1976)227

43. M. Hildebrand, "Im Beitrag zum Verhalten des Alpha Ferrits in Austenitisch Cr-Ni Stahlen beim Warmformung", Leipzig,1971

44. M. Zidek, Hutnicke Listy,28(1973)802

45. M.I. Vinograd, Metallurg.,(1957),No.5,303

46. M.R. Nassar, M.Met.Thesis,University of Sheffield,1975

47. B. Leffler and S. Malm, Met.Tech.,9(1977)81

48. H. Carvalhinhos et al., Fundicao,(1975),No87,19

49. S. Mayerhofer and H. Kohl, Berg und Huttenm.,111(1966)443

50. P.N. Bidulya, S.A. Iodkovskii and N.N. Sashchikhin, Russ.Cast.Prod.,6(1961)237

51. T. Tsuk, M. Hubert and C. Messager, Rev.Met.,68(1971)829

52. H. Takeuchi, Y. Ikehara, T. Yanai and S. Matsumura, Trans.I.S.I.J.,18(1978)352

53. R. Radchenko, Stal,(1960),No5,450

54. B. Matuschka, Berg und Huttenm.,103(1958),Mh.103

55. E. Marburg, J.Metals,5(1953)157

56. Y. Kinoshita, S. Tadeda and H. Yoshimura, Tetsu-to-Hagane,65(1979)1176

57. S.A. David, G.M. Goodwin and D.N. Braski, Weld.J.Res.Suppl.,58(1979)330s

58. M.J. Cieslak and W.F. Savage, Weld.J.Res.Suppl.,59(1980)136s

59. J.C. Lippold and W.F. Savage, Weld.J.Res.Suppl.,59(1980)48s

60. N. Suutala, T. Takalo and T. Moisio, Met.Trans.,10A(1979)512

61. N. Suutala, T. Takalo and T. Moisio, ibid.,1183

62. N. Suutala, T. Takalo and T. Moisio, Met.Trans.,11A(1980)717

63. G. Kurdjumov and G. Sachs, Ann.Phys.,64(1930)325

64. J.A. Brooks, "Trends in Welding Research in the US",(American Society of Metals,Metals Park)1982:p.331

65. J.C. Lippold and W.F. Savage, Weld.J.Res.Suppl.,58(1979)330s

66. E.L. Brown, "Technical Reports:Materials studies for Magnetic Fusion Energy Applications at Low Temperatures -IV", (ed. R.P.Reed, N.J.Simon),(US Dept. of Comm.,Nat. Bureau of Standards)1981:p.357

67. J.A. Brooks, J.C. Williams and A.W. Thompson, Met.Trans.,14A(1983)1271

68. L.R. Poole, Met.Prog.,65(1954)108

69. O.H. Henry, M.A, Cordovi and G.J. Fisher, Weld.J.Res.Suppl.,34(1955)75s

70. H. von Kohl, Arch.Eisenh.,40(1969)143

71. J.H. Andrew, J.N Greenwood and G.W. Green, J.I.S.I.,100(1919)231

72. M. Thomas, Circ.d'Inform.Tech.C.D.S.,9(1953)1421

73. B.H.C. Waters, Met.Treat.Drop Forg.,20(1953)79

74. B.H.C. Waters, ibid.,103

75. D.R. Thornton, J.I.S.I.,183(1956)300

76. G.A. Sedach, N.P. Izotov and G.N. Kamychev, Stal in English,(1967)(No.2)124

77. G.A. Panev, A.M. Ofengenden, G.G. Zhitnik, M.L. Plebler and L.I. Krupman, Steel in the USSR,2(1972)16

78. I.I. Chaika, N.G. Belousova, T.M. Kats, M.M. Shanina and V.S. Zhernovski, Steel in the USSR,4(1974)71

79. Yu.G. Volovich, V.I. Zhalybin, K.P. Verbitskii, V.A. Morozov and I.B. Gutovskii, ibid.,206

80. I.G. Saucedo, Ph.D. Thesis,University of Sheffield,1981

81. P. Ackermann W. Heinemann and W. Kurz, Arch.Eisenh.,55(1984)1

82. P. Wray, Met.Trans.,12B(1981)167

83. H. Jacobi, Stahl und Eisen,96(1976)964

84. H. Tomono, W. Kurz and W. Heinemann, Met.Trans.,12B(1981)409

85. H. Tomono, Doctoral Thesis,EPFL,Lausanne,1979

86. R.S. Laki, J. Beech and G.J. Davies,
Proc.Conf."Modelling of Casting and Welding Processes",(Engineering Foundation,New York)1983

87. D.K. Stemple, E.N. Zulueta and M.C. Flemings,
Met.Trans.,13B(1982)503

88. S.N. Singh and K.E. Blazek, J.Metals,26(1974)17

89. A. Grill and J.K. Brimacombe, Ironm.Steelm.,3(1976)76

90. M. Wolf and W. Kurz, Met.Trans.,12B(1981)85

91. T.W. Clyne, A. Garcia, P. Ackermann and W. Kurz, J.Metals,34(1982)34

92. D.J. Hurtuk and A.A. Tzavaras, ibid.,40

93. G. Siebel, D. Altenpohl and M. Cohen, Z.Metallkunde,44(1953)173

94. G. Trapied, J.I.M.,92(1963)305

95. D.L.W. Collins, Metallurgia,76(1967)137

96. V.A. Efimov, Stal,12(1962)927

97. I. Ohnaka et al., J.Jap.Inst.Light Metals,28(1978)26

98. H. Jacobi, Arch.Eisenh.,47(1976)345

99. I.G. Saucedo, J. Beech and G.J. Davies
Proc.6th Vacuum Met.Conf.on Special Melting, (American Vacuum Society,New York)1980:p.23

100. J. Menter, "Continuous Casting of Steel",(The Metals Society-IRSID, London)1977

101. F. Fitzgerald, Proc."4th Int. Iron and Steel Congress, Continuous Casting"(The Metals Society,London)1982

102. I.V. Samarasekera and J.K. Brimacombe, Int.Met.Rev.,23(1978)286

103. I.M.D. Halliday, "Continuous Casting of Steel",(The Iron and Steel Inst., London)1965:p.1

104. J.S. Morton and M.G. Lyne, ibid.,145

105. H. Nemoto, Trans.I.S.I.J.,16(1976)51

106. K.G. Speith and A. Bungeroth, Met.Treat.Drop Forg.,20(1953)197

107. J. Savage and W.H. Pritchard, J.I.S.I.,178(1954)269

108. H.S. Marr, Iron and Steel Intern.,(1978)(4)87

109. A.D. Akimenko and A.A. Skvortsov, Izv.VUZ Cher.Metall.,12(1958)45

110. K. Ushijima, Tetsu-to-Hagane,47(1961)390

111. J.J. Gautier, Y. Morillon and J. Dumont-Fillon,
J.I.S.I.,208(1970)1053

112. P.V. Riboud and M. Larrecq, Steelm.Proc.(ISS-AIME,Detroit)62(1979)78

113. G. Meller, M.Sc.Dissertation,Royal Inst. of Tech.,Stockholm,1978

114. J. Chone', O. Grinder and P. Hasselstrom,
Swedish Inst.Met.Research,IM Report No.1570,1981

115. K. Sorimachi, H. Yamanaka, M.Kuga, H. Shikata and M.Suigusa,
Proc.Conf."Modelling of Casting and Welding
Processes",(Engineering Foundation, New York)1983

116. P.V. Riboud, M. Olette, J. Leclerc and W. Pollak,
Swedish Inst.Met.Research,IM Report No.1491,1980

117. P. Hasselstrom, Swedish Inst.Met.Research,IM Report No.1467,1980

118. C.R. Taylor, Met.Trans.,6B(1975)359

119. N.T. Mills and R.W. Joseph, Ironm.Steelm.,4(1977)181

120. R. Jauch, Stahl und Eisen,98(1978)244

121. J.K. Brimacombe, Can.Met.Quart.,15(1976)163

122. H. Schrewe, Ironm.Steelm.,8(1981)85

123. P. Benoit and P. Pithois, "Continuous Casting of Steel",(The Metals
Society-IRSID,London)1977:p.92

124. A. Etienne, Swedish Inst.Met.Research,IM Report No.1491,1980

125. A. Etienne and P.H. Dauby, Proc."4th Int. Iron and Steel Congress,
Continuous Casting",(The Metals Society,London)1982

126. T. Nozaki, J. Matsuno, K. Murata, H. Ooi and M. Kodama,
Trans.I.S.I.J.,18(1978)330

127. L. Schmidt and A. Josefsson, Scand.J.Met.,3(1974)193

128. W.R. Irving and A. Perkins, Ironm.Steelm.,4(1977)292

129. W. Heinemann, OHP,Iron and Steel Div.AIME,61(1978)335

130. A. Grill, Ironm.Steelm.,6(1979)62

131. J.P. Birat, M. Larrecq, A. Le Bon, M. Jeanneau, M. Poupon and D. Senaneuch, Steelm.Conf.,(ISS-AIME,Toronto)64(1981)53

132. F. Weinberg, Can.Min.Metall.Bulletin,74(1981)96

133. M. Takeda, T. Komano, T. Yanai and T. Hino, Nippon Steel Tech.Rep.No.13,(1979)36

134. J.D. Thomas and A.A. Tzavaras, Proc.Con.Cast.Symp.102 AIME Ann.Meeting, (AIME,Chicago)1973:p.125

135. H. Fredriksson and M.Thegerstrom, Scand.J.Met.,8(1979)232

136. J. Arnoult, A. Kohn and J.P. Plumensi, Rev.Met.,66(1969)585

137. S.K. Morton and F. Weinberg, J.I.S.I.,211(1973)13

138. J.K. Brimacombe and F. Weinberg, ibid.,23

139. J.E. Lait, J.K. Brimacombe and F. Weinberg, Ironm.Steelm.,1(1974)35

140. J.E. Lait, J.K. Brimacombe and F. Weinberg, ibid.,90

141. H. Fujii, T. Ohashi, T. Ono and K. Asano, Nippon Steel Tech.Rep.No.13,(1979)48

142. Mitsubishi Heavy Ind., Japan Patent Publ.No.21092,(1971)

143. J. Savage, J.I.S.I.,200(1962)41

144. A.W.D. Hills, J.I.S.I.,203(1965)18

145. E.A. Mizikar, Trans.Met.Soc.AIME,239(1967)1747

146. H. Jones, J.I.M.,97(1969)38

147. M. Wolf, Doctoral Thesis,EPFL,Lausanne,1978

148. M. Wolf, T.W. Clyne and W Kurz, Arch.Eisenh.,53(1982)91

149. R. Alberny and J.P. Birat, "Continuous Casting of Steel",(The Metals Society-IRSID,London)1977:p.116

150. L. Westin, ibid.,p.158

151. J.P. Birat and J. Chone', Ironm.Steelm.,10(1983)269

152. J. Savage, Met.Treat.Drop Forg.,22(1955)277

153. J. Savage, Iron and Coal Trades Rev.,182(1961)787

154. E.V. Surin, M.Ya. Brovman, Yu.P. Boiko and V.A. Zhukova,
Steel in the USSR,2(1972)533

155. R.E. Aseev, V.N. Zhuckin and V.M. Kondrashin, ibid.,284

156. T. Emi, H. Nakato, Y. Iida, K.Emoto, R. Tachibana, T.Imai and H. Bada,
OHP Iron Steel Div.AIME,61(1978)350

157. M. Wolf and W. Kurz, Met.Trans.,12B(1981)85

158. H. Takeuchi, S. Matsumura, R. Hidaka, Y. Nagano and Y. Suzuki,
Trans.I.S.I.J.,22(1982)B-16

159. H. Takeuchi, S. Matsumura, Y. Ikehara, T. Kosuge and R. Hidaka,
ibid.,B-205

160. J.P. Birat, Rev.Met.-CIT,79(1982)603

161. M. Wolf, Trans.I.S.I.J.,22(1982)B-91

162. T. Kuwano, N. Shigematsu, F. Hoshi and H. Ogiwara,
Ironm.Steelm.,10(1983)75

163. C. Offerman, Scand.J.Met.,10(1981)25

164. N.A. McPherson and R.E. Mercer, Ironm.Steelm.,7(1980)167

165. J.K. Brimacombe and K. Sorimachi, Met.Trans.,8B(1977)489

166. Y. Nakano, Y. Nogushi, F. Hoshi and Y. Muranaka,
"Continuous Casting of Steel",(The Metals
Society-IRSID,London)1977:p.273

167. A.W.D. Hills, Trans.Met.Soc.AIME,245(1969)1471

168. A. Garcia and M. Prates, Met.Trans.,9B(1978)449

169. A. Garcia, T.W. Clyne and M. Prates, Met.Trans.,10B(1979)82

170. T.W. Clyne and A. Garcia, Int.J.Heat Mass Transf.,23(1980)773

171. T.W. Clyne and A. Garcia, "Continuous Casting of Small Cross Sections", (TMS-AIME, Pittsburgh)1980:p.17

172. T.W. Clyne, Met.Sci.,16(1982)441

173. T.W. Clyne, Met.Trans.,13B(1982)471

174. Y.K. Shin, Ph.D. Thesis,University of Sheffield,1981

175. M.J. Stewart and F. Weinberg, J.Crystal Growth,12(1972)217

176. R. Mehrabian, M. Keane and M.C. Flemings, Met.Trans.,1(1970)1209

177. T.S. Piwonka and M.C. Flemings, Trans.Met.Soc.AIME,236(1966)1157

178. T.W. Clyne,"Numerical Methods in Thermal Problems",vol.II, (Swansea)1981:p.240

179. N. El-Mahallawy, Giessereiforschung,33(1981)139

180. W.C. Erickson, AFS Int.Cast Metals J.,5(1980)30

181. R.J. Sarjant and M.R. Slack, J.I.S.I.,177(1954)428

182. A. Lazaradis, Int.J.Heat Mass Transf.,13(1970)1459

183. N. Shamsundar and E.M. Sparrow, Trans.ASME(c), J.Heat Transf.,97(1975)333

184. L. Saroff, Proc.Cont.Cast.Symp.,102 AIME Ann.Meeting,(AIME, Chicago)1973:p.323

185. I.G. Saucedo, J. Beech and G.J. Davies, Met.Tech.,9(1982)282

186. D.C. Weckmann, R.J. Pick and P. Niessen, Z.Metallkunde,70(1979)750

187. M. Zorzi and P. Mazzantini, "Numerical Methods in Industrial Forming Processes", (Pineridge Press,Swansea,UK)1982:p.401

188. R.G. Blossey, Proc.Cont.Cast.Symp.,102 AIME Ann.Meeting,(AIME, Chicago)1973:p.141

189. A. Grill, J.K. Brimacombe and F. Weinberg, Ironm.Steelm.,3(1976)38

190. K. Sorimachi and J.K. Brimacombe, Ironm.Steelm.,4(1977)240

191. A. Grill and K. Schwerdtfeger, Ironm.Steelm.,6(1979)131

192. K. Miyazawa and K. Schwerdtfeger, Ironm.Steelm.,6(1979)68

193. S. Kojima, T. Matsukawa and M. Kodama, 3rd Process Techn.Conf., vol.3,(ISS-AIME, Pittsburgh)1982:p.255

194. S.S. Daniel, Ironm.Steelm.,9(1982)16

195. A. Grill, K. Sorimachi and J.K. Brimacombe, Met.Trans.,7B(1976)177

196. J.O. Kristiansson and E.H. Zetterlund, "Numerical Methods in Industrial Forming Processes",(Pineridge Press,Swansea,UK)1982:p.413

197. I.V. Samarasekera and J.K. Brimacombe, 3rd Process Techn.Conf.,vol.3, (ISS-AIME,Pittsburgh)1982:p.283

198. I.V. Samarasekera and J.K. Brimacombe, Ironm.Steelm.,9(1982)1

199. M. Larrecq, J.P. Birat, C. Saguez and J. Henry, 3rd Process Techn.Conf., vol.3,(ISS-AIME,Pittsburgh)1982:p.273

200. D.W. Peaceman and H.H. Rachford, J.Soc.Indust.Appl.Math.,3(1955)28

201. J. Crank and P. Nicholson, Proc.Camb.Phil.Soc.,43(1947)50

202. G.D. Smith, "Numerical Solution of Partial Differential Equations", (Oxford Univ.Press,London)1969:p.8

203. V.I. Lebedev and D.P. Evteev, Steel USSR,3(1973)(4)M21763

204. J.J. Valencia and J. Beech, "Solidification Technology in the Foundry and Casthouse",(The Metals Society,London)1983:p.359

205. A.J.W. Ogilvy, Ph.D. Thesis,University of Sheffield,1983

206. T.W. Clyne and W. Kurz, Met.Trans.,12A(1981)965

207. J.P. Holman, "Heat Transfer",(McGraw-Hill Kogakusha,Tokyo)1981:p.137

208. M.C. Flemings, R.G. Riek and K.P. Young, Mat.Sci.Eng.,25(1976)103

209. M.C. Flemings, "Solidification Processing",(McGraw-Hill,New York) 1974:p.256

210. S.A. Metz and M.C. Flemings, Trans.AFS,78(1970)453

211. S.N. Singh and M.C. Flemings, Trans.TMS-AIME,245(1969)1803

212. R.A. Tanzilli and R.W. Heckel, Trans.TMS-AIME,242(1968)2313

213. R.A. Tanzilli and R.W. Heckel, Trans.TMS-AIME,245(1969)1363

214. D. Murray and F. Landis, Trans.ASME Ser.D,81(1959)106

215. As ref.207,p.8

216. F. Al-Jouni, Ph.D. Thesis,University of Sheffield,1983

217. A. Gittins, J.R. Everett and W.J. McG. Tegart, Met.Tech.,9(1977)377

218. A. Vogel, R.D. Doherty and B. Cantor, "Solidification and Casting of Metals",(The Metals Society, London) 1979:p.518

219. G. Lesoult, P. Neu and J.P. Birat, Conf."Progress in Modelling of Solidification Processes",(The Metals Society, London)1983

220. As 207,p.287

221. S. Ohmiya, K-H Tacke and K. Schwerdtfeger, Ironm.Steelm.10(1983)24

222. K.C. Mills, R.F. Brooks and A. Olusanya, Int.Symp."The Physical Chemistry of Iron and Steel Making",CIM,Met.Soc. of CIM, Toronto,1982:p.III-45

223. M.D. Lanyi and C.J. Rosa, Ironm.Steelm.9(1982)25

224. As 207,p.170

225. P. Hasselstrom, Swedish Inst.Met.Research,IM Report No.1468,1981

226. K.C. Mills and P. Grieveson, to be published,"Centenary Conference", Dept. of Metallurgy,University of Sheffield,July 1984

227. I.M. Estrada, Ph.D. Thesis (in preparation), University of Sheffield,1984

228. F.B. Hildebrand, "Finite-Difference Equations and Simulations", (Prentice-Hall,Englewood Cliffs,NJ)1968:p.266

229. R.V. Viswanathan, Math.Tables,Washington,11(1957)67

230. A.S. Ballantyne and A. Mitchell, Ironm.Steelm.,4(1977)222

231. L.F. Carvajal and G.E. Geiger, Met.Trans.,2(1971)2087

232. M.R. Bridge and G.D. Rogers, Proc.Conf."Modelling of Casting and Welding Processes",(Engineering Foundation,New York)1983

233. E. Beraha and B. Shpigler, "Color Metallography", (ASM, Metals Park) 1977:p.32

234. C.J. Smithells, "Metals Reference Book", vol.3, (4th edition) (Butterworths, London) 1967:p.696

235. Y.S. Touloukian and E.H. Buyco, "Thermophysical properties of matter", vol.4, (IFI/Plenum, New York) 1971:p.678

236. Y.S. Touloukian, R.W. Powell, C.Y. Ho and P.G. Klemens, "Thermophysical properties of matter", vol.1, (IFI/Plenum, New York) 1971:p.1174

237. "Handbook of Chemistry and Physics", (ed. R.C. Weast and M.J. Astle), (62nd. edition), (CRC Press, Boca Raton, USA) 1982:p.F-56

LIST OF SYMBOLS

a,b	relative distances between boundary intersection points and node next to the curved boundary
A,B	constants in the expression for temperature dependent thermal conductivity
C_p	specific heat, kJ $kg^{-1}K^{-1}$
C	composition, at.%
f_s	fraction solid
h	Newtonian heat transfer coefficient, kW $m^{-2}K^{-1}$
h_{con}	convective heat transfer coefficient, kW $m^{-2}K^{-1}$
H	enthalpy, kJ kg^{-1}
H_f	enthalpy of pure solvent, kJ kg^{-1}
H_L	enthalpy at T_L, kJ kg^{-1}
H_S	enthalpy at T_S, kJ kg^{-1}
K	thermal conductivity, W $m^{-1}K^{-1}$
k_f	thermal conductivity of casting flux/powder, W $m^{-1}K^{-1}$
k	partition coefficient
l	thickness of layer of liquid flux, m
L_f	latent heat of fusion, kJ kg^{-1}
P	constant determining shape of meniscus
q	heat flux, kW m^{-2}
q_{r+c}	heat flux by radiation and convection through metal/atmosphere or metal/metal cover interface, kW m^{-2}
q_x	heat flux through mould/metal interface, kW m^{-2}
q_X,q_Y	components of heat flux through liquid slag/melt interface, kW m^{-2}

r	radius, m
Δr	radial increment (VAR), m
t	time, s
Δt	time increment, s
t_h	healing time, s
T	temperature, K
T_A	ambient temperature, K
T_f	melting temperature of pure solvent, K
T_L	liquidus temperature, K
T_M	mould temperature, K
T_P	pouring temperature, K
T_{sx}	temperature of flux at mould wall, K
T_{sy}	temperature at sintered flux/liquid flux interface, K
T_S	solidus temperature, K
ΔT	superheat, K
T_w	temperature at 'fictitious' node, K
U	meniscus height, m
x,y,z	coordinates of physical system, m
Δx	grid size, m
X	distance from mould wall to intersection, m
Y	distance from sintered flux/liquid flux interface to boundary intersection, m
Z	constant determining shape of meniscus
Δz	vertical increment (VAR), m
α	angle between normal to boundary and x-axis, rad
ϵ	emissivity
ξ	radius of δ-ferrite, m
ρ	density, kg m^{-3}

σ	Stefan-Boltzmann constant, (5.669×10^{-11} kW $m^{-2}K^{-4}$)
λ_2	secondary dendrite arm spacing, m

Subscripts

1,2	identifying values of parameters at intersections 1 and 2 on curved boundary
m,n,i	location of field element

Superscripts

t	previous value of parameter
t+1	present value of parameter

A P P E N D I C E S

APPENDIX I

Derivation of Finite-Difference Equations for Nodes related to the Curved Boundary and the Mould-Metal Interface.

The complete derivations of the finite-difference equations for a type 2 intersection are given here, together with the equations for the other three types of intersection. Also, the equation for the nodes at the mould-metal interface is derived.

The general equation for non-steady-state heat transfer in two dimensions, expressed here in terms of enthalpy, contains both first- and second-order partial differentials when allowance is made for a temperature-dependent thermal conductivity in the form $K_{m,n} = A + BT_{m,n}$:

$$\rho\frac{\partial H}{\partial t} = K_{m,n}\left[\frac{\partial^2 T}{\partial x^2} + \frac{\partial^2 T}{\partial y^2}\right] + B_{m,n}\left[\left(\frac{\partial T}{\partial x}\right)^2 + \left(\frac{\partial T}{\partial y}\right)^2\right] \qquad \text{...(I.1)}$$

Thus, finite-difference equations of the first and second order are required for the nodes in the system, in order to solve the non-steady-state heat-transfer completely.

Curved Boundary

For a type 2 intersection, the parameters q, α, T_1 and a are defined (Figure AI.1) as the heat flux across the curved boundary, the angle between the normal to the curve and the horisontal x-axis, the temperature at intersection 1 on the boundary, and the relative distance between the node (m,n) and the intersection, respectively.

(i) Node next to boundary, (m,n)

In the x-direction, Taylor expansions of the temperatures at the fictitious node on the boundary and at (m+1,n) in terms of (m,n), after eliminating the first- and second-order differentials, respectively, give,

$$\frac{\partial^2 T_{m,n}}{\partial x^2} = \frac{2}{\Delta x^2}\left[\frac{T_1 + aT_{m+1,n} - (a+1)T_{m,n}}{a(a+1)}\right] \qquad \text{...(I.2)}$$

$$\frac{\partial T_{m,n}}{\partial x} = \frac{1}{\Delta x}\left[\frac{(1-a^2)T_{m,n} + a^2 T_{m+1,n} - T_1}{a(a+1)}\right] \qquad \text{...(I.3)}$$

In the y-direction, the standard (central) finite-difference expressions are applicable, assuming a square grid, and give,

$$\frac{\partial^2 T_{m,n}}{\partial y^2} = \frac{1}{\Delta x^2}(T_{m,n+1} + T_{m,n-1} - 2T_{m,n}) \qquad \text{...(I.4)}$$

$$\frac{\partial T_{m,n}}{\partial y} = \frac{1}{2\Delta x}(T_{m,n+1} - T_{m,n-1}) \qquad \text{...(I.5)}$$

Substituting equations (I.2)-(I.5) into equation (I.1) gives,

$$H_{m,n}^{t+1} = H_{m,n}^{t} + \frac{\Delta t}{\rho}\left[\frac{K_{m,n}}{\Delta x^2}\left[2\left[\frac{T_1 + aT_{m+1,n} - (a+1)T_{m,n}}{a(a+1)}\right] + T_{m,n+1} + T_{m,n-1} - 2T_{m,n}\right] + \frac{B_{m,n}}{\Delta x^2}\left[\left[\frac{(1-a^2)T_{m,n} + a^2T_{m+1,n} - T_1}{a(a+1)}\right]^2 + \left[\frac{T_{m,n+1} - T_{m,n-1}}{2}\right]^2\right]\right] \qquad \ldots(I.6)$$

(ii) 'Fictitious' node on boundary.

In the x-direction, a Taylor expansion of the first-order differential of the temperature at (m,n) in terms of the fictitious node gives,

$$\frac{\partial^2 T_1}{\partial x^2} = \frac{1}{a\Delta x}\left[\frac{\partial T_{m,n}}{\partial x} - \frac{\partial T_1}{\partial x}\right] \qquad \ldots(I.7)$$

The heat flux across the boundary is given by the Fourier equation, considering the direction of the temperature gradient,

$$q_x = q\cos\alpha = K_1\frac{\partial T_1}{\partial x} \qquad \ldots(I.8)$$

$$q_y = q\sin\alpha = -K_1\frac{\partial T_1}{\partial y} \qquad \ldots(I.9)$$

Substituting equations (I.3) and (I.8) into equation (I.7) yields,

$$\frac{\partial^2 T_1}{\partial x^2} = \frac{1}{a\Delta x^2}\left[\frac{(1 - a^2)T_{m,n} + a^2 T_{m+1,n} - T_1}{a(a + 1)} - \frac{\Delta x q \cos\alpha}{K_1}\right] \qquad \ldots(I.10)$$

When obtaining the second-order differential in the y-direction, a cross-derivative will appear in the finite-difference equations. This can be determined either by involving more nodes in the calculations, which increases the complexity of the resulting equations, or by adopting an alternative treatment of the curved-boundary problem[228,229]. However, in the present analysis the second-order differential is determined by projecting the surface node onto the orthogonal grid used, thus eliminating cross-derivatives. This procedure is based on the assumption that the second-order terms show little variation and remain comparatively small during the computations. The consistency of the results obtained demonstrates the validity of this assumption. Thus, an expansion of the first-order differential of (m,n-1) in terms of the fictitious node gives the second-order differential in the y-direction as,

$$\frac{\partial^2 T_1}{\partial y^2} = \frac{1}{(a^2 + 1)^{1/2}\Delta x}\left[\frac{\partial T_1}{\partial y} - \frac{\partial T_{m,n-1}}{\partial y}\right] \qquad \ldots(I.11)$$

Now,

$$\frac{\partial T_{m,n-1}}{\partial y} = \frac{\partial T_{m,n}}{\partial y} - \Delta x \frac{\partial^2 T_{m,n}}{\partial y^2} \qquad \text{...(I.12)}$$

which, together with equations (I.4), (I.5) and (I.9) gives,

$$\frac{\partial^2 T_1}{\partial y^2} = \frac{1}{(a^2 + 1)^{1/2} \Delta x^2} \left[\frac{T_{m,n+1} + 3T_{m,n-1} - 4T_{m,n}}{2} - \frac{\Delta xq \sin\alpha}{K_1} \right] \qquad \text{...(I.13)}$$

Thus, the governing equation for heat transfer at the fictitious node becomes,

$$H_1^{t+1} = H_1^t + \frac{\Delta t}{\rho} \left[\frac{K_1}{\Delta x^2} \left[\frac{1}{a} \left[\frac{(1 - a^2)T_{m,n} + a^2 T_{m+1,n} - T_1}{a(a + 1)} - \frac{\Delta xq \cos\alpha}{K_1} \right] \right. \right.$$

$$\left. \left. + \frac{1}{(a^2 + 1)^{1/2}} \left[\frac{T_{m,n+1} + 3T_{m,n-1} - 4T_{m,n}}{2} - \frac{\Delta xq \sin\alpha}{K_1} \right] \right] + B_1 \left[\frac{q}{K_1} \right]^2 \right] \qquad \text{(I.14)}$$

Using the same approach as above, the governing equations for heat transfer at the other types of intersection can also be derived. For type 1 intersections (Figure AI.2),

$$H_{m,n}^{t+1} = H_{m,n}^t + \frac{\Delta t}{\rho} \left[\frac{2K_{m,n}}{\Delta x^2} \left[\frac{T_2 + bT_{m,n-1} - (b + 1)T_{m,n}}{b(b + 1)} \right. \right.$$

$$\left. + \frac{T_1 + aT_{m+1,n} - (a + 1)T_{m,n}}{a(a + 1)} \right]$$

$$+\frac{B_{m,n}}{\Delta x^2}\left[\left[\frac{(1-a^2)T_{m,n}+a^2T_{m+1,n}-T_1}{a(a+1)}\right]^2\right.$$

$$\left.+\left[\frac{T_2-b^2T_{m,n-1}-(1-b^2)T_{m,n}}{b(b+1)}\right]^2\right]\qquad\text{...(I.15)}$$

$$H_1^{t+1}=H_1^t+\frac{\Delta t}{\rho}\left[\frac{K_1}{\Delta x^2}\left[\frac{1}{a}\left[\frac{(1-a^2)T_{m,n}+a^2T_{m+1,n}-T_1}{a(a+1)}-\frac{\Delta x q_1\ \cos\alpha_1}{K_1}\right]\right.\right.$$

$$+\frac{1}{(a^2+1)^{1/2}}\left[\frac{b(2+b)T_{m,n-1}-(b+1)^2T_{m,n}+T_2}{b(b+1)}\right.$$

$$\left.\left.\left.-\frac{\Delta x q_1\ \sin\alpha_1}{K_1}\right]\right]+B_1\left[\frac{q_1}{K_1}\right]^2\right]\qquad\text{...(I.16)}$$

$$H_2^{t+1}=H_2^t+\frac{\Delta t}{\rho}\left[\frac{K_2}{\Delta x^2}\left[\frac{1}{b}\left[\frac{(1-b^2)T_{m,n}+b^2T_{m,n-1}-T_2}{b(b+1)}-\frac{\Delta x q_2\ \sin\alpha_2}{K_2}\right]\right.\right.$$

$$+\frac{1}{(b^2+1)^{1/2}}\left[\frac{a(2+a)T_{m+1,n}-(a+1)^2T_{m,n}+T_1}{a(a+1)}\right.$$

$$- \frac{\Delta x q_2 \cos\alpha_2}{K_2}\Bigg]\Bigg] + B_2\left[\frac{q_2}{K_2}\right]^2\Bigg] \qquad \text{...(I.17)}$$

For type 3 intersections (Figure AI.3),

$$H_{m,n}^{t+1} = H_{m,n}^{t} + \frac{\Delta t}{\rho}\left[\frac{K_{m,n}}{\Delta x^2}\left[2\left[\frac{T_2 + bT_{m,n-1} - (b+1)T_{m,n}}{b(b+1)}\right]\right.\right.$$

$$\left. + T_{m+1,n} + T_{m-1,n} - 2T_{m,n}\right] + \frac{B_{m,n}}{\Delta x^2}\left[\left[\frac{T_{m+1,n} - T_{m-1,n}}{2}\right]^2\right.$$

$$\left.\left. + \left[\frac{T_2 - b^2T_{m,n-1} - (1-b^2)T_{m,n}}{b(b+1)}\right]^2\right]\right] \qquad \text{...(I.18)}$$

$$H_2^{t+1} = H_2^{t} + \frac{\Delta t}{\rho}\left[\frac{K_2}{\Delta x^2}\left[\frac{1}{b}\left[\frac{(1-b^2)T_{m,n} + b^2T_{m,n-1} - T_2}{b(b+1)} - \frac{\Delta x q \sin\alpha}{K_2}\right]\right.\right.$$

$$\left.\left. + \frac{1}{(b^2+1)^{1/2}}\left[\frac{T_{m-1,n} + 3T_{m+1,n} - 4T_{m,n}}{2} - \frac{\Delta x q \cos\alpha}{K_2}\right]\right] + B_2\left[\frac{q}{K_2}\right]^2\right] \qquad \text{(I.19)}$$

For type 4 intersections (Figure AI.4),

$$H_{m,n}^{t+1} = H_{m,n}^{t} + \frac{\Delta t}{\rho}\left[\frac{2K_{m,n}}{\Delta x^2}\left[T_{m+1,n} + T_{m,n-1} - 2T_{m,n} - \frac{\Delta x q}{K_{m,n}}(\cos\alpha + \sin\alpha)\right] + B_{m,n}\left[\frac{q}{K_{m,n}}\right]^2\right] \qquad \ldots(I.20)$$

Mould-Metal Interface

At this interface, the heat flux q is given by,

$$q_x = K_{m,n}\frac{\partial T_{m,n}}{\partial x} \qquad \ldots(I.21)$$

The finite-difference approximation for the first-order derivative in the x-direction is,

$$\frac{\partial T_{m,n}}{\partial x} = \frac{1}{2\Delta x}(T_{m+1,n} - T_{m-1,n}) \qquad \ldots(I.22)$$

Now, substituting equation (I.22) into (I.21) gives,

$$q_x = K_{m,n}\left[\frac{T_{m+1,n} - T_{m-1,n}}{2\Delta x}\right] \qquad \ldots(I.23)$$

Using equation (I.23), the term $T_{m-1,n}$ in equation (3.3) can be substituted, giving,

$$H_{m,n}^{t+1} = H_{m,n}^{t} + \frac{\Delta t}{\rho}\left[\frac{K_{m,n}}{\Delta x^2}\left[T_{m,n+1} + T_{m,n-1} - 2T_{m,n} + 2\left[T_{m+1,n} - \frac{\Delta x q_x}{K_{m,n}} - T_{m,n}\right]\right]\right]$$

$$+ \frac{B_{m,n}}{\Delta x^2}\left[\left[\frac{T_{m,n+1} - T_{m,n-1}}{2}\right]^2 + \left[\frac{q_x}{K_{m,n}}\right]^2\right] \quad \ldots(\mathrm{I}.24)$$

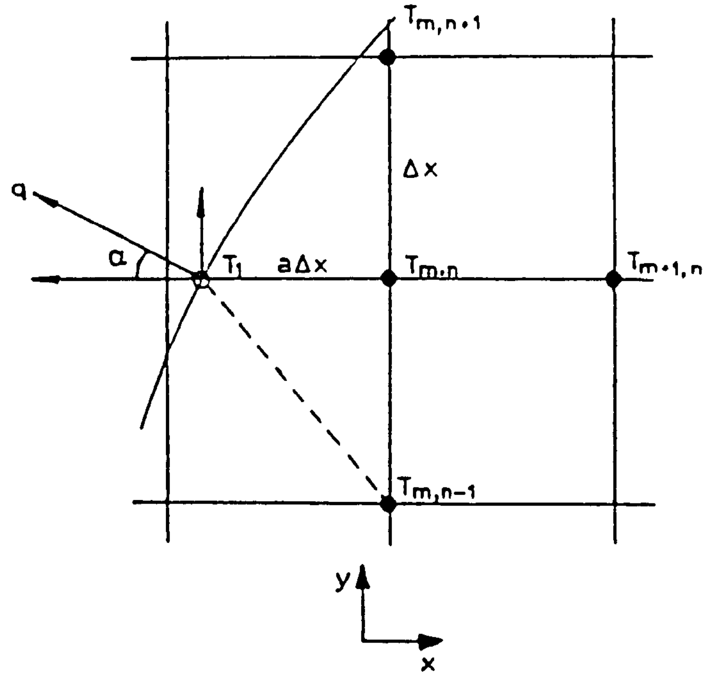

Figure AI.1 Schematic representation of a type 2 intersection.

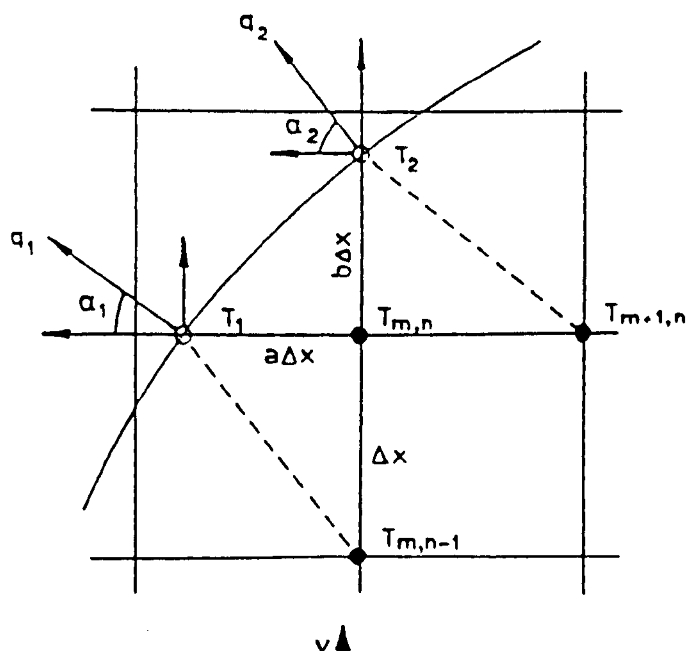

Figure AI.2 Schematic representation of a type 1 intersection.

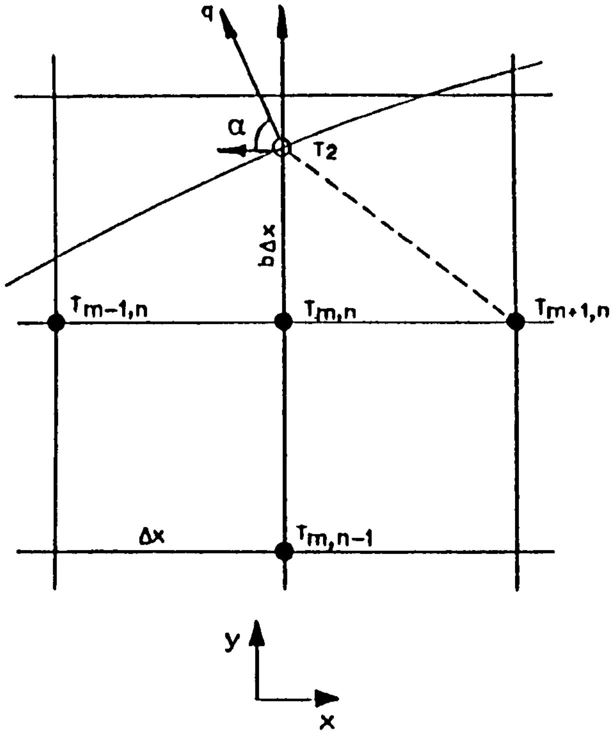

Figure AI.3 Schematic representation of a type 3 intersection.

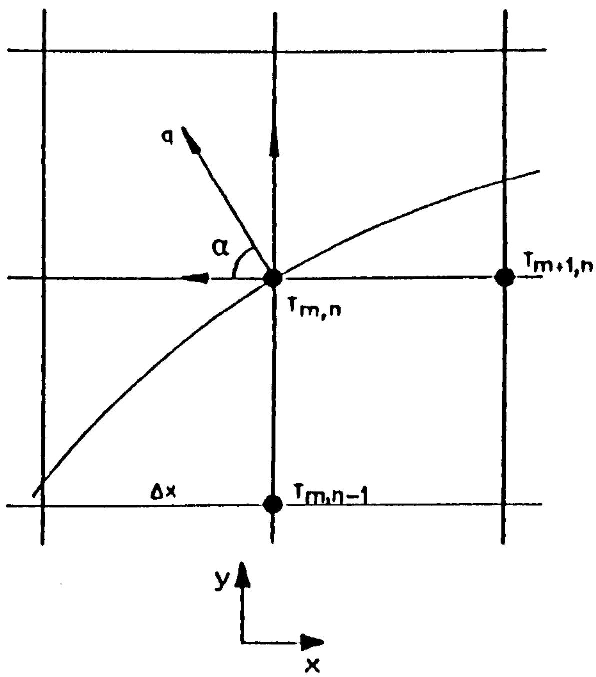

Figure AI.4 Schematic representation of a type 4 intersection.

APPENDIX II

A Heat Transfer Model for the VAR-Process

II:1 Introduction

In the following a heat transfer model for the VAR-process is presented. The aim was to describe the solidification processes occurring during vacuum-arc remelting (VAR) in order to achieve a better understanding for the influence of different parameters such as thermophysical properties, melt rate and solidification characteristics. This is intended to make it feasible to optimise the melting sequence, e.g. melt rate, for the most cost effective route and to produce a high integrity product.

In the literature, several models of varying complexity have been described, the most useful of these being that of Ballantyne et al.[230] However, one of the major assumptions made in this was that of a temperature-independent thermal conductivity. This assumption allows the adoption of the so-called Peaceman-Rachford alternating direction method[200] for the numerical solutions. The advantage of this method is that the solutions are stable for any time-increment. Since, in VAR, the temperature difference between the top and the bottom of the ingot is significant, the validity of the above-mentioned assumption is questionable. Thus, the present model was developed using fully explicit finite-difference analysis. The model was set up so that the melt rate was determined by the total casting time together with the final height of the ingot, i.e. a linear melt rate was assumed. A cylindrical geometry was used and, taking symmetry into account, half the ingot was considered. In addition, the possibility of making two step-wise reductions in the melt rate during the process was provided for.

II:2 Governing Equations and Analytic Formulations

One of the major difficulties in the numerical analysis of solidification processes is the treatment of the latent heat of fusion. In the present analysis this was dealt with by making use of an enthalpy field rather than a temperature field. Considering cylindrical coordinates and a temperature dependent thermal conductivity ($K = A + BT$, where A and B are constants), the governing equation to be solved numerically is,

$$\rho\frac{\partial H}{\partial t} = K\left[\frac{\partial T}{r\partial r} + \frac{\partial^2 T}{\partial r^2} + \frac{\partial^2 T}{\partial z^2}\right] + B\left[\left[\frac{\partial T}{\partial r}\right]^2 + \left[\frac{\partial T}{\partial z}\right]^2\right] \qquad \text{...(II.1)}$$

where ρ is the density, H the enthalpy, t the time, r the radius, z the axial direction and T the temperature.

Applying explicit finite-difference analysis, equation (II.1) becomes,

$$H^{t+1}_{m,n} = H^{t}_{m,n} + \frac{\Delta t}{\rho}\left[K\left[\frac{1}{r_m 2\Delta r}(T_{m+1,n} - T_{m-1,n}) + \frac{1}{\Delta r^2}(T_{m+1,n} - 2T_{m,n} + T_{m-1,n}) + \frac{1}{\Delta z^2}(T_{m,n+1} - 2T_{m,n} + T_{m,n-1})\right.\right]$$

$$+ B\left[\left[\frac{1}{2\Delta r}(T_{m+1,n} - T_{m-1,n})\right]^2 + \left[\frac{1}{2\Delta z}(T_{m,n+1} - T_{m,n-1})\right]^2\right] \quad \ldots(II.2)$$

The boundary conditions used were,

(i) at the centre line, $\frac{\partial T}{\partial r} = 0$, $t \geq 0$, $r = 0$;

(ii) at the bottom of the ingot, $\frac{\partial T}{\partial z} = h_b(T_{m,n} - T_{mould})$, $t \geq 0$, $z = 0$ where h_b is the interface heat transfer coefficient;

(iii) at the vertical mould/metal interface, adopting a time dependent heat transfer coefficient,

$$\frac{\partial T}{\partial r} = h_n(t)(T_{m,n} - T_{mould}),\ t \geq 0,\ r = R$$

where $h_n(t) = h_\infty + (h_{max} - h_\infty)e^{-kt}$ after[232] ; and

(iv) at the top of the ingot a "slice" of metal of uniform temperature is added according to the grid size and the melt rate used. This "slice" is then in essence isolated until the subsequent "slice" is added, i.e. heat is only allowed to be conducted down into the ingot. The temperature of this incoming liquid is determined by the superheat.

The initial condition used required that a part of the ingot was already present at the bottom of the mould before the start of the calculations (the height of this being, for example, equal to the radius of the ingot). This condition needs to be adopted because the events taking place in the system during the initial transient are not known. Thus, the calculations begin with this part of the ingot liquid and at a uniform temperature given by the superheat. The initial calculations continue until a time has elapsed which is equal to the time it takes to produce an ingot of that size with the given melt rate. This determines the starting enthalpy field when the first "slice" of liquid is added. In the analysis, non-equilibrium solidification behaviour according to the Scheil equation[9] (complete mixing in the liquid) was assumed. Thus, a treatment of the solidification process as presented in Section 3.1.6 was used.

The values used for c_p, L_f, T_L and k, together with other parameters are given in Table 6.2. In Table II.1 the heat transfer data used are given. A print-out of the computer program written for the analysis is given in Appendix II-1.

II:3 Conditions Modelled

In the study of the influence of different parameters on the pool profiles, an ingot 250mm in diameter and 1675mm high was considered. This geometry, together with a total casting time of 10 hours was taken to be representative of commercial conditions. The effects of parameters such as the thermal conductivity of the liquid (i.e. the ratio K_L/K_S) (Figures AII.1 and AII.2), the superheat of the incoming liquid (Figures AII.1 and AII.3) and the interface heat transfer coefficient (Figures AII.4 and AII.5) were studied.

The magnitude of the ratio K_L/K_s can be used as a measure of the extent of turbulent mixing in the liquid. In the continuous casting of steels, this ratio has been found to be approximately 7. This is a consequence of the agitation produced by the stream of liquid being teemed into the mould. In VAR the ratio can be expected to be smaller since the casting rate is very low in comparison with continuous casting. The superheat used must be interpreted as an input temperature which, during the time between two subsequent "slice" additions, produces a realistic average superheat of the incoming liquid droplets during the casting. The partition coefficient determines the position of the iso-f_s curves in the region where solid and liquid co-exist and thus, has little influence on the position of the isotherm for $T_{m,n} = T_L$. This means that when adopting the previously-mentioned criterion of defining the solidus temperature as the position where $f_s = 0.95$, the partition coefficient describes the extent of the mushy zone. When this is known, an assessment of the possibility of the formation of defects such as freckles can be carried out. However, in order to do so, it is essential that the correct value of the partition coefficient is known together with the solidification sequence in terms of the formation of, for example, eutectic structures.

II:4 Results and Discussion

In the following, the results from the model, using an austenitic stainless steel as a modelling material, are presented and discussed.

A possible way of obtaining experimental results from the VAR-process is to adopt intermittent electro-magnetic stirring during a trial cast. The stirring has the effect of breaking down the solidification structure, which can be observed by longitudinal sectioning of the ingot and metallographic investigation. Based on findings reported in the literature[232], it can be assumed that the profiles outlined in a trial casting by intermittent stirring represent the position of the liquidus. This is because there is only a limited degree of penetration of the liquid metal into the mushy zone during stirring and thus, if remelting is negligible, the delineation defined by the stirring indicates positions close to the liquidus. The two main parameters determining this position are the ratio of the thermal conductivities in the liquid and the solid and the superheat of the incoming liquid. It was found that an increase in the ratio K_L/K_S resulted in a decrease in the pool depth, whereas an increase of the superheat had the opposite effect. From the above it can also be concluded that the ratio K_L/K_S has no effect on the position of the isotherm describing the solidus temperature.

Reasonable pool depths were predicted by adopting a value of the ratio K_L/K_S of between 2 and 3 and a superheat of each slice of 300-400°C, i.e. a pool depth towards the end of the casting of 250mm at the centre. (N.b. that this is the <u>starting</u> superheat at the time a new slice is added. The superheat relaxes to much lower values before the next slice is added.)

Having a combination of K_L/K_S and the superheat, which gives the correct pool depth at the centre of the ingot, an identical shape of the pool profiles as compared with those in an experimental ingot can be obtained by adjusting the heat transfer coefficient at the mould wall (Figures AII.4 and AII.5). When this has been achieved, a more extensive study of the effects of the different process and material parameters can be undertaken.

II:5 Summary

A model for the VAR-process has been developed, utilising a fully explicit finite-difference analysis. The model differs from other models in that it considers a temperature dependent thermal conductivity and non-equilibrium solidification according to the Scheil equation. A time dependent heat transfer coefficient at the mould wall was adopted, allowing for both variable contact between the mould and the metal and air-gap formation. It has been shown that an increase of the thermal conductivity in the liquid reduces the liquid metal pool depth. Reasonable pool depths were predicted when the ratio between the thermal conductivity in the liquid and the solid was between 2 and 3, together with a superheat of 300-400^{o}C.

Table II.1

Heat Transfer Data used in the Analysis

$$h_n(t) = 0.092 + (0.3 - 0.092)e^{-0.004667t} \quad (kWm^{-2o}C^{-1})$$ (Refs.83 and 231)

$$h_b = 0.3 \quad (kWm^{-2o}C^{-1})$$

APPENDIX.II-1

```
      LIBRARY(SUBGROUPGHOS)
      LIBRARY(SUBGROUPGHOS)
      PROGRAM(VARSS)
       INPUT 1=CRO
      OUTPUT 2=LPO
      TRACE 0
      END
C
C+++++++  MAIN PART OF THE PROGRAM  ++++++++++++++++++++++++
C
C
      NOLIST
      BLOCK DATA
      COMMON/A1/H(30,250),T(30,250),FL(30,250),FS(30,250),
     1TC(30,250),BB(30,250),HM(250),HH(4)
      DATA HH/0.0,0.3,0.6,0.95/
      END
C
C
      MASTER VARSS
C
C  **********************************************************
C  *  PROGRAM FOR THE MODELLING OF THE SOLIDIFICATION PROCESS *
C  *  IN VAR, CONSIDERING AN ENTHALPY FIELD,TEMP. DEPENDENT    *
C  *  THERMAL CONDUCTIVITY, CYLINDRICAL COORDINATES AND USING *
C  *  EXPLICIT FINITE DIFFERENCE ANLYSIS.                     *
C  *  THIS VERSION CAN TREAT TWO CHANGES OF                   *
C  *  THE MELTING RATE.                                       *
C  **********************************************************
C
      COMMON/A1/H(30,250),T(30,250),FL(30,250),FS(30,250),
     1TC(30,250),BB(30,250),HM(250),HH(4)
      COMMON/A2/PK,C,A,B,HF,CP,TA,KLOWX,KHIGHX,KLOWY,KHIGHY,KKK,
     1HLIQ,HSOL,HFE,TFE,TL,TS,FS2,DIA,HEIGHT,TIME2(250),R(30),I,
     2J,TIME,TIME1
      CALL PAPER(1)
      CALL GARGS(1)
      CALL PAPLEN(1000.0)
C
C     READING OF INPUT DATA
C
      READ(1,1000)TL,FS2,TFE,TMO,HF,CP,A,B,DT,PK,C,HEIGHT,
     1TIME,N,M,DELT,TA,DIA,HEIGHT2,RHO,HMAX,HINF,HMB,PLOT,
     2CHANGE1,CHANGE2,RATE1,RATE2,DELT1,DELT2
```

```
 1000 FORMAT(30G0.0)
      WRITE(2,2000)
 2000 FORMAT(1H ,25X,'********  INPUT DATA  ********')
      WRITE(2,2100)TL,TFE
 2100 FORMAT(1H ,'ALLOY WITH TL=',F6.1,1X,'TFE=',F6.1)
      WRITE(2,2200)PK,HF,CP,RHO
 2200 FORMAT(1H ,'AND K=',F5.3,1X,'HF=',F6.1,1X,'CP=',F7.4,1X,'DENS.=',
     1F6.1)
      WRITE(2,2300)DIA,HEIGHT
 2300 FORMAT(1H ,'INGOT IS ',F5.0,' WIDE AND ',F5.0,' HIGH')
      WRITE(2,2400)DELT,TMO,TA
 2400 FORMAT(1H ,'SUPERHEAT=',F4.0,1X,'MOULD TEMP.=',F4.0,1X,
     1'AMBIENT TEMP.=',F4.0)
      WRITE(2,2500)A,B
 2500 FORMAT(1H ,'THERM. COND.=',F8.6,'+',F8.6,'*T')
      WRITE(2,2600)HINF,HMAX,HINF
 2600 FORMAT(1H ,'HEAT TRANSF. COEFF.=',F6.4,'+(',F6.4,'-',F6.4,')*EXP
     1(-0.004667*TIME)')
      WRITE(2,2700)HMB
 2700 FORMAT(1H ,'AND AT THE BOTTOM, H=',F4.2)
      WRITE(2,2800)
 2800 FORMAT(1H ,'OTHER PARAMETERS:')
      WRITE(2,2900)DT,C,TIME,N,M,HEIGHT2,PLOT
 2900 FORMAT(1H ,'DT=',F4.1,1X,'C=',F3.1,1X,'TIME=',F7.0,/,1X,'N=',I3,
     11X,'M=',I3,1X,'HEIGHT2=',F5.1,1X,'PLOT=',F7.0)
      WRITE(2,2920)
 2920 FORMAT(1H ,'MELTING RATE CHANGED:HEIGHT,REL.CHANGE,NEW SUPERHEAT'
      WRITE(2,2925)CHANGE1,RATE1,DELT1
 2925 FORMAT(1H ,F4.1,4X,F5.3,4X,F4.0)
      WRITE(2,2950)CHANGE2,RATE2,DELT2
 2950 FORMAT(1H ,F4.1,4X,F5.3,4X,F4.0)
C
C
C     TL=LIQUIDUS OF ALLOY (DEG.C), FS2=FRACTION SOL. GIVING "TRUE" SOL.TEMP.
C     TFE=LIQUIDUS OF SOLVENT (PURE METAL, DEG.C),TMO=MOULD TEMP.(DEG.C)
C     HF=HEAT OF FUSION (KJ/KG), CP=SPECIFIC HEAT (KJ/KG,C),
C     A AND B ARE CONSTANTS IN THE EXPRESSION FOR THE TEMP. DEPENDENT
C     THERMAL CONDUCTIVITY, TC=A+B*T, DT=TIME INCREMENT (S)
C     PK=PARTITION COEFFICIENT OF A SOLUTE, TO BE USED IN THE SCHEIL EQN.
C     C=THE RATIO COND.(LIQUID)/COND.(SOLID), HEIGHT=FINAL HEIGHT OF INGOT(MM)
C     TIME=TOTAL TIME OF CASTING (S), N=NO. OF NODES IN THE RADIAL DIRECTION
C     M=NO. OF NODES IN THE AXIAL DIRECTION (START!)
C     DELT=SUPERHEAT OF INCOMING LIQUID (DEG.C), TA=AMBIENT TEMP. (DEG.C)
C     DIA=DIAMETER OF INGOT (MM), HEIGHT2=STARTING HEIGHT OF INGOT (MM)
C     RHO=DENSITY (KG/M3)
C     HMAX AND HINF ARE THE MAX. AND MIN. HEAT TRANSFER COEFFICIENTS
C     IN THE EXPRESSION FOR THE TIME DEPENDENT HEAT TRANSFER COEFFICIENT
C     (HM=HINF+(HMAX-HINF)*EXP(-K*TIME)) AT THE MOULD WALL
C     HMB=HEAT TRANSFER COEFF. AT THE BOTTOM OF THE INGOT (KJ/M2,C,S)
C     PLOT=TIME INTERVAL AFTER WHICH A PLOT OF THE CURRENT FRACTION
C     SOLID PROFILE IS PRODUCED (S)
C     CHANGE1 AND CHANGE2 ARE THE HEIGHTS (IN M) AFTER WHICH THE MELTING
C     RATE IS CHANGED AND RATE1,RATE2,DELT1 AND DELT2 ARE THE RELATIVE
C     CHANGES IN MELTING RATE AND THE NEW SUPERHEATS ON THE TOP SURFACE,
C     RESPECTIVELY
C
```

```
C
C*********  DEFINITION OF VARIOUS PARAMETERS AT TIME=0  *********
C
C
      HFE=CP*(TFE-TA)+HF
      HLIQ=CP*(TL-TA)+HF
      TS=TFE-(TFE-TL)*(1.0-FS2)**(PK-1.0)
      HSOL=CP*(TS-TA)+(1.0-FS2)*HF
      DR=DIA/(2.*1000.*FLOAT(N-1))
      DZ=HEIGHT2/(1000.*FLOAT(M-1))
      DP=DT/RHO
      DT2=DZ*TIME/(HEIGHT/1000.)
      TIME1=0.0
      TIME3=0.0
      TIME4=TIME*HEIGHT2/HEIGHT
      TPLOT=0.0
      SLICE=0.0
      KKK=1
      KLOWX=1
      KHIGHX=N
      KLOWY=1
      KHIGHY=INT(HEIGHT/1000./DZ)+1
C
C
      DO 100 I=1,N
      DO 110 J=1,M
      T(I,J)=TL+DELT
      TC(I,J)=C*(A+B*(T(I,J)+273.15))
      BB(I,J)=C*B
      H(I,J)=CP*(T(I,J)-TA)+HF
      FL(I,J)=1.0
      FS(I,J)=0.0
  110 CONTINUE
  100 CONTINUE
C
C
C  CALCULATION OF THE HEAT TRANSFER COEFFICIENTS ALONG THE SURFACE
C  AND THE RADIAL DISTANCE OF THE NODES (FROM THE CENTRE)
C
C
      L=1
  120 TIME2(L)=(M-1-L)*DT2
      HM(L)=HINF+(HMAX-HINF)*EXP(-0.004667*TIME2(L))
      L=L+1
      IF(L.EQ.M)GO TO 125
      GO TO 120
  125 RAD=DIA/(2.*1000.)
      K=1
  130 R(K)=RAD
      RAD=RAD-DR
      K=K+1
      IF(K.GT.N)GO TO 135
      GO TO 130
  135 DO 140 L=1,M-1
      WRITE(2,3000)HM(L)
  140 CONTINUE
```

```
 3000 FORMAT(1H ,F6.4)
      DO 145 L=1,N
      WRITE(2,3100)R(L)
  145 CONTINUE
 3100 FORMAT(1H ,F7.5)
C
C *******   START OF CALCULATIONS   ************
C
C
    1 TIME3=TIME3+DT
    2 TIME1=TIME1+DT
      SLICE=SLICE+DT
      TPLOT=TPLOT+DT
      DO 200 I=1,N
      IF(I.EQ.1)GO TO 300
      IF(I.EQ.N)GO TO 305
      DO 210 J=1,M
      IF(J.EQ.1)GO TO 310
      IF(J.EQ.M)GO TO 311
C
C  INTERNAL NODES
C
      H(I,J)=H(I,J)+DP*(TC(I,J)*(1./(R(I)*2.*DR)*(T(I+1,J)-T(I-1,J))
     1+1./DR**2.*(T(I+1,J)-2.*T(I,J)+T(I-1,J))+1./DZ**2.*(T(I,J+1)
     2-2.*T(I,J)+T(I,J-1)))+BB(I,J)*((1./(2.*DR)*(T(I+1,J)-T(I-1,J))
     3)**2.+(1./(2.*DZ)*(T(I,J+1)-T(I,J-1)))**2.))
      CALL CONV
      GO TO 210
C
C  NODES AT THE BOTTOM OF THE MOULD
C
  310 QZ=HMB*(T(I,J)-TMO)
      H(I,J)=H(I,J)+DP*(TC(I,J)*((1./(R(I)*2.*DR)*(T(I+1,J)-T(I-1,J)))
     1+1./DR**2.*(T(I+1,J)-2.*T(I,J)+T(I-1,J))+2./DZ**2.*(T(I,J+1)-
     2QZ*DZ/TC(I,J)-T(I,J)))+BB(I,J)*((1./(2.*DR)*(T(I+1,J)-T(I-1,J)
     3))**2.+(QZ/TC(I,J))**2.))
      CALL CONV
      GO TO 210
C
C  NODES AT THE TOP OF THE INGOT
C
  311 H(I,J)=H(I,J)+DP*(TC(I,J)*(1./(R(I)*2.*DR)*(T(I+1,J)-T(I-1,J))
     1+1./DR**2.*(T(I+1,J)-2.*T(I,J)+T(I-1,J))+2./DZ**2.*(T(I,J-1)-
     2T(I,J)))+BB(I,J)*((1./(2.*DR)*(T(I+1,J)-T(I-1,J)))**2.))
      CALL CONV
  210 CONTINUE
      GO TO 200
  300 DO 220 J=1,M
      IF(J.EQ.1)GO TO 230
      IF(J.EQ.M)GO TO 235
C
C  NODES AT THE MOULD WALL
C
      TIME2(J)=TIME2(J)+DT
      HM(J)=HINF+(HMAX-HINF)*EXP(-0.004667*TIME2(J))
      QR=HM(J)*(T(I,J)-TMO)
```

```
      H(I,J)=H(I,J)+DP*(TC(I,J)*(QR/(R(I)*TC(I,J))+2./DR**2.*(T(I+1,J)-
     1QR*DR/TC(I,J)-T(I,J))+1./DZ**2.*(T(I,J+1)-2.*T(I,J)+T(I,J-1)))+
     2BB(I,J)*((QR/TC(I,J))**2.+(1./(2.*DZ)*(T(I,J+1)-T(I,J-1)))**2.))
      CALL CONV
      GO TO 220
C
C  NODE AT THE CORNER MOULD WALL/BOTTOM
C
  230 TIME2(J)=TIME2(J)+DT
      HM(J)=HINF+(HMAX-HINF)*EXP(-0.004667*TIME2(J))
      QR=HM(J)*(T(I,J)-TMO)
      QZ=HMB*(T(I,J)-TMO)
      H(I,J)=H(I,J)+DP*(TC(I,J)*(1./R(I)*(QR)/TC(I,J)+2./DR**2.*(T(I+1,J)
     1)-QR*DR/TC(I,J)-T(I,J))+2./DZ**2.*(T(I,J+1)-QZ*DZ/TC(I,J)-T(I,J)))
     2+BB(I,J)*((QR/TC(I,J))**2.+(QZ/TC(I,J))**2.))
      CALL CONV
      GO TO 220
C
C  NODE AT THE CORNER MOULD WALL/INGOT TOP
C
  235 TIME2(J)=TIME2(J)+DT
      H(I,J)=H(I,J)+DP*(TC(I,J)*(2./DR**2.*(T(I+1,J)-
     1T(I,J))+2./DZ**2.*(T(I,J-1)-T(I,J))))
      CALL CONV
  220 CONTINUE
      GO TO 200
  305 DO 308 J=1,M
      IF(J.EQ.1)GO TO 307
      IF(J.EQ.M)GO TO 306
C
C  NODES AT THE CENTRE LINE
C
      H(I,J)=H(I,J)+DP*(TC(I,J)*(2./DR**2.*(T(I-1,J)-T(I,J))+1./DZ**2.*
     1(T(I,J+1)-2.*T(I,J)+T(I,J-1)))+BB(I,J)*((1./(2.*DZ)*(T(I,J+1)-T(I
     2,J-1)))**2.))
      CALL CONV
      GO TO 308
C
C  NODE AT THE 'CORNER' CENTRE LINE/BOTTOM
C
  307 QZ=HMB*(T(I,J)-TMO)
      H(I,J)=H(I,J)+DP*(TC(I,J)*(2./DR**2.*(T(I-1,J)-T(I,J))+2./DZ**2.*
     1(T(I,J+1)-QZ*DZ/TC(I,J)-T(I,J)))+BB(I,J)*((QZ/TC(I,J))**2.))
      CALL CONV
      GO TO 308
C
C  NODE AT THE 'CORNER' CENTRE LINE/INGOT TOP
C
  306 H(I,J)=H(I,J)+DP*(TC(I,J)*(2./DR**2.*(T(I-1,J)-T(I,J))+2./DZ**2.*
     1(T(I,J-1)-T(I,J))))
      CALL CONV
  308 CONTINUE
  200 CONTINUE
C
C********  END OF CALCULATIONS  ************************
C
```

```
C
C  CHECK OF THE DIFFERENT 'CLOCKS' TO SEE IF IT IS TIME TO ADD A
C  SLICE OR TO PRODUCE A PLOT ETC.
C
      IF(TIME1.GT.TIME)GO TO 400
      IF(TIME3.LT.TIME4)GO TO 1
      IF(TPLOT.GE.PLOT)GO TO 420
  440 IF(SLICE.GE.DT2)GO TO 430
  445 IF((CHANGE1.AND.CHANGE2).EQ.10.)GO TO 2
      IF(M*DZ.GE.CHANGE1)GO TO 446
      IF(M*DZ.GE.CHANGE2)GO TO 447
      GO TO 2
  420 CALL PICASSO
      TPLOT=0.0
      PH=M*DZ
      TIH=TIME1/3600.
      WRITE(2,3200)TIH,PH
 3200 FORMAT(1H ,20X,'TEMPERATURE FIELD AT TIME=',F6.3,/,21X,
     1'INGOT HEIGHT (IN M)=',F5.3)
      DO 425 J=1,M
      K=M+1-J
      WRITE(2,3300)(T(I,K),I=1,N)
  425 CONTINUE
 3300 FORMAT(1H ,21(1X,F6.1))
      GO TO 440
  430 M=M+1
      SLICE=0.0
      TIME2(M)=-DT
      DO 450 I=1,N
      T(I,M)=TL+DELT
      H(I,M)=CP*(T(I,M)-TA)+HF
      TC(I,M)=C*(A+B*(T(I,M)+273.15))
      BB(I,M)=C*B
      FL(I,M)=1.0
      FS(I,M)=0.0
  450 CONTINUE
      GO TO 445
  446 DT2=DT2/RATE1
      TIME=TIME1+(TIME-TIME1)/RATE1
      DELT=DELT1
      CHANGE1=10.
      GO TO 2
  447 DT2=DT2/RATE2
      TIME=TIME1+(TIME-TIME1)/RATE2
      DELT=DELT2
      CHANGE2=10.
      GO TO 2
  400 CALL PICASSO
      PH=M*DZ
      TIH=TIME1/3600.
      WRITE(2,3400)TIH,PH
 3400 FORMAT(1H ,20X,'FINAL TEMPERATURE FIELD, TIME=',F6.3,/,21X,
     1'FINAL INGOT HEIGHT (IN M)=',F5.3)
      DO 460 J=1,M
```

```
      K=M+1-J
      WRITE(2,3500)(T(I,K),I=1,N)
  460 CONTINUE
 3500 FORMAT(1H ,21(1X,F6.1))
      WRITE(2,3600)TIH
 3600 FORMAT(1H ,20X,'FINAL FRACTION SOLID DISTRIBUTION, TIME=',F6.3)
      DO 470 J=1,M
      K=M+1-J
      WRITE(2,3700)(FS(I,K),I=1,N)
  470 CONTINUE
 3700 FORMAT(1H ,21(1X,F5.3))
      CALL GREND
      STOP
      END
C.......................................................................
C
C+++++++  FIRST SUBROUTINE, WHICH CONVERTS ENTHALPIES  +++++++
C          INTO TEMPERATURES AND CALCULATES FRACTION
C          LIQUID AND SOLID.
C
      SUBROUTINE CONV
      COMMON/A1/H(30,250),T(30,250),FL(30,250),FS(30,250),
     1TC(30,250),BB(30,250),HM(250),HH(4)
      COMMON/A2/PK,C,A,B,HF,CP,TA,KLOWX,KHIGHX,KLOWY,KHIGHY,
     1KKK,HLIQ,HSOL,HFE,TFE,TL,TS,FS2,DIA,HEIGHT,TIME2(250),R(30),I,
     2J,TIME,TIME1
      IF(H(I,J).GE.HLIQ)GO TO 600
      IF(H(I,J).LE.HSOL)GO TO 610
      IF(FL(I,J).EQ.0.0)GO TO 610
      FFLO=FL(I,J)
  605 GFL=(HFE-HF-H(I,J)+FFLO*HF)/(HFE-HLIQ)-FFLO**(PK-1)
      DGFL=HF/(HFE-HLIQ)-(PK-1.)*FFLO**(PK-2.)
      FFL1=FFLO-GFL/DGFL
      FFLO=FFL1
      E=GFL/DGFL
      DIV=ABS(E)
      IF(DIV.GT.0.001)GO TO 605
      FL(I,J)=FFLO
      IF(FL(I,J).LE.(1.0-FS2))GO TO 610
      T(I,J)=(H(I,J)-FL(I,J)*HF)/CP+TA
      FS(I,J)=1.-FL(I,J)
      TC(I,J)=(1.+(C-1.)*FL(I,J)**2.)*(A+B*(T(I,J)+273.15))
      BB(I,J)=(1.+(C-1.)*FL(I,J)**2.)*B
      GO TO 620
  600 T(I,J)=(H(I,J)-HF)/CP+TA
      FL(I,J)=1.0
      FS(I,J)=0.0
      TC(I,J)=C*(A+B*(T(I,J)+273.15))
      BB(I,J)=C*B
      GO TO 620
  610 T(I,J)=(H(I,J)-FL(I,J)*HF)/CP+TA
      FL(I,J)=0.0
      FS(I,J)=1.0
      TC(I,J)=A+B*(T(I,J)+273.15)
      BB(I,J)=B
```

```
  620 RETURN
      END
C
C+++++++  SECOND SUBROUTINE, WHICH PERFORMS THE PLOTTING   +++++++++
C         OF THE FRACTION SOLID PROFILES FOR FS=0.1,0.3,0.6
C         AND 0.9.
C
      SUBROUTINE PICASSO
      COMMON/A1/H(30,250),T(30,250),FL(30,250),FS(30,250),
     1TC(30,250),BB(30,250),HM(250),HH(4)
      COMMON/A2/PK,C,A,B,HF,CP,TA,KLOWX,KHIGHX,KLOWY,KHIGHY,
     1KKK,HLIQ,HSOL,HFE,TFE,TL,TS,FS2,DIA,HEIGHT,TIME2(250),R(30),I,
     2J,TIME,TIME1
C
      CALL CSPACE(0.15,0.85,0.01,0.99)
      CALL PSPACE(0.28,0.77,0.14,0.91)
      CALL GPINFO('PEN NUMBER 7L-4 IN HOLDER NUMBER 1, BLACK INK',45)
      CALL INKPEN(1)
      CALL CTRSET(0)
      CALL CTRMAG(12)
      CALL POSITN(0.34,0.08)
      CALL TYPECS('FRACTION SOLID DISTRIBUTION IN A VAR-UNIT',41)
      CALL CTRMAG(10)
      CALL POSITN(0.40,0.13)
      CALL TYPECS('DISTANCE FROM THE SURFACE, (CM)',31)
      CALL POSITN(0.33,0.33)
      CALL CTRORI(1.0)
      CALL TYPECS('DISTANCE ALONG THE INGOT, (CM)',30)
      CALL CTRORI(0.0)
      TIH=TIME1/3600.0
      TIF=TIME/3600.0
      CALL POSITN(0.40,0.84)
      CALL TYPECS('AFTER ',6)
      CALL TYPENF(TIH,1)
      CALL TYPECS(' HOURS, OUT OF ',15)
      CALL TYPENF(TIF,1)
      CALL MAP(0.0,DIA/20.,0.0,HEIGHT/10.)
      CALL PSPACE(0.15,0.84,0.0,0.99)
      CALL BORDER
      CALL PSPACE(0.40,0.487,0.18,0.82)
      CALL BORDER
      CALL AXESSI(10.0,10.0)
      CALL CONTRA(FS,KLOWX,KHIGHX,30,KLOWY,KHIGHY,250,HH,1,4)
      CALL MAP(0.28,0.77,0.14,0.91)
      CALL FRAME
      RETURN
      END
      FINISH
```

Figure AII.1

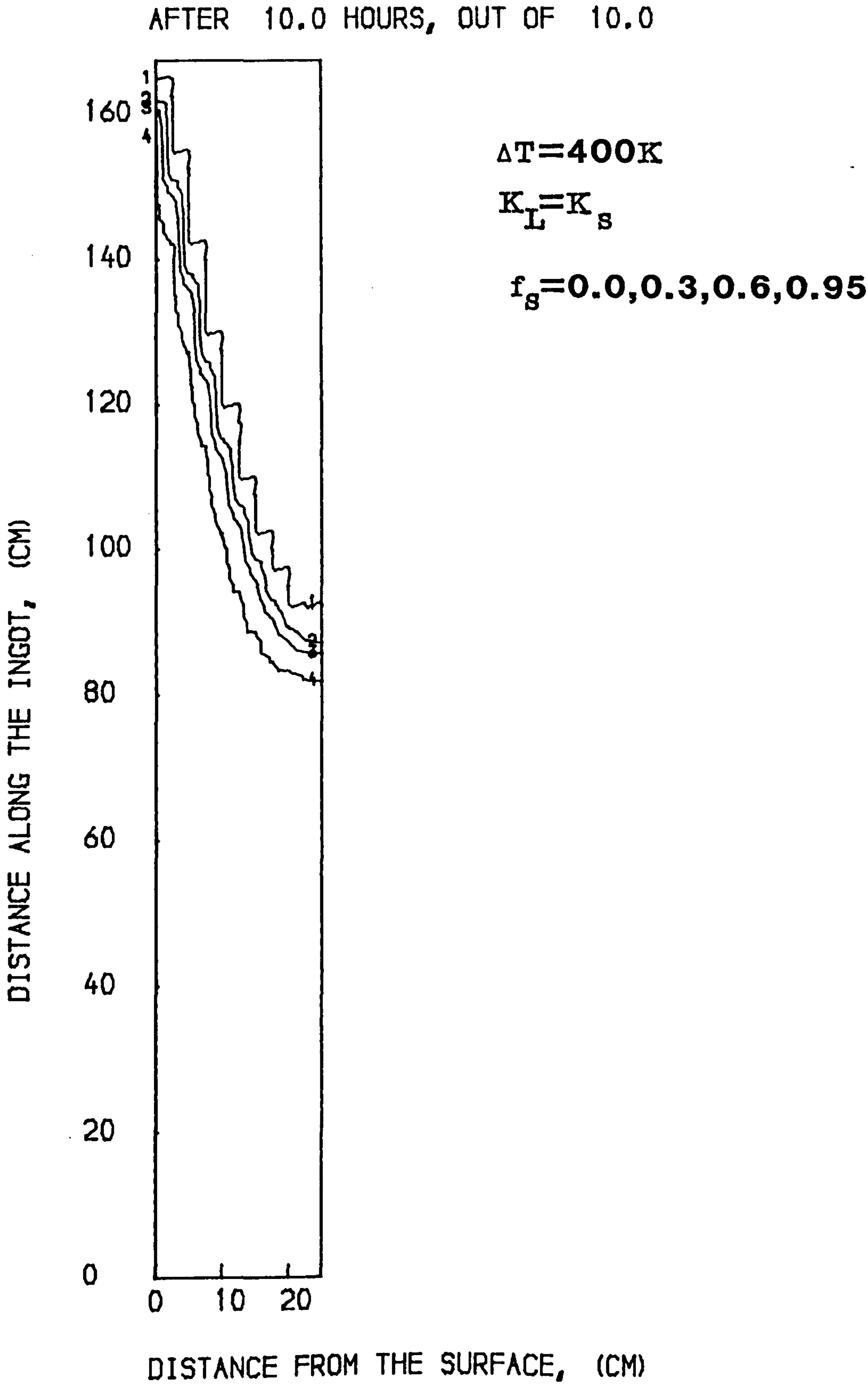

FRACTION SOLID DISTRIBUTION IN A VAR-UNIT

Figure AII.2

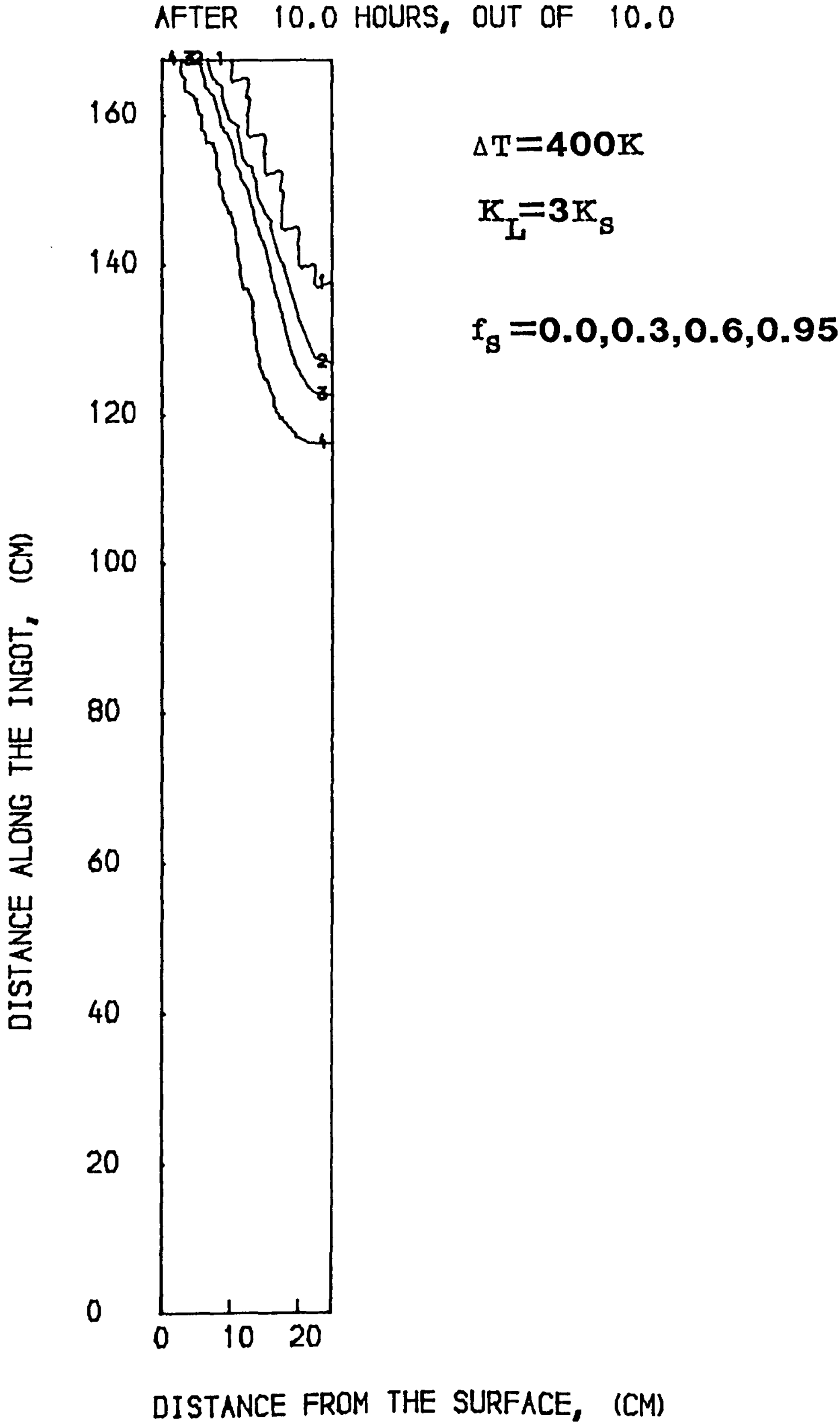

FRACTION SOLID DISTRIBUTION IN A VAR-UNIT

Figure AII.3

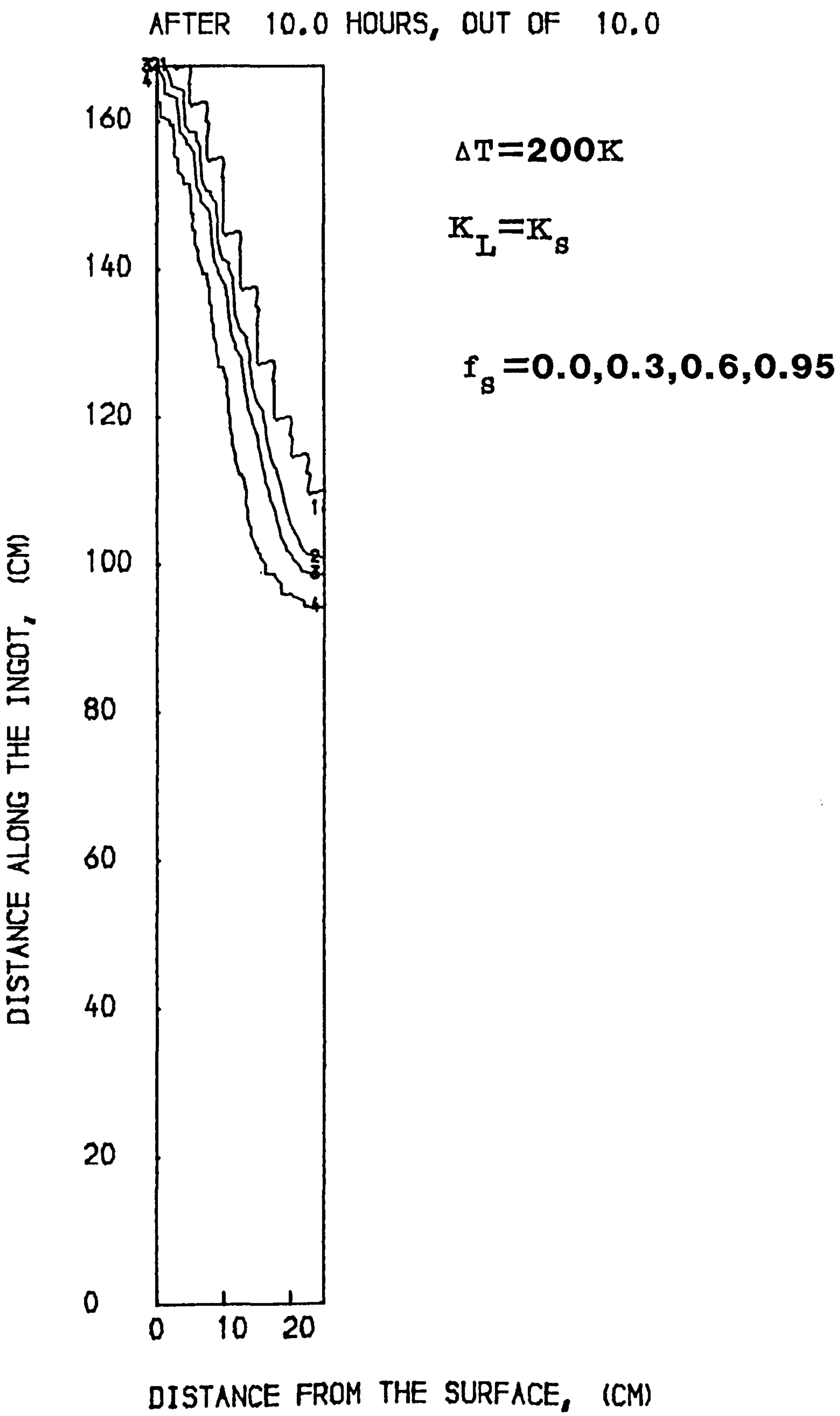

FRACTION SOLID DISTRIBUTION IN A VAR-UNIT

Figure AII.4

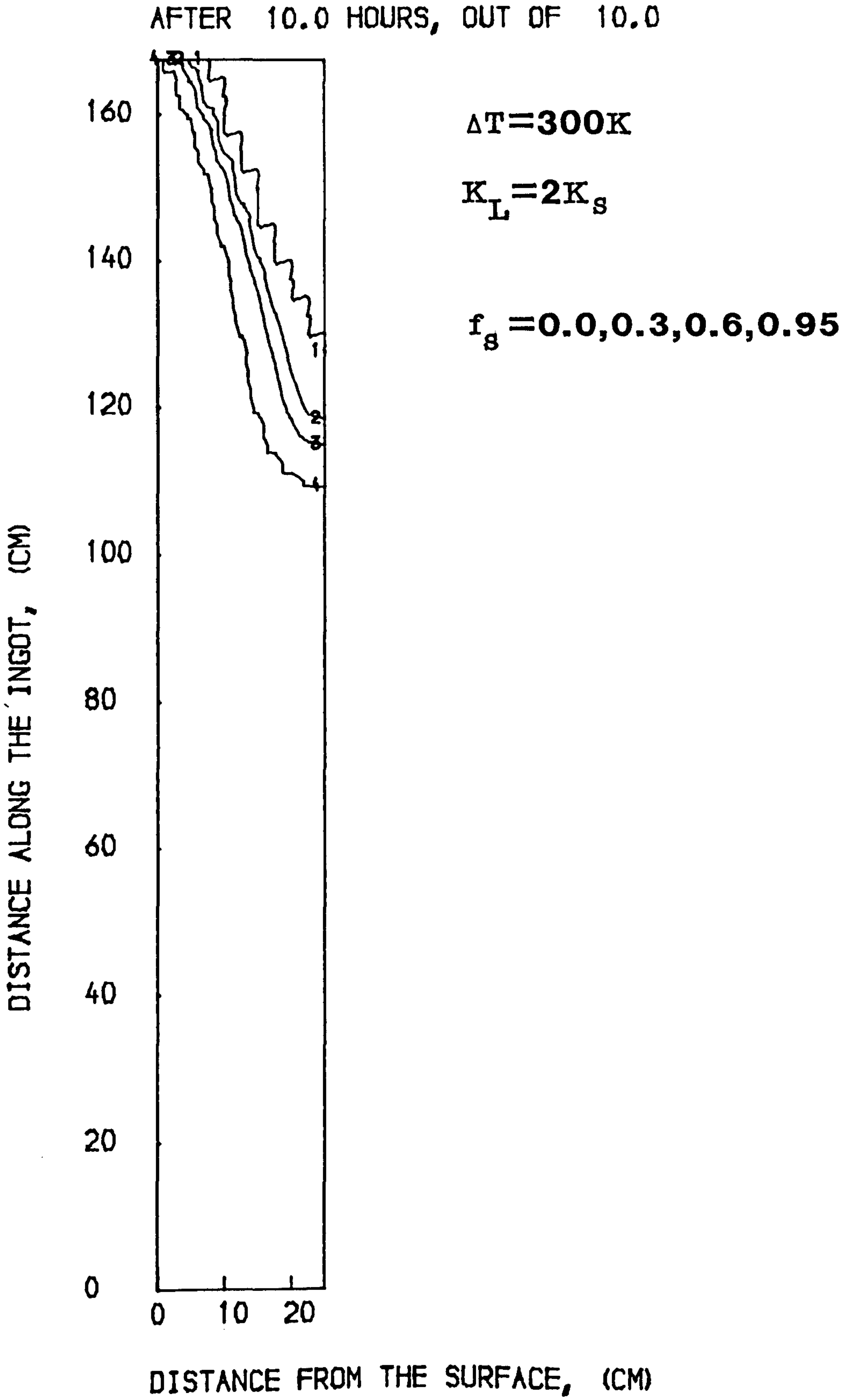

FRACTION SOLID DISTRIBUTION IN A VAR-UNIT

Figure AII.5

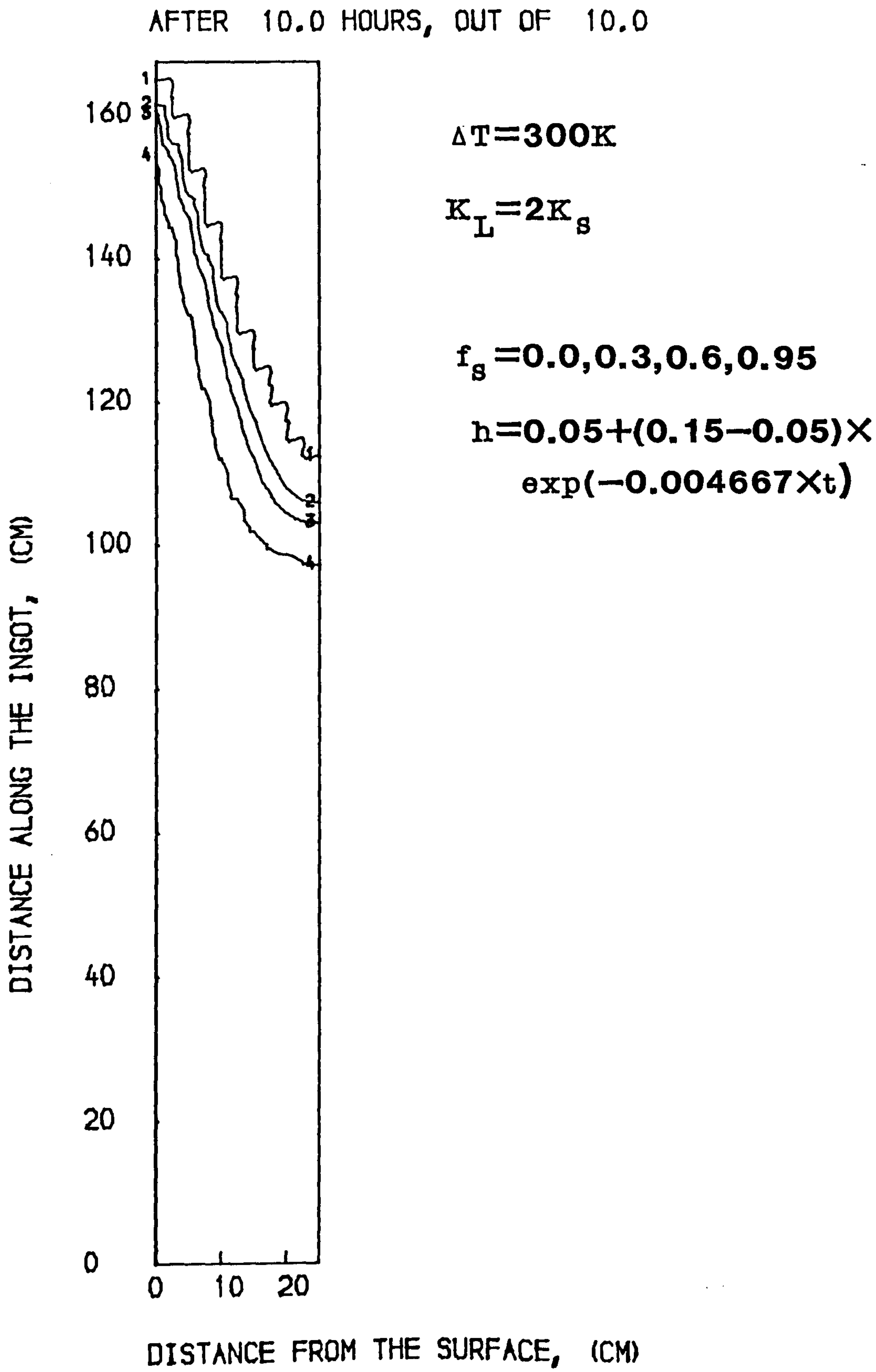

FRACTION SOLID DISTRIBUTION IN A VAR-UNIT

APPENDIX III

Line-by-line Description of the Computer Program for Heat Transfer in the Meniscus Region during Casting

Lines 1-53

The library for the plotting is called, followed by a program-description with definition of input- and output-channels (1-9). A BLOCK DATA statement is used for the definition of the levels of fraction solid to be used in the plotting of the iso-f_s curves (12-18). After the dimensioning of the arrays and matrices, the plotter is set-up and the input-data are read (32-53).

```
      LIBRARY(SUBGROUPGHOS)
      LIBRARY(SUBGROUPGHOS)
      PROGRAM(CURVED)
      INPUT 1=CRO
      OUTPUT 2=LPO
      TRACE 0
      END
C
C
      NOLIST
      BLOCK DATA
      COMMON/A/H(45,101),T(45,101),TK(45,101),FL(45,101),FS(45,101),
     1CP,TA,TFE,TL,TS,FSS2,I,J,HFE,HLIQ,HSOL,HF,PK,BB(45,101),HT(5),
     2A,B,C,FILM
      DATA HT/0.0,0.2,0.6,1.0/
      END
C
      MASTER CURVED
C     *********************************************
C     *                                           *
C     *  MENISCUS FREEZING,DIRECT DERIVATION USING  *
C     *  CONDITIONS FOR A CURVED BOUNDARY.          *
C     *  THIS VERSION IS FOR GRID SIZES >=0.5MM.    *
C     *  IT CONSIDERS A SLAG LAYER ON THE MENISCUS  *
C     *  AND A SLAGFILM BETWEEN THE MOULD AND THE   *
C     *  METAL.                                     *
C     *                                           *
C     *          STAINLESS STEEL (SCHEIL)           *
C     *********************************************
      EXTERNAL YVAL
      COMMON/A4/ICASE(300),XVALUE(300),YVALUE(300)
      COMMON/A2/HMO,TIME,DELT,KLOWX,KHIGHX,KLOWY,KHIGHY,XMAP,YMAP,DX,
     1GDX,DT
      COMMON/A0/H1(300),H2(300),T1(300),T2(300),TK1(300),TK2(300),
     1FL1(300),FL2(300),FS1(300),FS2(300),A1(300),B2(300),ALFA1(300),
     2ALFA2(300),ALFA(300),BB1(300),BB2(300),L,K,KPR,LL
      COMMON/A/H(45,101),T(45,101),TK(45,101),FL(45,101),FS(45,101),
     1CP,TA,TFE,TL,TS,FSS2,I,J,HFE,HLIQ,HSOL,HF,PK,BB(45,101),HT(5),
     2A,B,C,FILM,YSLAG,TKSLAG
      COMMON/A3/U,V,Z
      CALL PAPER(1)
      CALL GARGS(1)
      CALL PAPLEN(1000.0)
C
C++++ READING OF INPUT DATA,N.B. THAT THE MAXIMUM MENISCUS HEIGHT +++
C     IS 15.0 MM.
C
      READ(1,1200)CP,HF,N,DT,U,V,Z,DELT,HEALT,
     1TL,FSS2,PK,TKSLAG,TSX,TSY,YSLAG,TA,A,B,C,FILM
 1200 FORMAT(21G0.0)
C
```

Lines 1-53

The library for the plotting is called, followed by a program-description with definition of input- and output-channels (1-9). A BLOCK DATA statement is used for the definition of the levels of fraction solid to be used in the plotting of the iso-f_s curves (12-18). After the dimensioning of the arrays and matrices, the plotter is set-up and the input-data are read (32-53).

```
      LIBRARY(SUBGROUPGHOS)
      LIBRARY(SUBGROUPGHOS)
      PROGRAM(CURVED)
      INPUT 1=CR0
      OUTPUT 2=LP0
      TRACE 0
      END
C
C
      NOLIST
      BLOCK DATA
      COMMON/A/H(45,101),T(45,101),TK(45,101),FL(45,101),FS(45,101),
     1CP,TA,TFE,TL,TS,FSS2,I,J,HFE,HLIQ,HSOL,HF,PK,BB(45,101),HT(5),
     2A,B,C,FILM
      DATA HT/0.0,0.2,0.6,1.0/
      END
C
      MASTER CURVED
C  *************************************************
C  *                                               *
C  *  MENISCUS FREEZING,DIRECT DERIVATION USING    *
C  *  CONDITIONS FOR A CURVED BOUNDARY.            *
C  *  THIS VERSION IS FOR GRID SIZES >=0.5MM.      *
C  *  IT CONSIDERS A SLAG LAYER ON THE MENISCUS    *
C  *  AND A SLAGFILM BETWEEN THE MOULD AND THE     *
C  *  METAL.                                       *
C  *                                               *
C  *          STAINLESS STEEL (SCHEIL)             *
C  *************************************************
      EXTERNAL YVAL
      COMMON/A4/ICASE(300),XVALUE(300),YVALUE(300)
      COMMON/A2/HMO,TIME,DELT,KLOWX,KHIGHX,KLOWY,KHIGHY,XMAP,YMAP,DX,
     1GDX,DT
      COMMON/A0/H1(300),H2(300),T1(300),T2(300),TK1(300),TK2(300),
     1FL1(300),FL2(300),FS1(300),FS2(300),A1(300),B2(300),ALFA1(300),
     2ALFA2(300),ALFA(300),BB1(300),BB2(300),L,K,KPR,LL
      COMMON/A/H(45,101),T(45,101),TK(45,101),FL(45,101),FS(45,101),
     1CP,TA,TFE,TL,TS,FSS2,I,J,HFE,HLIQ,HSOL,HF,PK,BB(45,101),HT(5),
     2A,B,C,FILM,YSLAG,TKSLAG
      COMMON/A3/U,V,Z
      CALL PAPER(1)
      CALL GARGS(1)
      CALL PAPLEN(1000.0)
C
C++++ READING OF INPUT DATA,N.B. THAT THE MAXIMUM MENISCUS HEIGHT +++
C     IS 15.0 MM.
C
      READ(1,1200)CP,HF,N,DT,U,V,Z,DELT,HEALT,
     1TL,FSS2,PK,TKSLAG,TSX,TSY,YSLAG,TA,A,B,C,FILM
 1200 FORMAT(21G0.0)
C
```

Lines 54-96

The notations used in the program are given (54-67). The pouring temperature is calculated together with the enthalpy of pure Fe at its melting point and the enthalpy of the steel at its liquidus temperature. The solidus temperature is calculated using the Scheil-equation and the fraction solid at which solidification is assumed to be completed. The corresponding enthalpy is also calculated (76-80). The size of the grid is calculated, the time is set to zero and the number of nodes in the x- and y-direction are determined (81-87). The real size of the plotting space and the size of the matrix used by the plotter are calculated (91-96).

```
C      TM=MOULDTEMP(DEG.C),CP=SPECIFIC HEAT(KJ/KG,C)
C      HF=HEAT OF FUSION(KJ/KG)
C      N=MESH NUMBER,DT=TIME INCREMENT(S),
C      U=MENISCUS HEIGHT(MM),V AND Z ARE CONSTANTS IN EQN. FOR MENISCUS
C      SHAPE,DELT=SUPERHEAT(DEG.C),HEALT=HEALING TIME(S)(UP TO 1.5S),
C      TL=LIQUIDUS TEMP.(DEG.C),TS=SOLIDUS TEMP.(DEG.C),PK=PART.COEFF.
C      FSS2=THE FRACTION SOLID WHICH DEFINES FULLY SOLID (DUE TO SCHEIL).
C      TKSLAG=THERMAL CONDUCTIVITY OF SLAG(KW/M,C),TSX=TEMP.OF SLAG AT
C      MOULD WALL(DEG.C),TSY=TEMP. OF SLAG AT THE INTERFACE SOLID/LIQ.
C      SLAG(DEG.C),YSLAG=THICKNESS OF LIQ.SLAG LAYER(MM).
C      TA=AMBIENT TEMPERATURE (C)
C      A AND B ARE THE CONSTANTS IN THE EXPRESSION FOR THE THERMAL
C      CONDUCTIVITY, K=A+B*T (KW/M,C), C=THE RATIO KLIQ/KSOL.
C      FILM=THICKNESS OF THE SLAGFILM (MOULD/METAL) (MM)
C
C      LIQUIDUS FOR PURE FE
C
       TFE=1537.0
C
C++++ INITIAL STATE OF THE SYSTEM:SHAPE OF MENISCUS,DEF. OF GRID,++++
C      DEF. OF THERMAL STATE AT TIME=0
C
       TP=TL+DELT
       HFE=CP*(TFE-TA)+HF
       HLIQ=CP*(TL-TA)+HF
       TS=TFE-(TFE-TL)*(1.0-FSS2)**(PK-1.0)
       HSOL=CP*(TS-TA)+(1.0-FSS2)*HF
       EN=FLOAT(N)
       DX=(10./1000.)/EN
       GDX=10./EN
       DR=DT/7900.
       TIME=0.0
       MAX=INT(10./GDX)
       MAY=INT((10.+U)/GDX)+1)
C
C      PARAMETERS NEEDED FOR THE PLOTTING(SIZE OF THE SYSTEM)
C
       KLOWX=2
       KHIGHX=MAX
       KLOWY=2
       KHIGHY=MAY
       XMAP=10.0
       YMAP=10.5+U
```

Lines 97-150

All the data used are printed (97-119). Superimposing the curvature of the meniscus onto the grid, the system is scanned along the curve by sub-dividing each square by a factor of 100 in the x-direction. Calculation of the distance from each intersection to the node next to the meniscus is carried out (126-150).

```
C
C
C     PRINTING OF INPUT DATA.
C
C
      WRITE(2,2000)
 2000 FORMAT(1H ,25X,'**** INPUT DATA ****')
      WRITE(2,2100)PK,TL,TS
 2100 FORMAT(1H ,'STAINLESS STEEL WITH K=',F5.3,1X,'TLIQ=',F7.2,1X,
     1'TSOL=',F7.2)
      WRITE(2,2200)TSX,TSY,TKSLAG,YSLAG
 2200 FORMAT(1H ,1X,'TSX=',F7.2,1X,'TSY=',F7.2,
     11X,1X,'COND OF SLAG=',F7.5,
     21X,'THICKNESS OF LIQ.SLAG=',F7.2)
      WRITE(2,2300)CP,HF
 2300 FORMAT(1H ,'CP=',F6.4,1X,'HEAT OF FUSION=',F7.2)
      WRITE(2,2400)N,U,DT,V,Z
 2400 FORMAT(1H ,'MESH NO=',I3,1X,'MEN. HEIGHT=',F4.1,1X,
     1'TIME INCR.=',F6.4,1X,'CONSTANTS=',F4.2,1X,F4.2)
      WRITE(2,2450)TA,A,B,C
 2450 FORMAT(1H ,'TA=',F5.2,1X,'A=',F7.6,1X,'B=',F8.7,1X,'C=',F3.1)
      WRITE(2,2475)FILM
 2475 FORMAT(1H ,'FILM THICKNESS=',F7.4)
C
C
C++++ CALCULATION OF MENISCUS CURVATURE AND INTERSECTIONS OF CURVE ++
C     WITH IMPOSED GRID,IDENTIFYING NODE TYPE.
C
C
      HEIGHT=10.0
      XINCR=GDX/100.
      XSTRT=0.0
      YGRID=HEIGHT
      XGRID=GDX
      L=1
   10 IF(XSTRT/GDX.GT.MAX) GO TO 26
      YTEST=YVAL(XSTRT)
      IF(YTEST.GT.YGRID) GO TO 20
      IF(XSTRT.GE.XGRID) GO TO 25
      XSTRT=XSTRT+XINCR
      GO TO 10
   20 XVALUE(L)=-(1/V)*ALOG(1-((YGRID-10.)/U)**(1/Z))
      YVALUE(L)=YGRID
      L=L+1
      YGRID=YGRID+GDX
      XSTRT=XSTRT+XINCR
      GO TO 10
   25 XVALUE(L)=XGRID
      YVALUE(L)=YVAL(XGRID)
      XSTRT=XSTRT+XINCR
      XGRID=XGRID+GDX
      L=L+1
      GO TO 10
   26 CONTINUE
```

Lines 151-256

Having the distances from the intersections to the neighbouring nodes, the system is traced again in order to identify the type of the intersections and their coordinates. Also, the relative distance between each intersection and the node next to the curved boundary is calculated and stored together with the angle between the normal to the curve and the x-direction. The locations, types, relative distances and angles are then printed (151-256).

```
      NTOTAL=L-1
      K=2
   30 IF((XVALUE(K).EQ.GDX*INT(XVALUE(K)/GDX)).AND.(YVALUE(K)
     1.EQ.GDX*INT(YVALUE(K)/GDX)))GO TO 35
      IF((YVALUE(K).EQ.GDX*INT(YVALUE(K+1)/GDX)).AND.(YVALUE(K+1)
     1.LT.GDX*INT(YVALUE(K+1)/GDX+1)))GO TO 36
      IF(YVALUE(K).EQ.GDX*INT(YVALUE(K)/GDX))GO TO 33
      IF(YVALUE(K).GT.GDX*INT(YVALUE(K)/GDX))GO TO 32
   33 ICASE(K)=2
      A1(K)=1.-(XVALUE(K)/GDX-INT(XVALUE(K)/GDX))
      IF(A1(K).LT.0.08)GO TO 35
      B2(K)=0.0
      ALFA1(K)=ABS(ATAN(-1./(U*Z*(1.-EXP(-V*XVALUE(K)))**(Z-1.)*
     1V*EXP(-V*XVALUE(K)))))
      ALFA2(K)=0.0
      ALFA(K)=0.0
      GO TO 39
   32 ICASE(K)=3
      A1(K)=0.0
      B2(K)=YVALUE(K)/GDX-INT(YVALUE(K)/GDX)
      IF(B2(K).LT.0.08)GO TO 35
      ALFA1(K)=0.0
      ALFA2(K)=ABS(ATAN(-1./(U*Z*(1.-EXP(-V*XVALUE(K)))**(Z-1.)*
     1V*EXP(-V*XVALUE(K)))))
      ALFA(K)=0.0
      GO TO 39
   35 ICASE(K)=4
      A1(K)=0.0
      B2(K)=0.0
      ALFA1(K)=0.0
      ALFA2(K)=0.0
      ALFA(K)=ABS(ATAN(-1./(U*Z*(1.-EXP(-V*XVALUE(K)))**(Z-1.)*
     1V*EXP(-V*XVALUE(K)))))
      GO TO 39
   36 ICASE(K)=1
      A1(K)=(XVALUE(K+1)-XVALUE(K))/GDX
      B2(K)=0.0
      A1(K+1)=0.0
      B2(K+1)=(YVALUE(K+1)-YVALUE(K))/GDX
      IF((A1(K).LT.0.08).AND.(B2(K+1).LT.0.08))GO TO 31
      IF(A1(K).LT.0.08)GO TO 37
      IF(B2(K+1).LT.0.08)GO TO 38
      ALFA1(K)=ABS(ATAN(-1./(U*Z*(1.-EXP(-V*XVALUE(K)))**(Z-1.)*
     1V*EXP(-V*XVALUE(K)))))
      ALFA2(K)=0.0
      ALFA1(K+1)=0.0
      ALFA2(K+1)=ABS(ATAN(-1./(U*Z*(1.-EXP(-V*XVALUE(K+1)))**
     1(Z-1.)*V*EXP(-V*XVALUE(K+1)))))
      ALFA(K+1)=0.0
      ALFA(K)=0.0
      K=K+1
      GO TO 39
```

```
   31 ICASE(K)=4
      L1=ICASE(K)
      A1(K)=0.0
      B2(K)=0.0
      B2(K+1)=0.0
      ALFA1(K)=0.0
      ALFA1(K+1)=0.0
      ALFA2(K)=0.0
      ALFA2(K+1)=0.0
      ALFA(K)=ABS(ATAN(-1./(U*Z*(1.-EXP(-V*XVALUE(K+1)))**
     1(Z-1.)*V*EXP(-V*XVALUE(K+1)))))
      K=K+1
      GO TO 39
   37 ICASE(K)=4
      L2=ICASE(K)
      A1(K)=0.0
      A1(K+1)=0.0
      B2(K)=0.0
      B2(K+1)=0.0
      ALFA1(K)=0.0
      ALFA1(K+1)=0.0
      ALFA2(K+1)=0.0
      ALFA2(K)=0.0
      ALFA(K+1)=0.0
      ALFA(K)=ABS(ATAN(-1./(U*Z*(1.-EXP(-V*XVALUE(K+1)))**
     1(Z-1.)*V*EXP(-V*XVALUE(K+1)))))
      K=K+1
      GO TO 39
   38 B2(K+1)=0.0
      ICASE(K)=4
      L3=ICASE(K)
      B2(K)=0.0
      A1(K)=0.0
      A1(K+1)=0.0
      ALFA1(K)=0.0
      ALFA1(K+1)=0.0
      ALFA2(K)=0.0
      ALFA2(K+1)=0.0
      ALFA(K+1)=0.0
      ALFA(K)=ABS(ATAN(-1./(U*Z*(1.-EXP(-V*XVALUE(K+1)))**
     1(Z-1.)*V*EXP(-V*XVALUE(K+1)))))
      K=K+1
      GO TO 39
   39 K=K+1
      IF(K.EQ.NTOTAL+1)GO TO 34
      GO TO 30
   34 WRITE(2,1300)
 1300 FORMAT(1H,/,15X,'TABLE OF THE INTERSECTIONS WITH THE GRID',
     1/,2X,'L',3X,'Y(L)',4X,'X(L)',2X,'ICASE(L)',3X,'A1(L)',1X,
     2'B2(L)',2X,'ALFA1(L)',1X,'ALFA2(L)',1X,'ALFA(L)')
      WRITE(2,1400)(L,YVALUE(L),XVALUE(L),ICASE(L),A1(L),B2(L),
     1ALFA1(L),ALFA2(L),ALFA(L),L=1,NTOTAL)
 1400 FORMAT(1X,I2,1X,F7.4,1X,F7.4,3X,I2,5X,F6.4,1X,F6.4,1X,F6.4,
     11X,F6.4,1X,F6.4)
```

Lines 257-327

The pouring temperature together with the corresponding enthalpy and thermal conductivity are assigned to each node of the system, including the fictitious nodes on the curved boundary (257-327).

```
C
C
C++++ DEFINITION OF THERMAL STATE OF THE SYSTEM AT TIME=0 +++++
C
C
      DO 45 I=2,MAX
      DO 44 J=2,MAY
      XV=GDX*(I-2)
      IF(J.GT.INT(YVAL(XV)/GDX))GO TO 40
      T(I,J)=TP
      TK(I,J)=C*(A+(T(I,J)+273.15)*B)
      BB(I,J)=C*B
      H(I,J)=CP*(T(I,J)-TA)+HF
      FL(I,J)=1.0
      FS(I,J)=0.0
      GO TO 44
   40 T(I,J)=TA
      H(I,J)=0.0
      TK(I,J)=0.0
      BB(I,J)=0.0
      FS(I,J)=2.0
   44 CONTINUE
   45 CONTINUE
      KPR=2
   49 IF(KPR.EQ.(NTOTAL+1))GO TO 1
      ITYPE=ICASE(KPR)
      GO TO(47,46,43,42),ITYPE
   42 T1(KPR)=TP
      TK1(KPR)=C*(A+(T1(KPR)+273.15)*B)
      BB1(KPR)=C*B
      H1(KPR)=CP*(T1(KPR)-TA)+HF
      FL1(KPR)=1.0
      FS1(KPR)=0.0
      KPR=KPR+1
      GO TO 49
```

```
   47 T1(KPR)=TP
      TK1(KPR)=C*(A+(T1(KPR)+273.15)*B)
      BB1(KPR)=C*B
      H1(KPR)=CP*(T1(KPR)-TA)+HF
      FL1(KPR)=1.0
      FS1(KPR)=0.0
      T2(KPR)=0.0
      TK2(KPR)=0.0
      BB2(KPR)=0.0
      H2(KPR)=0.0
      FL2(KPR)=0.0
      FS2(KPR)=0.0
      T2(KPR+1)=TP
      TK2(KPR+1)=C*(A+(T2(KPR+1)+273.15)*B)
      BB2(KPR+1)=C*B
      H2(KPR+1)=CP*(T2(KPR+1)-TA)+HF
      FL2(KPR+1)=1.0
      FS2(KPR+1)=0.0
      KPR=KPR+2
      GO TO 49
   46 T1(KPR)=TP
      TK1(KPR)=C*(A+(T1(KPR)+273.15)*B)
      BB1(KPR)=C*B
      H1(KPR)=CP*(T1(KPR)-TA)+HF
      FL1(KPR)=1.0
      FS1(KPR)=0.0
      KPR=KPR+1
      GO TO 49
   43 T2(KPR)=TP
      TK2(KPR)=C*(A+(T2(KPR)+273.15)*B)
      BB2(KPR)=C*B
      H2(KPR)=CP*(T2(KPR)-TA)+HF
      FL2(KPR)=1.0
      FS2(KPR)=0.0
      KPR=KPR+1
      GO TO 49
```

Lines 328-364

A clock is started and enthalpies for ordinary internal nodes and nodes located at the bottom of the system are calculated. A call is made to the subroutine dealing with the conversion from enthalpy to temperature after each calculation (333-362). Reaching the node next to the curved boundary, location of appropriate equation depending on type of intersection is given (363,364).

```
C
C
C+++++++++++++++ START OF CALCULATIONS +++++++++++++++++++++
C
C
    1 TIME=TIME+DT
      LL=2
      DO 59 I=2,MAX
      XP=GDX*(I-2)
      JLIM=INT(YVAL(XP)/GDX)
      IF(I.EQ.2)GO TO 58
      IF(I.EQ.MAX)GO TO 57
      DO 55 J=2,JLIM
      IF(J.EQ.2)GO TO 54
      IF(J.EQ.JLIM)GO TO 53
      IF(J.EQ.INT(YVALUE(LL)/GDX))GO TO 53
C
C     ORDINARY INTERNAL ELEMENTS
C
      H(I,J)=H(I,J)+DR*((TK(I,J)/DX**2.)*(T(I+1,J)+T(I-1,J)+T(I,J+1)+
     1T(I,J-1)-4.*T(I,J))+BB(I,J)/(4.*DX**2.)*((T(I+1,J)**2.+T(I-1,J)
     2**2.+T(I,J+1)**2.+T(I,J-1)**2.)-2.*(T(I+1,J)*T(I-1,J)+T(I,J+1)*
     3T(I,J-1))))
      CALL CONV
      GO TO 55
C
C     INTERNAL ELEMENTS AT BOTTOM OF SYSTEM
C
   54 T(I,J-1)=T(I,J+1)
      H(I,J)=H(I,J)+DR*((TK(I,J)/DX**2.)*(T(I+1,J)+T(I-1,J)+T(I,J+1)+
     1T(I,J-1)-4.*T(I,J))+BB(I,J)/(4.*DX**2.)*((T(I+1,J)**2.+T(I-1,J)
     2**2.+T(I,J+1)**2.+T(I,J-1)**2.)-2.*(T(I+1,J)*T(I-1,J)+T(I,J+1)*
     3T(I,J-1))))
      CALL CONV
   55 CONTINUE
   53 ITYPE=ICASE(LL)
      GO TO(65,64,63,62),ITYPE
```

Lines 365-461

Calculation of the enthalpies for the nodes next to the meniscus and the fictitious nodes on the meniscus are carried out for the different types of intersection.

```
C
C
C     CALCULATION OF THE ENTHALPY IN THE NODE NEXT TO THE MENISCUS PLUS
C     THE ENTHALPY IN THE POINTS WHERE THE MENISCUS INTERSECTS
C     WITH THE GRID: TYPE 1 (2 PTS.)
C
C
   65 H(I,J)=H(I,J)+DR*(2.*TK(I,J)/DX**2.*(T2(LL+1)/(B2(LL+1)*(
     1B2(LL+1)+1.))+T(I,J-1)/(B2(LL+1)+1.)-T(I,J)/B2(LL+1)+T1(LL)/(
     2A1(LL)*(A1(LL)+1.))+T(I+1,J)/(A1(LL)+1)-T(I,J)/A1(LL))+BB(I
     3,J)/DX**2.*(((1.-A1(LL))*T(I,J)/A1(LL)+A1(LL)*T(I+1,J)/(1.+A1
     4(LL))-T1(LL)/(A1(LL)*(A1(LL)+1.)))**2.+(T2(LL+1)/(B2(LL+1)*(B2(
     5LL+1)+1))-B2(LL+1)*T(I,J-1)/(B2(LL+1)+1.)-(1.-B2(LL+1))*T(I,J
     6)/B2(LL+1))**2.))
      CALL CONV
C
C     AND FOR THE TWO FICTITIOUS NODES ON THE MENISCUS
C
      Q1X=1000.*TKSLAG/(XVALUE(LL)+FILM)*(T1(LL)-TSX)
      Q1Y=1000.*TKSLAG/(10.+U+YSLAG-YVALUE(LL))*(T1(LL)-TSY)
      Q1=Q1X+Q1Y
      H1(LL)=H1(LL)+DR*(TK1(LL)/DX**2.*(1/A1(LL)*((1-A1(LL))*T(I,J)/
     1A1(LL)+A1(LL)*T(I+1,J)/(A1(LL)+1)-T1(LL)/(A1(LL)*(A1(LL)+1))-
     2DX*Q1*COS(ALFA1(LL))/TK1(LL))+1./SQRT(A1(LL)**2.+1.)*((2.+B2(LL+
     31))*T(I,J-1)/(B2(LL+1)+1.)-(B2(LL+1)+1.)*T(I,J)/B2(LL+1)+T2(LL+1)
     4/(B2(LL+1)*(B2(LL+1)+1.))-DX*Q1*SIN(ALFA1(LL))/TK1(LL)))+BB1(LL)*
     5(Q1/TK1(LL))**2.)
C
      Q2X=1000.*TKSLAG/(XVALUE(LL+1)+FILM)*(T2(LL+1)-TSX)
      Q2Y=1000.*TKSLAG/(10.+U+YSLAG-YVALUE(LL+1))*(T2(LL+1)-TSY)
      Q2=Q2X+Q2Y
      H2(LL)=0.0
      H2(LL+1)=H2(LL+1)+DR*(TK2(LL+1)/DX**2.*(1/SQRT(B2(LL+1)**2.+1.)*
     1((2.+A1(LL))*T(I+1,J)/(A1(LL)+1.)-(1.+A1(LL))*T(I,J)/A1(LL)+T1
     2(LL)/(A1(LL)*(1.+A1(LL)))-DX*Q2*COS(ALFA2(LL+1))/TK2(LL+1))+1/B2(
     3LL+1)*(B2(LL+1)*T(I,J-1)/(1.+B2(LL+1))+(1.-B2(LL+1))*T(I,J)/B2(LL
     4+1)-T2(LL+1)/(B2(LL+1)*(1.+B2(LL+1)))-DX*Q2*SIN(ALFA2(LL+1))/TK2(
     5LL+1)))+BB2(LL+1)*(Q2/TK2(LL+1))**2.)
      CALL CONV1
      LL=LL+2
      GO TO 59
C
C
```

```
C     CALCULATION OF THE ENTHALPY IN THE NODE NEXT TO THE MENISCUS PLUS
C     THE ENTHALPY IN THE POINT WHERE THE MENISCUS INTERSECTS
C     WITH THE GRID: TYPE 2 (1 PT.)
C
C
   64 H(I,J)=H(I,J)+DR*(TK(I,J)/DX**2.*(2.*(T1(LL)/(A1(LL)*(A1(LL)
     1+1.))+T(I+1,J)/(A1(LL)+1.)-T(I,J)/A1(LL))+T(I,J+1)+T(I,J-1)-2.
     2*T(I,J))+BB(I,J)/DX**2.*(((1.-A1(LL))*T(I,J)/A1(LL)+A1(LL)*T(
     3I+1,J)/(1.+A1(LL))-T1(LL)/(A1(LL)*(1.+A1(LL))))**2.+((T(I,J+1)
     4-T(I,J-1))/2.)**2.))
      CALL CONV
C
C     AND FOR THE FICTITIOUS NODE ON THE MENISCUS
C
      Q1X=1000.*TKSLAG/(XVALUE(LL)+FILM)*(T1(LL)-TSX)
      Q1Y=1000.*TKSLAG/(10.+U+YSLAG-YVALUE(LL))*(T1(LL)-TSY)
      Q1=Q1X+Q1Y
      H2(LL)=0.0
      H1(LL)=H1(LL)+DR*(TK1(LL)/DX**2.*(1/A1(LL)*((1.-A1(LL))*T(I,J)
     1/A1(LL)+A1(LL)*T(I+1,J)/(1.+A1(LL))-T1(LL)/(A1(LL)*(1.+A1(LL))
     2)-DX*Q1*COS(ALFA1(LL))/TK1(LL))+1/SQRT(A1(LL)**2.+1.)*(T(I,J+1
     3)+T(I,J-1)-2.*T(I,J)-(T(I,J+1)-T(I,J-1))/2.-DX*Q1*SIN(ALFA1(LL
     4))/TK1(LL)))+BB1(LL)*(Q1/TK1(LL))**2.)
      CALL CONV1
      LL=LL+1
      GO TO 55
C
C
C     CALCULATION OF THE ENTHALPY IN THE NODE NEXT TO THE MENISCUS PLUS
C     THE ENTHALPY IN THE POINT WHERE THE MENISCUS INTERSECTS
C     WITH THE GRID: TYPE 3 (1 PT.)
C
C
   63 H(I,J)=H(I,J)+DR*(TK(I,J)/DX**2.*(2.*(T2(LL)/(B2(LL)*(B2(LL)+1.
     1))+T(I,J-1)/(B2(LL)+1.)-T(I,J)/B2(LL))+T(I+1,J)+T(I-1,J)-2.*T(I,
     2J))+BB(I,J)/DX**2.*(((T(I+1,J)-T(I-1,J))/2.)**2.+(T2(LL)/(B2(LL)*
     3(B2(LL)+1.))-B2(LL)*T(I,J-1)/(1.+B2(LL))-(1.-B2(LL))*T(I,J)/B2(LL
     4))**2.))
      CALL CONV
C
C     AND FOR THE FICTITIOUS NODE ON THE MENISCUS
C
      Q2X=1000.*TKSLAG/(XVALUE(LL)+FILM)*(T2(LL)-TSX)
      Q2Y=1000.*TKSLAG/(10.+U+YSLAG-YVALUE(LL))*(T2(LL)-TSY)
      Q2=Q2X+Q2Y
      H1(LL)=0.0
      H2(LL)=H2(LL)+DR*(TK2(LL)/DX**2.*(1/SQRT(B2(LL)**2.+1.)*((T(I+1
     1,J)-T(I-1,J))/2.+T(I+1,J)+T(I-1,J)-2.*T(I,J)-DX*Q2*COS(ALFA2(LL
     2))/TK2(LL))+1/B2(LL)*(B2(LL)*T(I,J-1)/(1.+B2(LL))+(1.-B2(LL))*
     3T(I,J)/B2(LL)-T2(LL)/(B2(LL)*(1.+B2(LL)))-DX*Q2*SIN(ALFA2(LL))/
     4TK2(LL)))+BB2(LL)*(Q2/TK2(LL))**2.)
      CALL CONV1
      LL=LL+1
      GO TO 59
```

Lines 462-506

The enthalpy for a node corresponding to a type 4 intersection is calculated (462-484). In lines 488-506, the enthalpies for the nodes located at the mould/metal interface are calculated.

```
C
C
C     CALCULATION OF THE ENTHALPY IN A NODE WHICH INTERSECTS WITH THE
C     MENISCUS: TYPE 4
C
C
   62 QX=1000.*TKSLAG/(XVALUE(LL)+FILM)*(T(I,J)-TSX)
      QY=1000.*TKSLAG/(10.+U+YSLAG-YVALUE(LL))*(T(I,J)-TSY)
      Q=QX+QY
      H2(LL)=0.0
      H1(LL)=H(I,J)+DR*(2.*TK1(LL)/DX**2.*(T(I+1,J)+T(I,J-1)-2.*T(I,J)-
     1DX*Q/TK1(LL)*(COS(ALFA(LL))+SIN(ALFA(LL))))+BB1(LL)*(Q/TK1(LL))**
     22.)
      CALL CONV1
      H(I,J)=H1(LL)
      CALL CONV
      IF(ICASE(LL).EQ.L1)GO TO 3
      IF(ICASE(LL).EQ.L2)GO TO 3
      IF(ICASE(LL).EQ.L3)GO TO 3
      LL=LL+1
      GO TO 59
    3 LL=LL+2
      GO TO 59
C
C     CALCULATION OF THE ENTHALPIES ON THE MOULD/METAL INTERFACE
C
   58 DO 50 J=2,JLIM
      IF(J.EQ.2)GO TO 52
      IF(J.EQ.JLIM)GO TO 51
      QMO=1000.*TKSLAG/FILM*(T(I,J)-TSX)
      H(I,J)=H(I,J)+DR*(TK(I,J)/(DX**2.)*((T(I,J+1)-2.*T(I,J)+T(I,J-1))+
     12.*(T(I+1,J)-DX*QMO/TK(I,J)-T(I,J)))+BB(I,J)/4.*((T(I,J+1)**2.-2.*
     2T(I,J+1)*T(I,J-1)+T(I,J-1)**2.)/DX**2.+(2.*QMO/TK(I,J))**2.))
      CALL CONV
      GO TO 50
C
C     THE ELEMENT AT THE BOTTOM CORNER OF THE SYSTEM
C
   52 QMO=1000.*TKSLAG/FILM*(T(I,J)-TSX)
      T(I,J-1)=T(I,J+1)
      H(I,J)=H(I,J)+DR*(TK(I,J)/(DX**2.)*((T(I,J+1)-2.*T(I,J)+T(I,J-1))+
     12.*(T(I+1,J)-DX*QMO/TK(I,J)-T(I,J)))+BB(I,J)/4.*((T(I,J+1)**2.-2.*
     2T(I,J+1)*T(I,J-1)+T(I,J-1)**2.)/DX**2.+(2.*QMO/TK(I,J))**2.))
      CALL CONV
      GO TO 50
```

Lines 507-542

The node at the triple-point mould/metal/slag is treated (511-518). Furthermore, the enthalpies of the nodes located on the right-hand boundary of the system are calculated (522-542).

```
C
C     THE ELEMENT WHERE THE MENISCUS AND THE MOULD WALL MEET,I.E.THE
C     CORNER MOULD/METAL/SLAG.
C
   51 QMO=1000.*TKSLAG/FILM*(T(I,J)-TSX)
      QY=1000.*TKSLAG/(U+YSLAG)*(T(I,J)-TSY)
      H(I,J)=H(I,J)+DR*(2.*(TK(I,J)/(DX**2.))*(T(I,J-1)+T(I+1,J)-2.*T(I,
     1J)-(DX/TK(I,J))*(QY+QMO))+(BB(I,J)/TK(I,J)**2.)*(QY**2.+QMO**2
     2.))
      CALL CONV
      GO TO 59
   50 CONTINUE
C
C     CALCULATION OF ENTHALPIES ON THE RIGHT-HAND BOUNDARY OF THE SYSTEM.
C
   57 DO 56 J=2,JLIM
      T(I+1,J)=T(I,J)
      IF(J.EQ.2)GO TO 60
      IF(J.EQ.JLIM)GO TO 61
      H(I,J)=H(I,J)+DR*((TK(I,J)/(DX**2.))*(T(I+1,J)+T(I-1,J)+T(I,J+1)+
     1T(I,J-1)-4.*T(I,J))+BB(I,J)/(4.*DX**2.)*((T(I+1,J)**2.+T(I-1,J)**
     22.+T(I,J+1)**2.+T(I,J-1)**2.)-2.*(T(I+1,J)*T(I-1,J)+T(I,J+1)*T(I,
     3J-1))))
      CALL CONV
      GO TO 56
C
C     CALCULATION OF THE ENTHALPY OF THE ELEMENT AT THE BOTTOM RIGHT-HAND
C     CORNER OF THE SYSTEM.
C
   60 T(I,J-1)=T(I,J+1)
      H(I,J)=H(I,J)+DR*((TK(I,J)/(DX**2.))*(T(I+1,J)+T(I-1,J)+T(I,J+1)+
     1T(I,J-1)-4.*T(I,J))+BB(I,J)/(4.*DX**2.)*((T(I+1,J)**2.+T(I-1,J)**
     22.+T(I,J+1)**2.+T(I,J-1)**2.)-2.*(T(I+1,J)*T(I-1,J)+T(I,J+1)*T(I,
     3J-1))))
      CALL CONV
      GO TO 56
```

Lines 543-640

The node located at the upper right-hand corner of the system is treated, depending on type of intersection (543-640).

```
C
C     CALCULATION OF THE ENTHALPY OF THE UPPER RIGHT-HAND CORNER OF THE
C     SYSTEM.
C
   61 LL=NTOTAL
      IF(ICASE(LL-1).EQ.1)GO TO 66
      ITYPE=ICASE(LL)
      GO TO(66,67,69,68),ITYPE
C
C     IF TYPE 3
C
   69 H(I,J)=H(I,J)+DR*(TK(I,J)/DX**2.*(2.*(T2(LL)/(B2(LL)*(B2(LL)+1)
     1+T(I,J-1)/(B2(LL)+1)-T(I,J)/B2(LL))+T(I+1,J)+T(I-1,J)-2.*T(I,J))
     2+BB(I,J)/DX**2.*(((T(I+1,J)-T(I-1,J))/2.)**2.+(T2(LL)/(B2(LL)*(
     3B2(LL)+1))-B2(LL)*T(I,J-1)/(1+B2(LL))-(1-B2(LL))*T(I,J)/B2(LL))
     4**2.))
      CALL CONV
      Q2X=1000.*TKSLAG/(XVALUE(LL)+FILM)*(T2(LL)-TSX)
      Q2Y=1000.*TKSLAG/(10.+U+YSLAG-YVALUE(LL))*(T2(LL)-TSY)
      Q2=Q2X+Q2Y
      H1(LL)=0.0
      H2(LL)=H2(LL)+DR*(TK2(LL)/DX**2.*(1/SQRT(B2(LL)**2.+1.)*((T(I+1,J)
     1-T(I-1,J))/2.+T(I+1,J)+T(I-1,J)-2*T(I,J)-DX*Q2*COS(ALFA2(LL))/TK2
     2(LL))+1/B2(LL)*(B2(LL)*T(I,J-1)/(1+B2(LL))+(1-B2(LL))*T(I,J)/B2(
     3LL)-T2(LL)/(B2(LL)*(1+B2(LL)))-DX*Q2*SIN(ALFA2(LL))/TK2(LL)))+
     4BB2(LL)*(Q2/TK2(LL))**2.)
      CALL CONV1
      GO TO 71
C
C     IF TYPE 4
C
   68 QX=1000.*TKSLAG/(XVALUE(LL)+FILM)*(T(I,J)-TSX)
      QY=1000.*TKSLAG/(10.+U+YSLAG-YVALUE(LL))*(T(I,J)-TSY)
      Q=QX+QY
      H2(LL)=0.0
      H1(LL)=H(I,J)+DR*(2.*TK1(LL)/DX**2.*(T(I+1,J)+T(I,J-1)-2.*T(I,
     1J)-DX*Q/TK1(LL)*(COS(ALFA(LL))+SIN(ALFA(LL))))+BB1(LL)*(Q/TK1(
     2LL))**2.)
      CALL CONV1
      H(I,J)=H1(LL)
      CALL CONV
      GO TO 71
```

```
C
C     IF TYPE 1
C
   66 LL=NTOTAL-1
      H(I,J)=H(I,J)+DR*(2*TK(I,J)/DX**2.*(T2(LL+1)/(B2(LL+1)*(B2(LL
     1+1)+1.))+T(I,J-1)/(B2(LL+1)+1.)-T(I,J)/B2(LL+1)+T1(LL)/(A1(LL)
     2*(A1(LL)+1.))+T(I+1,J)/(A1(LL)+1)-T(I,J)/A1(LL))+BB(I,J)/DX**2
     3.*(((1.-A1(LL))*T(I,J)/A1(LL)+A1(LL)*T(I+1,J)/(1.+A1(LL))-T1(L
     4L)/(A1(LL)*(A1(LL)+1.)))**2.+(T2(LL+1)/(B2(LL+1)*(B2(LL+1)+1.)
     5)-B2(LL+1)*T(I,J-1)/(1.+B2(LL+1))-(1.-B2(LL+1))*T(I,J)/B2(LL+1
     6))**2.))
      CALL CONV
      Q1X=1000.*TKSLAG/(XVALUE(LL)+FILM)*(T1(LL)-TSX)
      Q1Y=1000.*TKSLAG/(10.+U+YSLAG-YVALUE(LL))*(T1(LL)-TSY)
      Q1=Q1X+Q1Y
      H1(LL)=H1(LL)+DR*(TK1(LL)/DX**2.*(1./A1(LL)*((1-A1(LL))*T(I,J)/
     1A1(LL)+A1(LL)*T(I+1,J)/(1.+A1(LL))-T1(LL)/(A1(LL)*(1.+A1(LL)))-
     2DX*Q1*COS(ALFA1(LL))/TK1(LL))+1/SQRT(A1(LL)**2+1.)*((2.+B2(LL+1))
     3*T(I,J-1)/(B2(LL+1)+1)-(B2(LL+1)+1.)*T(I,J)/B2(LL+1)+T2(LL+1)/
     4(B2(LL+1)*(B2(LL+1)+1.))-DX*Q1*SIN(ALFA1(LL))/TK1(LL)))+BB1(LL)*
     5(Q1/TK1(LL))**2.)
C
      Q2X=1000.*TKSLAG/(XVALUE(LL+1)+FILM)*(T2(LL+1)-TSX)
      Q2Y=1000.*TKSLAG/(10.+U+YSLAG-YVALUE(LL+1))*(T2(LL+1)-TSY)
      Q2=Q2X+Q2Y
      H2(LL)=0.0
      H2(LL+1)=H2(LL+1)+DR*(TK2(LL+1)/DX**2.*(1./SQRT(B2(LL+1)**2.+1.)
     1*((2.+A1(LL))*T(I+1,J)/(A1(LL)+1.)-(1.+A1(LL))*T(I,J)/A1(LL)+
     2T1(LL)/(A1(LL)*(1.+A1(LL)))-DX*Q2*COS(ALFA2(LL+1))/TK2(LL+1))+
     31/B2(LL+1)*(B2(LL+1)*T(I,J-1)/(1.+B2(LL+1))+(1.-B2(LL+1))*T(I,J)
     4/B2(LL+1)-T2(LL+1)/(B2(LL+1)*(1.+B2(LL+1)))-DX*Q2*SIN(ALFA2(LL+
     51))/TK2(LL+1)))+BB2(LL+1)*(Q2/TK2(LL+1))**2.)
      CALL CONV1
      GO TO 71
C
C     IF TYPE 2
C
   67 H(I,J)=H(I,J)+DR*(TK(I,J)/DX**2.*(2.*(T1(LL)/(A1(LL)*(A1(LL)
     1+1.))+T(I+1,J)/(A1(LL)+1)-T(I,J)/A1(LL))+T(I,J+1)+T(I,J-1)-2.*
     2T(I,J))+BB(I,J)/DX**2.*(((1.-A1(LL))*T(I,J)/A1(LL)+A1(LL)*
     3T(I+1,J)/(1.+A1(LL))-T1(LL)/(A1(LL)*(1.+A1(LL))))**2.+((T(I,J+1)
     4-T(I,J-1))/2.)**2.))
      CALL CONV
      Q1X=1000.*TKSLAG/(XVALUE(LL)+FILM)*(T1(LL)-TSX)
      Q1Y=1000.*TKSLAG/(10.+U+YSLAG-YVALUE(LL))*(T1(LL)-TSY)
      Q1=Q1X+Q1Y
      H2(LL)=0.0
      H1(LL)=H1(LL)+DR*(TK1(LL)/DX**2.*(1./A1(LL)*((1.-A1(LL))*T(I,J)
     1/A1(LL)+A1(LL)*T(I+1,J)/(1.+A1(LL))-T1(LL)/(A1(LL)*(1.+A1(LL)))
     2-DX*Q1*COS(ALFA1(LL))/TK1(LL))+1/SQRT(A1(LL)**2.+1.)*(T(I,J+1)
     3+T(I,J-1)-2.*T(I,J)-(T(I,J+1)-T(I,J-1))/2.-DX*Q1*SIN(ALFA1(LL))
     4/TK1(LL)))+BB1(LL)*(Q1/TK1(LL))**2.)
      CALL CONV1
      GO TO 71
   56 CONTINUE
   59 CONTINUE
```

Lines 641-671

The thermal and 'fraction-solid' fields are printed and a plot is produced. (Print-outs and plots are produced after half the healing time as well as at the end of the calculations.)

```
   71 CCC=CCC+1
      IF((CCC*DT).LT.(HEALT/2.))GO TO 2
C
      WRITE(2,1700)TIME
 1700 FORMAT(1H ,/,20X,'TEMPERATURE DISTRIBUTION AT TIME=',F7.3)
      DO 100 J=2,MAY
      JA=MAY+2-J
      WRITE(2,1800)(T(I,JA),I=2,20)
 1800 FORMAT(1H ,19(1X,F5.0))
  100 CONTINUE
      WRITE(2,2700)TIME
 2700 FORMAT(1H ,/,10X,'SURFACE TEMP.AND FS AT TIME=',F7.3)
      WRITE(2,2800)(LL,T1(LL),T2(LL),FS1(LL),FS2(LL),LL=2,NTOTAL)
 2800 FORMAT(1H ,I2,3X,F5.0,5X,F5.0,6X,F5.3,3X,F5.3)
      WRITE(2,2500)TIME
 2500 FORMAT(1H ,/,10X,'FRACTION SOLID DISTRIBUTION AT TIME=',F7.3)
      DO 120 J=2,MAY
      JA=MAY+2-J
      WRITE(2,2600)(FS(I,JA),I=2,20)
 2600 FORMAT(1H ,19(1X,F4.2))
  120 CONTINUE
C
C
      CCC=0.0
      CALL RITA
    2 IF(TIME.LT.HEALT)GO TO 1
      WRITE(2,3000
 3000 FORMAT(1H ,'ZIS IS ZE END')
      CALL GREND
      STOP
      END
```

Lines 672-711

First subroutine, in which fraction liquid is calculated and a conversion from enthalpy to temperature is carried out for the internal nodes. Also, a new thermal conductivity is calculated (672-711).

```
C------------------------------------------------------------------
C
C**** SUBROUTINE FOR CONVERTING H INTO T AND CALC. OF FRACTION ******
C     SOLID AND LIQUID PLUS NEW TK'S ETC.(GRID POINTS)
C
      SUBROUTINE CONV
      COMMON/A/H(45,101),T(45,101),TK(45,101),FL(45,101),FS(45,101),
     1CP,TA,TFE,TL,TS,FSS2,I,J,HFE,HLIQ,HSOL,HF,PK,BB(45,101),HT(5),
     2A,B,C,FILM,YSLAG,TKSLAG
C
      IF(H(I,J).GE.HLIQ)GO TO 510
      IF(H(I,J).LE.HSOL)GO TO 520
      FFLO=FL(I,J)
  666 GFL=(HFE-HF-H(I,J)+FFLO*HF)/(HFE-HLIQ)-FFLO**(PK-1.)
      DGFL=HF/(HFE-HLIQ)-(PK-1.)*FFLO**(PK-2.)
      FFL1=FFLO-GFL/DGFL
      FFLO=FFL1
      E=GFL/DGFL
      DIV=ABS(E)
      IF(DIV.GT.0.001)GO TO 666
      FL(I,J)=FFLO
      IF(FL(I,J).LE.(1.0-FSS2))GO TO 520
      T(I,J)=(H(I,J)-FL(I,J)*HF)/CP+TA
      FS(I,J)=1.-FL(I,J)
      TK(I,J)=(1.+(C-1.)*FL(I,J)**2.)*(A+(T(I,J)+273.15)*B)
      BB(I,J)=(1.+(C-1.)*FL(I,J)**2.)*B
      GO TO 500
  510 T(I,J)=(H(I,J)-HF)/CP+TA
      FL(I,J)=1.0
      FS(I,J)=0.0
      TK(I,J)=C*(A+(T(I,J)+273.15)*B)
      BB(I,J)=C*B
      GO TO 500
  520 T(I,J)=H(I,J)/CP+TA
      FL(I,J)=0.0
      FS(I,J)=1.0
      TK(I,J)=A+(T(I,J)+273.15)*B
      BB(I,J)=B
  500 RETURN
      END
```

Lines 712-903

Enthalpy is converted to temperature, fraction liquid and thermal conductivity is calculated for the fictitious nodes on the curved boundary (712-903).

```
C-----------------------------------------------------------------------
C
C**** SUBROUTINE DOING THE SAME AS CONV,EXCEPT THAT IT IS DONE ******
C     FOR THE FICTITIOUS NODES.
C
      SUBROUTINE CONV1
      COMMON/A0/H1(300),H2(300),T1(300),T2(300),TK1(300),TK2(300),
     1FL1(300),FL2(300),FS1(300),FS2(300),A1(300),B2(300),ALFA1(300),
     2ALFA2(300),ALFA(300),BB1(300),BB2(300),L,K,KPR,LL
      COMMON/A/H(45,101),T(45,101),TK(45,101),FL(45,101),FS(45,101),
     1CP,TA,TFE,TL,TS,FSS2,I,J,HFE,HLIQ,HSOL,HF,PK,BB(45,101),HT(5),
     2A,B,C,FILM,YSLAG,TKSLAG
      COMMON/A4/ICASE(300),XVALUE(300),YVALUE(300)
C
      ITYPE=ICASE(LL)
      GO TO(610,611,612,613),ITYPE
C
  610 IF(H1(LL).GE.HLIQ)GO TO 615
      IF(H1(LL).LE.HSOL)GO TO 616
      FFLO=FL1(LL)
  667 GFL=(HFE-HF-H1(LL)+FFLO*HF)/(HFE-HLIQ)-FFLO**(PK-1.)
      DGFL=HF/(HFE-HLIQ)-(PK-1.)*FFLO**(PK-2.)
      FFL1=FFLO-GFL/DGFL
      FFLO=FFL1
      E=GFL/DGFL
      DIV=ABS(E)
      IF(DIV.GT.0.001)GO TO 667
      FL1(LL)=FFLO
      FL1(LL+1)=0.0
      IF(FL1(LL).LE.(1.0-FSS2))GO TO 616
      T1(LL)=(H1(LL)-FL1(LL)*HF)/CP+TA
      T1(LL+1)=0.0
      FS1(LL)=1.-FL1(LL)
      FS1(LL+1)=0.0
      TK1(LL)=(1.+(C-1.)*FL1(LL)**2.)*(A+(T1(LL)+273.15)*B)
      TK1(LL+1)=0.0
      BB1(LL)=(1.+(C-1.)*FL1(LL)**2.)*B
      BB1(LL+1)=0.0
      GO TO 618
  615 T1(LL)=(H1(LL)-HF)/CP+TA
      T1(LL+1)=0.0
      FL1(LL)=1.0
      FL1(LL+1)=0.0
      FS1(LL)=0.0
      FS1(LL+1)=0.0
      TK1(LL)=C*(A+(T1(LL)+273.15)*B)
      TK1(LL+1)=0.0
      BB1(LL)=C*B
      BB1(LL+1)=0.0
      GO TO 618
```

```
  616 T1(LL)=H1(LL)/CP+TA
      T1(LL+1)=0.0
      FL1(LL)=0.0
      FL1(LL+1)=0.0
      FS1(LL)=1.0
      FS1(LL+1)=0.0
      TK1(LL)=A+(T1(LL)+273.15)*B
      TK1(LL+1)=0.0
      BB1(LL)=B
      BB1(LL+1)=0.0
  618 IF(H2(LL+1).GE.HLIQ)GO TO 617
      IF(H2(LL+1).LE.HSOL)GO TO 619
      FFLO=FL2(LL+1)
  668 GFL=(HFE-HF-H2(LL+1)+FFLO*HF)/(HFE-HLIQ)-FFLO**(PK-1.)
      DGFL=HF/(HFE-HLIQ)-(PK-1.)*FFLO**(PK-2.)
      FFL1=FFLO-GFL/DGFL
      FFLO=FFL1
      E=GFL/DGFL
      DIV=ABS(E)
      IF(DIV.GT.0.001)GO TO 668
      FL2(LL+1)=FFLO
      FL2(LL)=0.0
      IF(FL2(LL+1).LE.(1.0-FSS2))GO TO 619
      T2(LL+1)=(H2(LL+1)-FL2(LL+1)*HF)/CP+TA
      T2(LL)=0.0
      FS2(LL+1)=1.-FL2(LL+1)
      FS2(LL)=0.0
      TK2(LL+1)=(1.+(C-1.)*FL2(LL+1)**2.)*(A+(T2(LL+1)+273.15)*B)
      TK2(LL)=0.0
      BB2(LL+1)=(1.+(C-1.)*FL2(LL+1)**2.)*B
      BB2(LL)=0.0
      GO TO 650
  617 T2(LL+1)=(H2(LL+1)-HF)/CP+TA
      T2(LL)=0.0
      FL2(LL+1)=1.0
      FL2(LL)=0.0
      FS2(LL+1)=0.0
      FS2(LL)=0.0
      TK2(LL+1)=C*(A+(T2(LL+1)+273.15)*B)
      TK2(LL)=0.0
      BB2(LL+1)=C*B
      BB2(LL)=0.0
      GO TO 650
  619 T2(LL+1)=H2(LL+1)/CP+TA
      T2(LL)=0.0
      FL2(LL+1)=0.0
      FL2(LL)=0.0
      FS2(LL+1)=1.0
      FS2(LL)=0.0
      TK2(LL+1)=A+(T2(LL+1)+273.15)*B
      TK2(LL)=0.0
      BB2(LL+1)=B
      BB2(LL)=0.0
      GO TO 650
```

```
611 IF(H1(LL).GE.HLIQ)GO TO 624
    IF(H1(LL).LE.HSOL)GO TO 625
    FFLO=FL1(LL)
669 GFL=(HFE-HF-H1(LL)+FFLO*HF)/(HFE-HLIQ)-FFLO**(PK-1.)
    DGFL=HF/(HFE-HLIQ)-(PK-1.)*FFLO**(PK-2.)
    FFL1=FFLO-GFL/DGFL
    FFLO=FFL1
    E=GFL/DGFL
    DIV=ABS(E)
    IF(DIV.GT.0.001)GO TO 669
    FL1(LL)=FFLO
    IF(FL1(LL).LE.(1.0-FSS2))GO TO 625
    T1(LL)=(H1(LL)-FL1(LL)*HF)/CP+TA
    FS1(LL)=1.-FL1(LL)
    TK1(LL)=(1.+(C-1.)*FL1(LL)**2.)*(A+(T1(LL)+273.15)*B)
    BB1(LL)=(1.+(C-1.)*FL1(LL)**2.)*B
    GO TO 650
624 T1(LL)=(H1(LL)-HF)/CP+TA
    FL1(LL)=1.0
    FS1(LL)=0.0
    TK1(LL)=C*(A+(T1(LL)+273.15)*B)
    BB1(LL)=C*B
    GO TO 650
625 T1(LL)=H1(LL)/CP+TA
    FL1(LL)=0.0
    FS1(LL)=1.0
    TK1(LL)=A+(T1(LL)+273.15)*B
    BB1(LL)=B
    GO TO 650
612 IF(H2(LL).GE.HLIQ)GO TO 634
    IF(H2(LL).LE.HSOL)GO TO 635
    FFLO=FL2(LL)
670 GFL=(HFE-HF-H2(LL)+FFLO*HF)/(HFE-HLIQ)-FFLO**(PK-1.)
    DGFL=HF/(HFE-HLIQ)-(PK-1.)*FFLO**(PK-2.)
    FFL1=FFLO-GFL/DGFL
    FFLO=FFL1
    E=GFL/DGFL
    DIV=ABS(E)
    IF(DIV.GT.0.001)GO TO 670
    FL2(LL)=FFLO
    IF(FL2(LL).LE.(1.0-FSS2))GO TO 635
    T2(LL)=(H2(LL)-FL2(LL)*HF)/CP+TA
    FS2(LL)=1.-FL2(LL)
    TK2(LL)=(1.+(C-1.)*FL2(LL)**2.)*(A+(T2(LL)+273.15)*B)
    BB2(LL)=(1.+(C-1.)*FL2(LL)**2.)*B
    GO TO 650
634 T2(LL)=(H2(LL)-HF)/CP+TA
    FL2(LL)=1.0
    FS2(LL)=0.0
    TK2(LL)=C*(A+(T2(LL)+273.15)*B)
    BB2(LL)=C*B
    GO TO 650
```

```
  635 T2(LL)=H2(LL)/CP+TA
      FL2(LL)=0.0
      FS2(LL)=1.0
      TK2(LL)=A+(T2(LL)+273.15)*B
      BB2(LL)=B
      GO TO 650
  613 IF(H1(LL).GE.HLIQ)GO TO 636
      IF(H1(LL).LE.HSOL)GO TO 637
      FFLO=FL1(LL)
  671 GFL=(HFE-HF-H1(LL)+FFLO*HF)/(HFE-HLIQ)-FFLO**(PK-1.)
      DGFL=HF/(HFE-HLIQ)-(PK-1.)*FFLO**(PK-2.)
      FFL1=FFLO-GFL/DGFL
      FFLO=FFL1
      E=GFL/DGFL
      DIV=ABS(E)
      IF(DIV.GT.0.001)GO TO 671
      FL1(LL)=FFLO
      IF(FL1(LL).LE.(1.0-FSS2))GO TO 637
      T1(LL)=(H1(LL)-FL1(LL)*HF)/CP+TA
      FS1(LL)=1.-FL1(LL)
      TK1(LL)=(1.+(C-1.)*FL1(LL)**2.)*(A+(T1(LL)+273.15)*B)
      BB1(LL)=(1.+(C-1.)*FL1(LL)**2.)*B
      GO TO 650
  636 T1(LL)=(H1(LL)-HF)/CP+TA
      FL1(LL)=1.0
      FS1(LL)=0.0
      TK1(LL)=C*(A+(T1(LL)+273.15)*B)
      BB1(LL)=C*B
      GO TO 650
  637 T1(LL)=(H1(LL)/CP)+TA
      FL1(LL)=0.0
      FS1(LL)=1.0
      TK1(LL)=A+(T1(LL)+273.15)*B
      BB1(LL)=B
  650 RETURN
      END
```

Lines 904-1009

Iso-f_s curves are plotted (903-998). Also, the shape of the meniscus is given as an external function (1004-1009).

```
C-------------------------------------------------------------------
C
C**** SUBROUTINE FOR THE PLOTTING OF THE MENISCUS,FRACTION SOLID ****
C     DISTRIBUTION AND SOME OF THE USED DATA.
C
      SUBROUTINE RITA
      COMMON/A2/HMO,TIME,DELT,KLOWX,KHIGHX,KLOWY,KHIGHY,XMAP,YMAP,DX,
     1GDX,DT
      COMMON/A0/H1(300),H2(300),T1(300),T2(300),TK1(300),TK2(300),
     1FL1(300),FL2(300),FS1(300),FS2(300),A1(300),B2(300),ALFA1(300),
     2ALFA2(300),ALFA(300),BB1(300),BB2(300),L,K,KPR,LL
      COMMON/A/H(45,101),T(45,101),TK(45,101),FL(45,101),FS(45,101),
     1CP,TA,TFE,TL,TS,FSS2,I,J,HFE,HLIQ,HSOL,HF,PK,BB(45,101),HT(5),
     2A,B,C,FILM,YSLAG,TKSLAG
C
C     DEF. OF SPACE
      CALL CSPACE(0.01,0.99,0.15,0.85)
      CALL PSPACE(0.14,0.91,0.28,0.77)
C     AXIS ANOTATION
      CALL GPINFO('PEN NUMBER 7L-6 IN HOLDER NUMBER 1,BLACK INK',44)
      CALL INKPEN(1)
      CALL CTRSET(0)
      CALL CTRMAG(12)
      CALL POSITN(0.10,0.23)
      CALL TYPECS('FRACTION SOLID DISTRIBUTION IN THE MENISCUS AREA',48)
C     THE X-AXIS
      CALL CTRMAG(10)
      CALL POSITN(0.20,0.28)
      CALL TYPECS('DISTANCE FROM MOULD WALL,(MM)',30)
C     THE Y-AXIS
      CALL POSITN(0.1,0.37)
      CALL CTRORI(1.0)
      CALL TYPECS('DISTANCE ALONG MOULD WALL,(MM)',31)
      CALL CTRORI(0.0)
      CALL POSITN(0.6,0.53)
      CALL TYPECS('CURVED BOUNDARY',15)
      CALL POSITN(0.6,0.5)
      CALL TYPECS('S',1)
      CALL CTRSET(2)
      CALL TYPECS('TAINLESS ',9)
      CALL CTRSET(1)
      CALL TYPECS('S',1)
      CALL CTRSET(2)
      CALL TYPECS('TEEL',4)
      CALL POSITN(0.6,0.48)
      CALL TYPECS('WITH K=',7)
      CALL TYPENF(PK,2)
      CALL POSITN(0.6,0.46)
      CALL TYPECS('KSLAG USED=',11)
      CALL TYPENF(TKSLAG,5)
      CALL POSITN(0.6,0.44)
      CALL CTRSET(1)
      CALL TYPECS('T',1)
      CALL CTRSET(2)
```

```
      CALL TYPECS('IME  =',6)
      CALL TYPENF(TIME,2)
      CALL POSITN(0.58,0.42)
      CALL CTRSET(1)
      CALL TYPECS('S',1)
      CALL CTRSET(2)
      CALL TYPECS('UPERHEAT=',9)
      CALL TYPENF(DELT,1)
      CALL POSITN(0.58,0.40)
      CALL CTRSET(1)
      CALL TYPECS('G',1)
      CALL CTRSET(2)
      CALL TYPECS('RID SIZE=',9)
      CALL TYPENF(GDX,2)
      CALL POSITN(0.57,0.38)
      CALL CTRSET(1)
      CALL TYPECS('T',1)
      CALL CTRSET(2)
      CALL TYPECS('IME INCR.=',10)
      CALL TYPENF(DT,5)
      CALL POSITN(0.6,0.36)
      CALL TYPECS('FILM=',5)
      CALL TYPENF(FILM,3)
      CALL POSITN(0.57,0.34)
      CALL TYPECS('SLAG LAYER=',11)
      CALL TYPENF(YSLAG,3)
      CALL CTRSET(0)
C     PLOTTING OF THE MENISCUS AND FRACTION SOLID
      CALL MAP(0.0,XMAP,0.0,YMAP)
      CALL PSPACE(0.0,0.992,0.15,0.85)
      CALL BORDER
      CALL PSPACE(0.16,0.494,0.32,0.659)
      CALL BORDER
      CALL AXESSI(2.0,4.0)
      EXTERNAL YVAL
      CALL GRAPHF(YVAL)
      CALL CONTRA(FS,KLOWX,KHIGHX,45,KLOWY,KHIGHY,101,HT,2,3)
      CALL MAP(0.14,0.91,0.28,0.77)
      CALL FRAME
      RETURN
      END
C-----------------------------------------------------------------
C
C*** FUNCTION FOR THE SHAPE OF THE MENISCUS,HERE USED IN AN *********
C     EXTERNAL MODE.
C
       FUNCTION YVAL(X)
       COMMON/A3/U,V,Z
       YVAL=10.+U*(1.-EXP(-V*X))**Z
       RETURN
       END
       FINISH
```

APPENDIX IV

Finite-Difference Equations Used for the Prediction of Fraction δ-ferrite (after Tanzilli and Heckel[212]).

(i) Internal node in the δ-ferrite.

$$\frac{C_i^{t+1} - C_i^t}{\Delta t} = \frac{i}{\frac{\xi}{2}} \frac{(C_{i+1}^t - C_{i-1}^t)}{2} \frac{d(\xi/2)^{t+1}}{dt}$$

$$+ D^{\delta} n^2 \frac{(C_{i-1}^t - 2C_i^t + C_{i+1}^t)}{\left[\frac{\xi}{2}\right]^2} + D^{\delta} n^2 \frac{(C_{i+1}^t - C_{i-1}^t)}{2i\left[\frac{\xi}{2}\right]^2} \quad \ldots(\text{IV.1})$$

where n is the node at the δ/γ-interface (i.e. at a distance ξ/2 from the centre of the ferrite).

(ii) Internal node in the austenite.

$$\frac{C_i^{t+1} - C_i^t}{\Delta t} = \frac{N - i}{\frac{\lambda_2}{2} - \frac{\xi}{2}} \frac{(C_{i+1}^t - C_{i-1}^t)}{2} \frac{d(\xi/2)^{t+1}}{dt}$$

$$+ D^{\gamma}(N - n)^2 \frac{(C_{i-1}^t - 2C_i^t + C_{i+1}^t)}{\left[\frac{\lambda_2}{2} - \frac{\xi}{2}\right]^2}$$

$$+ \frac{D^{\gamma}}{\left[\frac{\xi}{2} + \frac{(i - n)}{(N - n)}\left[\frac{\lambda_2}{2} - \frac{\xi}{2}\right]\right]} \frac{(N - n)}{2} \frac{(C_{i+1}^t - C_{i-1}^t)}{\left[\frac{\lambda_2}{2} - \frac{\xi}{2}\right]} \quad \ldots(\text{IV.2})$$

where N is the node at the outer boundary of the austenite (i.e. at a distance $\frac{\lambda_2}{2}$ from the centre).

(iii) Interface mass balance.

$$\frac{(\xi/2)^{t+1} - (\xi/2)^{t}}{\Delta t} = \frac{1}{(C_{\delta\gamma} - C_{\gamma\delta})}\left[D^{\gamma}\frac{(N-n)}{2}\,\frac{(-C^{t}_{n+2} + 4C^{t}_{n+1} - 3C^{t}_{\gamma\delta})}{\left[\frac{\lambda_2}{2} - \frac{\xi}{2}\right]} - D^{\delta}\frac{n}{2}\,\frac{(C^{t}_{n-2} - 4C^{t}_{n-1} + 3C^{t}_{\delta\gamma})}{\frac{\xi}{2}}\right] \qquad \text{...(IV.3)}$$

(iv) Boundary condition at the centre of the δ-ferrite.

$$\frac{C_0^{t+1} - C_0^{t}}{\Delta t} = 4D^{\delta}n^2\,\frac{C_1 - C_0}{\left[\frac{\xi}{2}\right]^2} \qquad \text{...(IV.4)}$$

APPENDIX V

Line-by-line description of the Computer Program for Heat Flow and Prediction of Fraction δ-ferrite during Continuous Casting

Lines 1-55

A program description is given, together with the input- and output-channels (1-9). The arrays and matrices used in the program are dimensioned (19-24). Notations and units used for the different parameters are given (29-47). The input-parameters are read (49-55).

```
      PROGRAM(CONCA)
       INPUT 1=CR0
      OUTPUT 2=LP0
      OUTPUT 3=LP1
      OUTPUT 4=LP2
      TRACE 0
      END
      NOLIST
      MASTER CONCAST
C +++++++++++++++++++++++++++++++++++++++++++++++++++++++++++++++++++++
C +   COMPUTER PROGRAM FOR THE MODELLING OF CONTINUOUS CASTING OF     +
C +   STAINLESS STEEL (18CR/10NI). A ONE DIMENSIONAL HEAT TRANSFER   +
C +   MODEL IS UTILIZED, BASED ON THE MIZIKAR MODEL MODIFIED BY      +
C +   Y.K.SHIN. THE PREDICTED THERMAL HISTORY PROVIDES THE BASIS     +
C +   FOR A SECOND FINITE DIFFERENCE MODEL PREDICTING THE VARIATION  +
C +   OF DELTA-FERRITE CONTENT ACROSS THE SLAB. THIS IS BASED ON A   +
C +   DIFFUSION MODEL BY TANZILLI AND HECKEL.                        +
C +++++++++++++++++++++++++++++++++++++++++++++++++++++++++++++++++++++
      DIMENSION H(21),HZ(21),T(21),TZ(21),FK(21),Y(15),RL(15),B(21),
     CVAR(5),FL(21),TO(21),X(21),X1(50),TITLE(5),GR(21),T1(21),CS(21)
     C,GRCHECK(21),CCO(21),DAS2(21),G(21),G1(21),XAI(21),CC(21,30),
     CCHECK(21),GRCHECK2(21),GRTIME(21),TT(50),TZT(50),HT(50),HZT(50),
     CFKT(50),BT(50),FLT(50),TOT(50),T1T(50),TBEND(21),GBEND(21)
      DATA NUMDATA,HLF,N,D,C,W,DZZ/3,275.0,12,7900.0,0.750,0.11,0.9/
C
C          NOTATIONS AND UNITS FOR HEAT FLOW PART.
C          ======================================
C
C     TIN: POURING TEMP,    TM: MELTING TEMP.OF SOLVENT,
C     TL: LIQUIDUS TEMP,    TS2: "SOLIDUS" TEMP.,
C     TW: SPRAY WATER TEMP,    TA: AIR TEMP,
C     HT(K): HEAT TRANSFER COEFF OF SPRAY ZONE (KW/M2 K),
C     RL(K): ACCUMULATED LENGTH OF SEGMENTS (M),  D: DENSITY (KG/M3),
C     C: SPECIFIC HEAT (KJ/KG K),   W: HALF THICKNESS OF SLAB (M),
C     V: CASTING SPEED (M/SEC),   DZZ: TIME INCREMENT (SEC),
C     HLF: LATENT HEAT OF FUSION (KJ/KG),  N: MESH NUMBER,
C     FK: THERMAL CONDUCTIVITY (KW/M K),
C     FL:CALCULATED FRACTION LIQUID, FLSTOP:FL DEFINING SOLIDUS TEMP.,
C     H,HZ:ENTHALPY OF TIME Z AND Z+DZ RESPECTIVELY(KJ/KG)
C     Q:HEAT FLUX FROM STRAND SURFACE(KW/M2)
C     PK:DISTRIBUTION COEFF., FLIQ:CONVECTION FACTOR IN THE LIQUID,
C     FILM:THICKNESS OF SLAG-FILM BETWEEN MOULD AND STRAND (M),
C     CSLAG:THERM. COND. OF SLAG (KW/M,K), TMOULD:MOULD TEMP. (WHEN
C     SLAG-FILM IS CONSIDERED), DIST:DISTANCE BELOW MENISCUS WHERE
C     BRIMACOMBE'S Q=U-V(SQRT TIME) IS USED IN THE CASE OF SLAG-FILM
C     GR(I):CALCULATED COOLING RATE (DEG/S),
C     DAS2(I):CALCULATED SEC. DENDRITE ARMSPACINGS (MICRONS)
C
      READ(1,1100)VAR
      WRITE(3,3000)VAR
      READ(1,1200)TIN,TM,TL,TW,TA,PK,FLSTOP
      READ(1,1200)HT1,HT2,HT3,HT4,HT5,HT6,HT7,V
      READ(1,1200)(RL(K),K=1,9
      READ(1,1200)NNN,CDG,CGD,COD,COG,TSTART,GDELTA,DTT,TSTOP
      READ(1,1200)FILM,CSLAG,DIST,TMOULD,FFLIQ,MOULD,CHOICE
```

Lines 56-102

Definition of the system: accumulated passing-times for the different cooling zones, grid size, enthalpy at the liquidus, solidus temperature and enthalpy at the solidus are calculated. Dummy-parameters are set to zero. The nodes in the 'slice' are given a casting temperature and a corresponding enthalpy (56-102).

```
C ****************************************************************
C *   CALCULATION OF PASSING-TIMES, DX AND CONSTANTS              *
C ****************************************************************
      DO 10 K=1,9
      Y(K)=RL(K)/V
   10 CONTINUE
      FN=FLOAT(N)
      FNN=FLOAT(MOULD)
      DXT=W/(FNN-1.0)
      DX=W/(FN-1.0)
      HZL=C*(TL-TW)+HLF
      ZZ2=DIST/V
      QMOULD=RL(1)/V*4.184*(640.0-53.0*SQRT(RL(1)/V))
      QTOTM=0.0
      HEBBE=0.0
C *******************************************************
C *   INITIAL CONDITIONS                                 *
C *******************************************************
      TS2=TM-(TM-TL)*(FLSTOP)**(PK-1.0)
      HZS2=C*(TS2-TW)
      DO 19 I=1,N
      GR(I)=0.0
      GRCHECK(I)=0.0
      GRCHECK2(I)=0.0
      GRTIME(I)=0.0
      DAS2(I)=0.0
   19 CONTINUE
      LARGE=0
    1 LARGE=LARGE+1
      FLIQ=FFLIQ
      R=0.0
      Z=0.0
      RML=Z*V*1000
      DO 21 J=1,MOULD
      X1(J)=1000.0*DXT*(J-1)
      TT(J)=TIN
      HT(J)=C*(TT(J)-TW)+HLF
      FLT(J)=1.0
   21 CONTINUE
      DO 20 I=1,N
      CHECK(I)=0.0
      X(I)=1000.*DX*(I-1)
      G1(I)=GDELTA
      T(I)=TIN
      H(I)=C*(T(I)-TW)+HLF
      FL(I)=1.0
   20 CONTINUE
```

Lines 103-180

The data used in the calculations are printed (103-115). The enthalpies and the thermal conductivities of the nodes of the fine mesh used in the mould are calculated (125-160). Conversion from enthalpy to temperature is carried out (161-180).

```
C ***********************************************************
C *   PRINTING OF DATA                                       *
C ***********************************************************
       IF(LARGE.EQ.2.0)GO TO 30
      WRITE(2,2000)VAR
      WRITE(2,2010)TIN,TM,TL,TS2,TW,TA,PK,FLSTOP,FFLIQ
      WRITE(2,2020)HT1,HT2,HT3,HT4,HT5,HT6,HT7
      WRITE(2,2030)FILM,CSLAG,DIST,ZZ2,TMOULD,MOULD
      WRITE(2,2040)CDG,CGD,COD,COG,TSTART,GDELTA,TSTOP,DTT,NNN
      WRITE(2,2050)D,C,W,V,DZZ,DX,DXT,HLF,N,CHOICE
      WRITE(2,499)
      WRITE(3,3100)T(N),RML
      WRITE(4,502)Z,T(1),T(3),T(5),T(7),T(9),T(10),T(11),T(12)
C *************************************************************
C *   CALCULATION OF FRACTION LIQUID AND THERMAL               *
C *   CONDUCTIVITY TOGETHER WITH THE                           *
C *   CALCULATION OF "FUTURE" ENTHALPIES, EXCEPT FOR THE       *
C *   SURFACE AND THE CENTRE NODE.                             *
C *************************************************************
C                  *               *
C                  * IN THE MOULD *
C                  ****************
      IF(CHOICE.EQ.1.0)FLIQ=FFLIQ
   30 IF((Z).GT.Y(1))GO TO 38
   37 DZ=(2.*DZZ*DXT**2.)/(2.*DX**2.)
      Z=Z+DZ
      R=R+1
      RML=Z*V*1000.0
      DO 110 J=1,MOULD
      IF(TT(J).LE.TS2)GO TO 115
      IF(TT(J).LT.TL)GO TO 120
      IF(TT(J).GE.TL)GO TO 125
  120 FLT(J)=((TM-TT(J))/(TM-TL))**(1./(PK-1.))
      GO TO 130
```

```
  125 FLT(J)=1.0
      GO TO 130
  115 FLT(J)=0.0
  130 FKT(J)=(1.+(FLIQ-1.)*FLT(J)**2.)*(0.02085+(TT(J)+273.)*
     113.9E-6)
      BT(J)=(1.+(FLIQ-1.)*FLT(J)**2.)*13.9E-6)
  110 CONTINUE
      DO 135 J=2,MOULD-1
      HZT(J)=FKT(J)*(TT(J+1)-2.*TT(J)+TT(J-1))+BT(J)/4.*(
     1(TT(J+1)-TT(J-1))**2.)
      HZT(J)=HZT(J)*DZ/(D*DXT*DXT)+HT(J)
  135 CONTINUE
C           ******************************************
C           *       AT THE SURFACE IN THE MOULD      *
C           ******************************************
      IF(Z.GT.ZZ2)GO TO 140
      Q=CSLAG/FILM*(TT(MOULD)-TMOULD)
      QTOTM=QTOTM+DZ*Q
      GO TO 136
  140 Q=4.184*(640.-80*SQRT(Z))
      QTOTM=QTOTM+DZ*Q
  136 HZT(MOULD)=(FKT(MOULD)*(TT(MOULD-1)-TT(MOULD))-DXT*Q)
     1*2.*DZ/(D*DXT*DXT)+HT(MOULD)+DZ/D*BT(MOULD)*(Q/
     1FKT(MOULD))**2.
      DO 150 J=2,MOULD
      IF(HZT(J).LT.HZL)GO TO 160
      TZT(J)=(HZT(J)-HLF)/C+TW
      GO TO 150
  160 IF(HZT(J).LE.HZS2)GO TO 170
      TOT(J)=1456.0
  175 FN=C*TOT(J)+HLF*((TM-TOT(J))/(TM-TL))**(1./(PK-1.))-
     1HZT(J)-C*TW
      DFN=C-HLF*(TM-TL)**(-1./(PK-1.))*(1./(PK-1.))*(TM-
     1TOT(J))**(1./(PK-1.)-1.0)
      E=FN/DFN
      T1T(J)=TOT(J)-E
      AE=ABS(E)
      TOT(J)=T1T(J)
      EL=0.05
      IF(AE.GT.EL)GO TO 175
      TZT(J)=T1T(J)
      GO TO 150
  170 TZT(J)=HZT(J)/C+TW
  150 CONTINUE
```

Lines 181-322

The temperature of the central node (in the mould) is calculated (181). The temperatures and enthalpies of the fine mesh are converted to the nodes of the coarser mesh used below the mould (186-195). The enthalpies and thermal conductivities of the mesh below the mould are calculated (200-262) after which a conversion from H to T is carried out (263-296). The temperature of the central node in the coarse mesh is calculated (300). The cooling rates and, subsequently, the secondary dendrite arm spacings are calculated using a 'clock' for each node (307-322).

```
      TZT(1)=4.*TZT(2)/3.-TZT(3)/3.
      DO 180 J=1,MOULD
      TT(J)=TZT(J)
      HT(J)=HZT(J)
  180 CONTINUE
      DO 190 I=1,N
      K=4*I-3
      T(I)=TT(K)
      TZ(I)=TZT(K)
      H(I)=HT(K)
      HZ(I)=HZT(K)
      FK(I)=FKT(K)
      B(I)=BT(K)
      FL(I)=FLT(K)
  190 CONTINUE
      GO TO 195
C           ************************************
C           *          BELOW THE MOULD         *
C           ************************************
   38 DZ=DZZ
   39 Z=Z+DZ
      IF((CHOICE.EQ.2.0).AND.(Z.GT.Y(1)))FLIQ=1.0
      IF(CHOICE.EQ.3.0)GO TO 101
      GO TO 102
  101 IF((Z.GT.Y(1)).AND.(Z.LT.Y(2)))GO TO 103
      IF(Z.GE.Y(2))FLIQ=1.0
      GO TO 102
  103 FLIQ=(FFLIQ-1.0)/(Y(1)-Y(2))*Z+1.0-(FFLIQ-1.0)/
     1(Y(1)-Y(2))*Y(2)
  102 R=R+1
      RML=Z*V*1000
      DO 40 I=1,N
      IF(T(I).LE.TS2)GO TO 32
      IF(T(I).LT.TL) GO TO 33
      IF(T(I).GE.TL) GO TO 31
   33 FL(I)=((TM-T(I))/(TM-TL))**(1/(PK-1))
      GO TO 35
   31 FL(I)=1.0
      GO TO 35
   32 FL(I)=0.0
   35 FK(I)=(1+(FLIQ-1.)*FL(I)**2)*(0.02085+(T(I)+273)*13.9E-6
      B(I)=(1+(FLIQ-1.)*FL(I)**2)*13.9E-6
   40 CONTINUE
      DO 50 I=2,N-1
   45 HZ(I)=FK(I)*(T(I+1)-2*T(I)+T(I-1))+((T(I+1)-T(I-1))**2)*B(I)/4
      HZ(I)=HZ(I)*DZ/(D*DX*DX)+H(I)
   50 CONTINUE
```

```
C ****************************************************************
C *   CALCULATION OF THE ENTHALPY AT THE SURFACE NODE.           *
C ****************************************************************
      IF(Z.GT.Y(1)) GO TO 60
      IF(Z.GT.ZZ2)GO TO 52
      Q=CSLAG/FILM*(T(N)-TMOULD)
      QTOTM=QTOTM+Q
      GO TO 200
   52 Q=4.184*(640-80*SQRT(Z))
      QTOTM=QTOTM+Q
      GO TO 200
   60 IF(Z.GT.Y(2)) GO TO 70
      Q=HT1*(T(N)-TW)
      GO TO 200
   70 IF(Z.GT.Y(3)) GO TO 80
      Q=HT2*(T(N)-TW)
      GO TO 200
   80 IF(Z.GT.Y(4)) GO TO 90
      Q=HT3*(T(N)-TW)
      GO TO 200
   90 IF(Z.GT.Y(5)) GO TO 91
      Q=HT4*(T(N)-TW)
      GO TO 200
   91 IF(Z.GT.Y(6))GO TO 92
      Q=HT5*(T(N)-TW)
      GO TO 200
   92 IF(Z.GT.Y(7))GO TO 93
      Q=HT6*(T(N)-TW)
      GO TO 200
   93 IF(Z.GT.Y(8))GO TO 100
      Q=HT7*(T(N)-TW)
      GO TO 200
  100 Q=0.8*5.6735E-11*((T(N)+273)**4-(TA+273)**4)
  200 HZ(N)=(FK(N)*(T(N-1)-T(N))-DX*Q)*2*DZ/(D*DX*DX)+H(N)
     1+DZ/D*B(N)*(Q/FK(N))**2.
      DO 300 I=2,N
      IF(HZ(I).LT.HZL) GO TO 210
      TZ(I)=(HZ(I)-HLF)/C+TW
      GO TO 300
  210 IF(HZ(I).LE.HZS2) GO TO 220
```

```
C *********************************************************************
C *        CALCULATION OF TZ(I) (THE "FUTURE" TEMPERATURE) VIA          *
C *        THE NEWTON-RAPHSON METHOD USING THE SCHEIL-EQN.              *
C *        (I.E. CONVERSION FROM H TO T)                                *
C *                                                                     *
C *   FL=((TM-TO(I))/(TM-TL))**(1.0/(PK-1.0))                  - - (1)*
C *                                                                     *
C *   FL=(H-C(TO(I)-TW))/HLF                                   - - (2)*
C *                                                                     *
C *   (1)=(2                                                            *
C *                                                                     *
C *   FN=C*TO(I)+HLF*((TM-TO(I))/(TM-TL)**(1.0/(PK-1))-H-C*TW          *
C *                                                                     *
C *********************************************************************
      TO(I)=1456.0
  215 FN=C*TO(I)+HLF*((TM-TO(I))/(TM-TL))**(1.0/(PK-1.0))-
     1HZ(I)-C*TW
      DFN=C-HLF*(TM-TL)**(-1.0/(PK-1.0))*1.0/(PK-1.0)*(TM-TO(I))
     1**(1.0/(PK-1.0)-1.0)
      E=FN/DFN
      T1(I)=TO(I)-E
      AE=ABS(E)
      TO(I)=T1(I)
      EL=0.05
      IF(AE.GT.EL)GO TO 215
      TZ(I)=TO(I)
      GO TO 300
  220 TZ(I)=HZ(I)/C+TW
  300 CONTINUE
C ***************************************************************
C *    CALCULATION OF THE TEMPERATURE OF THE CENTRAL NODE.       *
C ***************************************************************
  400 TZ(1)=4*TZ(2)/3-TZ(3)/3
  195 IF(LARGE.EQ.2)GO TO 440
      WRITE(3,3100)TZ(N),RML
C ***************************************************************
C *   CALCULATION OF THE COOLING RATE AND SECONDARY DENDRITE     *
C *   ARM SPACINGS AT DIFFERENT NODES.                           *
C ***************************************************************
      DO 500 I=1,N
      IF((T(I).GE.TL).AND.(TZ(I).LE.TS2))GO TO 510
  515 IF((T(I).LE.(TL-5.0)).AND.(GRCHECK(I).EQ.0.0))GO TO 516
      IF((T(I).LE.1280.0).AND.(GRCHECK2(I).EQ.0.0))GO TO 517
      GO TO 500
  516 GRTIME(I)=Z
      GRCHECK(I)=1.0
      GO TO 500
  517 GR(I)=(TL-5.0-1280.0)/(Z-GRTIME(I))
      DAS2(I)=63.91*GR(I)**(-0.347)
      GRCHECK2(I)=1.0
      GO TO 500
  510 WRITE(2,2080
 2080 FORMAT(2X,'--WARNING, MUSHY ZONE MISSED!!!--')
      GO TO 515
  500 CONTINUE
```

<u>Lines 323-401</u>

After the program has been re-initiated (using the dummy-parameter LARGE), the part for the calculation of fraction δ-ferrite is entered. First, notations and units used in this part are given. The number of nodes in the δ-ferrite (349) and its thickness (353) is calculated. The initial concentration-profile is given for each phase (354-360). The diffusion coefficients in each phase are calculated by considering a constant temperature for each time-interval (of the heat-flow part). The temperature is taken as the average between the 'new' and 'old' temperatures as calculated in the heat-flow part (362,363). The current position of the δ/γ-interface is calculated together with the speed at which the interface is moving (364-368). The concentrations of the central node (369) and the internal nodes in each phase are calculated (370-399). The 'new' fraction δ-ferrite is calculated at line 400.

```
C ************************************************************
C *     CALCULATION OF FRACTION DELTA FERRITE USING A FINITE  *
C *                                                           *
C *     DIFFERENCE MODEL BY TANZILLI AND HECKEL.              *
C *     (CYLINDRICAL GEOMETRY CONSIDERED)                     *
C ************************************************************
C
C      NOTATIONS AND UNITS FOR DELTA-FERRITE PART.
C      ========================================
C     NNN:MESH NUMBER, CDG:CONCENTRATION AT THE "DELTA-SIDE" OF
C     THE PHASE BOUNDARY (CONST.)(AT%), CGD:DITTO FOR "GAMMA-SIDE",
C     COD AND COG:STARTING CONC. IN DELTA AND GAMMA, RESPECTIVELY,
C     TSTART:USER-DEFINED TEMPERATURE FOR START OF REACTION,
C     GDELTA:FRACTION DELTA AT TSTART, DTT:TIME INCREMENT,
C     TSTOP:TEMP. BELOW WHICH REACTION IS NEGLIGIBLE,
C     M:NODE AT DELTA/GAMMA INTERFACE, XAI(I):SIZE (RADIUS) OF
C     DELTA (MICRONS), DDELT AND DGAMM:DIFFUSION COEFFS. IN
C     DELTA AND GAMMA (MICRONS**2/S), CC(I):CONCENTRATION (WT%),
C     G1(I):FRACTION DELTA FERRITE.
C
      GO TO 450
  440 DO 450 I=1,N
      TTOT=0.0
      IF(((T(I)+TZ(I))/2.0).GT.TSTART)GO TO 450
      IF(((T(I)+TZ(I))/2.0).LT.TSTOP)GO TO 450
      IF(CHECK(I).EQ.1.0)GO TO 455
      M=INT(G1(I)/100.0*NNN)
      P1=FLOAT(NNN)-FLOAT(M)
      P2=FLOAT(M)
      P3=FLOAT(NNN)
      XAI(I)=G1(I)/100.0*DAS2(I)/2.0
      CCO(I)=COD
      DO 460 J=1,M-1
      CC(I,J)=COD
  460 CONTINUE
      DO 470 J=M+1,NNN
      CC(I,J)=COG
  470 CONTINUE
      CHECK(I)=1.0
  455 DDELT=2.53*EXP(-57500.0/(1.987*((T(I)+TZ(I))/2.+273.)))*1.E8
      DGAMM=10.8*EXP(-69700.0/(1.987*((T(I)+TZ(I))/2.+273.)))*1.E8
```

```
  600 XXAI=XAI(I)
      XAI(I)=XAI(I)+DTT/(CDG-CGD)*(DGAMM*P1*((-CC(I,M+2)+4.*
     1CC(I,M+1)-3.*CGD)/(2.*(DAS2(I)/2.-XAI(I))))-DDELT*P2*(CC(I,M-2)
     2-4.*CC(I,M-1)+3.*CDG)/(2.*XAI(I)))
      DXAI=(XAI(I)-XXAI)/DTT
      CC0(I)=CC0(I)+DTT*4.*DDELT*P2**2./XXAI**2.*(CC(I,1)-CC0(I))
      DO 610 J=1,M-1
      P4=FLOAT(J)
      IF(J.EQ.1)GO TO 614
      IF(J.EQ.M-1)GO TO 615
  612 CC(I,J)=CC(I,J)+DTT*(P4/XXAI*(CC(I,J+1)-CC(I,J-1))/2.*DXAI+DDELT
     1*P2**2.*(CC(I,J-1)-2.*CC(I,J)+CC(I,J+1))/XXAI**2.+DDELT*P2**2.*
     2(CC(I,J+1)-CC(I,J-1))/(2.*P4*XXAI**2.))
      GO TO 610
  615 CC(I,M)=CDG
      GO TO 612
  614 CC(I,J)=CC(I,J)+DTT*(P4/XXAI*(CC(I,J+1)-CC0(I))/2.*DXAI+DDELT
     1*P2**2.*(CC0(I)-2.*CC(I,J)+CC(I,J+1))/XXAI**2.+DDELT*P2**2.*
     2(CC(I,J+1)-CC0(I))/(2.*P4*XXAI**2.))
  610 CONTINUE
      DO 620 J=M+1,NNN
      P4=FLOAT(J)
      IF(J.EQ.M+1)GO TO 622
      IF(J.EQ.NNN)GO TO 625
  621 CC(I,J)=CC(I,J)+DTT*((P3-P4)/(DAS2(I)/2.-XXAI)*(CC(I,J+1)-CC(I,
     1J-1))/2.*DXAI+DGAMM*P1**2.*(CC(I,J-1)-2.*CC(I,J)+CC(I,J+1
     2))/((DAS2(I)/2.-XXAI)**2.)+DGAMM/(XXAI+((P4-P2)*(DAS2(I)/2.-
     3XXAI)/P1))*P1*(CC(I,J+1)-CC(I,J-1))/(2.*(DAS2(I)/2.-XXAI)))
      GO TO 620
  622 CC(I,M)=CGD
      GO TO 621
  625 CC(I,NNN+1)=CC(I,NNN-1)
      GO TO 621
  620 CONTINUE
      TTOT=TTOT+DTT
      IF(TTOT.LE.DZ)GO TO 600
      G1(I)=2.*XAI(I)/DAS2(I)*100.0
  450 CONTINUE
```

Lines 402-490

'Clocks' are checked and results are printed (402-490).

```
C ****************************************************************
C *  MAINLY PRINTING OF RESULTS AND TIME-CHECKS.                 *
C ****************************************************************
      DO 700 I=1,N
      H(I)=HZ(I)
      T(I)=TZ(I)
  700 CONTINUE
      IF((LARGE.EQ.2).AND.(R.EQ.20))GO TO 703
      IF((FL(1).EQ.0.0).AND.(HEBBE.EQ.0.0))GO TO 701
      GO TO 702
  701 HEBBE=1.0
      FULLY=Z*V
  702 IF(R.EQ.20)GO TO 501
      IF(LARGE.EQ.2)GO TO 530
      GO TO 503
  501 WRITE(4,504)Z,T(1),T(3),T(5),T(7),T(9),T(10),T(11),T(12)
      GO TO 503
  703 WRITE(2,502)Z,G1(1),G1(3),G1(5),G1(7),G1(9),
     1G1(10),G1(11),G1(12)
      R=0.0
  530 IF(((Z-DZ).LT.Y(8)).AND.(Z.GE.Y(8)))GO TO 520
      GO TO 503
  520 DO 525 I=1,N
      TBEND(I)=T(I)
      GBEND(I)=G1(I)
  525 CONTINUE
  503 IF(Z.LT.1500.0.AND.RML.LT.25000.0)GO TO 30
      IF(LARGE.EQ.1)GO TO 1
      IF(T(1).GT.TSTOP)GO TO 30
      WRITE(4,504)Z,T(1),T(3),T(5),T(7),T(9),T(10),T(11),T(12)
      WRITE(2,502)Z,G1(1),G1(3),G1(5),G1(7),G1(9),
     1G1(10),G1(11),G1(12)
      WRITE(2,2399)
      WRITE(2,2400)(X(I),GBEND(N-I+1),TBEND(N-I+1),G1(N-I+1),
     1T(N-I+1),I=1,N)
      WRITE(2,2438
      WRITE(2,2439)(X1(J),FLT(MOULD-J+1),TT(MOULD-J+1
     1),J=1,MOULD)
      WRITE(2,2440)
      WRITE(2,2450)(X(I),GR(N-I+1),DAS2(N-I+1),I=1,N)
      QTOTM=QTOTM/2.0
      WRITE(2,2460)QMOULD,QTOTM
      WRITE(2,2470)FULLY
      WRITE(3,3200
      WRITE(3,3300
```

```
  499 FORMAT(1X,/,2X,'DELTA FERRITE DISTRIBUTION WITH TIME',/)
  502 FORMAT(2X,F7.1,8(1X,F7.4))
  504 FORMAT(2X,F7.1,8(1X,F7.2))
 1000 FORMAT(1G0.0)
 1100 FORMAT(5A8
 1200 FORMAT(11G0.0
 2000 FORMAT(1H ,5A8
 2010 FORMAT(2X,'TIN=',F6.1,1X,'TM=',F6.1,1X,'TL=',F6.1,1X,'TS='
     1,F6.1,1X,'TW=',F6.1,1X,'TA=',F6.1,/,2X,'PK=',F5.3,1X,
     1'FL(SOLID)=',F5.3,1X,'KL/KS=',F3.1)
 2020 FORMAT(2X,'H1=',F5.3,1X,'H2=',F5.3,1X,'H3=',F5.3,1X,'H4=',
     1F5.3,1X,'H5=',F5.3,1X,'H6=',F5.3,1X,'H7=',F5.3)
 2030 FORMAT(2X,'SLAG FILM=',F7.5,1X,'SLAG COND.=',F7.5,1X,
     1'GAP FORM.=',F5.3,/,2X,'TIME(GAP FORM.)=',F5.1,1X,'TMOULD=',
     1F6.1,1X,'MESH(MOULD)=',I3)
 2040 FORMAT(2X,'CDG=',F7.5,1X,'CGD=',F7.5,1X,'COD=',F7.5,1X,
     1'COG=',F7.5,/,2X,'TSTART=',F6.1,1X,'%DELTA(START)=',F5.2,
     11X,'TSTOP=',F6.1,/,2X,'TIME INCR.=',F7.5,1X,'MESH(DELTA)=',
     1I3)
 2050 FORMAT(2X,'RHO=',F6.1,1X,'CP=',F5.3,1X,'HALF THICKN.=',
     1F5.3,1X,'CAST.SPEED=',F6.4,1X,'TIME INCR.=',F4.2,
     1/,2X,'DX=',F6.4,1X,'DX(MOULD)='
     1,F6.4,1X,'HLF=',F5.1,1X,'MESH(BELOW MOULD)=',I3,1X,
     1'CHOICE=',F3.1)
 2399 FORMAT(1X,/,2X,'DELTA FERRITE AND TEMPERATURE DISTR. AT',
     11X,'THE UNBENDING POINT',/,'AND FINAL (TCENTRE<TSTOP)',
     11X,'RESPECTIVELY',/,'DIST.  DELTA    T(C)     DELTA      T(C)')
 2400 FORMAT(2X,F7.3,2X,F7.4,2X,F6.1,2X,F7.4,2X,F6.1)
 2438 FORMAT(1X,/,2X,'FRACTION LIQUID AND TEMP. AT MOULD EXIT',
     11X,'(FROM SURFACE)',/)
 2439 FORMAT(2X,F7.3,3X,F5.3,3X,F6.1)
 2440 FORMAT(2X,/,2X,'DISTANCE FROM SURFACE',3X,'COOLING RATE',4X,
     1'SEC.DAS',/)
 2450 FORMAT(7X,F7.3,12X,F7.3,7X,F7.3)
 2460 FORMAT(2X,'QMOULD=',F10.3,2X,'QTOTM=',F10.3)
 2470 FORMAT(2X,'SOLIDIFICATION COMPLETED',1X,F5.2,1X,
     1'METRES BELOW THE MENISCUS')
 3000 FORMAT(1H ,5A8)
 3100 FORMAT(1H ,F7.1,2X,F7.1)
 3200 FORMAT(1H ,'END')
 3300 FORMAT(1H ,'****')
      STOP
      END
      FINISH
```

APPENDIX VI

Etchants used for Metallographical Investigations

Colour etchant[233]:used for revealing dendritic structures in 18/8, 18/10 and 18/14-alloys.

20g	ammonium bifluoride
0.5g	potassium bisulfate
100ml	distilled water

Colours Ni-rich areas blue and Cr-rich areas yellow. δ-ferrite remains white. Etching-time dependent on alloy content (average time:1.5 minutes).

Electrolytic etchant:used for revealing dendritic structures in 25/20-alloys.

40g	iron chloride
3g	copper chloride
40ml	hydrochloric acid
500ml	distilled water

Originally used as a chemical etchant. Used as an electrolytic etchant, it proved to be useful for revealing dendritic structures in 25/20-alloys. 10V and 10 seconds used (area exposed: $\sim 2cm^2$).

Electrolytic etchant:used for revealing δ-ferrite in 18/10-type steels.

10N potassium hydroxide

Etchant attacks only δ-ferrite. 6V for 5 seconds (area exposed: $\sim 4cm^2$).

T A B L E S

TABLE 4.1

Chemical compositions of charge materials used in the experimental castings.

Charge Material	Composition, wt-%							
	C	S	Mn	O	N	Al	Fe	P
Armco Iron Billets	0.015	0.007	0.06	0.0084	0.0077	-	bal.	-
Armco Iron Punchings	0.012	0.006	0.05	0.0054	0.0044	0.02	bal.	-
Cr Briquettes	0.023	0.008	-	0.0102	0.0023	-	-	-
Cr Flake	-	-	-	0.1343	0.0038	-	-	-
Ni Pellets	0.011	0.001	-	-	-	-	-	-
Mn Flake	0.004	0.036	bal.	0.2500	0.0027	-	-	-
Si Metal	0.060	0.030	-	-	-	0.25	0.5	0.02

TABLE 5.1

Chemical compositions of experimental ingots.

Cast No.	Composition, wt.%								Cr_{eq}^{*}	Ni_{eq}^{*}	Type
	Cr	Ni	Mn	Si	C	P	S	N^{**}			
5129	18.5	10.1	1.04	0.19	0.062	0.010	0.006	934	18.5	11.79	B
5141	18.3	10.1	0.81	0.40	0.064	0.009	0.003	814	18.3	11.77	B
5202	18.4	8.2	0.82	0.22	0.060	0.010	0.004	867	18.4	9.79	A
5203	17.9	13.8	1.03	0.25	0.069	0.012	0.006	545	17.9	15.64	D
5275	16.9	-	0.84	0.16	0.021	0.010	0.008	579	-	-	-
5282	18.1	10.1	1.06	0.17	0.018	0.010	0.006	882	18.1	10.84	B
5298	17.9	14.5	1.00	0.25	0.016	0.011	0.006	350	17.9	15.17	D
5299	19.6	-	0.89	0.17	0.019	0.011	0.007	649	-	-	-
5333	25.9	19.6	1.03	0.17	0.017	0.009	0.006	657	25.9	20.30	D
5522	19.0	13.5	4.06	0.09	0.006	0.007	0.004	25	19.0	14.89	D
5525	26.0	19.2	3.91	0.04	0.005	0.009	0.004	39	26.0	20.52	D
5550	18.9	13.7	4.02	0.12	0.004	0.007	0.004	17	18.9	15.03	D
5551	18.8	13.8	3.95	0.10	0.006	0.007	0.003	29	18.8	15.16	D

* after Hammar[13]
** in ppm

TABLE 5.2

Casting conditions (air).

Cast No.	T_l (^oC)	ΔT (^oC)	Teeming time (s)
5129	1460	0	10
5141	1460	5	10
5202	1464	6	15
5203	1439	10	15
5275	1515	3	15
5282	1467	7	15
5298	1458	28	12*
5299	1512	3	17
5333	1423	27	18

*250mm high ingot

TABLE 5.3

Casting conditions (controlled atmosphere).

Cast No.	T_p (^oC)	Atm.	Teeming time (s)
5522	1550	He	8
5525	1510	He	8
5550	1550	vac.	8
5551	1550	He	25

TABLE 5.4

Chemical compositions of commercial slabs.

Slab	Composition, wt.%							
	Cr	Ni	Mn	Si	C	P	S	N
18/8	18.10	9.30	1.47	0.42	0.035	0.023	0.019	0.0283
302	18.18	8.71	1.61	0.45	0.040	0.025	0.004	0.0400
316	16.84	11.23	1.64	0.39	0.050	0.026	0.010	0.0440

TABLE 6.1

Properties of steel used in analysis

	Parameter	Reference
Carbon steel	ρ = 7400 kgm^{-3}	140
	C_p = 0.682 $kJkg^{-1}K^{-1}$	140
	L_f = 272 $kJkg^{-1}$	140
	A = 0.0159 $kWm^{-1}K^{-1}$	140
	B = 11.51 x 10^{-6} $kWm^{-1}K^{-2}$	140
Austenitic stainless steel	ρ = 7900 kgm^{-3}	234
	C_p = 0.750 $kJkg^{-1}K^{-1}$	235
	L_f = 275 $kJkg^{-1}$	
	A = 0.02085 $kWm^{-1}K^{-1}$	236
	B = 13.9 x 10^{-6} $kWm^{-1}K^{-2}$	236
	T_l = 1456.0 ^oC	
	k = 0.84	14
Aluminium	ρ = 2542 kgm^{-3}	81
	C_p = 1.076 $kJkg^{-1}K^{-1}$	81
	L_f = 402 $kJkg^{-1}$	81
	K = 0.249 $kWm^{-1}K^{-1}$	81

TABLE 6.2

Values of parameters used for different atmospheres

Atmosphere	Parameter	Reference
Air	$\varepsilon = 0.8$	181
	$h_{con} \sim 0.1^{+}$	
He	$\varepsilon \sim 0.4^{*}$	215
	$h_{con} \sim 0.4^{+}$	
Vacuum	$\varepsilon \sim 0.4^{*}$	215
	$h_{con} = 0.0$	

+ based on the assumption: $\frac{h^{He}}{h^{air}} \sim 4$

* allowing for a surface which is not prefectly flat and clean.

TABLE 6.3

Data used in diffusion-part of modelling of δ-ferrite

$T_{start} = 1404^{\circ}C$	$c_{0\delta}^{Cr} = 0.2157^{*}$ (20.3 wt.%)
$f_{start}^{\delta} = 22\%$	$c_{0\gamma}^{Cr} = 0.1865$ (17.5 wt.%)
$T_{stop} = 900^{\circ}C$	$c_{\delta\gamma}^{Cr} = 0.2157$ (20.3 wt.%)
Mesh = 20	$c_{\gamma\delta}^{Cr} = 0.1946$ (18.27 wt.%)
$\Delta t = 0.007s$	$D_{\delta}^{Cr} = 2.53\exp(\frac{-57500}{1.987T})$ $cm^2 s^{-1}$ (Ref.237)
	$D_{\gamma}^{Cr} = 10.8\exp(\frac{-69700}{1.987T})$ $cm^2 s^{-1}$ (Ref.237)

* in atomic fraction

TABLE 6.4

Heat transfer data used for analysis of continuous casting.

Data after Nozaki et al.[126]

Zone	Distance* (m)	Conventional h ($kWm^{-2}K^{-1}$)	Modified h ($kWm^{-2}K^{-1}$)
I	1.47	0.523	0.412
II	2.31	0.667	0.484
III	3.81	0.565	0.628
IV	5.31	0.644	0.628
V	8.31	0.507	0.838
VI	11.31	0.356	0.791
VII	15.81	0.292	0.835

* mould length: 0.63m

Data after Larrecq et al.[199]

Zone	Distance* (m)	Conventional h ($kWm^{-2}K^{-1}$)	Optimised h ($kWm^{-2}K^{-1}$)
I	1.25	0.86	0.85
II	1.70	0.72	0.70
III	3.80	0.50	0.56
IV	6.80	0.33	0.48
V	9.80	0.25	0.33
VI	12.70	0.20	0.26
VII	15.90	0.18	0.18

* mould length: 0.9m

F I G U R E S

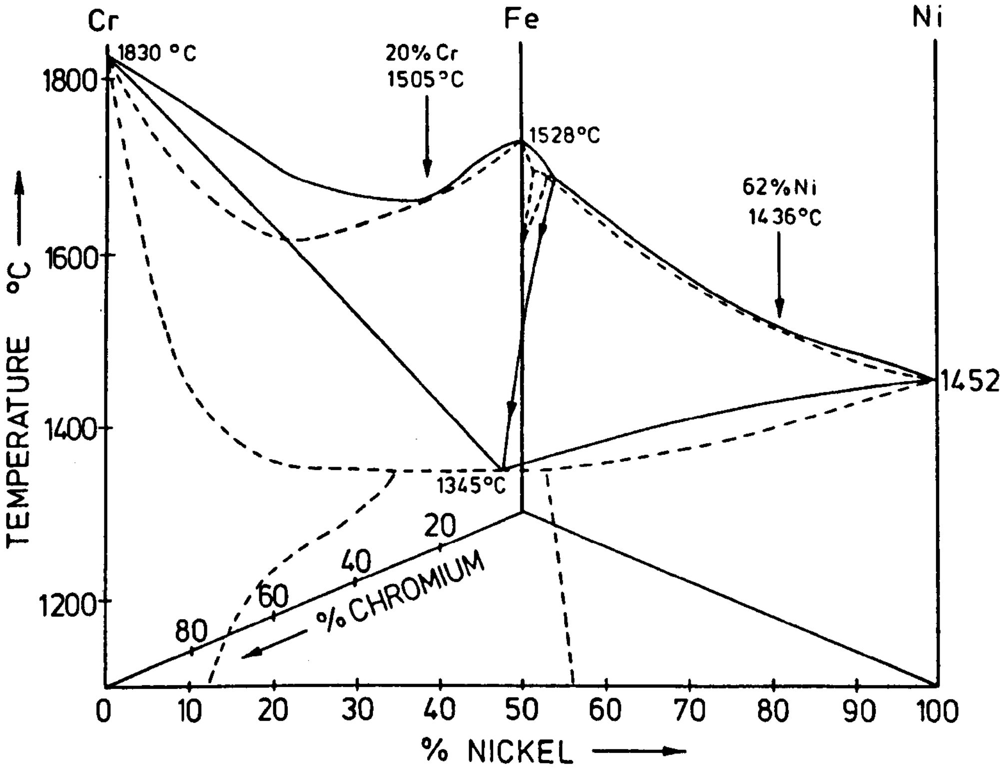

Figure 2.1 The ternary Fe-Cr-Ni equilibrium diagram.

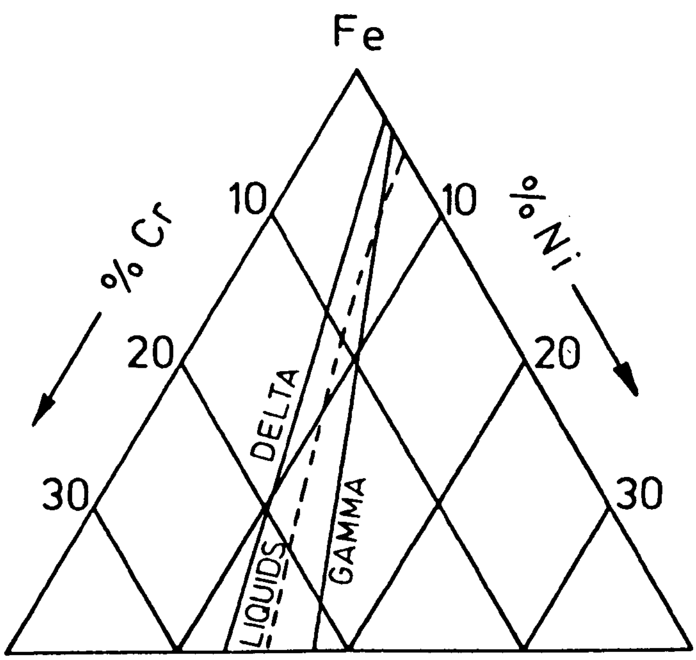

Figure 2.2 Projection showing the boundary-lines of the three-phase field (δ-ferrite + L + γ).

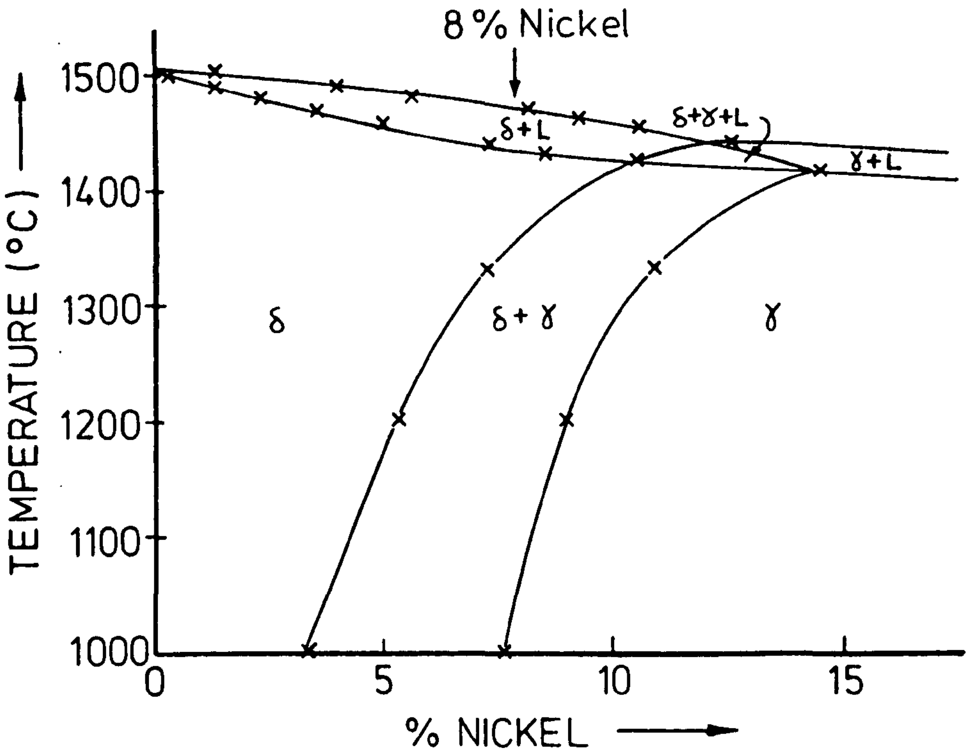

Figure 2.3 Vertical section of the Fe-Cr-Ni-system at constant Cr-content of 18 wt.%.

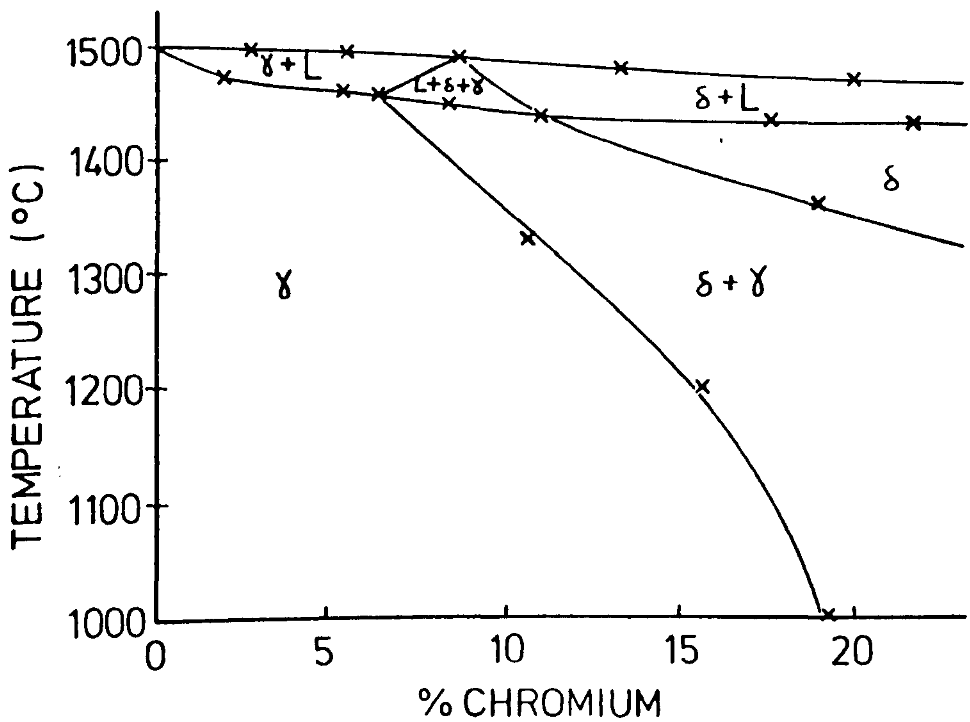

Figure 2.4 Vertical section of the Fe-Cr-Ni-system at constant Ni-content of 8 wt.%.

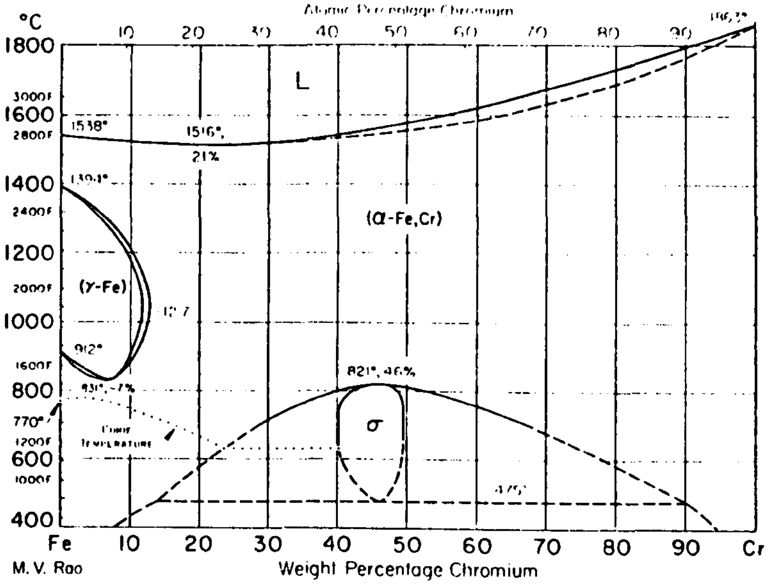

Figure 2.5 The binary Fe-Cr equilibrium diagram.

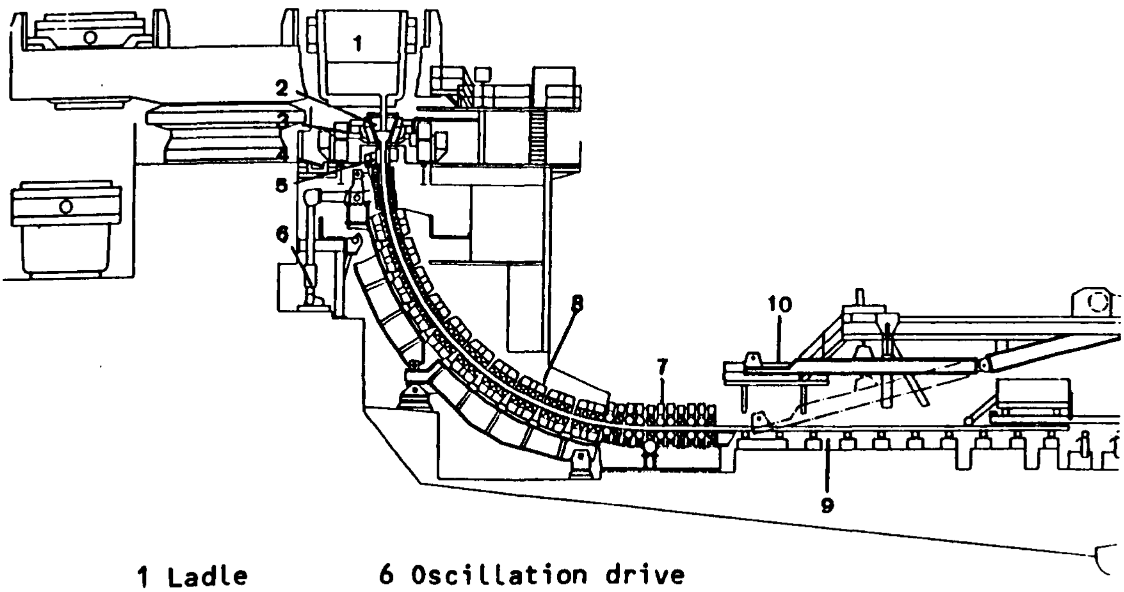

1 Ladle
2 Tundish
3 Tundish car
4 Slag-box
5 Mould
6 Oscillation drive
7 Withdrawal unit
8 Secondary cooling zone
9 Semi-finished product
10 Dummy-bar table

Figure 2.6 General lay-out of a continuous casting machine.

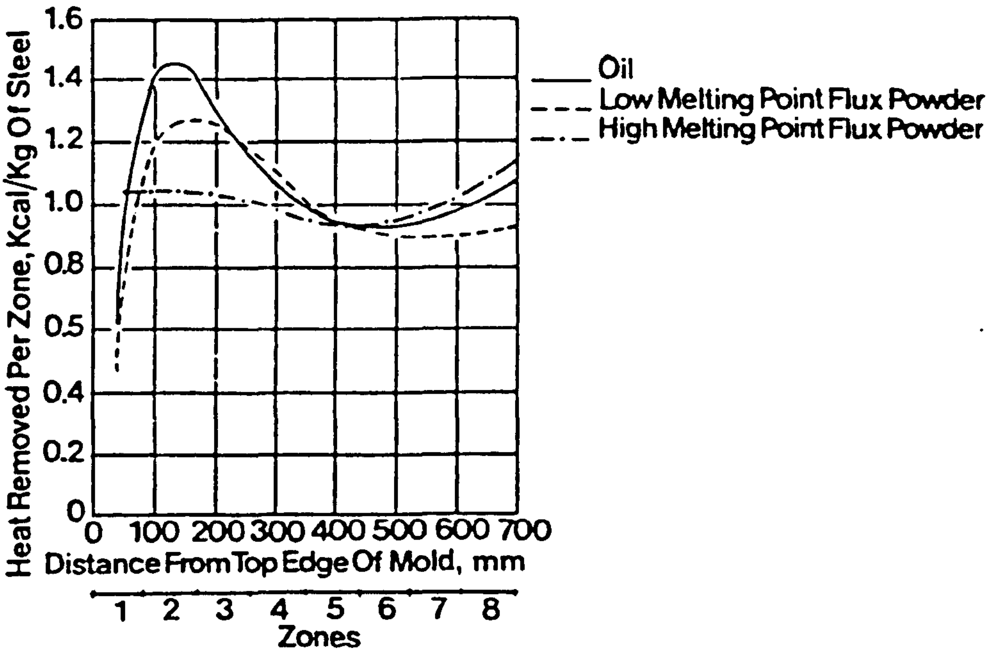

Figure 2.7 Effect of lubricant on the distribution of heat flux from top to bottom of the mould[118].

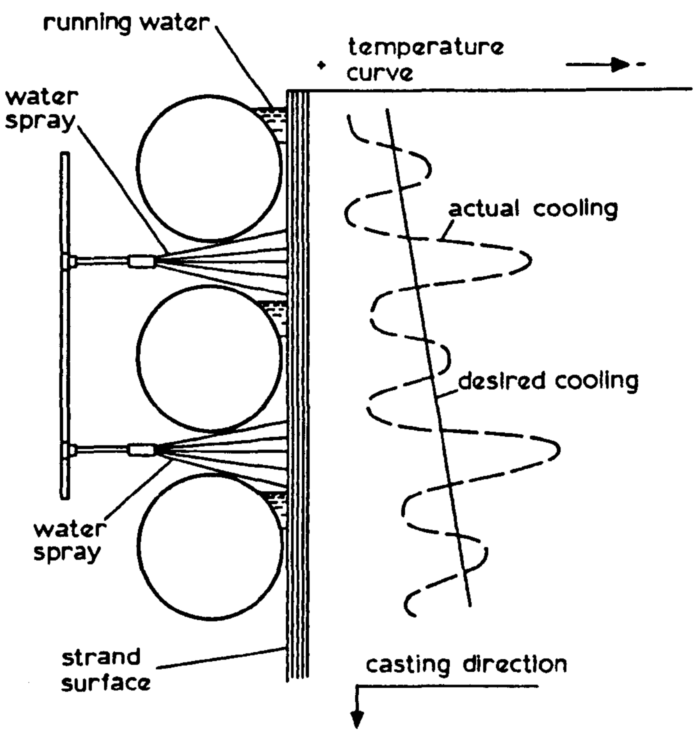

Figure 2.8 Schematic representation of the conditions prevailing in the secondary cooling zone[122].

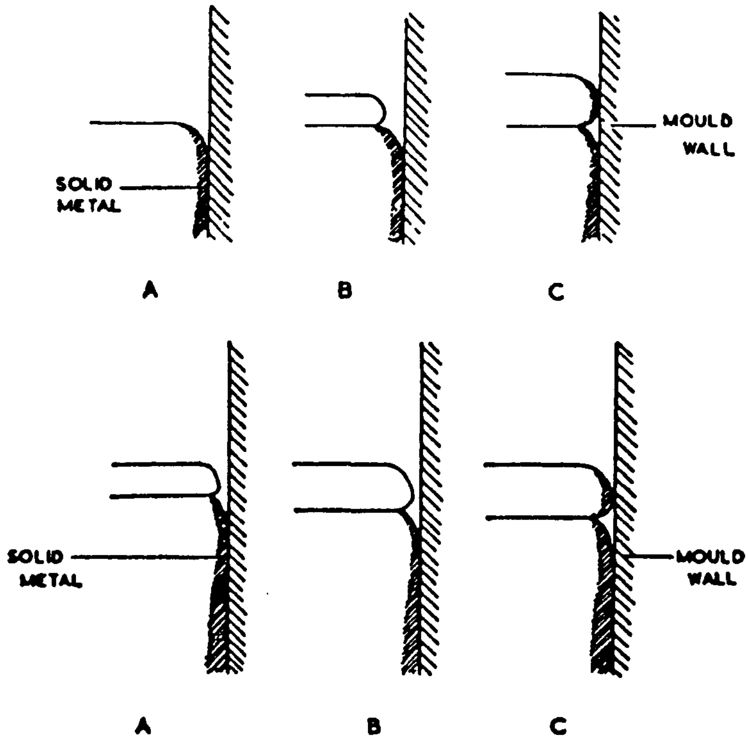

Figure 2.9 Mechanism of formation of surface depressions on continuously-cast non-ferrous alloys (after Waters[74]).

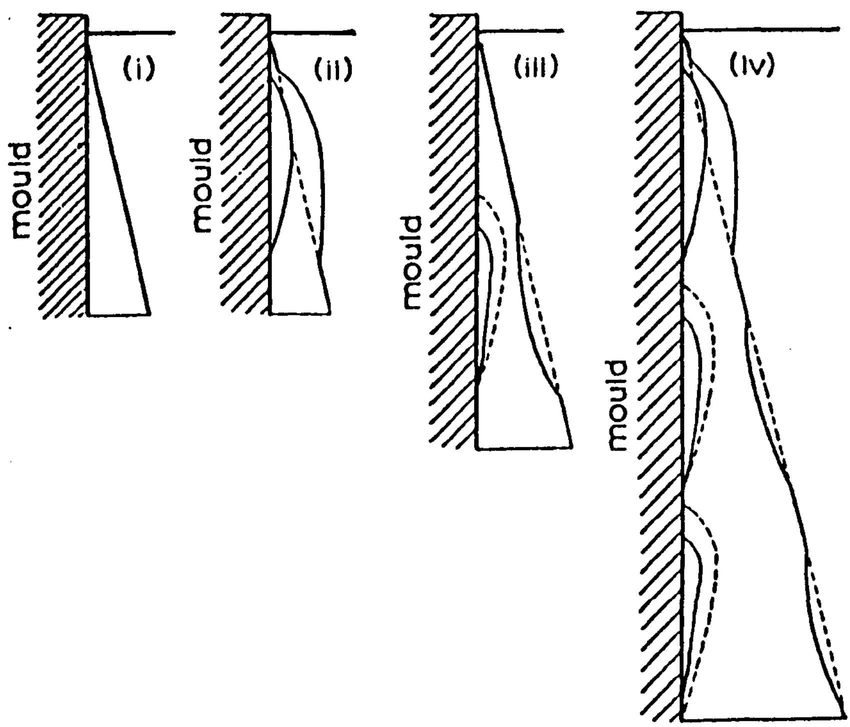

Figure 2.10 Mechanism of oscillation mark formation during continuous casting (after Grill et al.[89]).

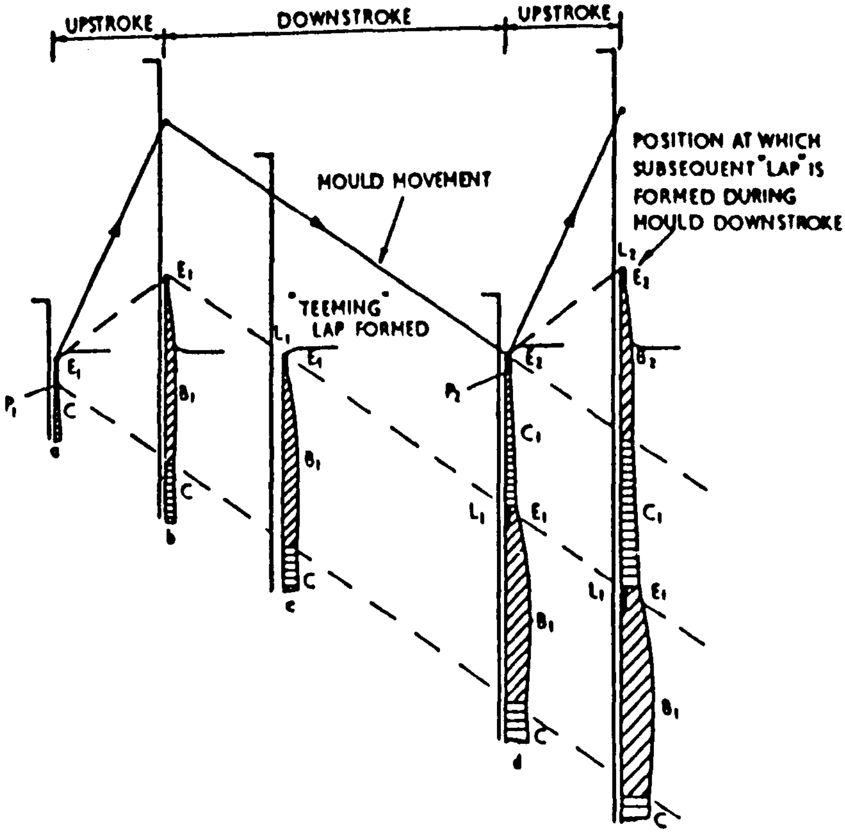

Figure 2.11 Mechanism of oscillation mark formation during continuous casting (after Savage[153]).

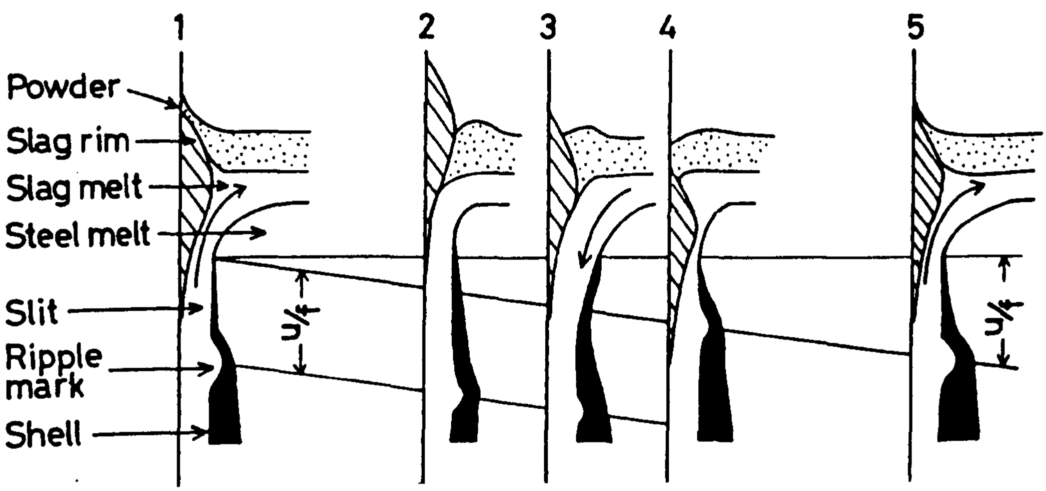

Figure 2.12 Sequence of oscillation mark formation (after Emi et al.[156]).

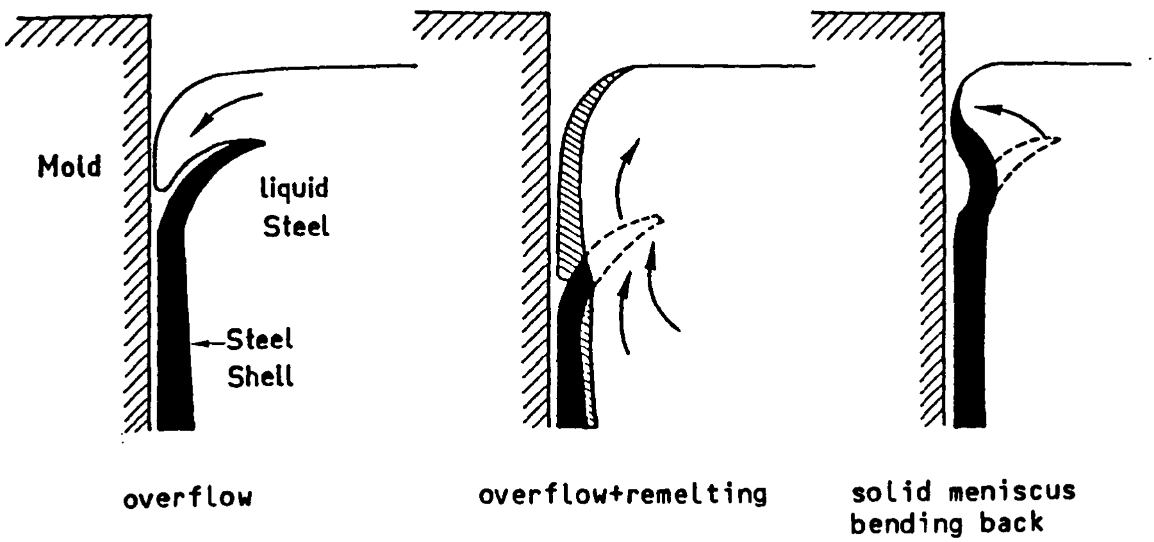

Figure 2.13 Mechanisms of oscillation mark formation during continuous casting (after Riboud et al.[112]).

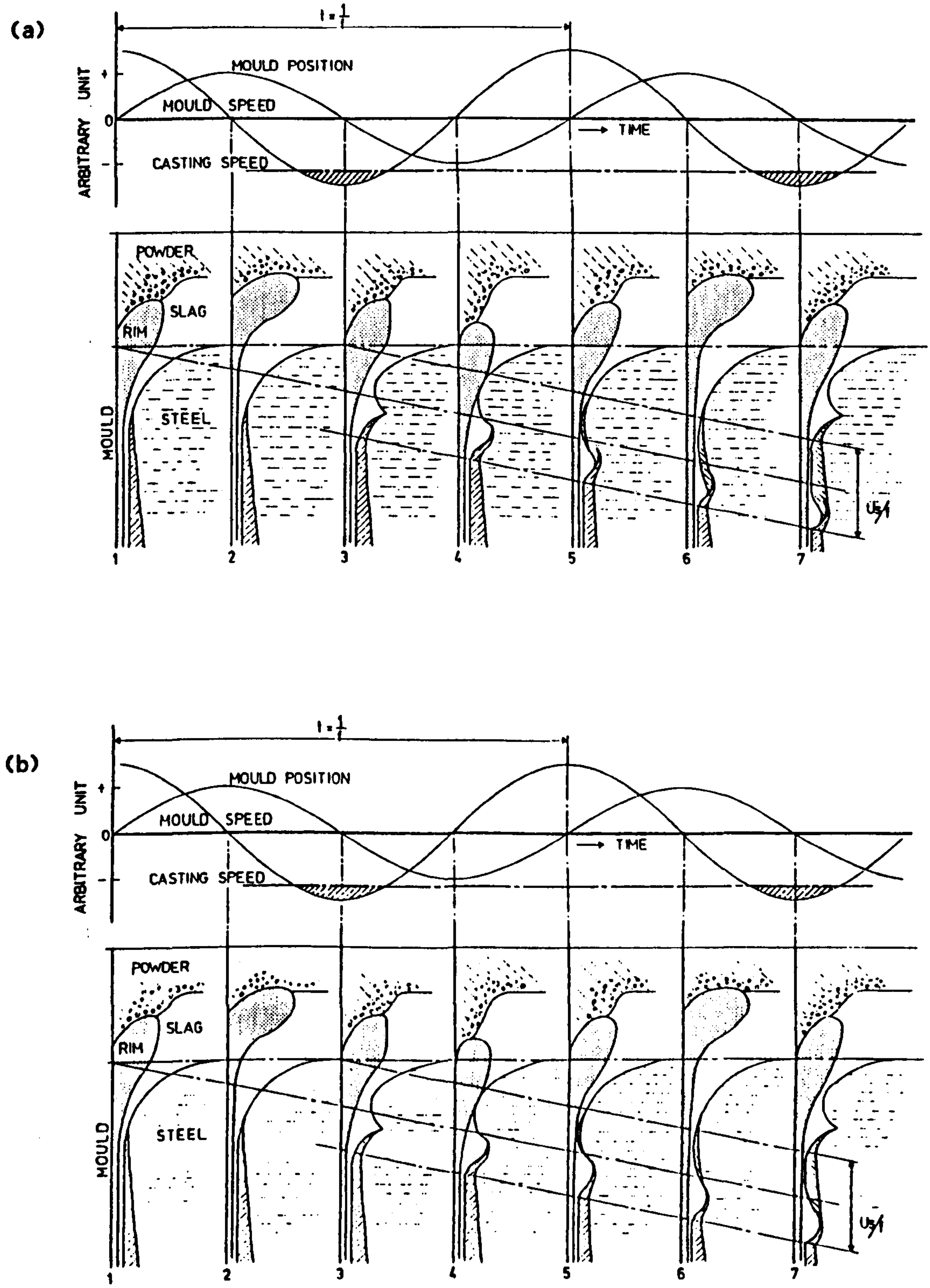

Figure 2.14 Mechanisms of oscillation mark formation during continuous casting (after Tomono[85]).
(a) by overflow
(b) by folding

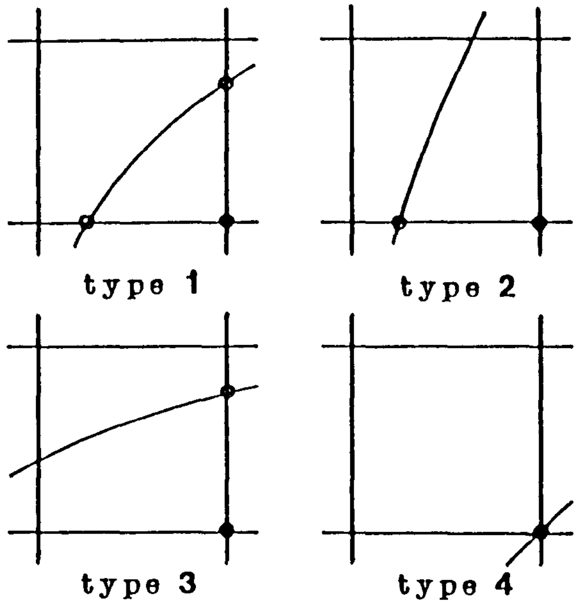

Figure 3.1 Schematic representation of the ways in which a curved boundary can intersect with a square grid.

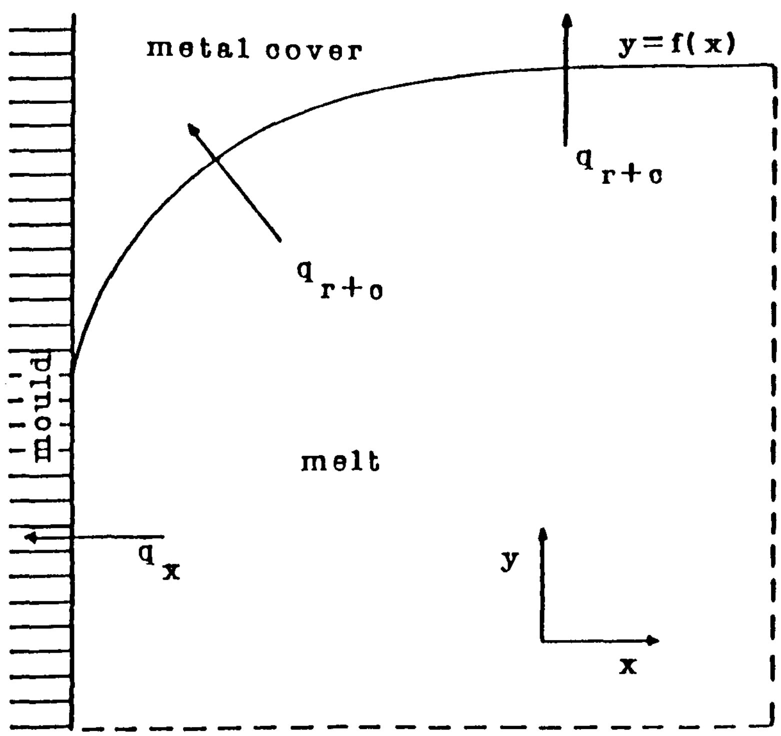

Figure 3.2 Physical system in the vicinity of the meniscus.

q_x = heat flux by conduction through mould/metal interface
q_{r+c} = heat flux by radiation and convection through metal/metal cover interface

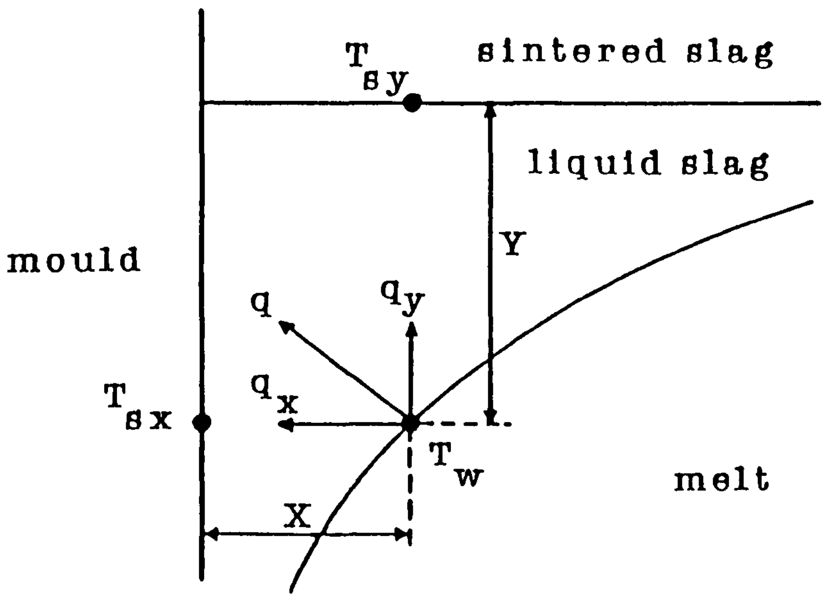

Figure 3.3 Schematic representation of the situation prevailing in the meniscus region during continuous casting.

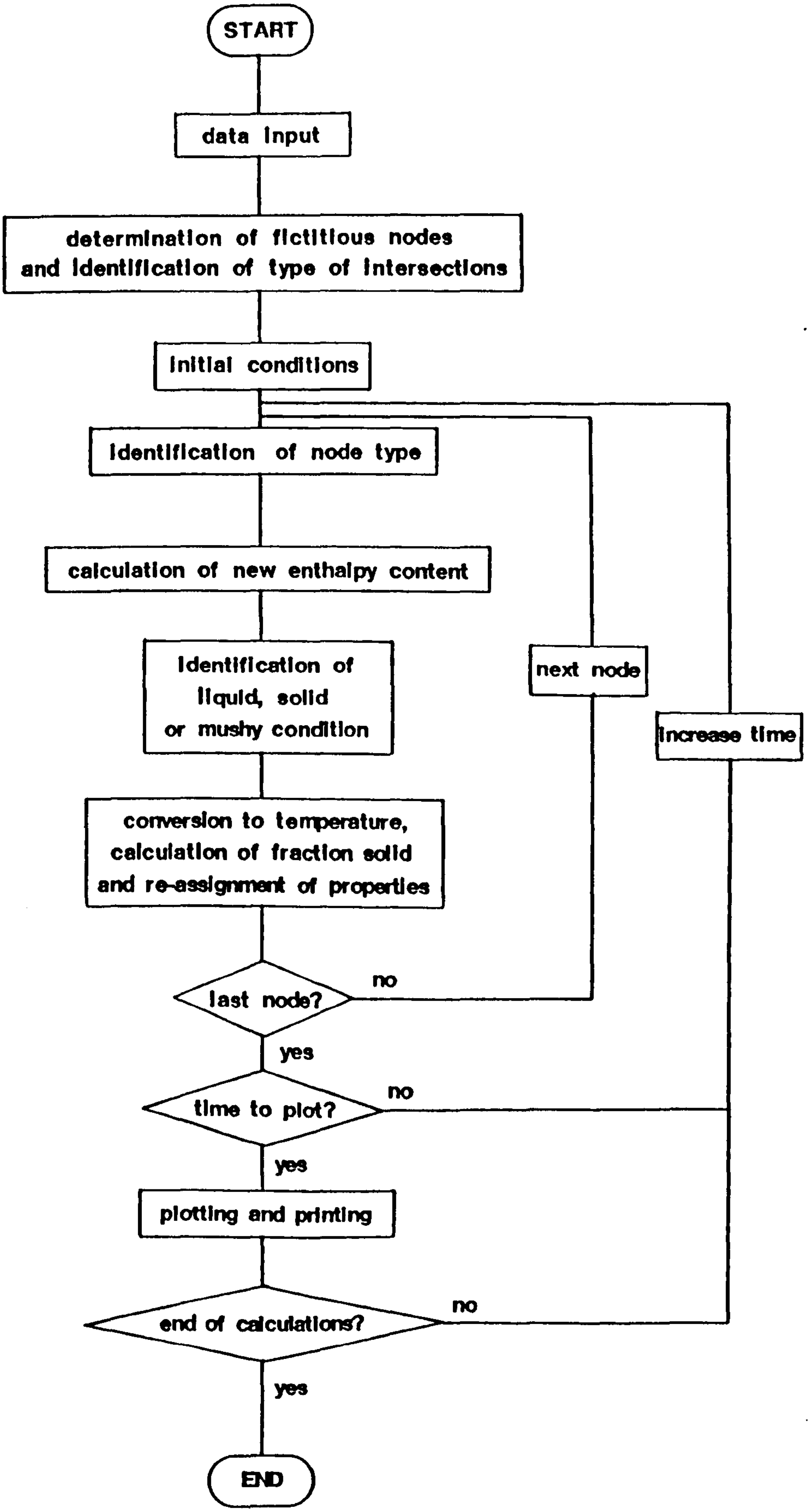

Figure 3.4 Schematic flow-diagram of the model for heat transfer in the meniscus region during casting.

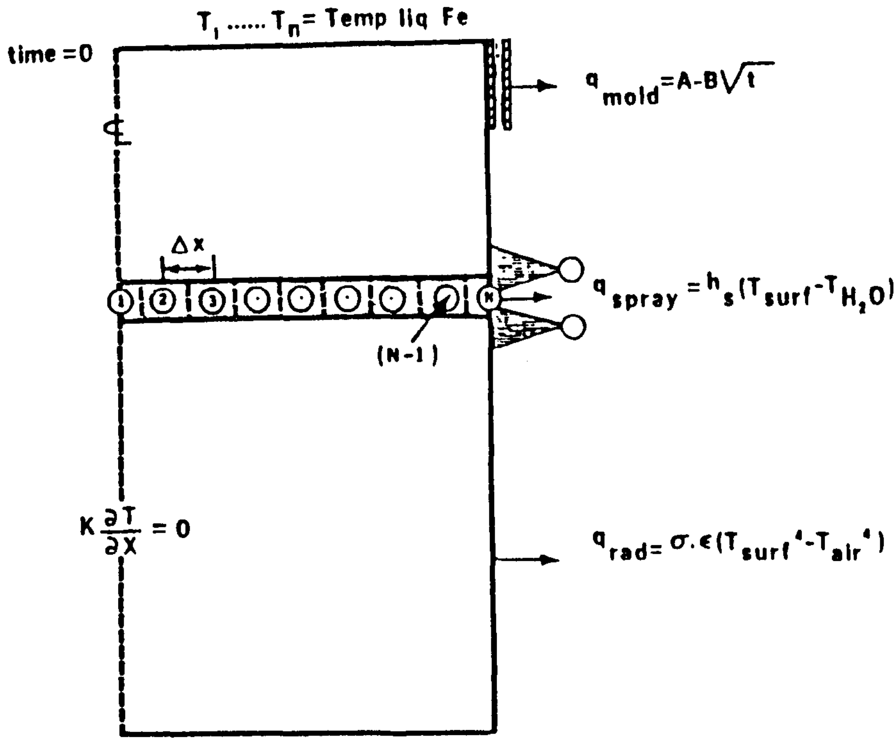

Figure 3.5 Schematic representation of the situation prevailing during continuous casting of slabs (after Mizikar[145]).

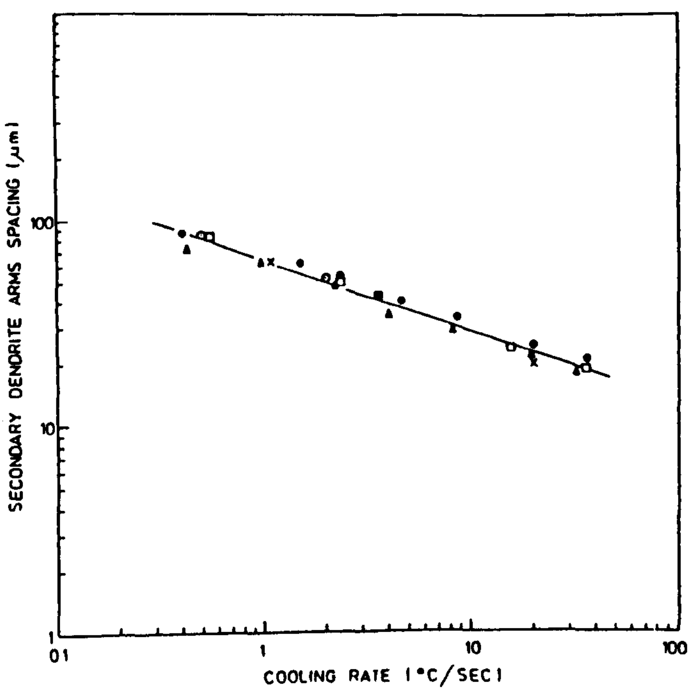

Figure 3.6 Secondary dendrite arm spacings vs. cooling rate for austenitic stainless steels (after Pereira[14]).

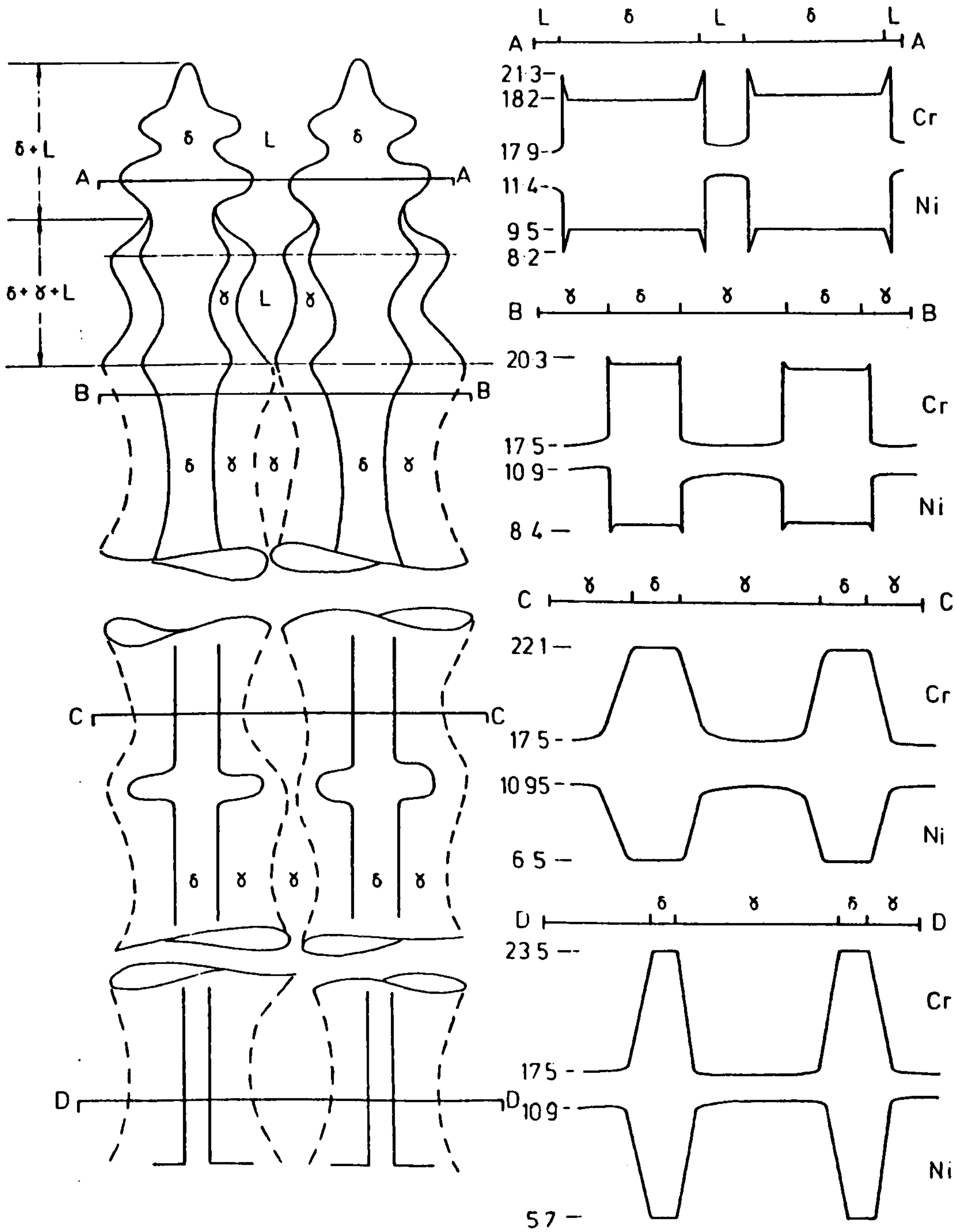

Figure 3.7 Schematic representation of the peritectic transformation in Type B alloys (after Pereira[14]).

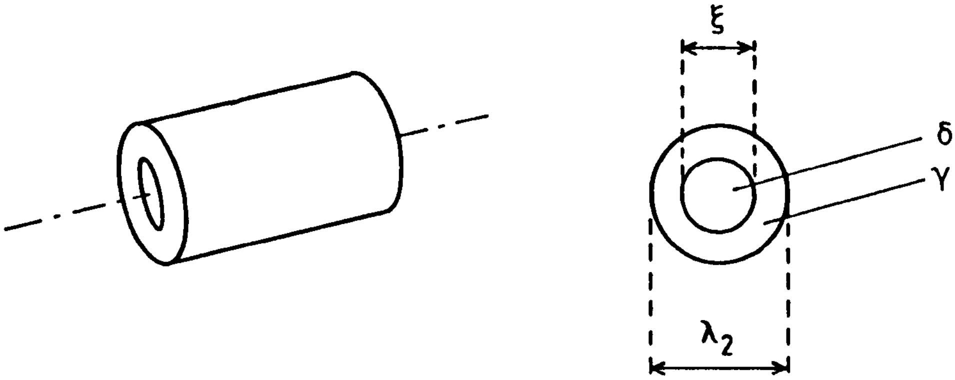

Figure 3.8 Schematic representation of the system considered in the numerical analysis of the $\delta \rightarrow \gamma$ transformation.

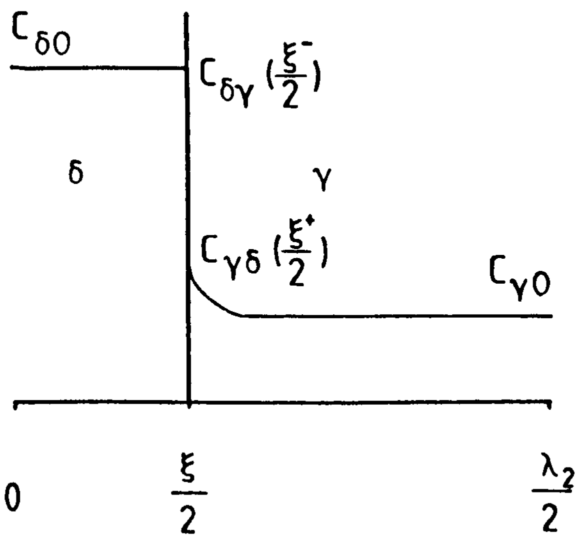

Figure 3.9 Schematic representation of the initial concentration profile of Cr across half a secondary dendrite arm spacing.

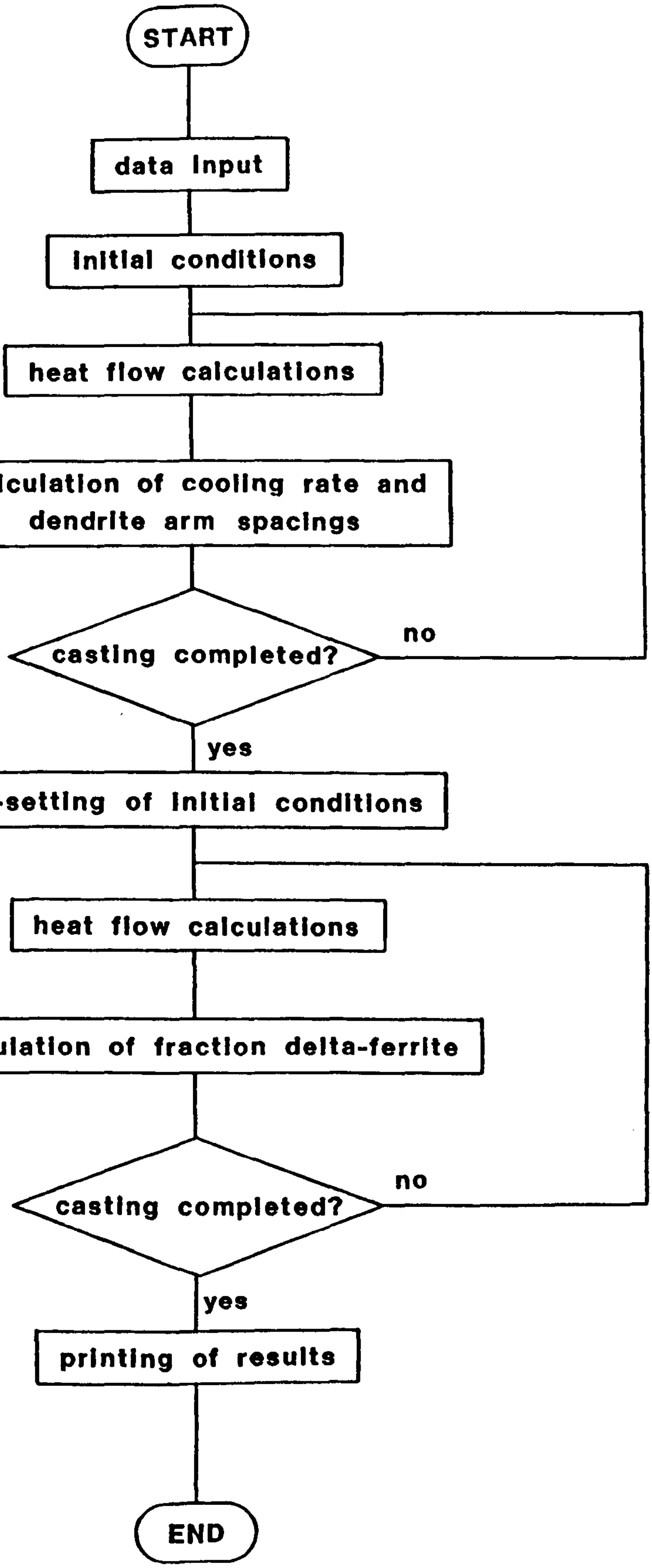

Figure 3.10 Schematic flow-diagram of the model for heat transfer and prediction of δ-ferrite content during continuous casting of stainless steel slabs.

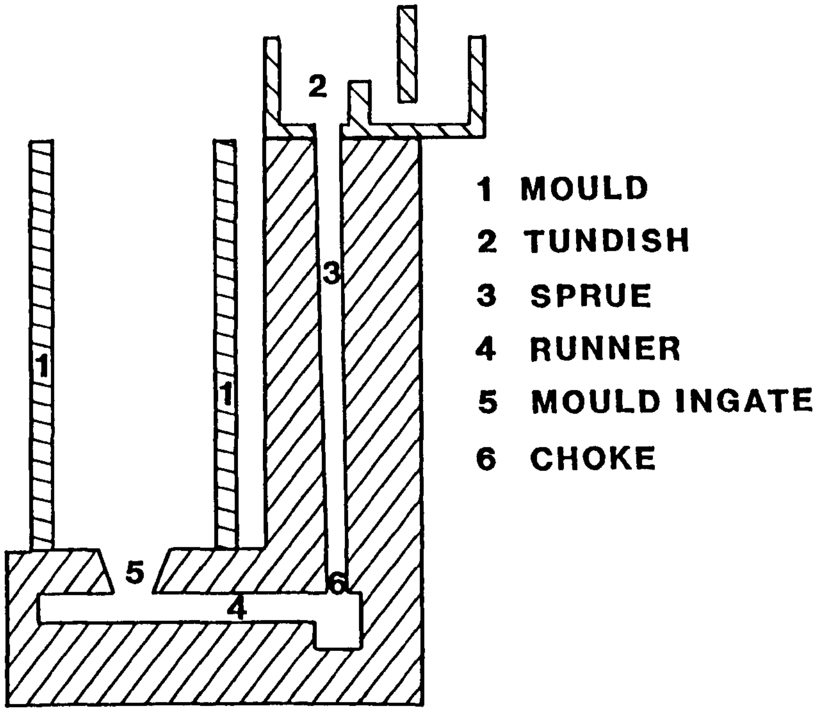

Figure 4.1 Schematic representation of laboratory-scale casting system.

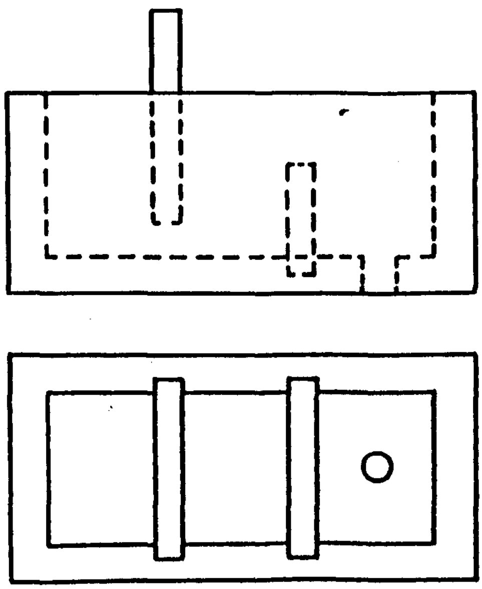

Figure 4.2 The wall and weir tundish used in the experiments.

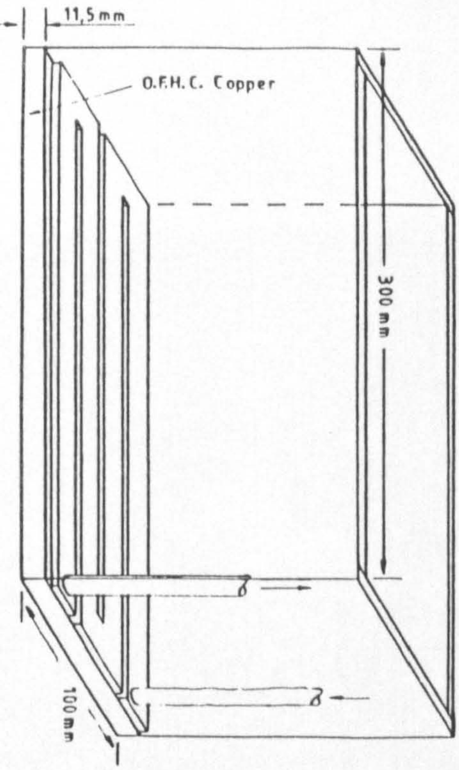

Figure 4.3 Schematic representation of the design of the water-cooled copper plate.

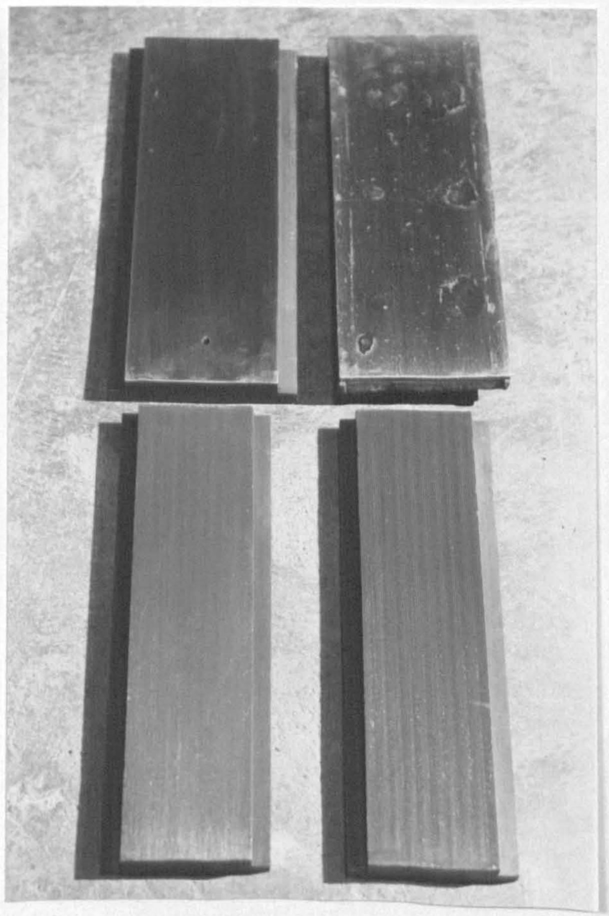

Figure 4.4 Mould walls used for casting in air.

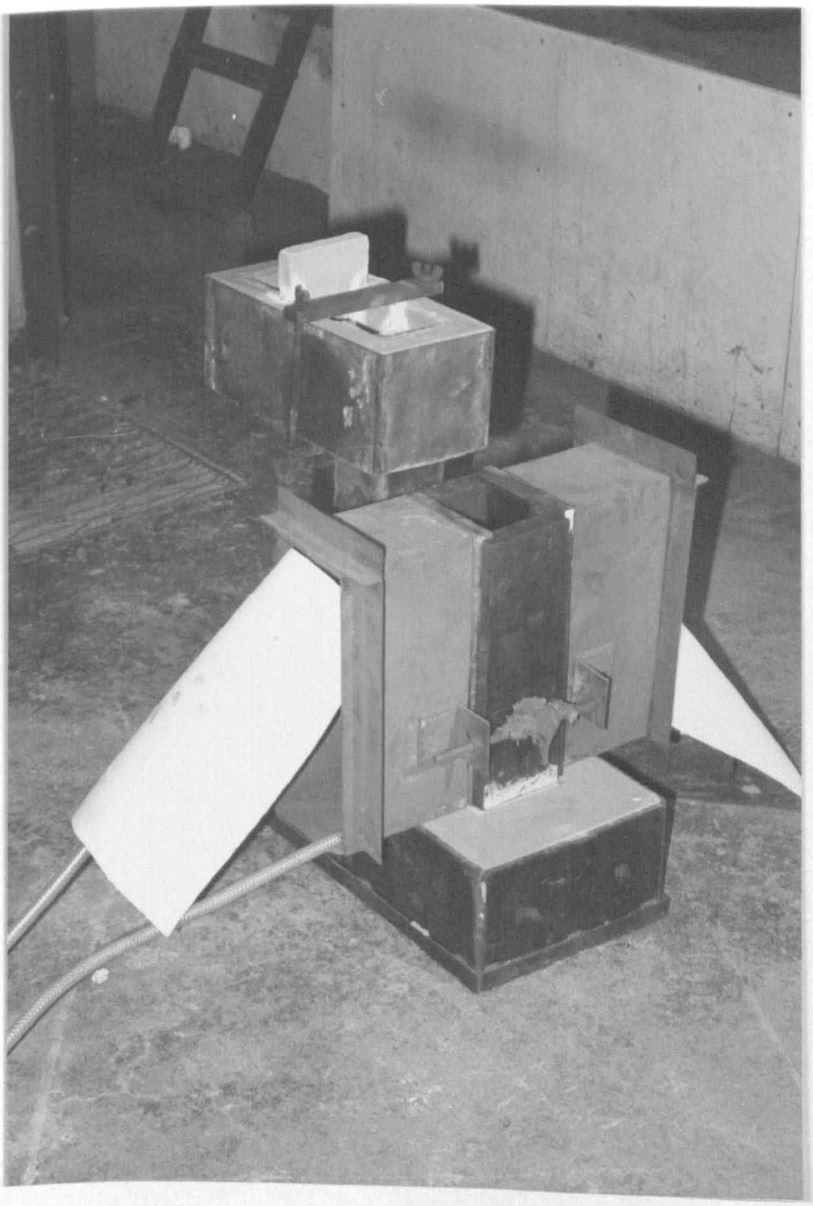

Figure 4.5 Experimental set-up for casting in air.

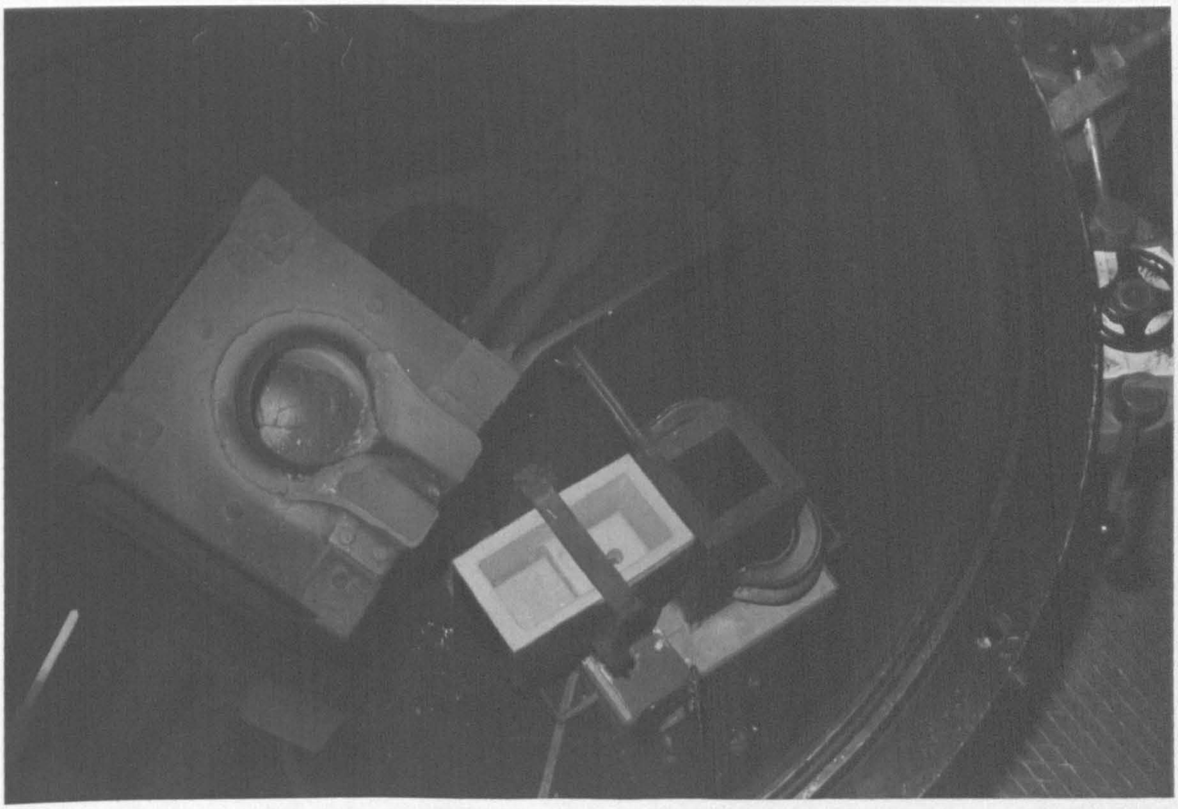

Figure 4.6 Experimental set-up for casting in controlled atmosphere.

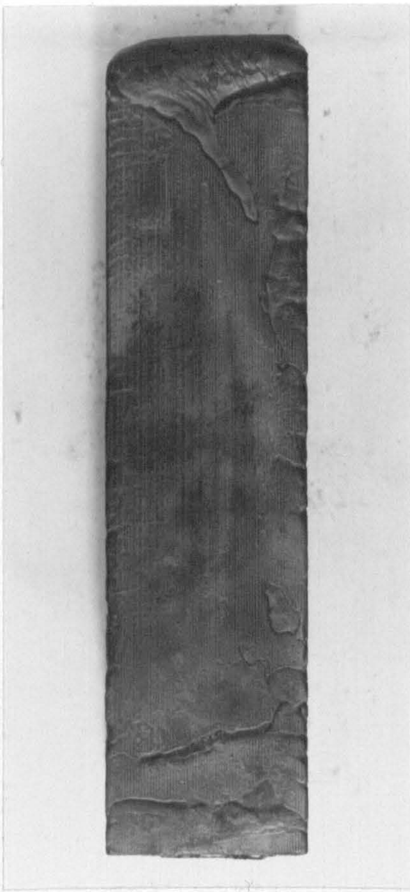

(a)

(b)

(c)

Figure 5.1 Influence of mould roughness on surface appearance of a fully ferritic alloy (Cast 5299).

(a) Rough mould wall
(b) Semi-rough mould wall
(c) Water-cooled copper wall

50 mm

CASTING DIRECTION

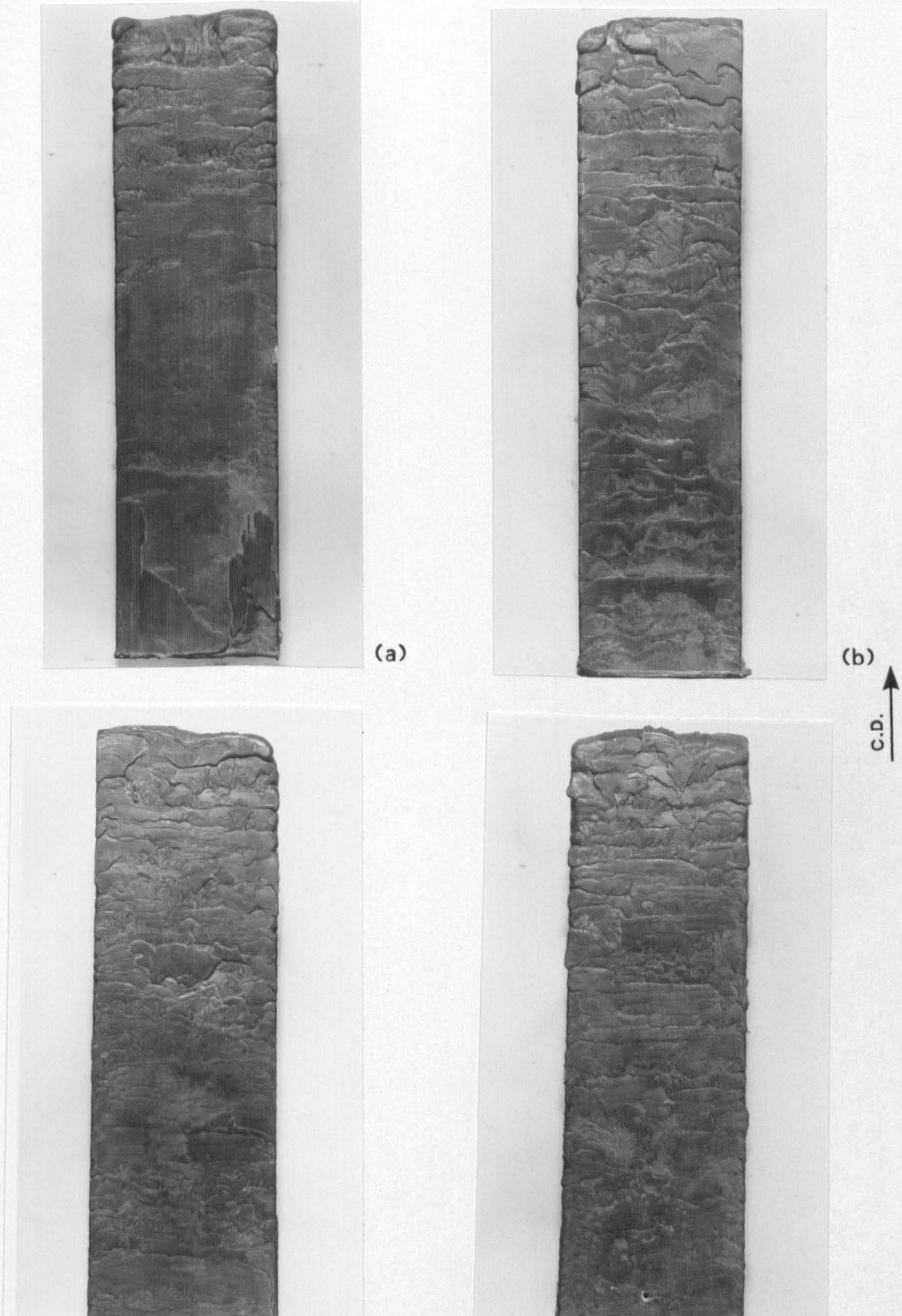

Figure 5.2 Influence of mould roughness on surface appearance of a 25/20-alloy (Cast 5333).
(a) Rough mould wall (b) Semi-rough mould wall
(c) Water-cooled mould wall (d) Ground mould wall

50mm

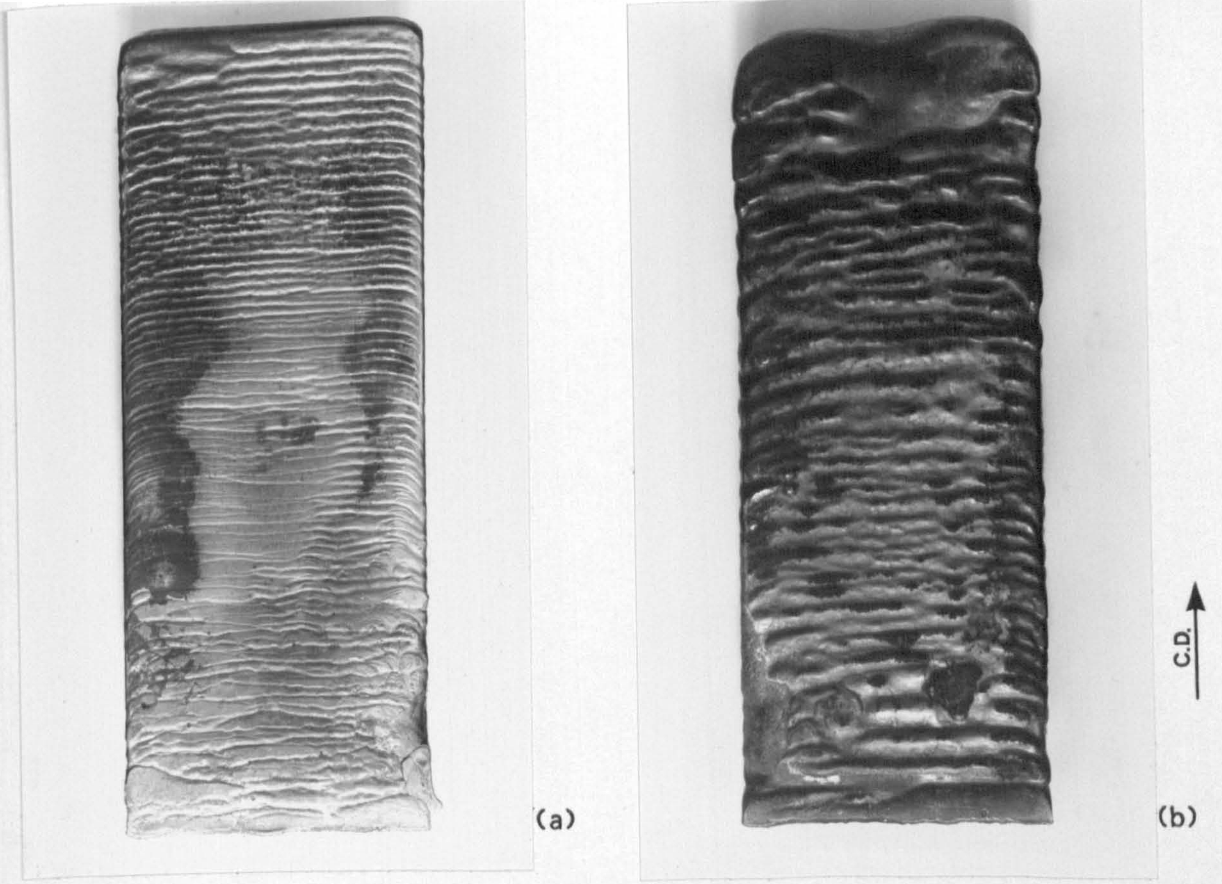

Figure 5.3 Influence of teeming rate on surface appearance (helium atmosphere)
(a) Teeming time 8s (Cast 5522) (b) Teeming time 25s (Cast 5551)

25mm

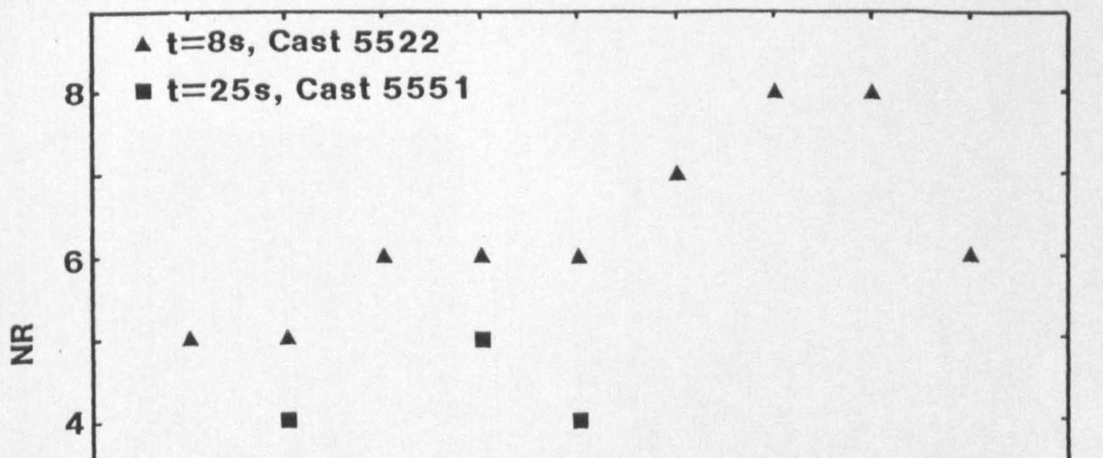

Figure 5.4 NR (number of ripples per 20mm) as a function of distance along the ingot (c.f. Figure 5.3)

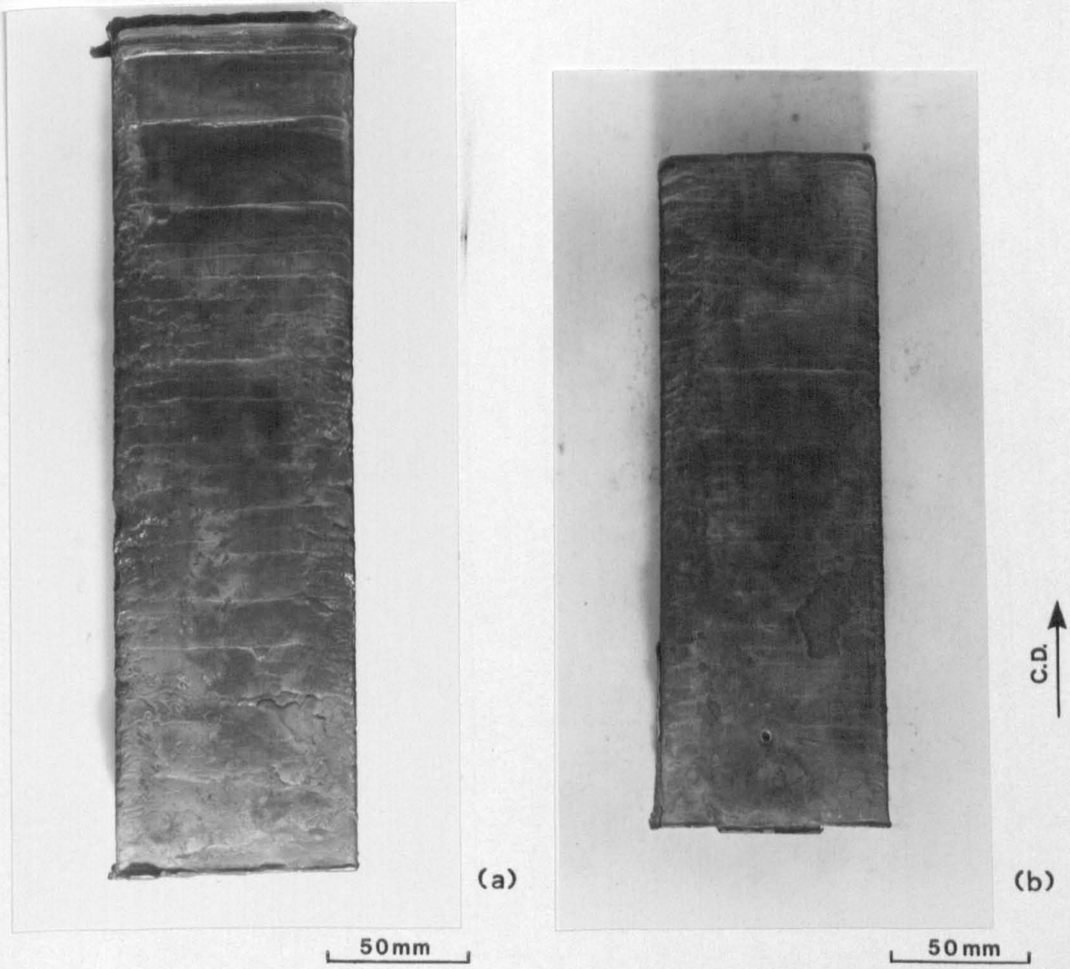

Figure 5.5 Influence of superheat on surface appearance of 18/14-alloys.
(a) ΔT = 10K (Cast 5203)
(b) ΔT = 28K (Cast 5298)

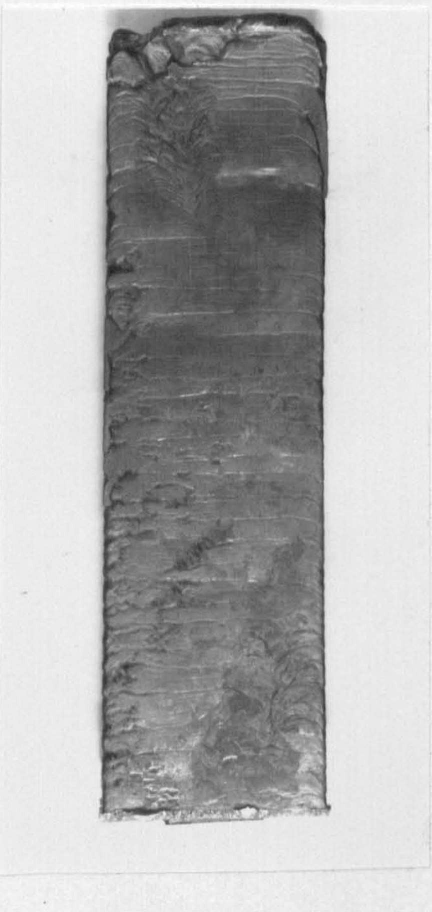

Figure 5.6 Influence of alloy content on surface appearance of fully ferritic grades (17%Cr-alloy, Cast 5275, c.f. Figure 5.1(c)).

50mm

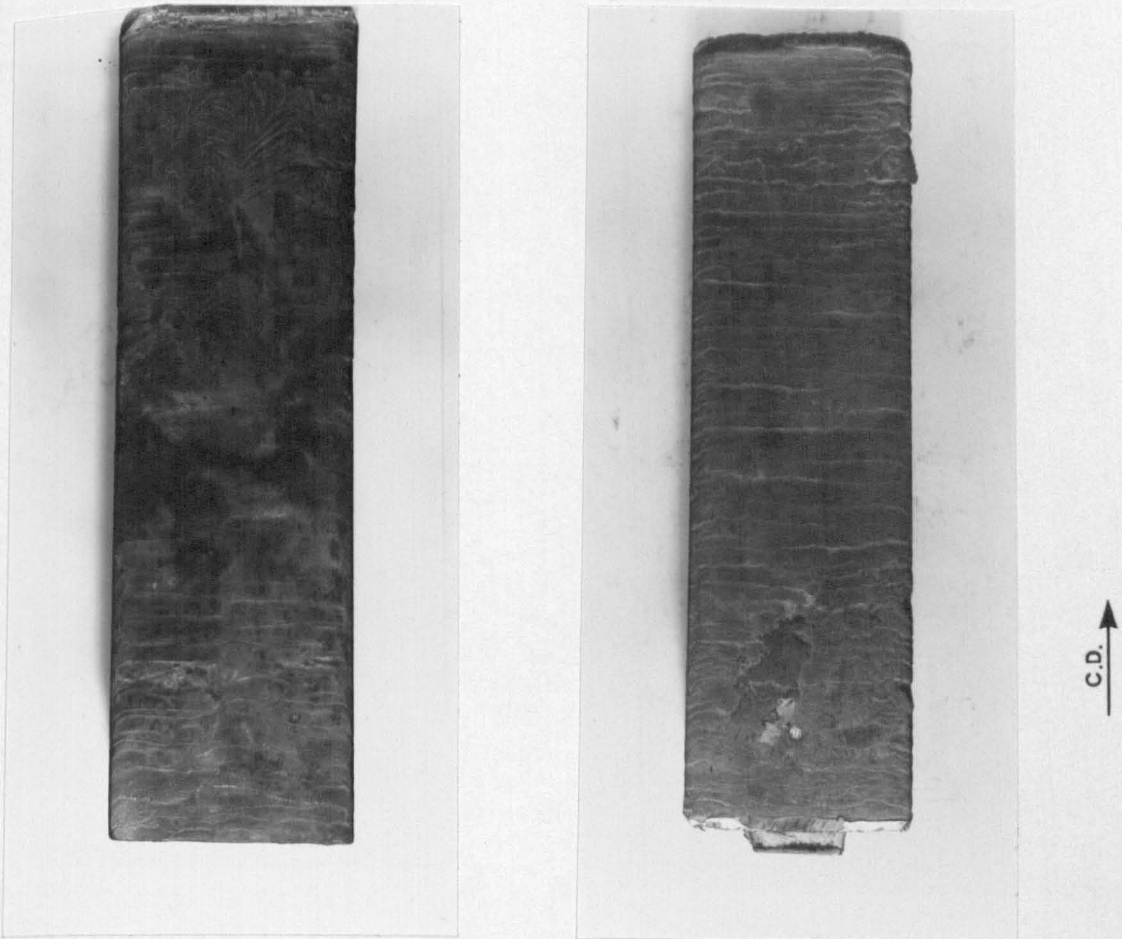

(a) (b)

50mm 50mm

Figure 5.7 Influence of solidification mode (alloy content) on surface appearance (c.f. Figure 5.5(a)).

(a) Type A (18/8, Cast 5202)
(b) Type B (18/10, Cast 5282)

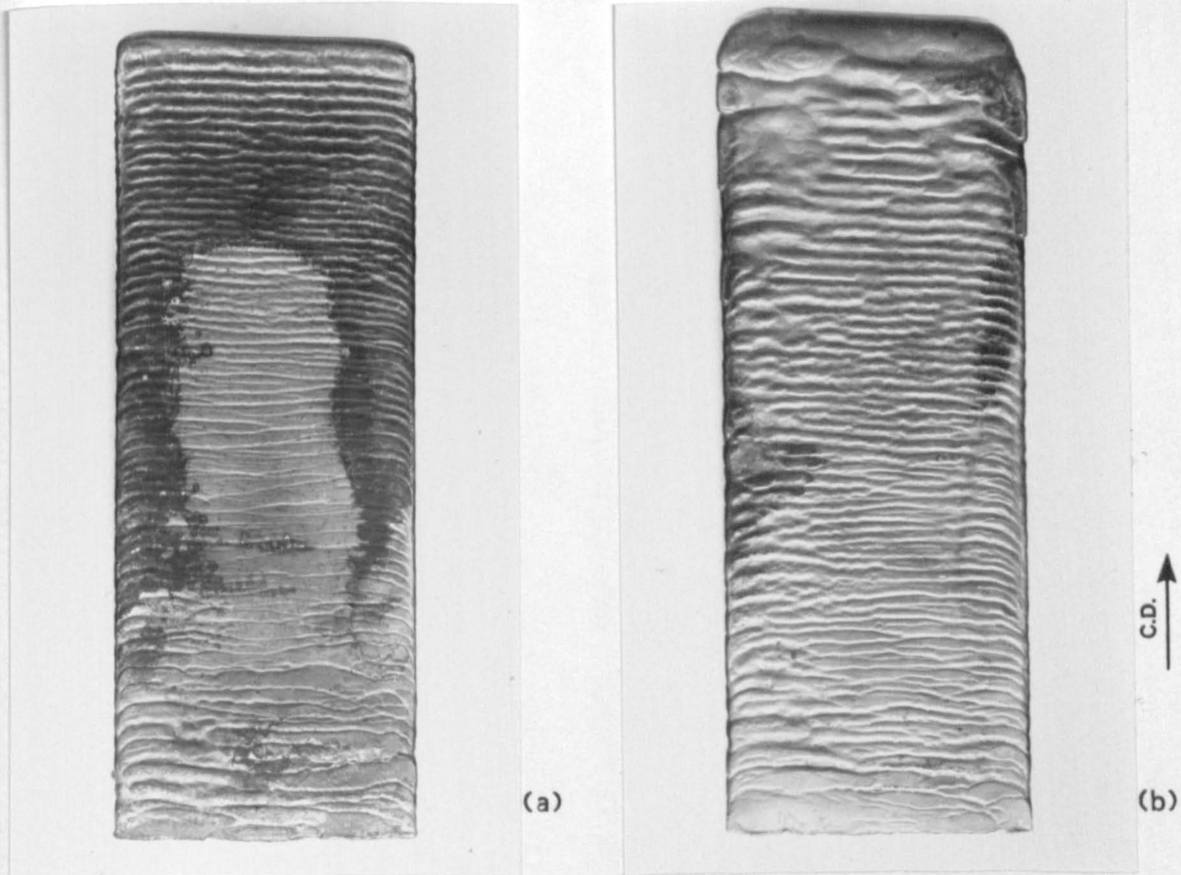

Figure 5.8 Influence of alloy content on surface appearance of fully austenitic alloys (helium atmosphere).
(a) 18/14 (Cast 5522) (b) 25/20 (Cast 5525) 25mm

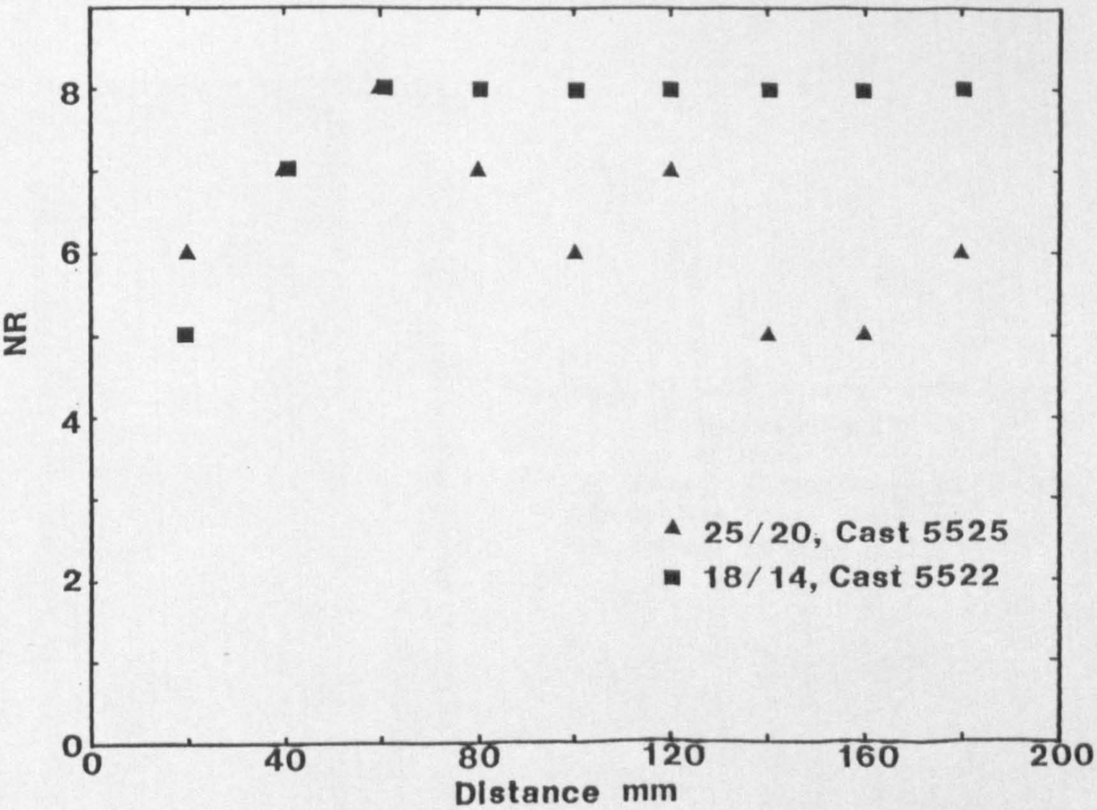

Figure 5.9 NR (number of ripples per 20mm) as a function of distance along the ingot (c.f. Figure 5.8).

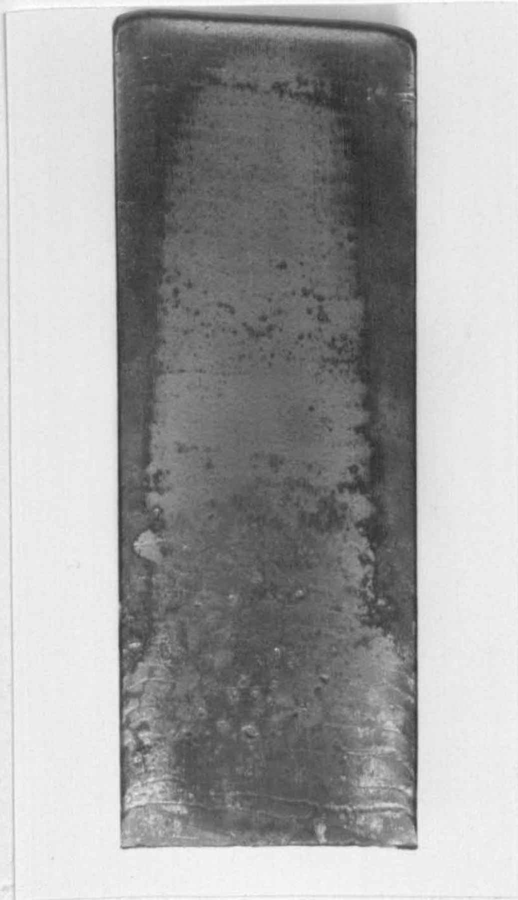

(a)

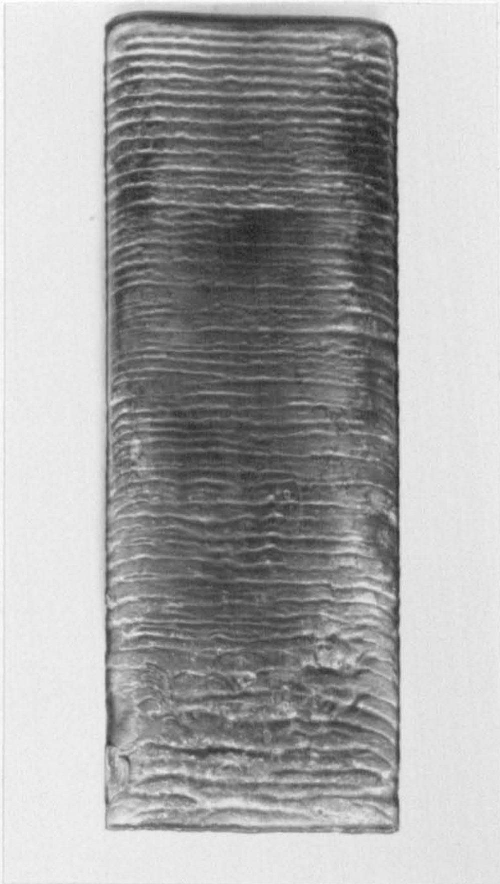

(b)

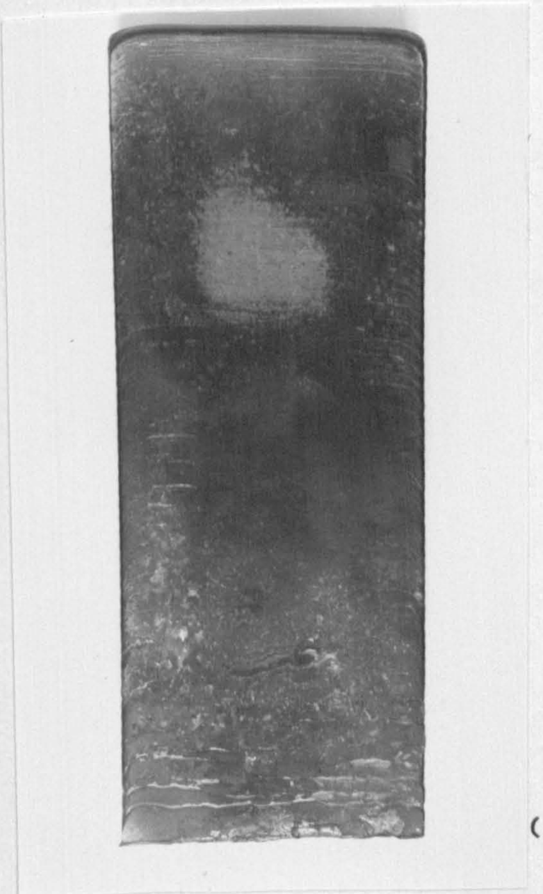

(c)

Figure 5.10 Influence of atmosphere on surface appearance of 18/14-alloys.
(a) Vacuum (Semi-rough wall, Cast 5550)
(b) Helium (Semi-rough wall, Cast 5522)
(c) Vacuum (Ground wall, Cast 5550)

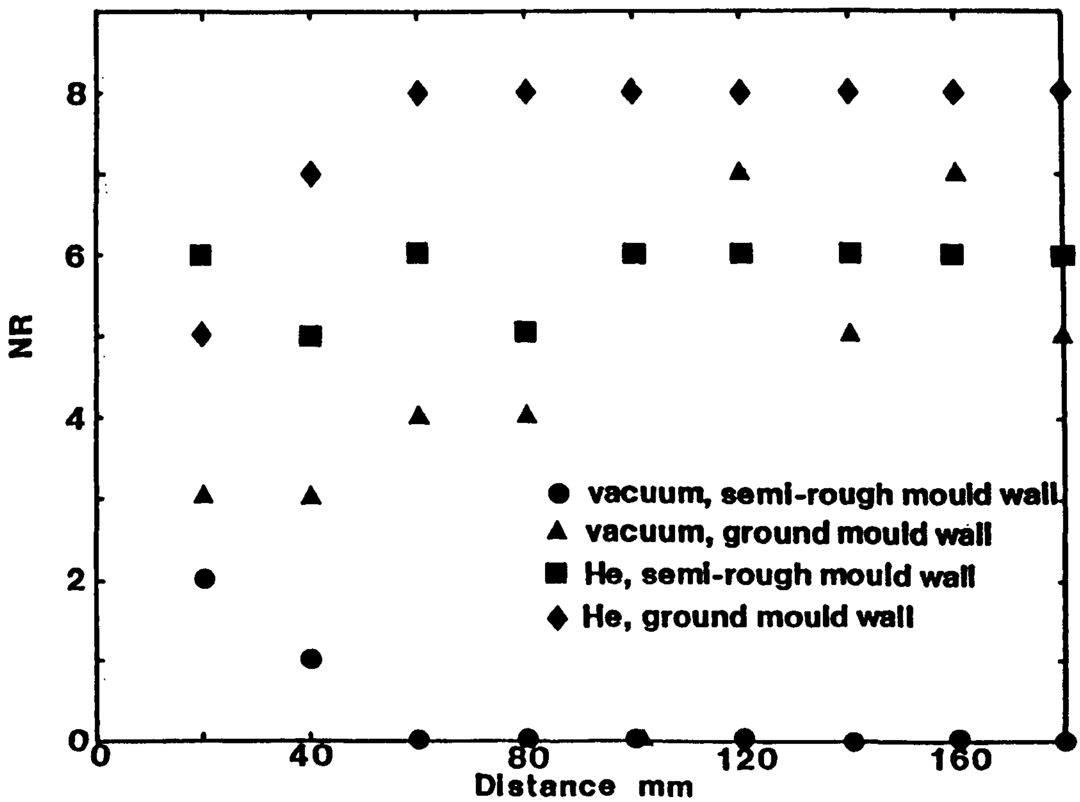

Figure 5.11 NR (number of ripples per 20mm) as a function of distance along the ingot for different atmospheres.

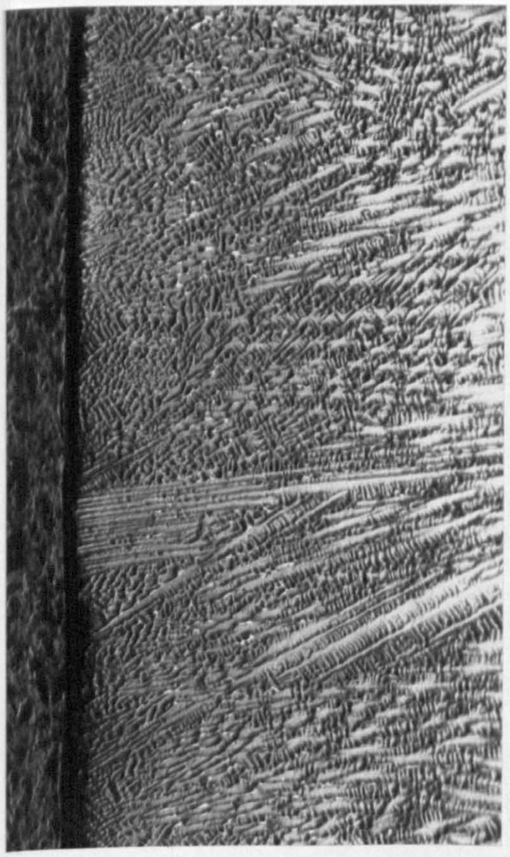

(a)

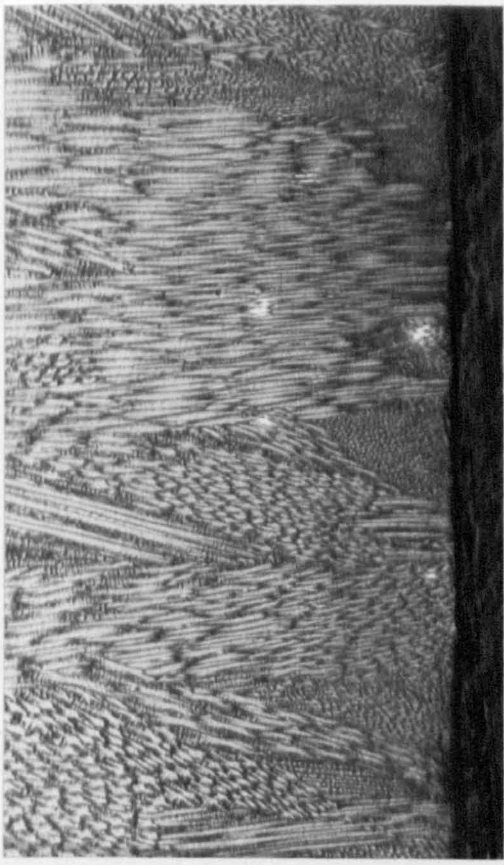

(b)

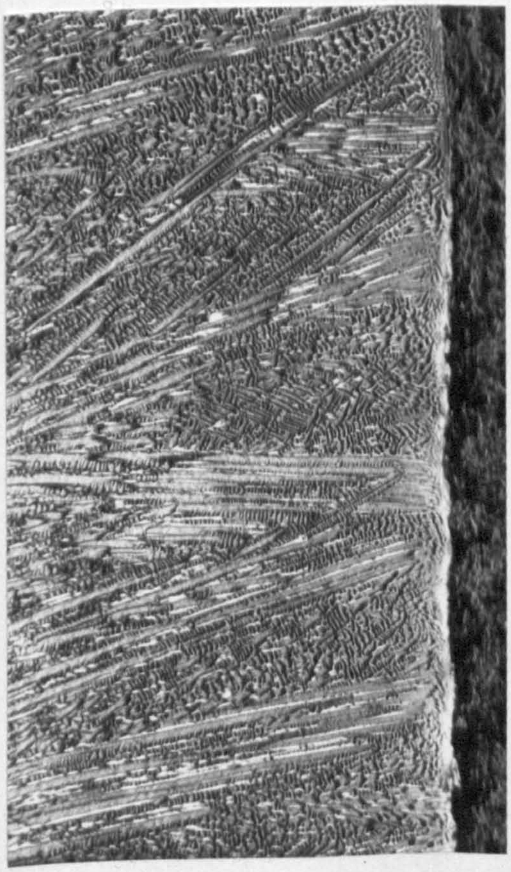

(c)

Figure 5.12 Structural variation with mould roughness (Cast 5550, vacuum, colour etchant).

(a) Rough mould wall
(b) Ground mould wall
(c) Semi-rough mould wall

0.5mm

C.D.

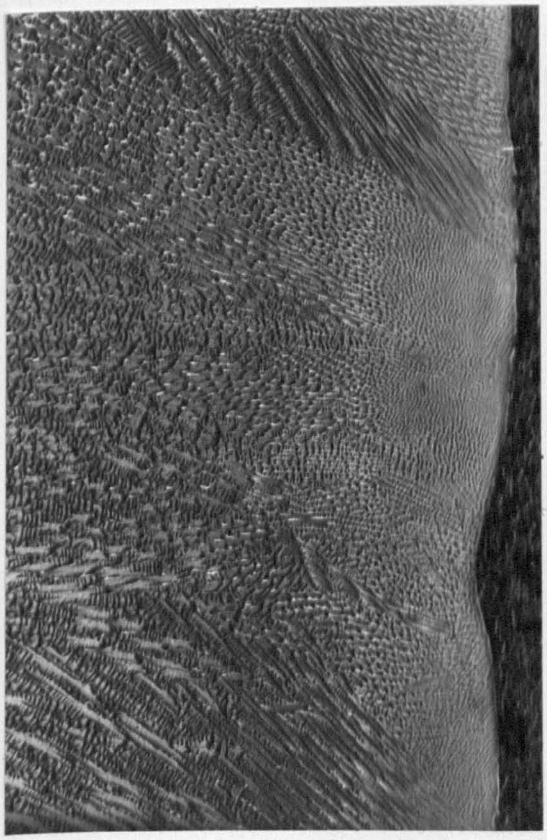

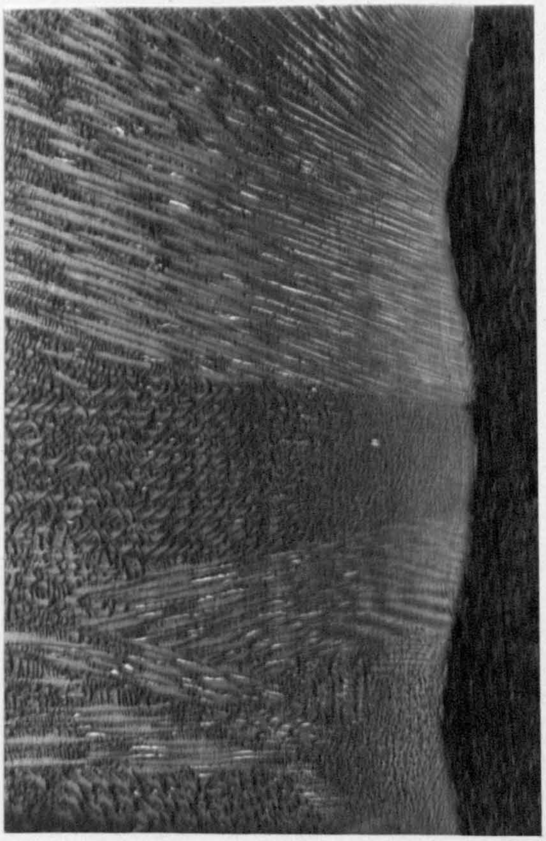

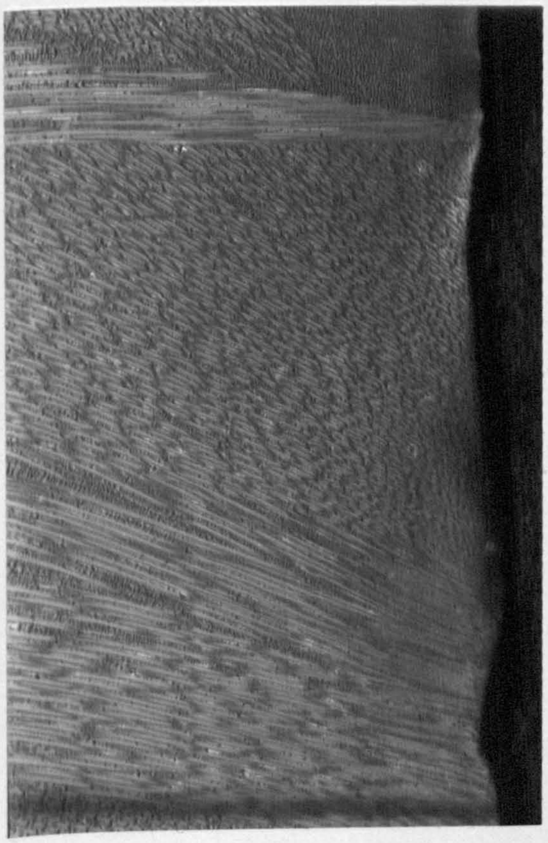

Figure 5.13 Microstructural features formed at high teeming rate (Cast 5522, helium, colour etchant).

0.5mm

C.D.

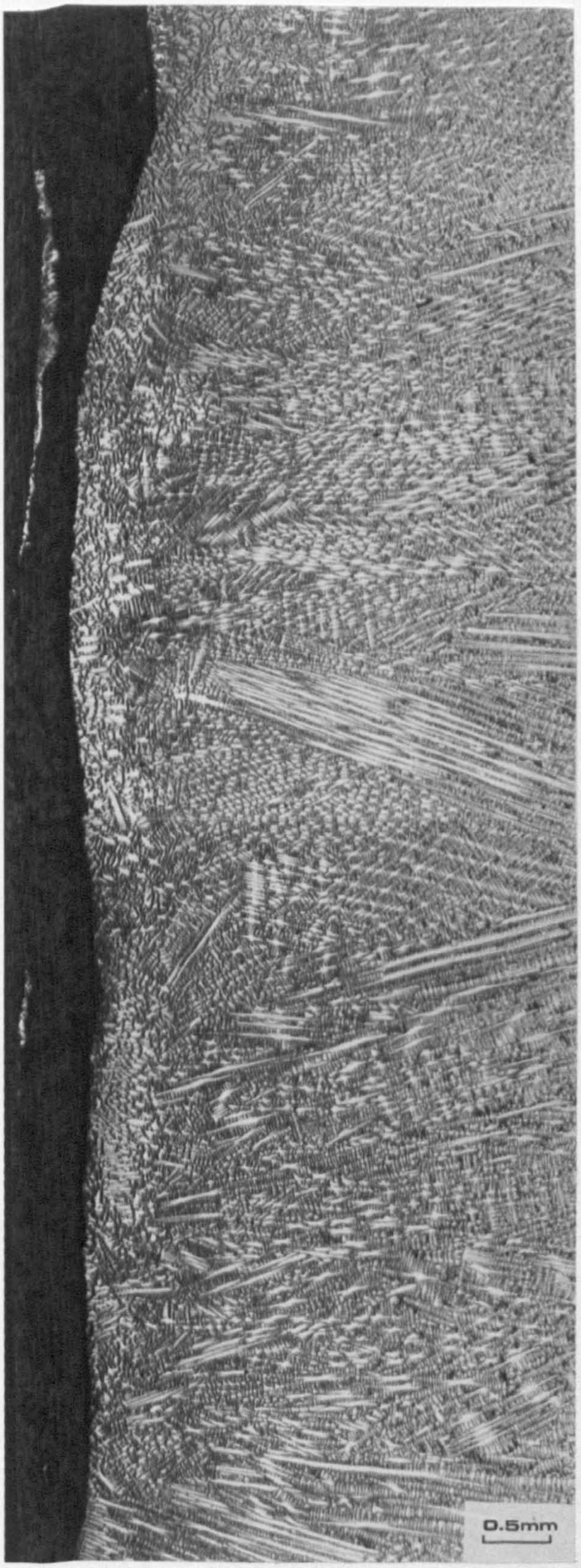

Figure 5.14 Microstructural features formed at low teeming rate (Cast 5551, helium, colour etchant).

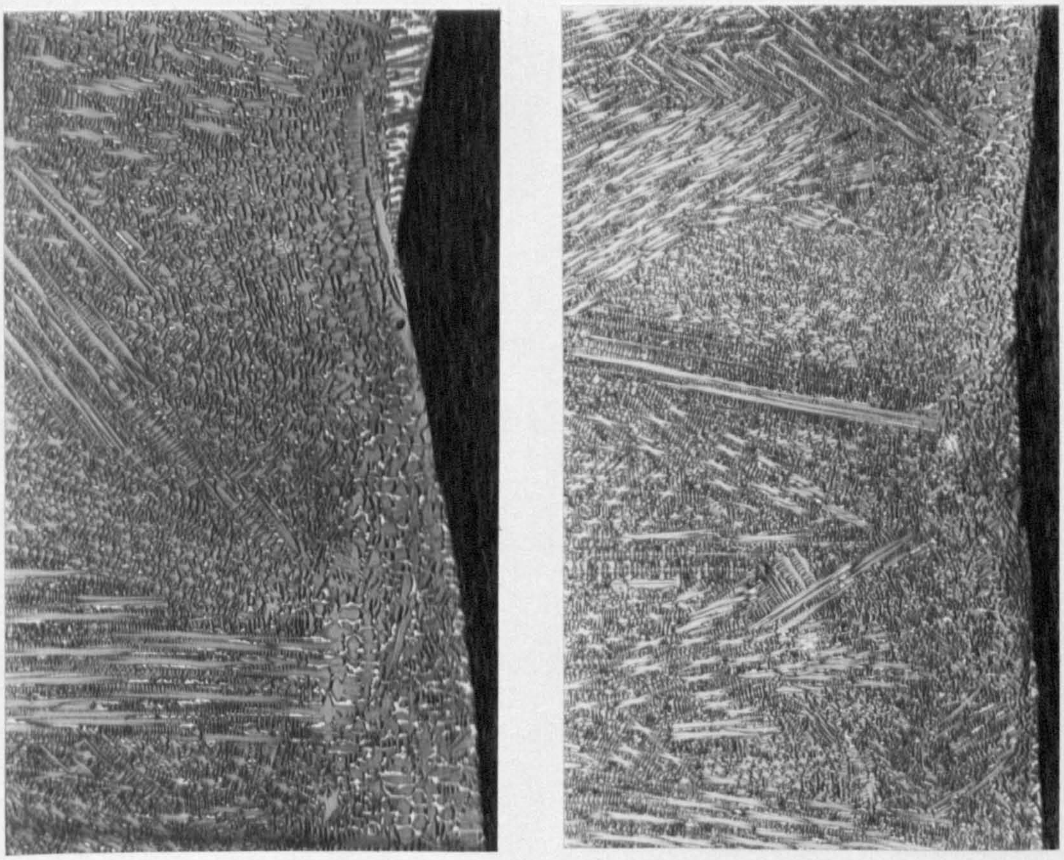

(a) 0.5 mm

(b) 1.0 mm

Figure 5.15 Microstructural features formed at low teeming rate (Cast 5551, helium, colour etchant).

(a) Tip of partially-solidified meniscus.
(b) Structures below region shown in (a).

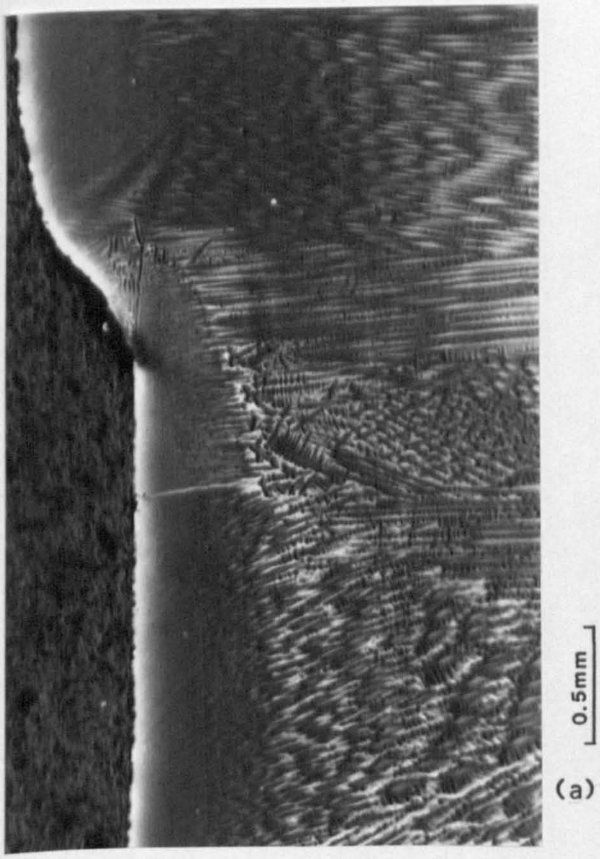

(a)

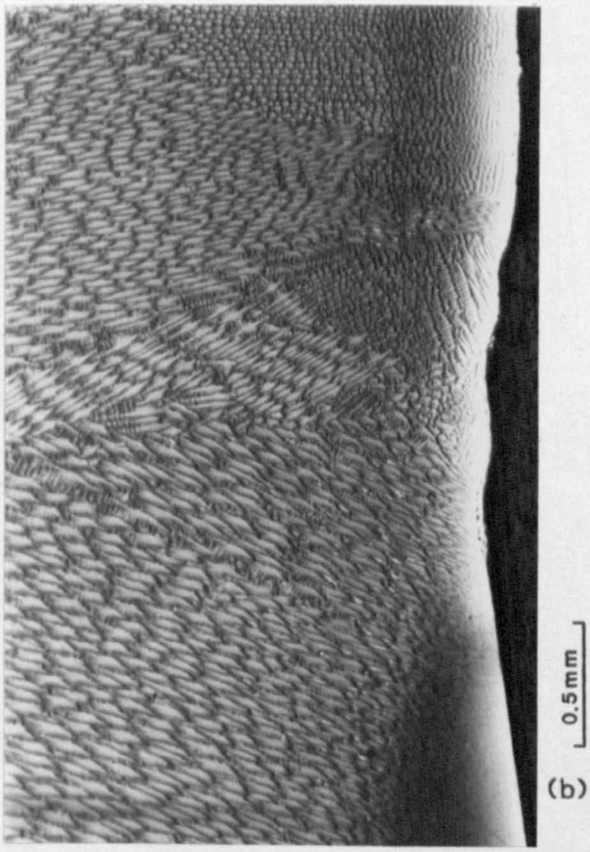

(b)

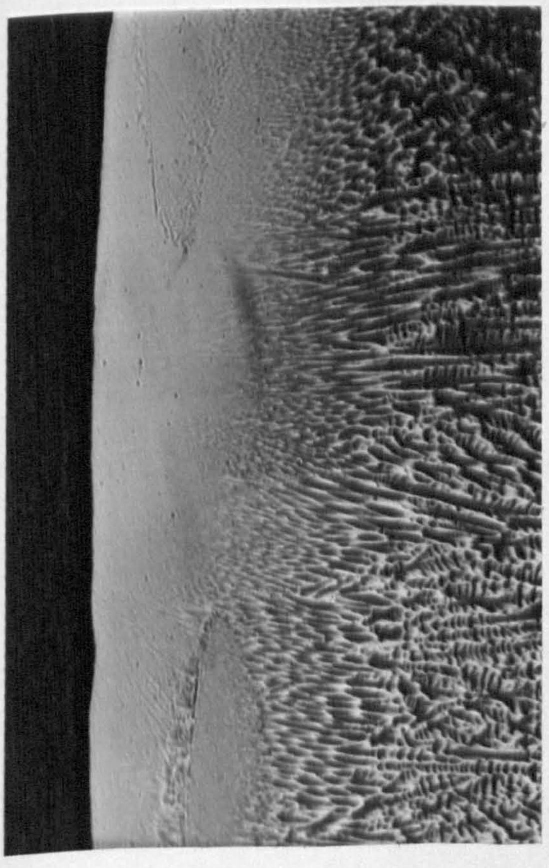

(c)

Figure 5.16 Influence of superheat on structures (colour etchant).

(a) Cast 5203, ΔT = 10K
(b) Cast 5298, ΔT = 28K
(c) Cast 5298, ΔT = 28K

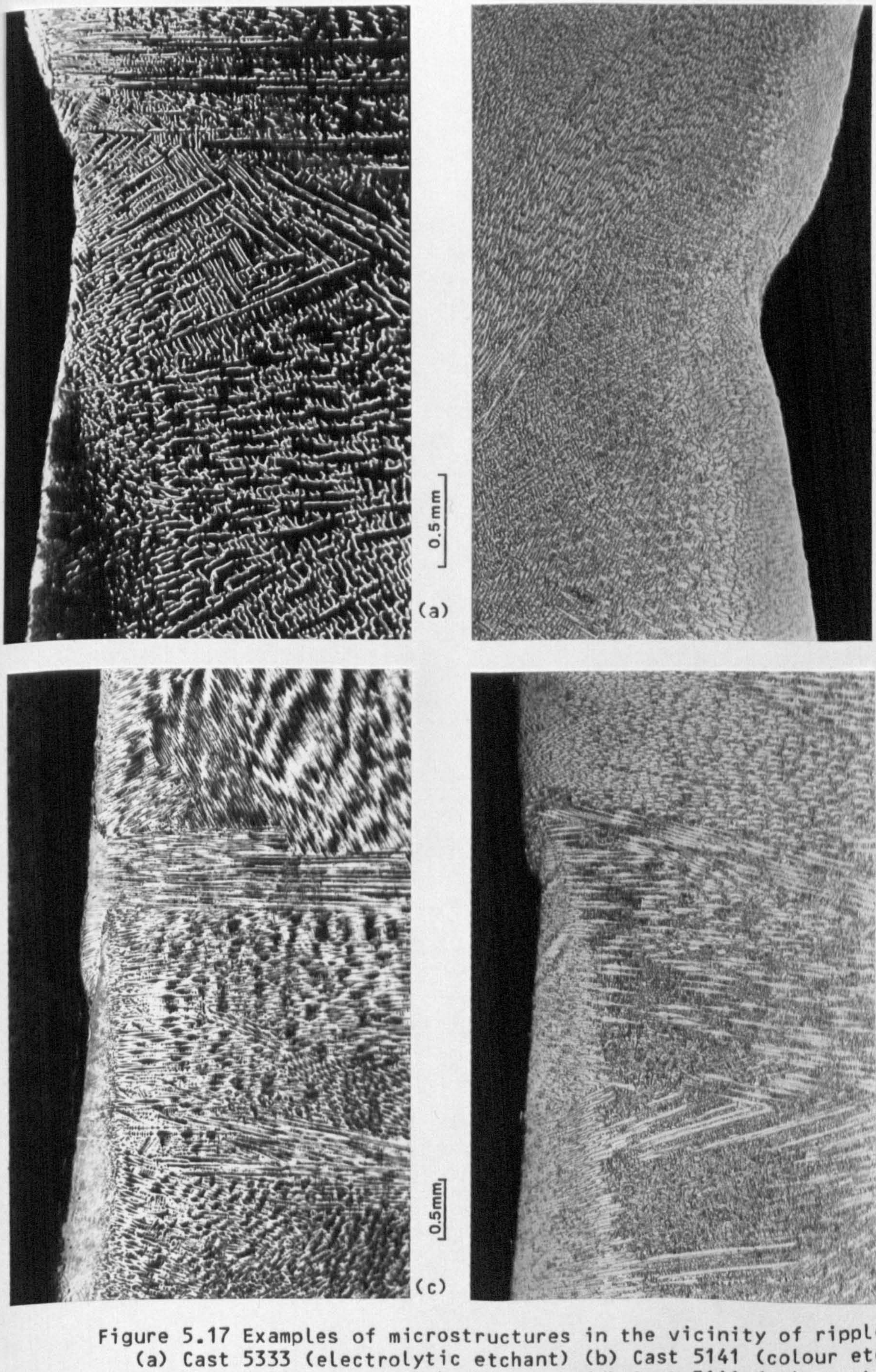

Figure 5.17 Examples of microstructures in the vicinity of ripples.
(a) Cast 5333 (electrolytic etchant) (b) Cast 5141 (colour etchant)
(c) Cast 5298 (colour etchant) (d) Cast 5141 (colour etchant)

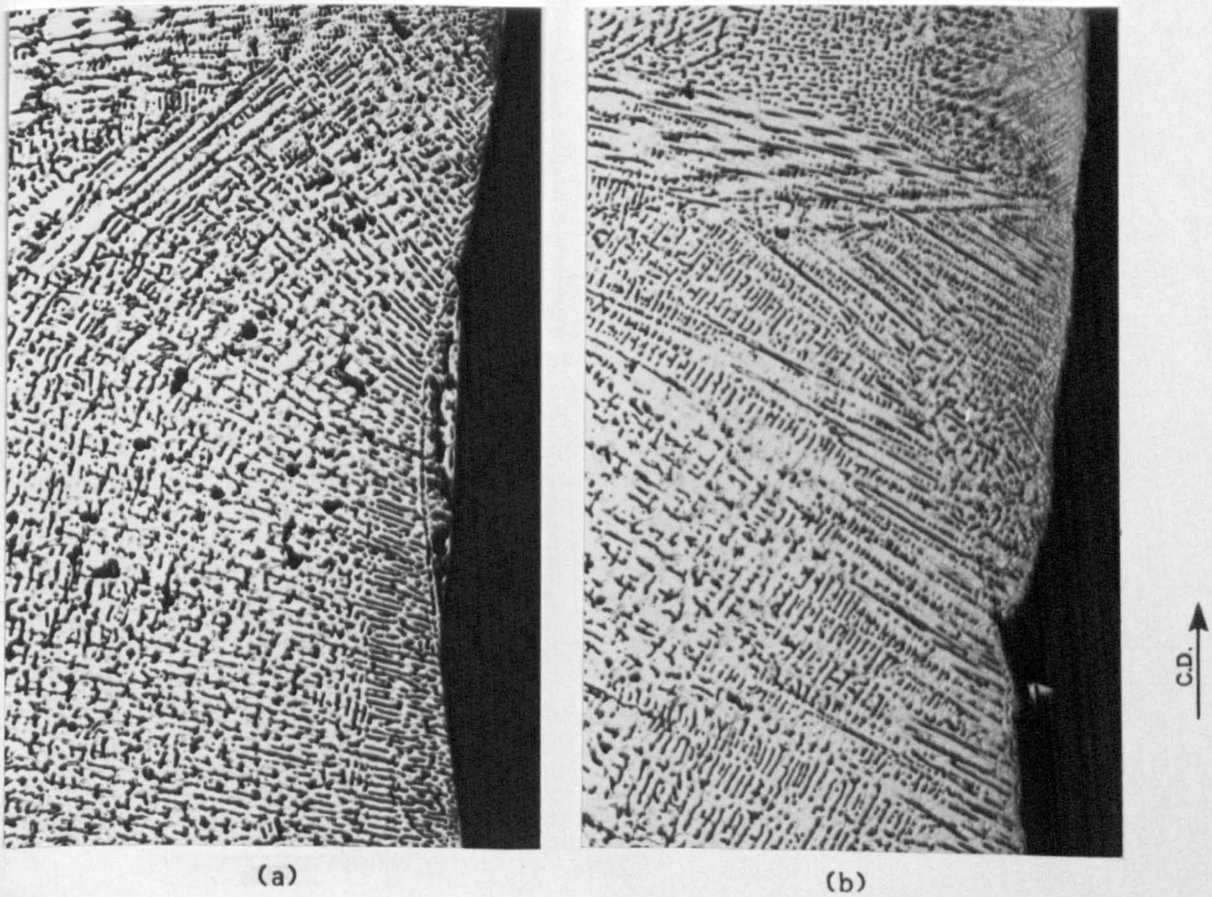

Figure 5.18 Microstructures in the vicinity of ripples in a Type A alloy (Cast 5202, electrolytic etchant).

(a) bending-back and lateral flow
(b) overflow

0.25 mm

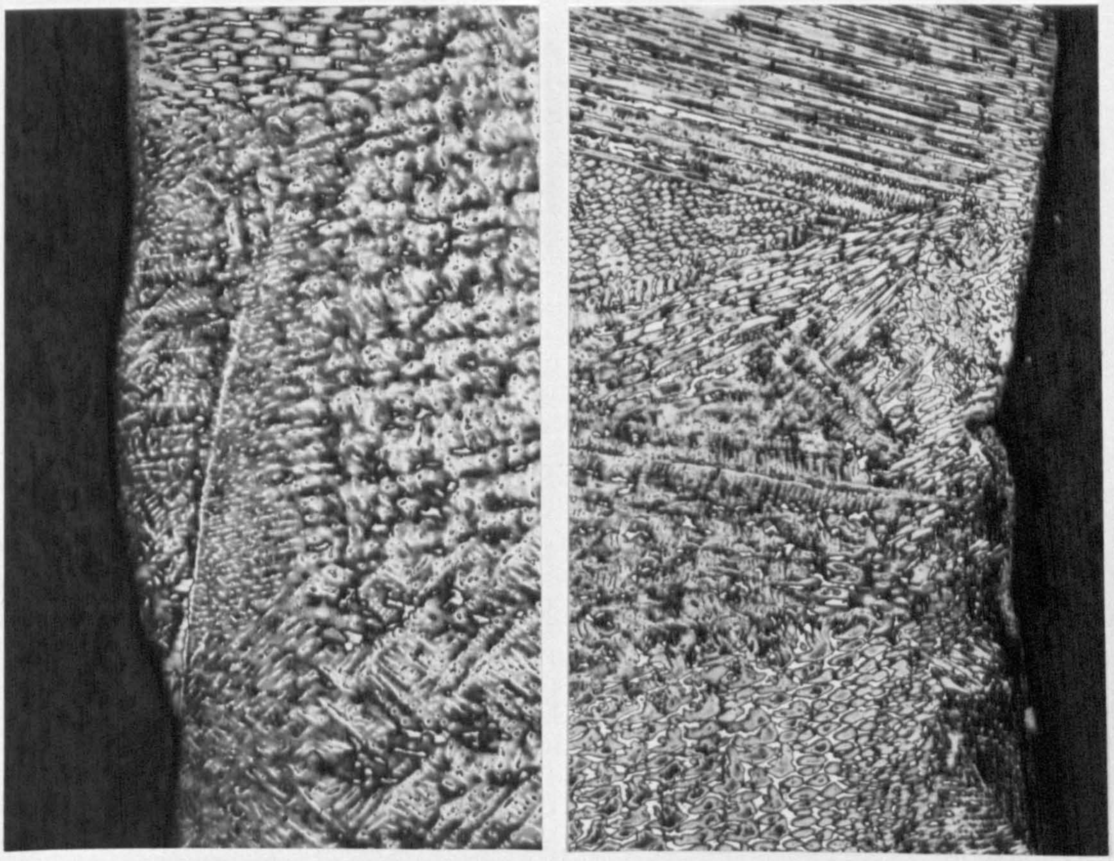

(a) (b)

Figure 5.19 Microstructures in the vicinity of ripples in a Type B alloy (Cast 5282, colour etchant).

(a) overflow
(b) bending-back

0.25mm

C.D.

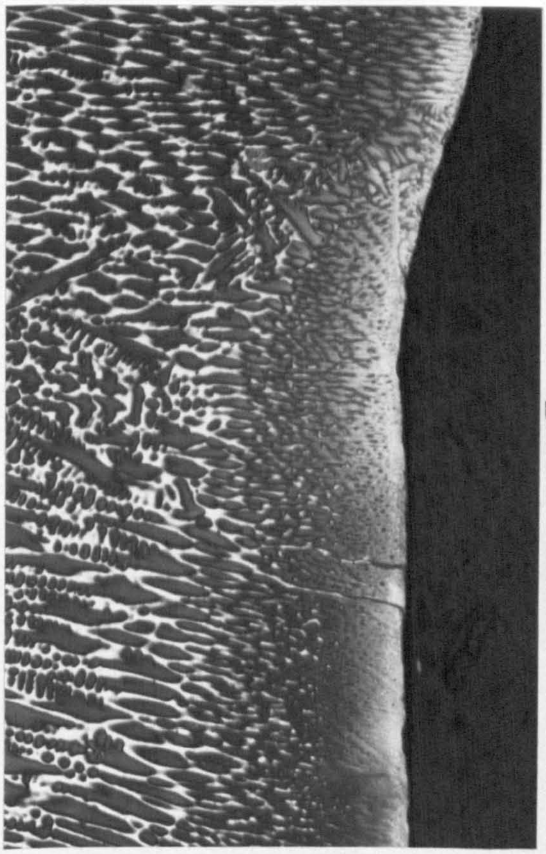

Figure 5.20 Microstructures in the vicinity of a ripple in a Type D alloy. (Cast 5203, colour etchant)

0.25mm

C.D.

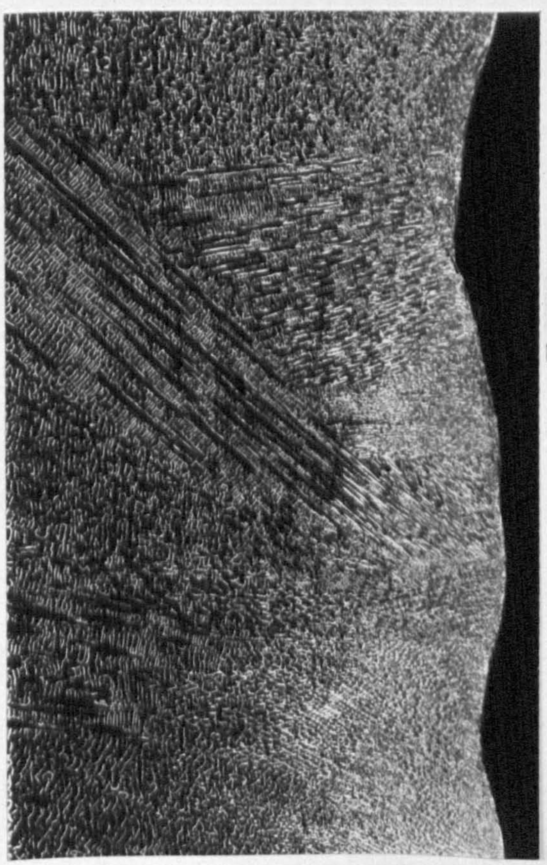

Figure 5.21 Microstructures in the vicinity of a ripple in a Type D alloy. (Cast 5525, electrolytic etch.)

0.5mm

C.D.

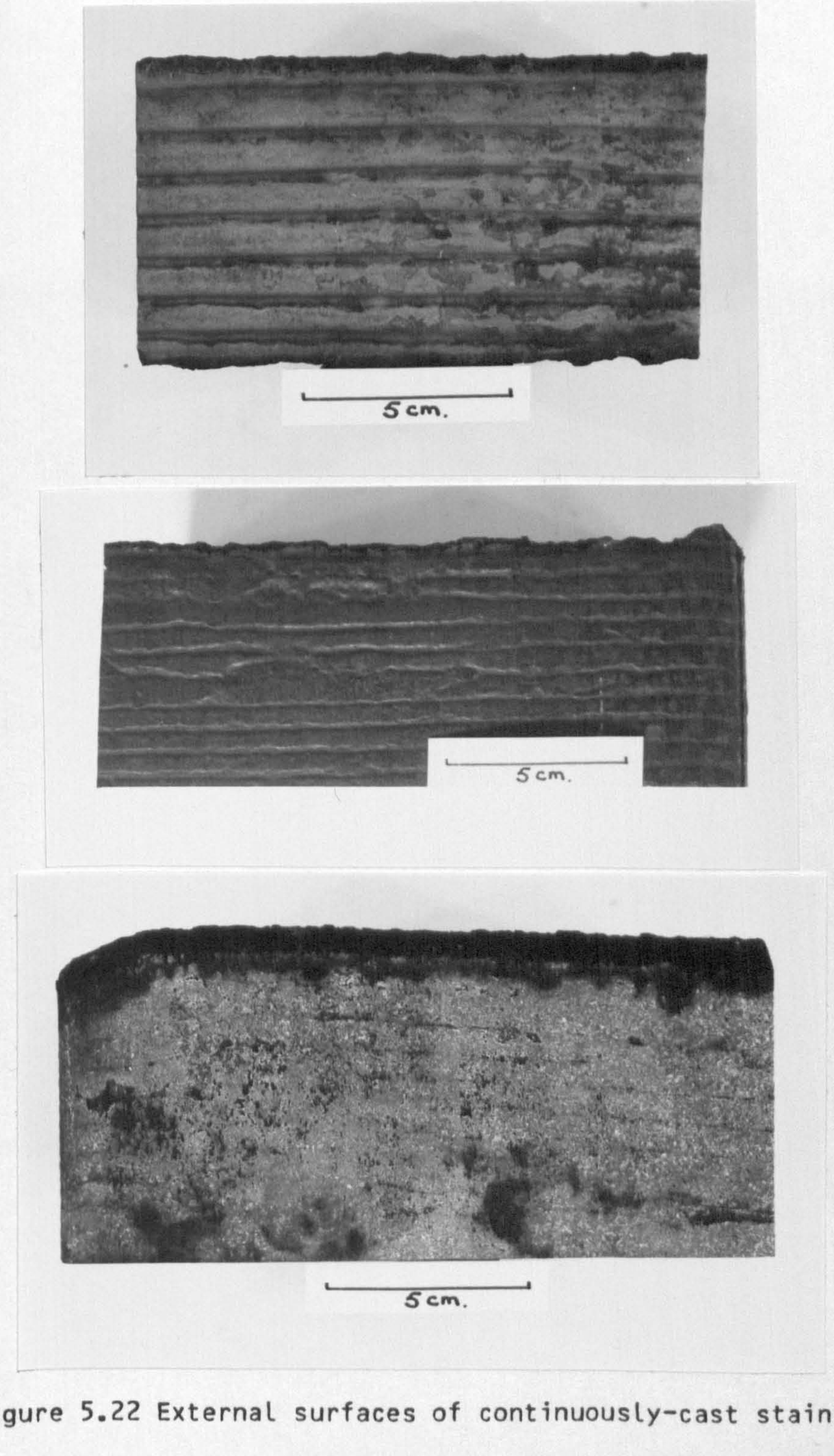

(a)

(b)

(c)

Figure 5.22 External surfaces of continuously-cast stainless steel slabs.

(a) 18/8-slab
(b) 302-slab
(c) 316-slab

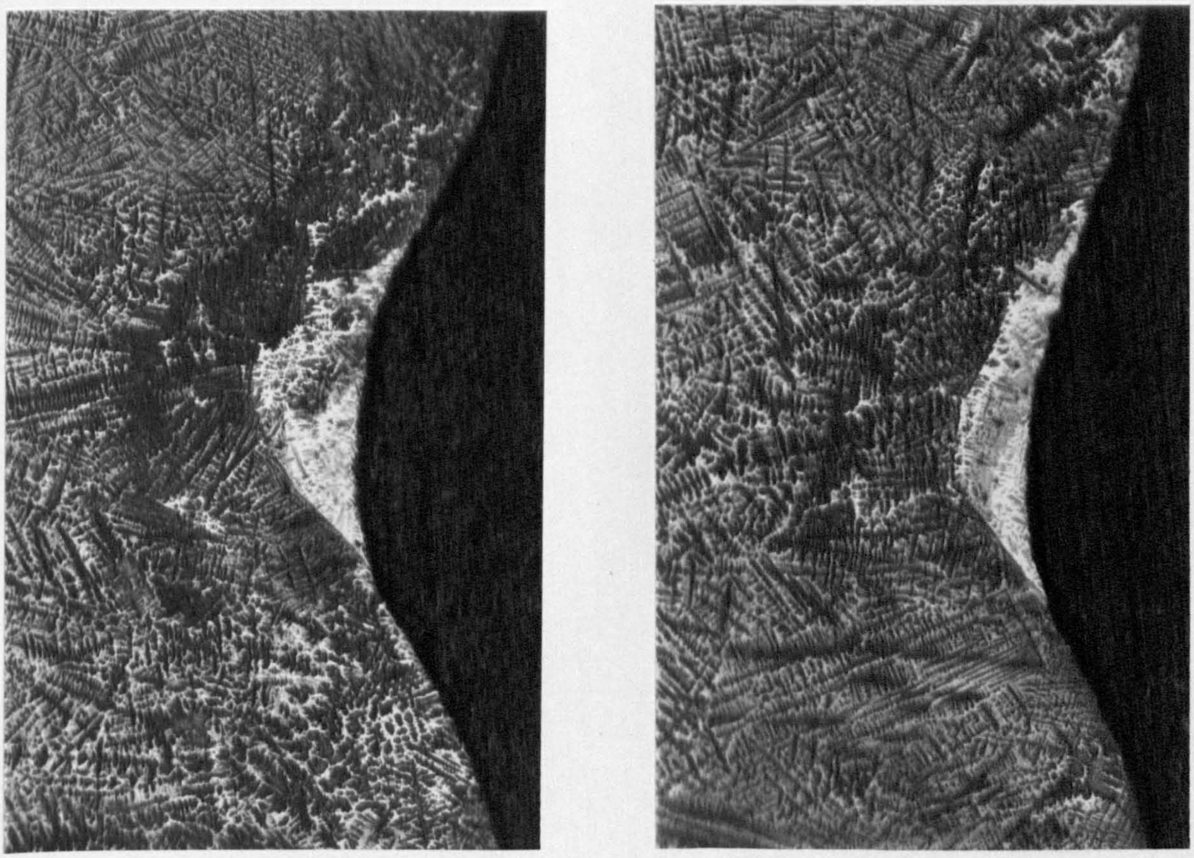

Figure 5.23 Microstructures in the vicinity of oscillation marks (18/8-slab, colour etchant).

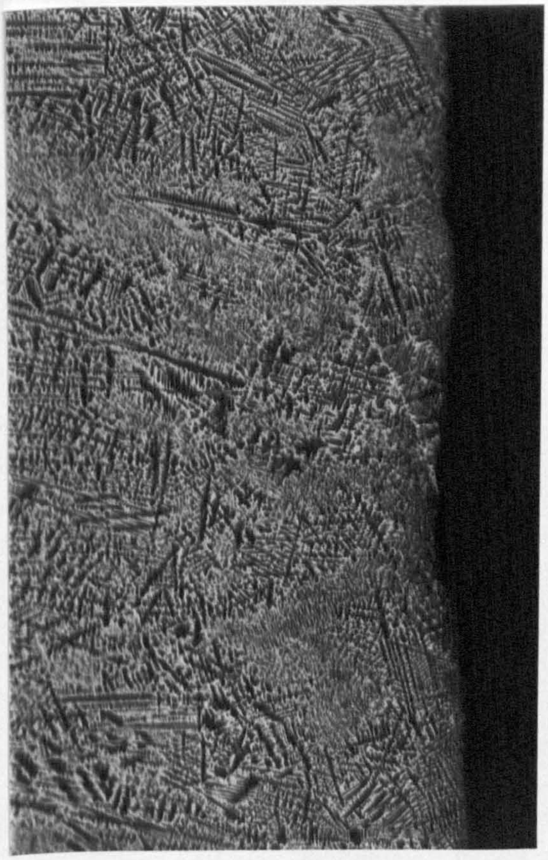

(a)

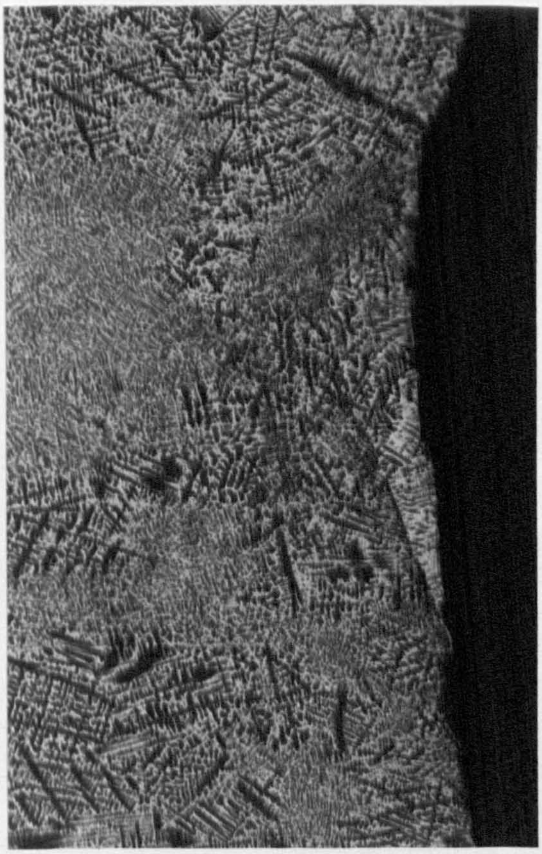

(b)

(c)

Figure 5.24 Microstructures in the vicinity of oscillation marks (colour etch)
(a) 316-slab
(b) 316-slab
(c) 302-slab

0.5mm

C.D.

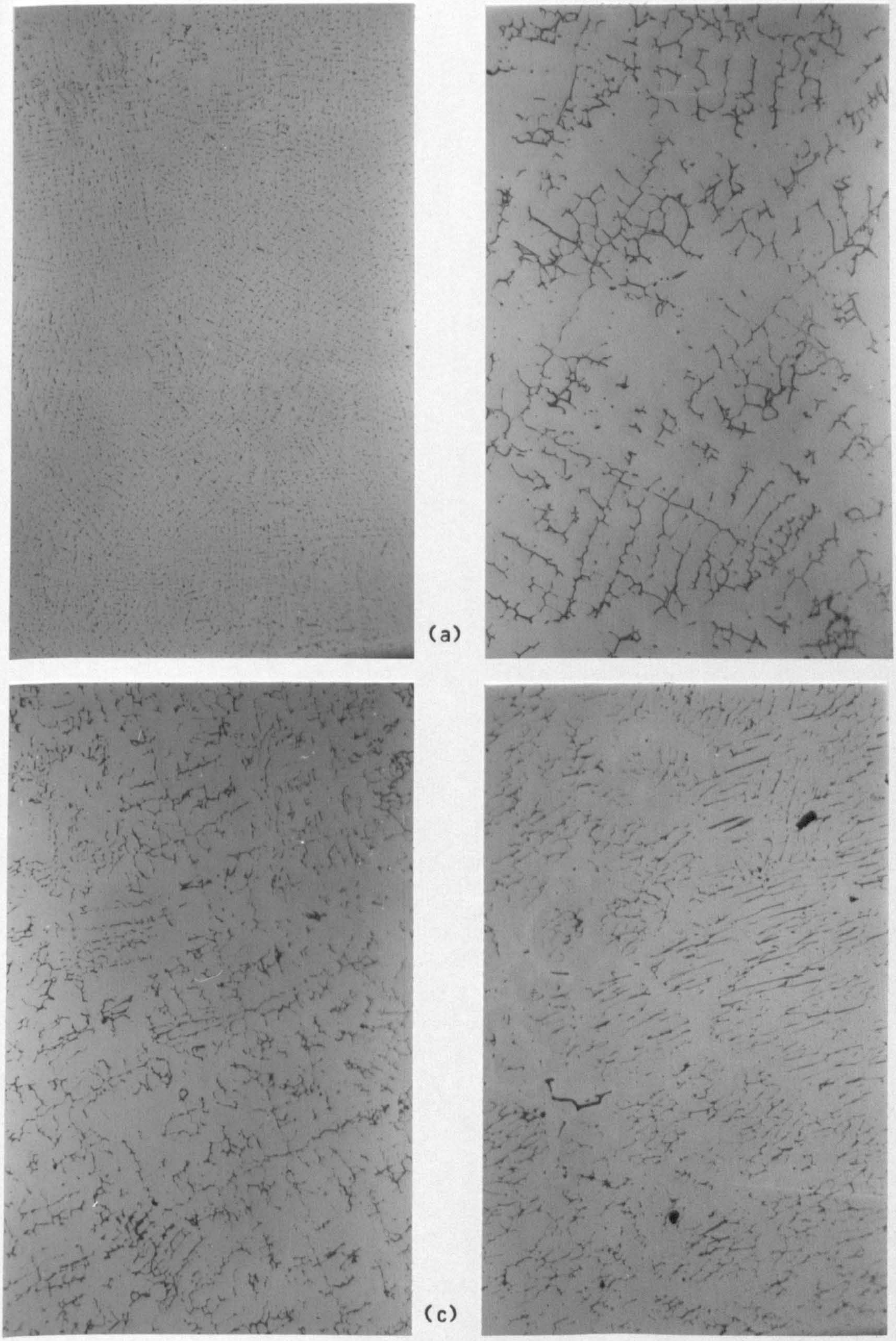

(a) (b)

(c) (d)

Figure 5.25 Structures of δ-ferrite at different distances from the surface of the 18/8-slab.
(a) 0mm (b) 30mm (c) 60mm (d) 80mm

0.25mm

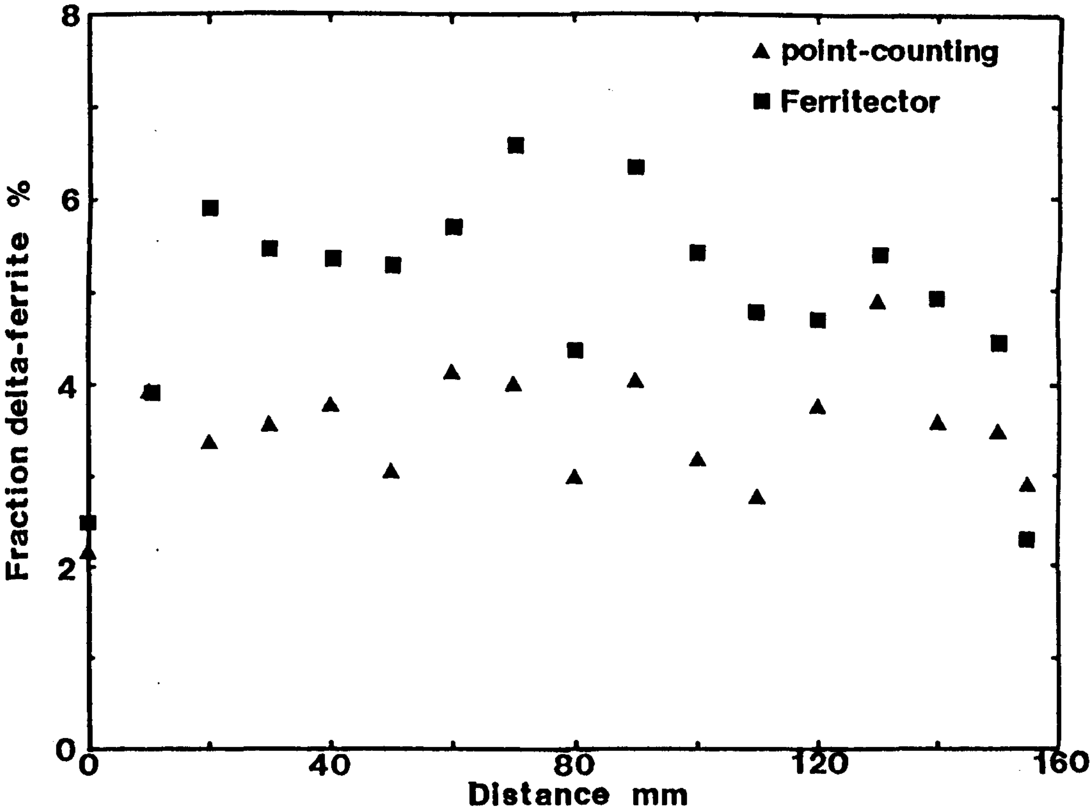

Figure 5.26 Fraction δ-ferrite vs. distance from the surface of the 18/8-slab.

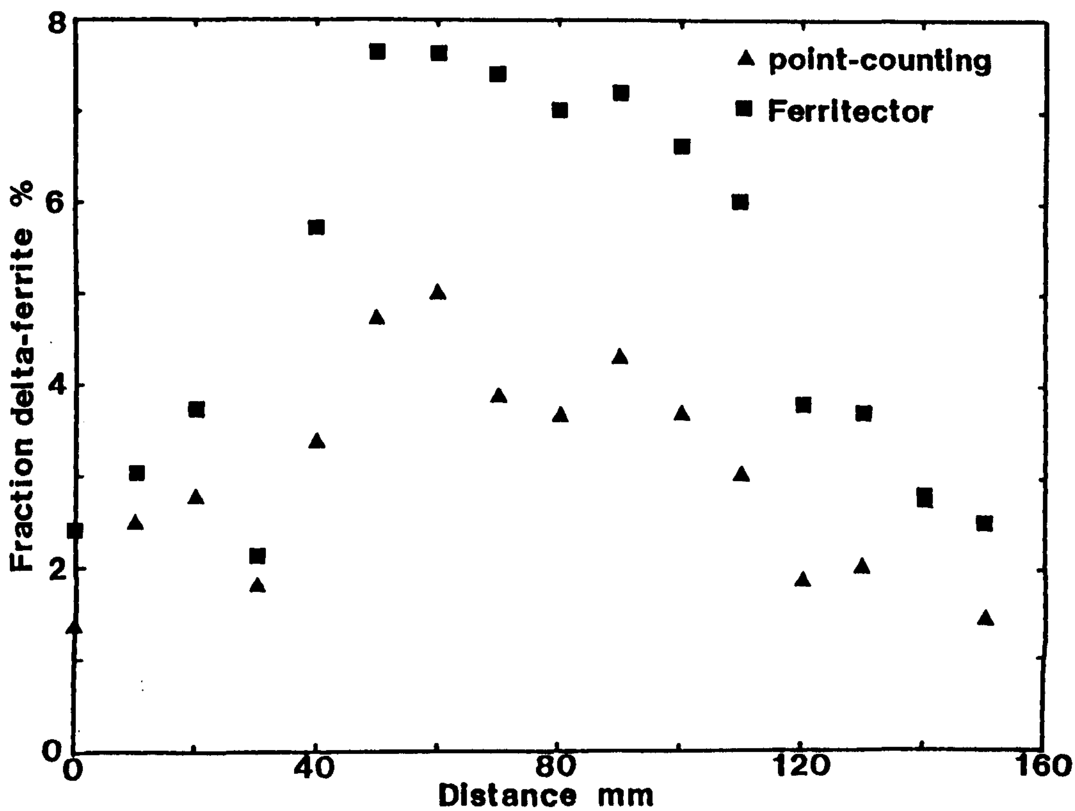

Figure 5.27 Fraction δ-ferrite vs. distance from the surface of the 302-slab.

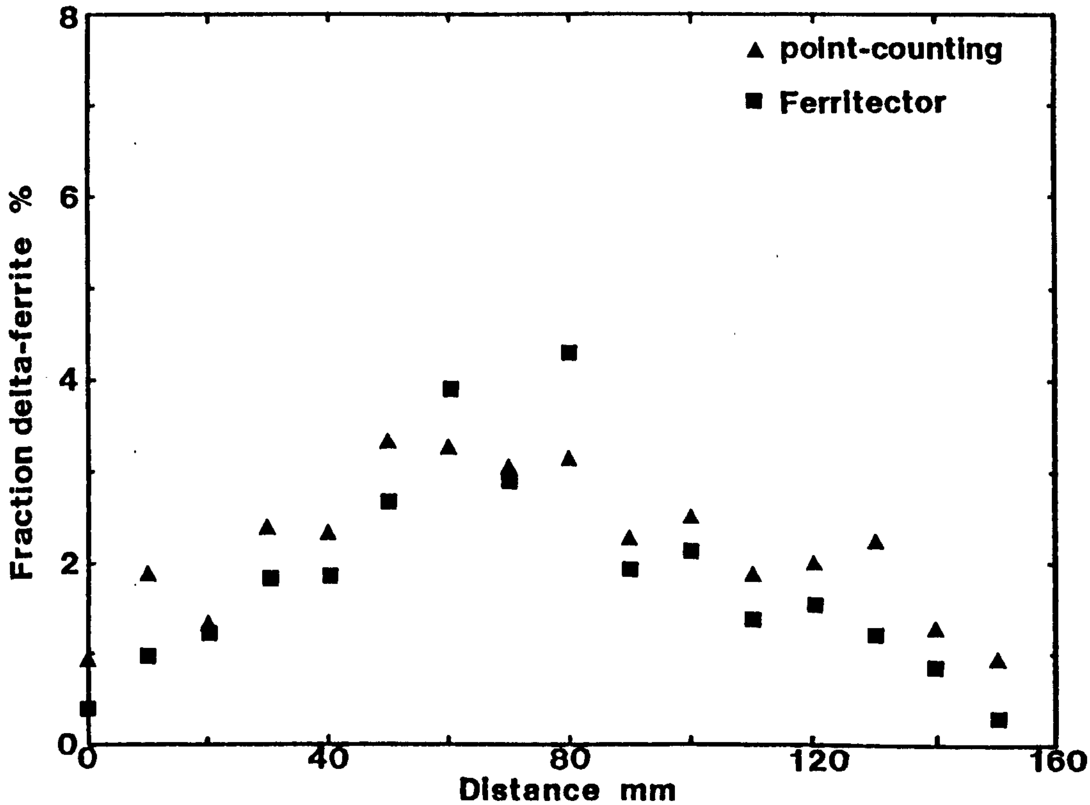

Figure 5.28 Fraction δ-ferrite vs. distance from the surface of the 316-slab.

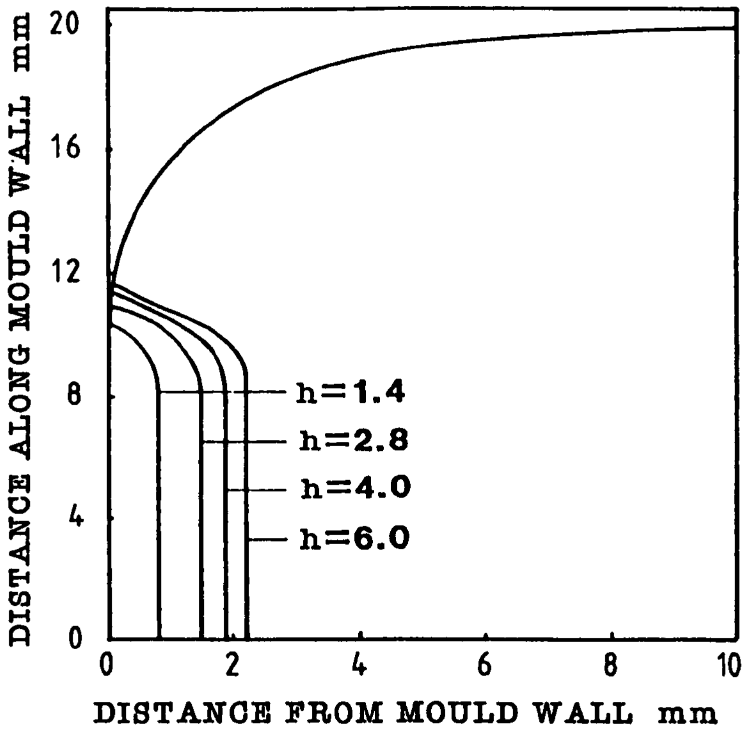

Figure 6.1 Predicted amount of meniscus freezing of 18/10-alloy for different heat transfer coefficients ($kWm^{-2}K^{-1}$).

(ΔT = 0K, t = 0.3s, f_s = 0.2, He)

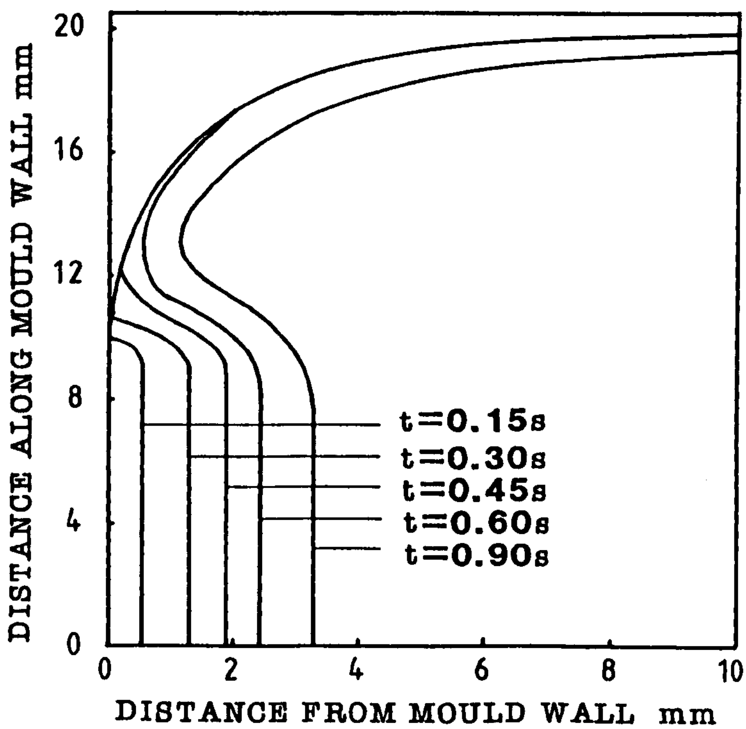

Figure 6.2 Predicted amount of meniscus freezing of 18/10-alloy for different healing times.

(ΔT = 5K, h = 2.5$kWm^{-2}K^{-1}$, f_s = 0.2, He)

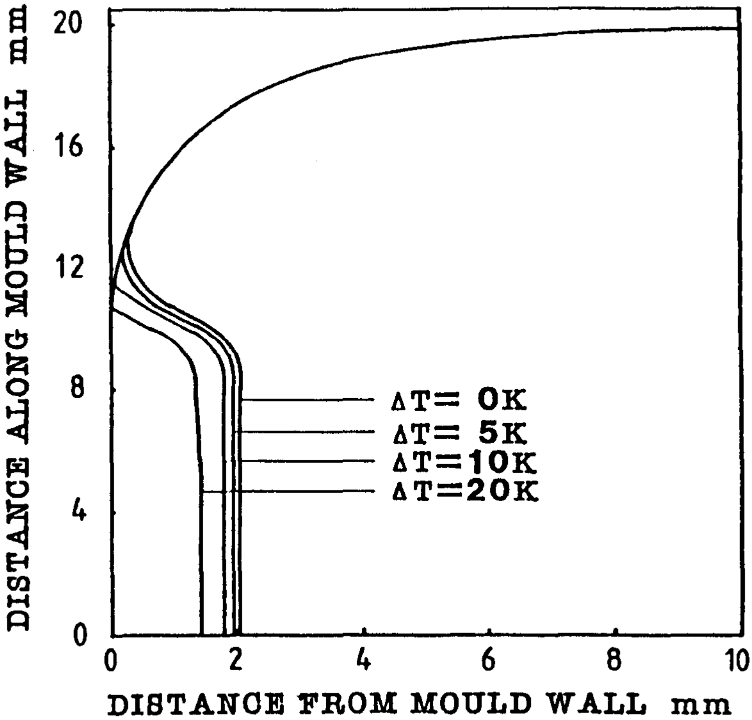

Figure 6.3 Predicted amount of meniscus freezing of 18/10-alloy for different superheats. (t = 0.6s, f_s = 0.2, h = 1.85 $kWm^{-2}K^{-1}$)

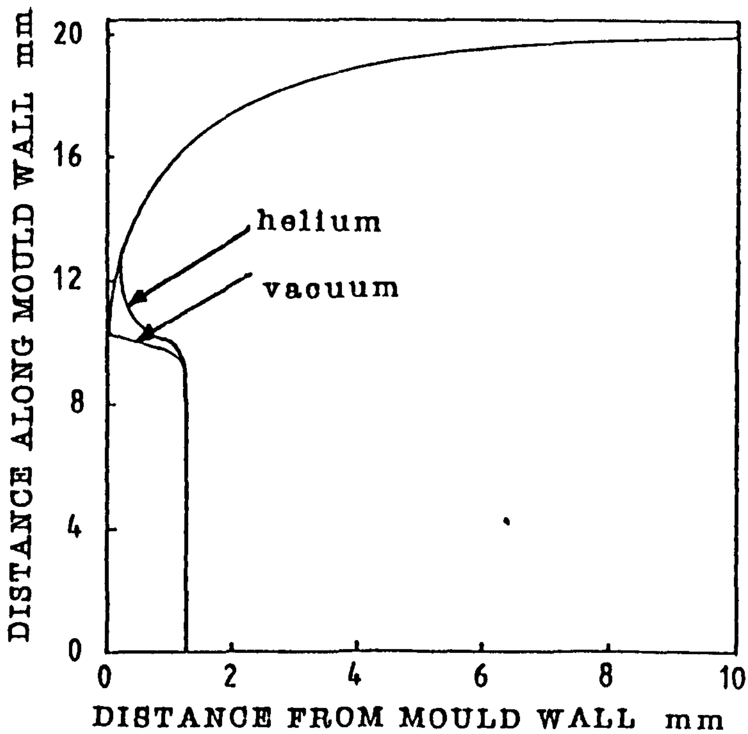

Figure 6.4 Predicted amount of meniscus freezing of 18/10-alloy for different atmospheres.
(ΔT=5K, t=0.3s, h=2.5kW $m^{-2}K^{-1}$)

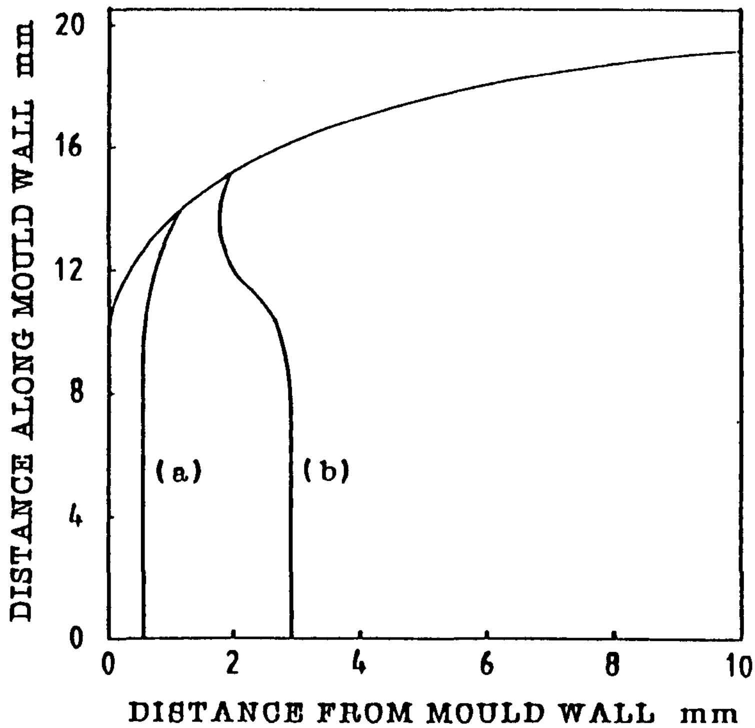

Figure 6.5 Predicted amount of meniscus freezing of 18/10-alloy for different film thicknesses.
(a) 1.0mm (b) 0.1mm

(ΔT=5K, k_f=1.5$Wm^{-1}K^{-1}$, f_s=0.2, t=0.3s, l=5mm)

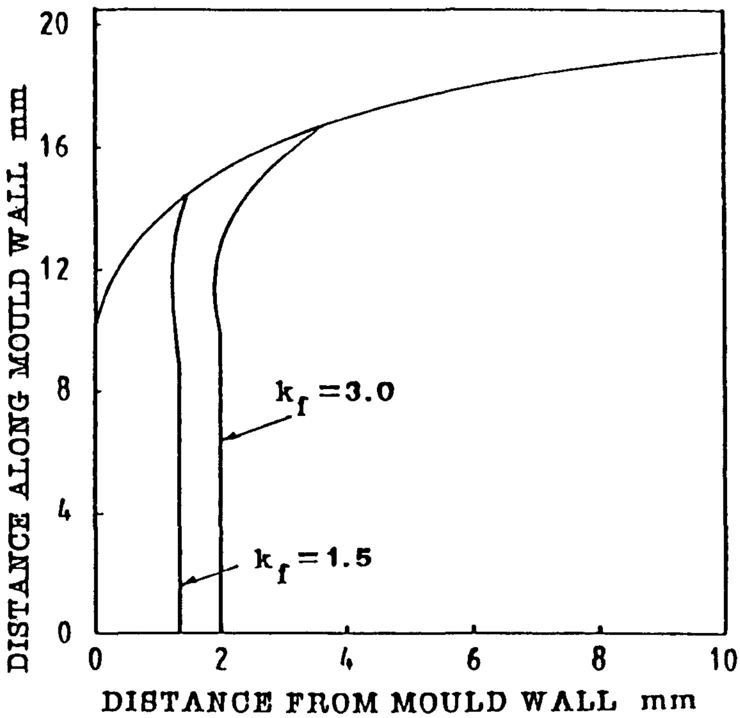

Figure 6.6 Predicted amount of meniscus freezing of 18/10-alloy for different conductivities of the casting flux ($Wm^{-1}K^{-1}$)
(ΔT=5K, t=0.3s, f_s=0.2, l=5.0mm, s=0.5mm)

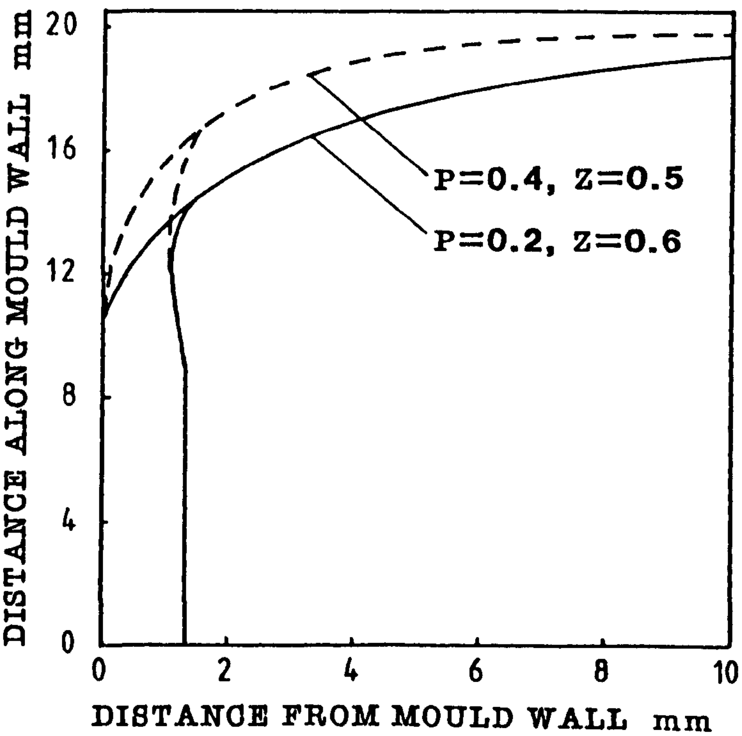

Figure 6.7 Predicted amount of meniscus freezing of 18/10-alloy for different meniscus shapes.

(ΔT=5K, t=0.3s, k_f=1.5$Wm^{-1}K^{-1}$, s=0.5mm, l=5mm)

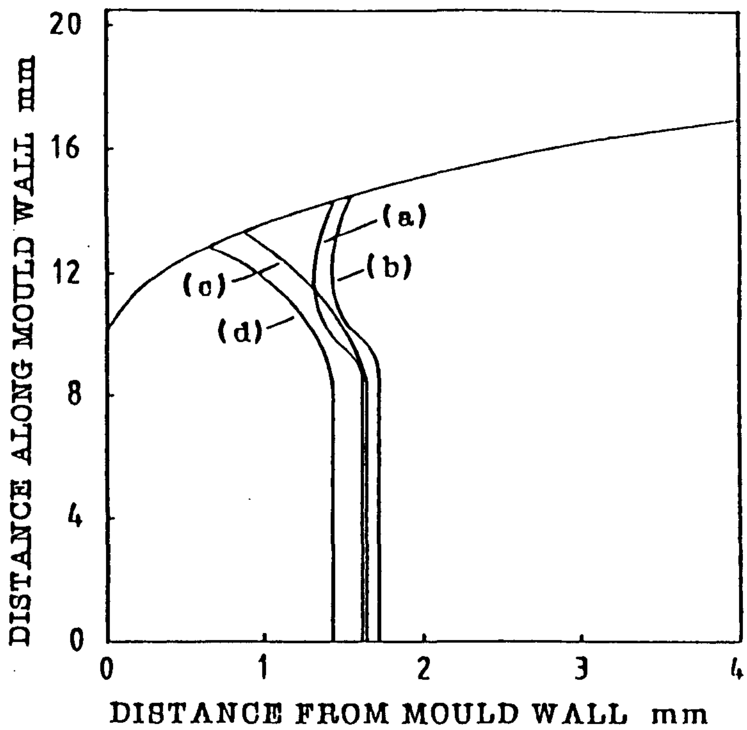

Figure 6.8 Predicted amount of meniscus freezing for steels of different compositions,
(a) 18/10 stainless steel (b) 0.1%C steel
(c) 0.52%C steel (d) 0.7%C steel

(ΔT=5K, k_f=1.5Wm^{-1}K^{-1}, s=0.5mm, t=0.3s)

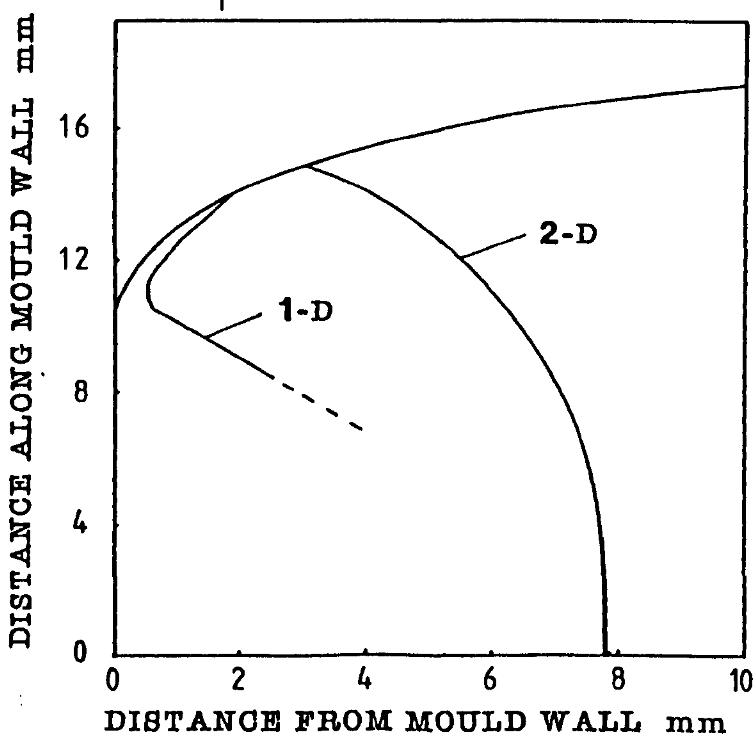

Figure 6.9 Predicted amount of meniscus freezing for 1-dimensional and 2-dimensional heat flow analyses.

(ΔT=0K, t=1.76s, k_{He}=0.36Wm^{-1}K^{-1},
h=11kWm^{-2}K^{-1})

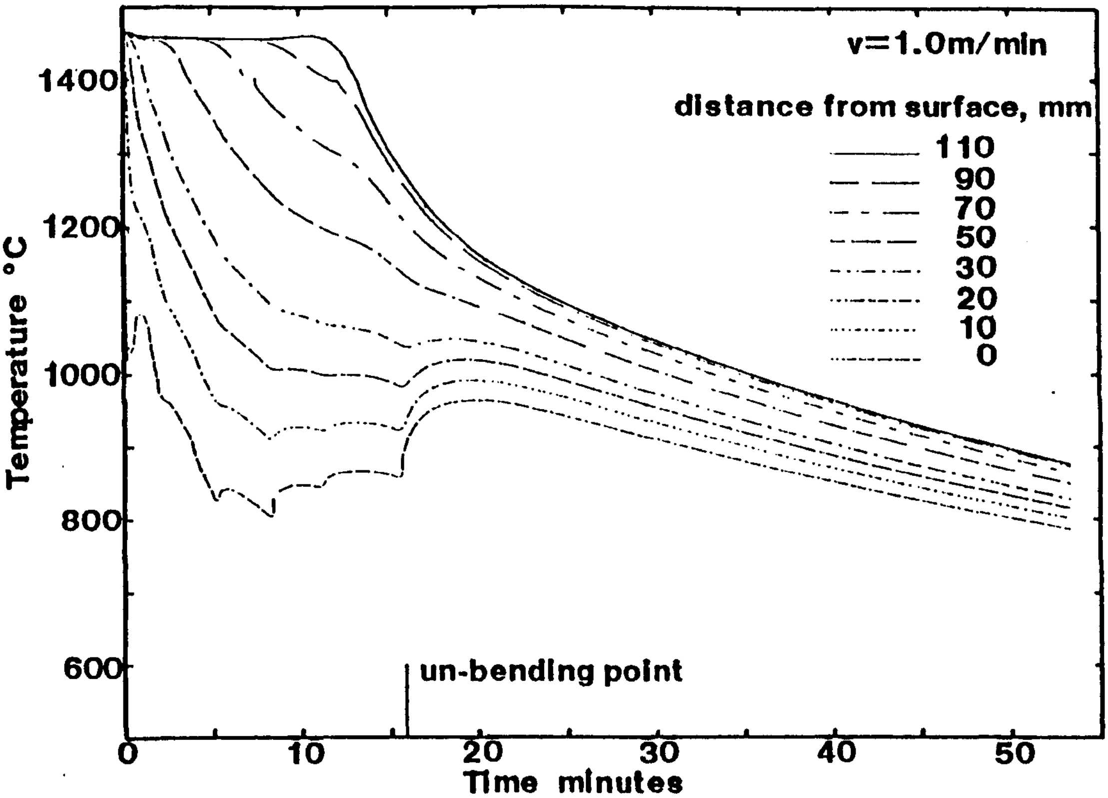

Figure 6.10(a) Predicted thermal history for the conventional cooling system of Nozaki et al.[126].

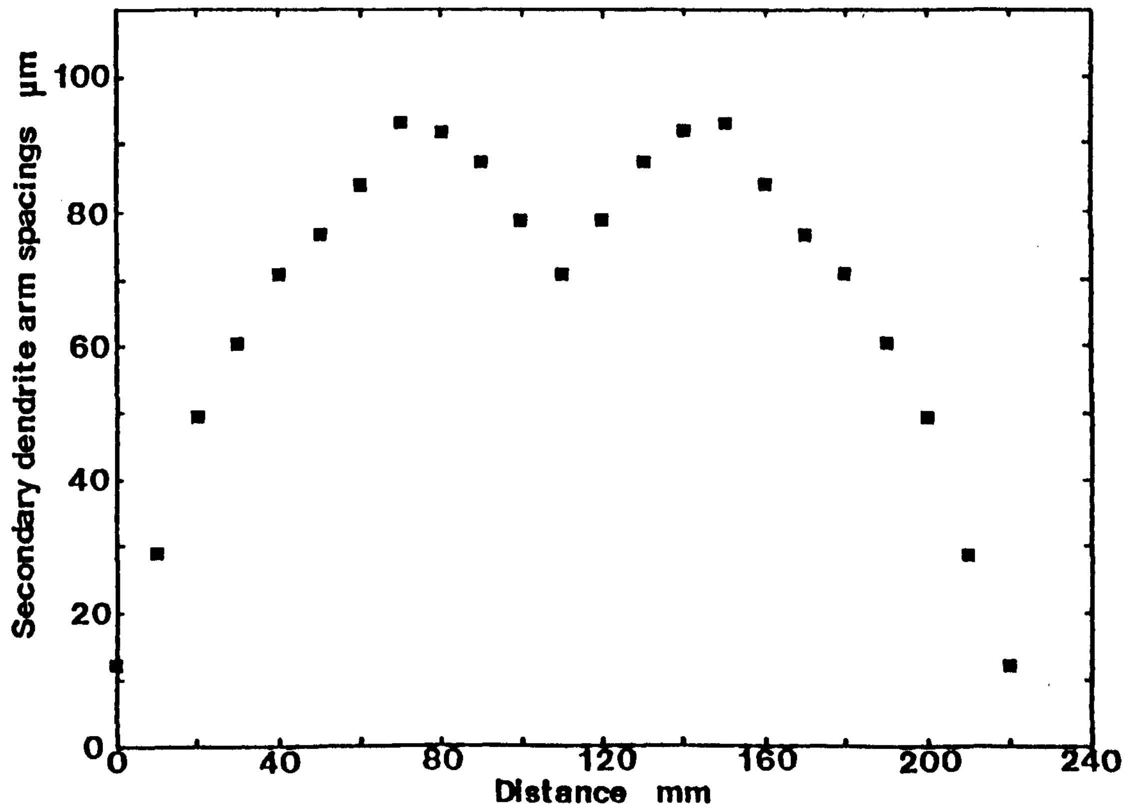

Figure 6.10(b) Secondary dendrite arm spacings vs. distance from the surface of the slab for the conventional cooling system[126].

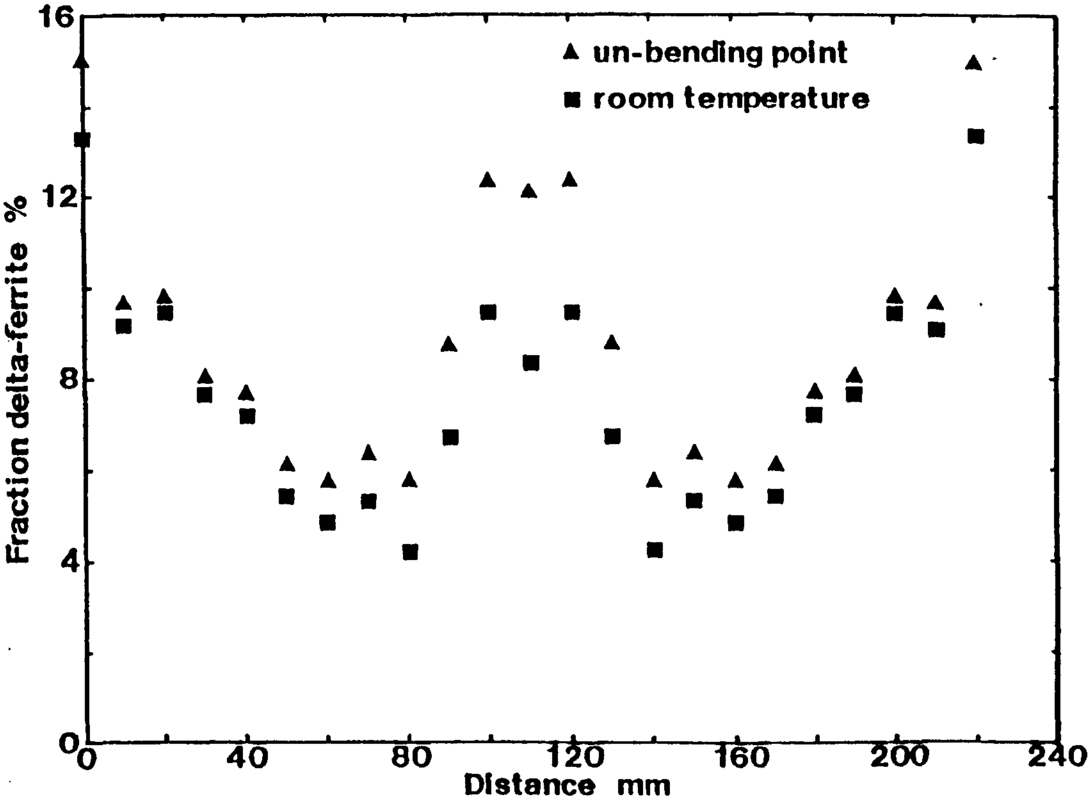

Figure 6.10(c) Fraction δ-ferrite vs. distance from surface for the conventional cooling system[126].

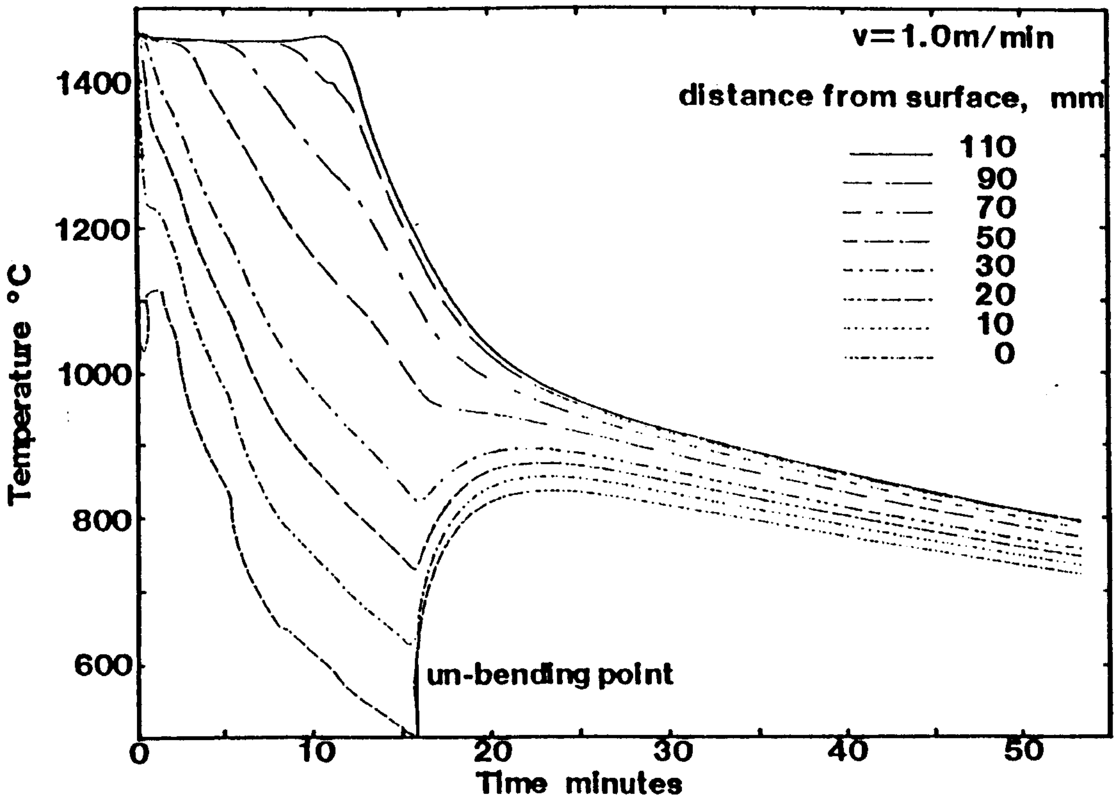

Figure 6.11(a) Predicted thermal history for the modified cooling system of Nozaki et al.[126]

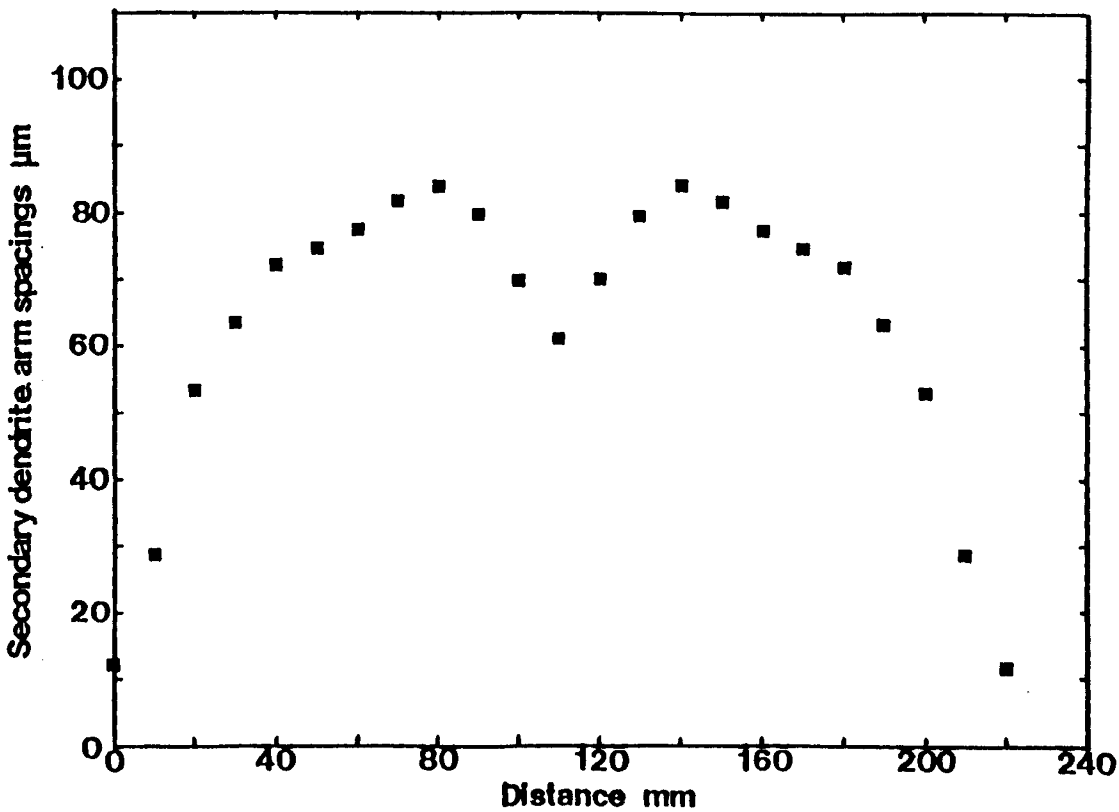

Figure 6.11(b) Secondary dendrite arm spacings vs. distance from surface for the modified cooling system[126].

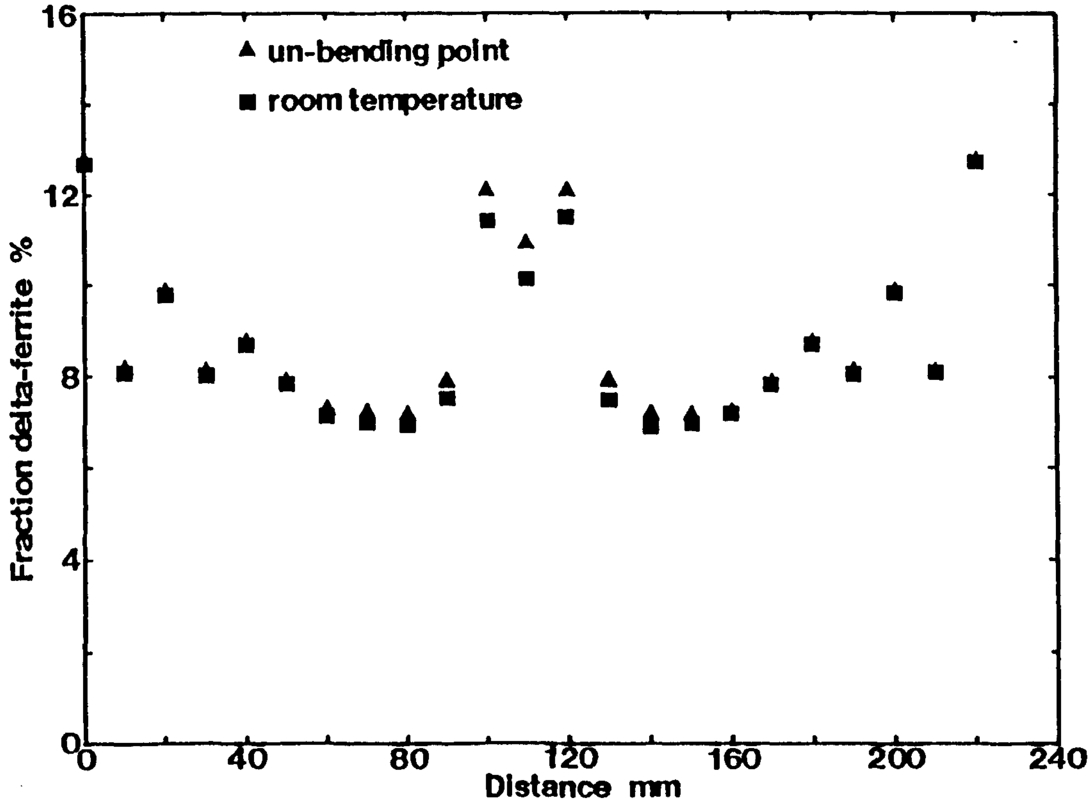

Figure 6.11(c) Fraction δ-ferrite vs. distance from surface for the modified cooling system[126].

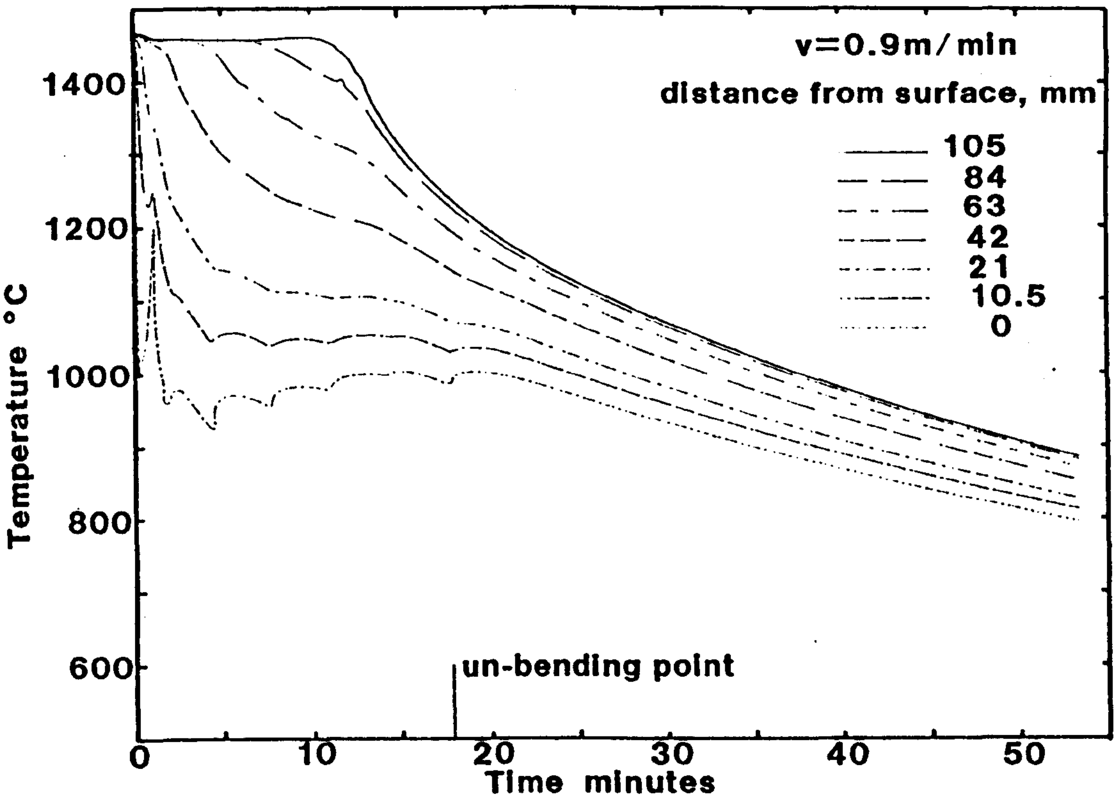

Figure 6.12(a) Predicted thermal history for the conventional cooling system of Larrecq et al.[199]

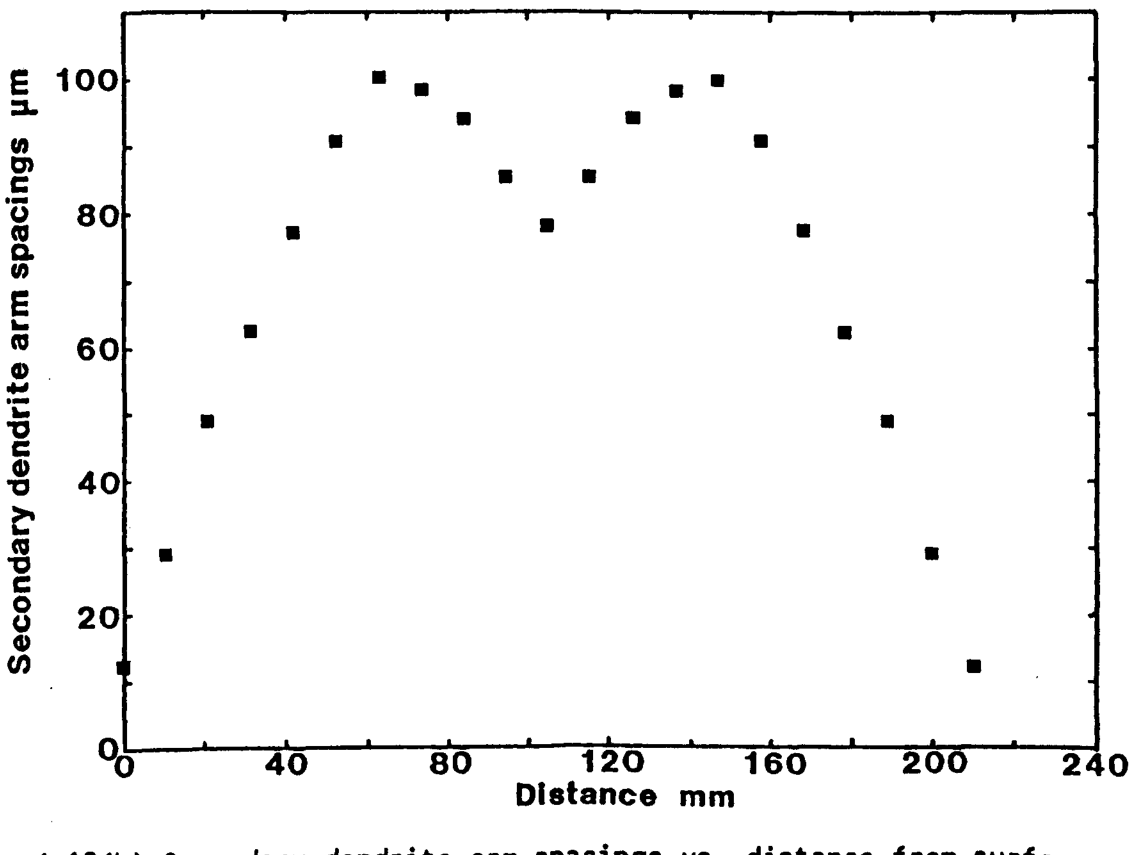

Figure 6.12(b) Secondary dendrite arm spacings vs. distance from surface for the conventional cooling system[199].

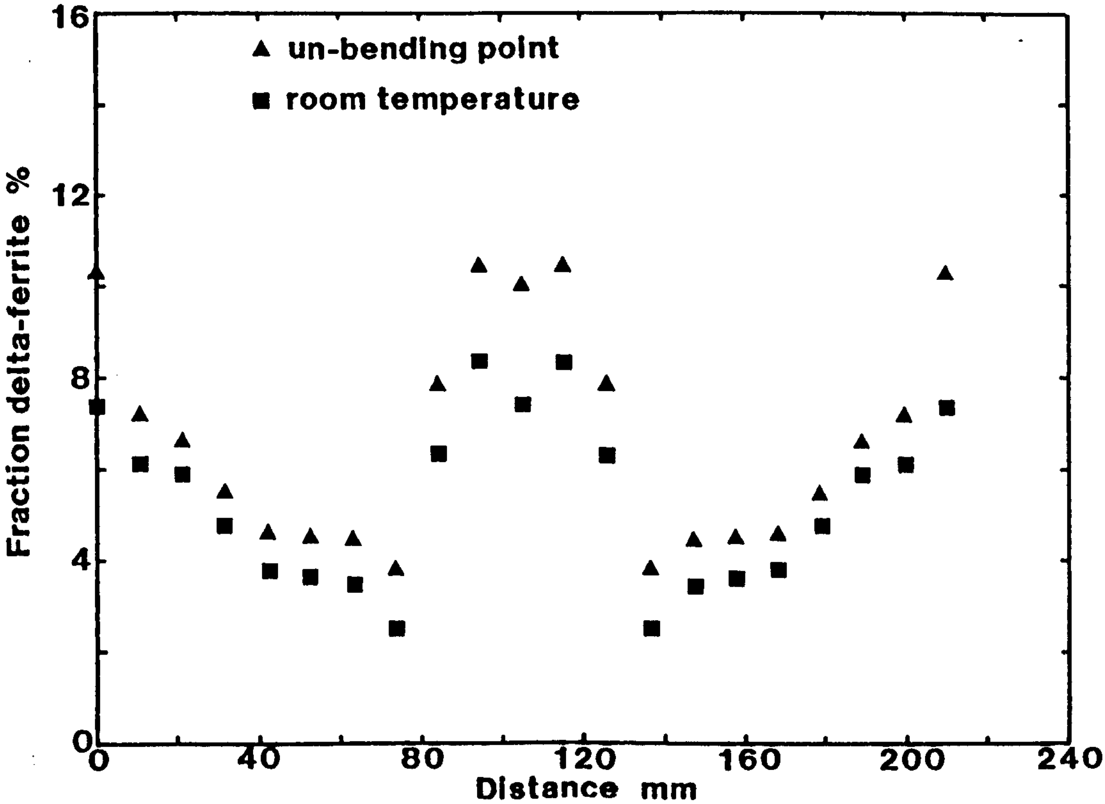

Figure 6.12(c) Fraction δ-ferrite vs. distance from surface for the conventional cooling system[199].

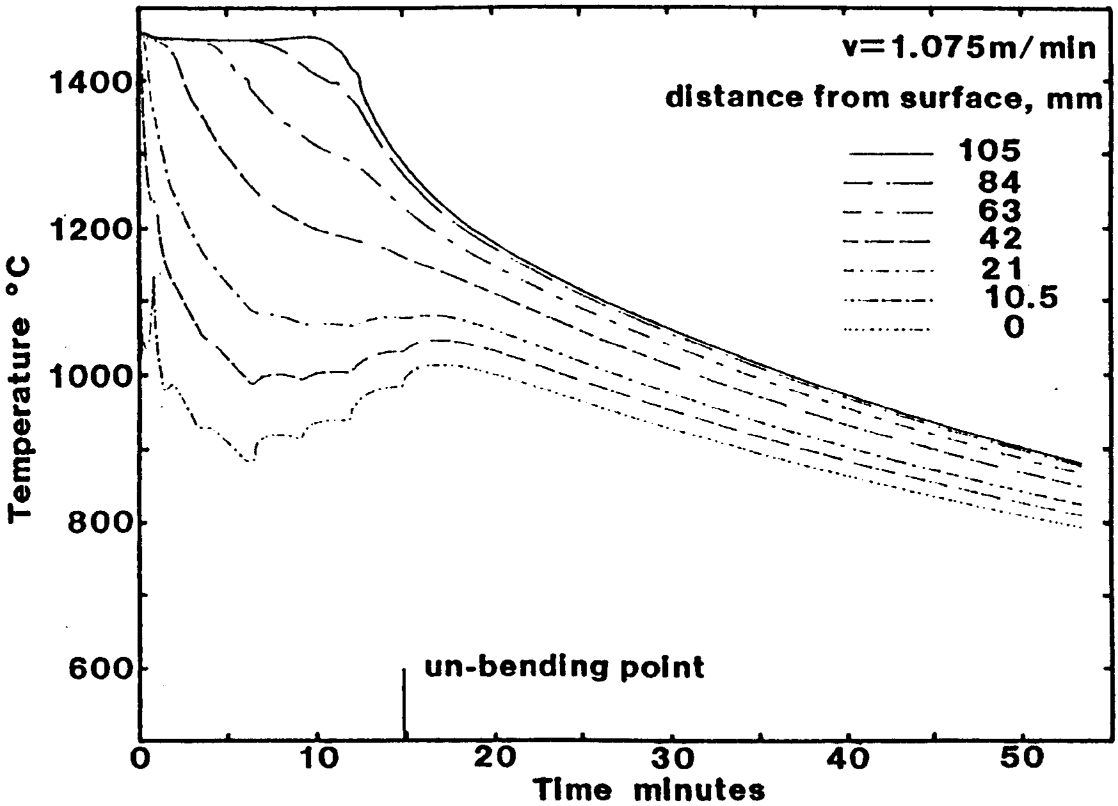

Figure 6.13(a) Predicted thermal history for the optimised cooling system of Larrecq et al.[199]

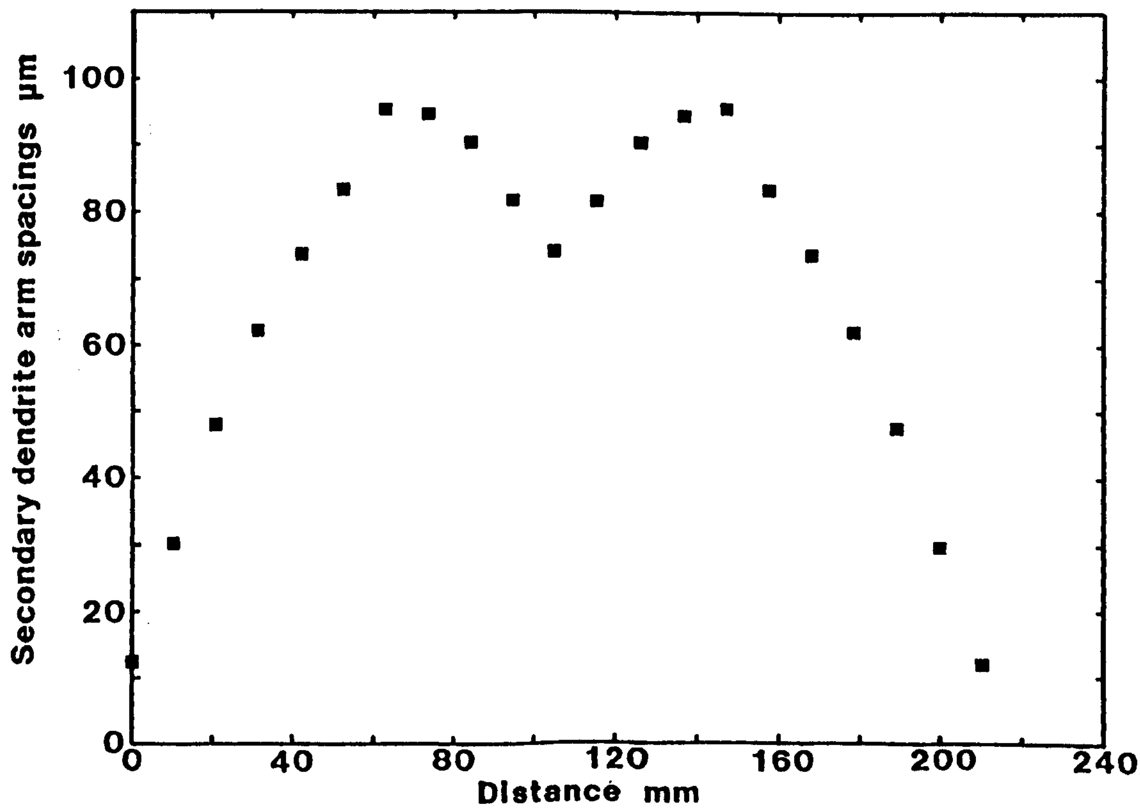

Figure 6.13(b) Secondary dendrite arm spacings vs. distance from surface for the optimised cooling system[199].

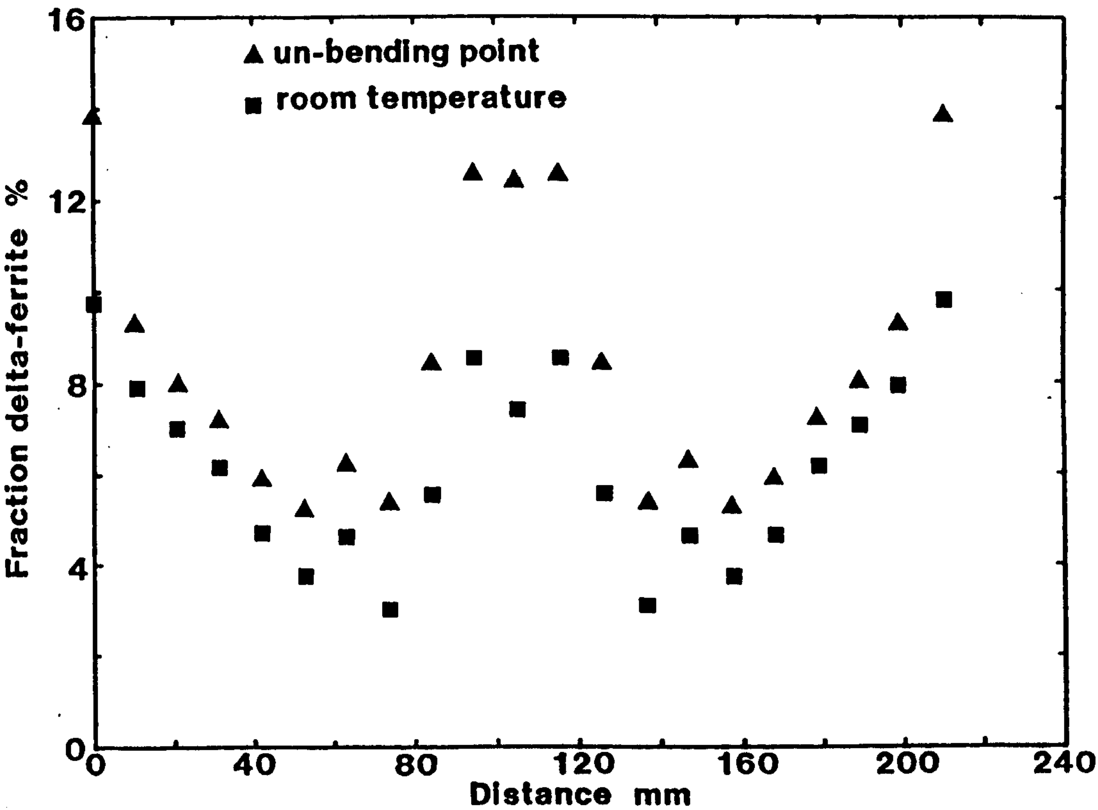

Figure 6.13(c) Fraction δ-ferrite vs. distance from surface for the optimised cooling system[199].

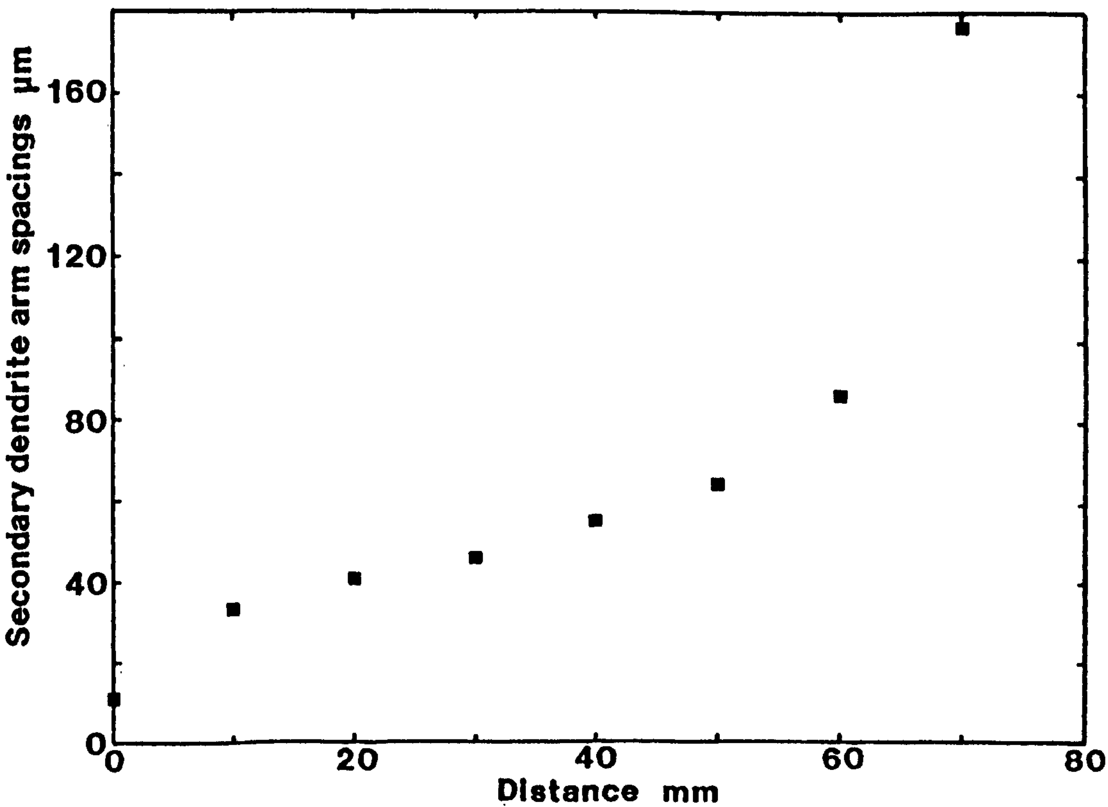

Figure 6.14 Measured variation of secondary dendrite arm spacings with distance from surface in the 18/8-slab (half-thickness).

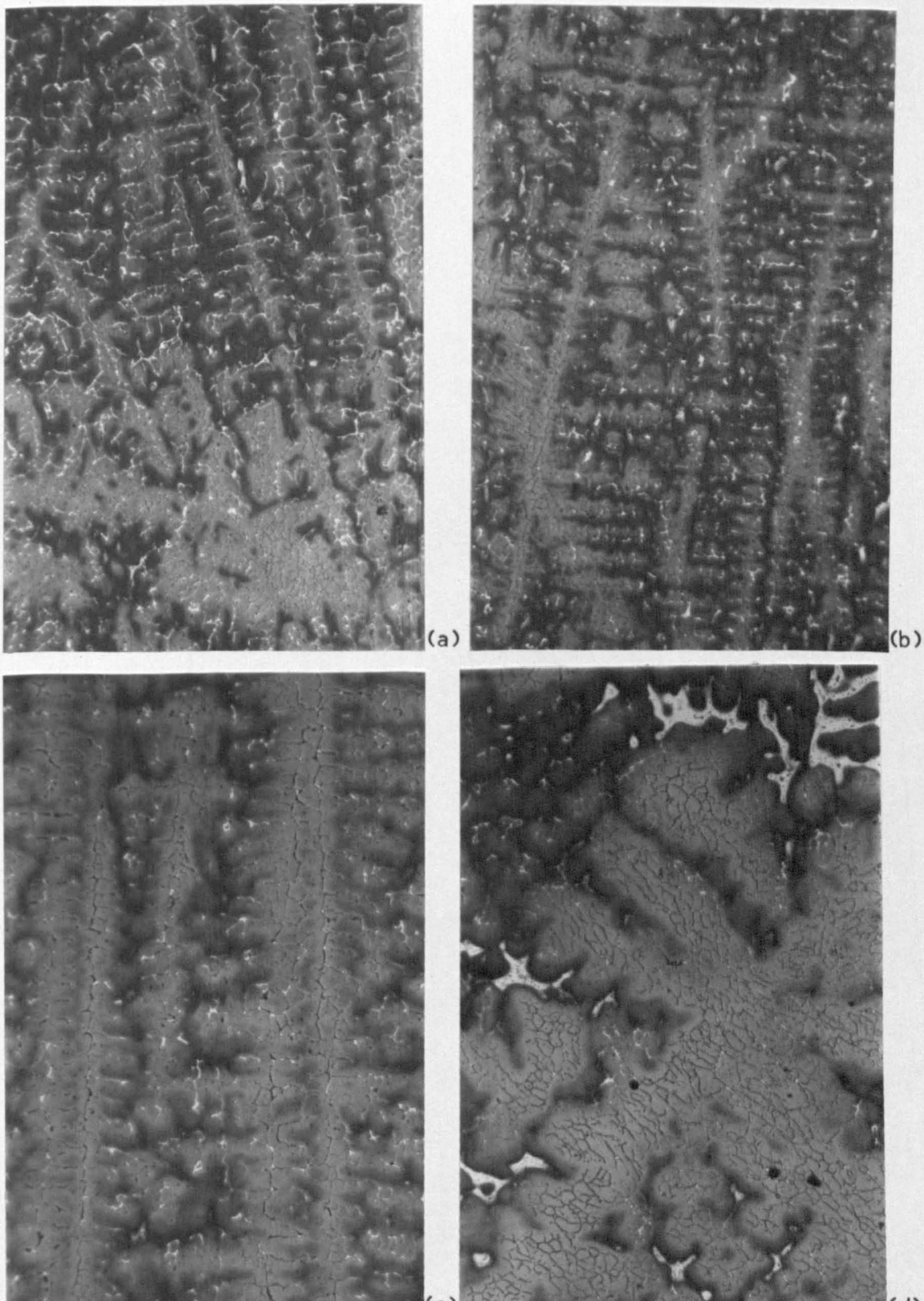

Figure 6.15 Microstructures at different distances from the surface of the 18/8-slab (colour etchant).
(a) 10mm (b) 30mm
(c) 50mm (d) 70mm

0.25mm

σ